Collisional Activation and Target Capture with Massive Ions by means of Magnetic-Sector Mass Spectrometry.

by Jacqueline Anne Mosely.

Submitted for the qualification of Doctor of Philosophy

University of Warwick

November 1996

Table of Contents.

List of Figures.

List of Tables.

Acknowledgements.

Throughout the course of my PhD, many people have given me invaluable support and assistance. In particular I would like to thank the following:

- Professor Peter Derrick for his guidance and encouragement which is greatly appreciated.

- Dr Richard Gallagher for his patient tuition on the mass spectrometer used in this work and for answering endless questions.

- Dr Helen Cooper for the introduction to mass spectrometry of fullerenes and for her support and motivation.

- Dr Albert Heck and Dr Thomas Drewello for their ideas and discussions regarding this thesis.

- All the members of Professor Derrick's research group (MMM), both past and present, whom I have had the pleasure of knowing and working alongside during my PhD. Especially I would like to thank Ms Tracey Rafferty, Mr Gary Shield, Ms Julie Varney, Mr James Wallace, Dr Ulla Andersen and Dr Jan Axelsson for their support and friendship.

- Dr David Bell and Mr Andrew West for their support regarding the studies on peptides.

- SmithKline Beecham Pharmaceuticals and the Engineering and Physical Sciences Research council for financial support.

- My parents David and Gayner Mosely for their encouragement and support throughout my educational life, especially the last three years.

- My brothers Iain and Paul Mosely for their encouragement and support and for being there.

- My husband Mr Adam Jarvis for his love and understanding and for all the encouragement and support he has given me both professionally and personally.

Declaration.

I hereby declare that this thesis is my own work and that, to the best of my knowledge and belief, it contains no material previously published or written by another person, nor material which has been accepted for the award of any other degree or diploma of a university or institute of higher education, except where due acknowledgement is made in the text.

Jacqueline Anne Mosely.

Abstract.

A significant part of this thesis is given to the study of the phenomena of target capture. The noble gases were observed to form adducts with $C_{60}^{+\cdot}$ and $C_{70}^{+\cdot}$, that are proposed to be endohedral in structure. The gas atom is proposed to penetrate the fullerene cage through a window formed by breaking carbon-cage bonds. The diatomic gases were observed to give a range of adducts that are proposed to be exohedral, endohedral and dopey-ball structures. The different structures are proposed to result from different mechanisms which take place preferentially depending on the collision energy. Multiatomic target gases also produced a range of adducts, proposed to be either exohedral or endohedral in structure although no further conclusion could be drawn from the evidence obtained. Target capture of methane was achieved with two peptides. This was found to be the most effective collision gas for the collision-induced decomposition of the protonated peptides.

CHAPTER ONE: *Introduction.*

1.1 History of Tandem Mass Spectrometry.

The first tandem mass spectrometer was constructed by JJ Thomson [1]. It comprised of two magnets, connected in series, whose fields were perpendicular to one another. At this period in time, the pressures within mass spectrometers were relatively high compared to those in modern day instruments. This resulted in a considerable number of ion-molecule reactions occurring in the instruments. JJ Thomson identified a number of such reactions, but the nature of metastable and collision-induced dissociative processes remained unexplained until 1945 [2,3-5]. The unduly high pressure was really a problem in JJ Thomson's time, so that a great deal of study went into improving the vacuum [6-7]. Today, mass spectrometrists aim to create and control circumstances of high pressures as a means to study ion-molecule reactions. In particular, tandem mass spectrometry has proved invaluable in the study of ion-molecule reactions, as it allows the selection of an ion and subsequent analysis of its reaction products. This application of mass spectrometry has helped scientists with the proverbial "*needle in a haystack*" problem. Components can be singled out from a mixture and analysed within the mass spectrometer. Mass spectrometry has the added advantage over other analytical techniques of using only extremely small sample concentrations. Modern instruments can detect attomolar amounts of sample [8].

There are three different stages in a mass spectrometer: generation of ions, analysis of ions and detection of ions. The methods for generating ions fall under three categories, the first of which is thermal ionisation. Thermal ionisation describes electron impact [9] and chemical ionisation [10], electron impact being the older of the two, and involves the sublimation or evaporation of the sample to form a gas. Fast atom bombardment [11-12] and liquid secondary ion mass spectrometry [13-14], which are essentially very similar to each other, matrix-assisted laser desorption/ionisation

[15-16] and plasma desorption [17] all rely on impinging beams of secondary particles to provide enough energy from an impact to induce both vapourisation and ionisation. The final group of ionising techniques contains electrospray [18-20], thermospray [21] and field desorption/ionisation [22].

Once ions are present in the gas phase, they can be mass analysed by one, or a combination of more than one, of the five types of mass analyser. The five options are electric and magnetic sectors [23-24], quadrupole [25-26], time-of-flight [27-28], ion trap [29] and ion cyclotron resonance [30-31]. Sector instruments were the first method of mass separating ions, being the technique introduced by JJ Thomson [32] and used by FW Aston [33] in the early days of mass spectrometry. The most recent development in mass analysers is the introduction of Fourier transforms to ion cyclotron resonance [34-35]. Such instruments are known as Fourier transform-ion cyclotron resonance mass spectrometers.

Detection of ions [36-38] in modern-day sector-instruments is by signal multiplication devices and direct measurement ion collectors. The type of detector employed is dependent wholly on the application. Signal multiplication (electron multiplication) is the most common form of detector as it allows rapid scanning of an ion beam.

1.2 Theory of Magnetic-Sector Instruments.

Magnetic-sector instruments employ magnetic fields sometimes combined with electric fields as a means of separating ions according to their mass-to-charge ratios [36-37, 39-40]. Electric fields are generated in electrostatic analysers, otherwise known as electric sectors. Magnetic fields are generated in magnetic analysers, otherwise known as magnetic sectors.

1.2.1 Electric Sectors.

Electric sectors use an electric field to separate ions subjected to the same accelerating potential (V_{acc}), yet differing in their kinetic energies. An electric field is applied across two parallel cylindrical plates of mean radius *r*. An ion beam diverging from the source slit passes between these plates. The radial electric field (*E*) produced by these plates will affect the ions such that ions of greater or lesser energies will follow paths of greater or lesser radii through the electric sector. From classical physics, the ion kinetic energy is given by,

$$V_{acc} ze = \frac{1}{2} mv^2 \qquad (1)$$

where *m* is the mass of the ion, *v* is the velocity of the ion, *z* is the number of charges on the ion and *e* is the charge of an electron. The equation of motion of an ion under the influence of a radial electric field (*E)* of radius *(r)* is given by,

$$Er = \frac{mv^2}{ze} \qquad (2)$$

Ion are spatially focused and dispersed according to their kinetic energy-to-charge ratios. This is illustrated in figure 1.1.

1.2.2 Magnetic Sectors.

When ions enter a homogeneous magnetic field, they travel in a circular path of radius *r'*, in a plane normal to the direction of the magnetic field (*B*). The effect on the ions can be described by equation (3).

$$Br' = \frac{mv}{ze} \qquad (3)$$

Ions will be dispersed according to their momentum-to-charge ratios. As the velocity of an ion will affect its motion in a magnetic field, magnetic sectors can be said to be velocity dispersive. This is illustrated in figure 1.2.

1.2.3 Combining Electric and Magnetic Sectors.

There is no significant difference in the results from instruments combining electric and magnetic sectors in different orders. Instruments which comprise an electric sector followed by a magnetic sector are known as forward-geometry instruments. A combination whereby the magnetic sector preceded the electric sector would give a reverse-geometry instrument.

1.2.3.1 The Double-Focusing Principle.

Electric sectors focus ions spatially and disperse ions according to their energies. Magnetic sectors also focus ions spatially and disperse them according to their momenta. It is arranged that the velocity dispersive action of an electric sector is contradictory to that of the magnetic sector and that when combined the velocity dispersive effects of the two sectors cancel each other out. Overall, therefore, ions are velocity focused to at least the first-order. The two counts of focusing, the overall velocity focusing and directional focusing, give rise to the term double-focusing, when a combination of magnetic and electric sectors is used [40-42]. This is illustrated in figure 1.3. The performance of double-focusing *tandem* mass spectrometers has been characterised by enhanced resolution and accuracy of mass assignment of $\pm$ 0.3 Da, or better, for some large peptides [43].

1.2.3.2 Linked Scanning.

There are three parameters in a double-focusing mass spectrometer which can be altered to give information on different aspects of mass spectrometry: the electric field, the magnetic field and the ion accelerating potential. These parameters can be varied independently or two of these parameters can be controlled simultaneously.

When two of the parameters are scanned simultaneously, the outcome is termed a linked scan [44-48]. Consider the reaction (4) taking place in a region of zero electric field.

$$m_1^+ = m_2^+ + m_n \qquad (4)$$

Following different types of scan law permits the suppression or promotion of particular components of this reaction. For example, the fragment ion m_2^+ will have the same velocity as the precursor ion m_1^+. The magnetic field and the electric field can be scanned simultaneously, so that only ions whose velocities are the same as m_1^+ (*i.e.* fragments of m_1^+) are able to pass through both sectors to the detector. The reason is evident from equation (5), which is the ratio of equations (3) and (2).

$$\frac{B}{E} = \frac{1}{v} \qquad (5)$$

This type of scan is termed a B/E = constant linked-scan and the resulting spectra show fragment ions produced from the decomposition of ions of velocity *v*. In the case of tandem mass spectrometry, precursor ions can be mass-selected in which case the product ions result from the decomposition of a single incident ion with mass m_1 and velocity v_1 [41].

1.2.3.3 Mass-Analysed Ion Kinetic Energy Spectroscopy.

If m_1^+ fragmented to m_2^+ in a field-free region, prior to entering an electric sector, the fragment ion, would pass through the electric sector at a potential V_2 given by,

$$V_2 = \frac{m_2}{m_1} \times V_1 \qquad (6)$$

where V_1 is the potential at which the parent ion would be transmitted in the absence of a gas. Scanning the electric field with a constant ion accelerating potential and magnetic field would separate ions according to their translational energies. The spectrum would represent a mass-analysed ion kinetic energy (MIKE) analysis [42,49-51].

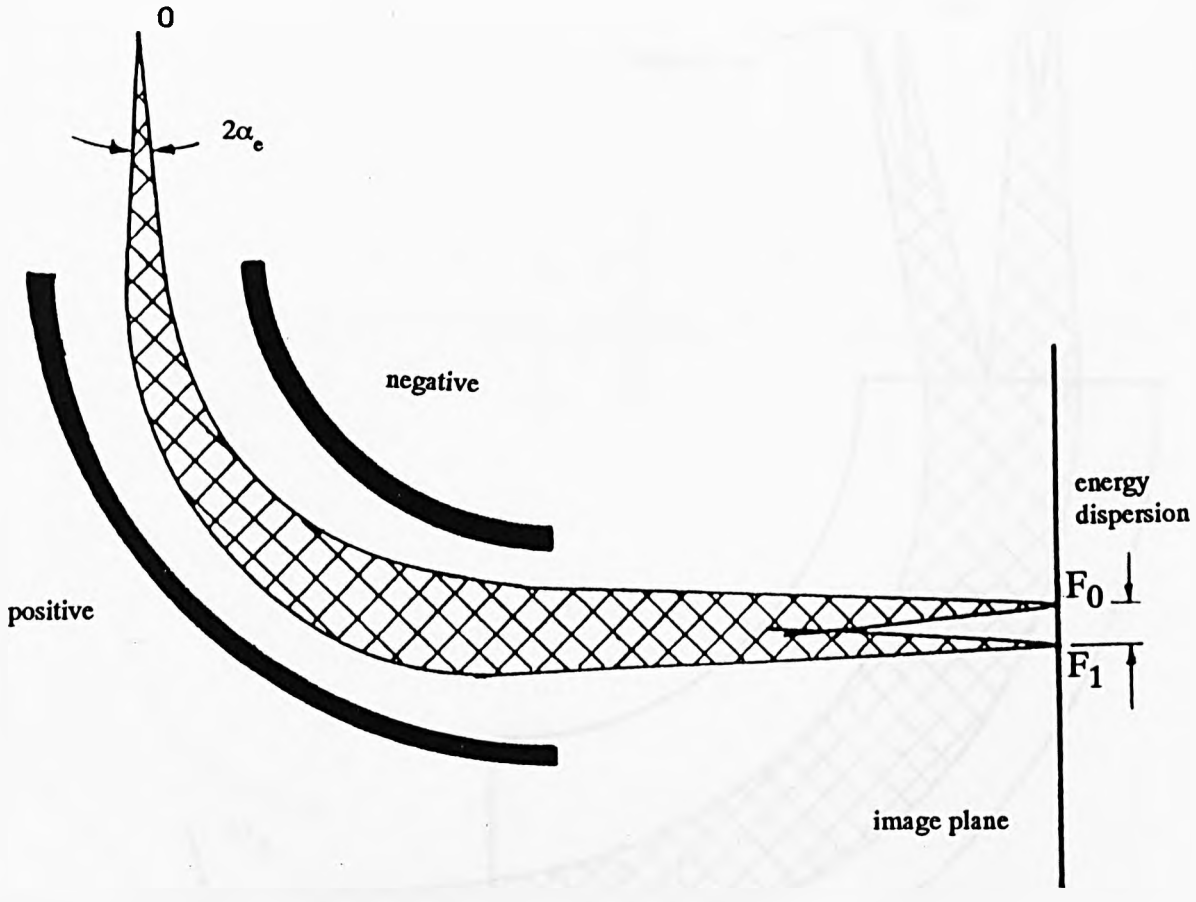

0 Object point for the source of ions with mass M_0 and M_1, energies E_0 and E_1, with angular divergence of $2\alpha_e$ (where $E_1 > E_0$).

F_0 Focus point for ions with energy E_0 , mass M_0 and M_1 and with angular divergence of $2\alpha_e$.

F_1 Focus point for ions with energy E_1 , mass M_0 and M_1 and with angular divergence of $2\alpha_e$.

Figure 1.1: Ion optics for an electric sector.

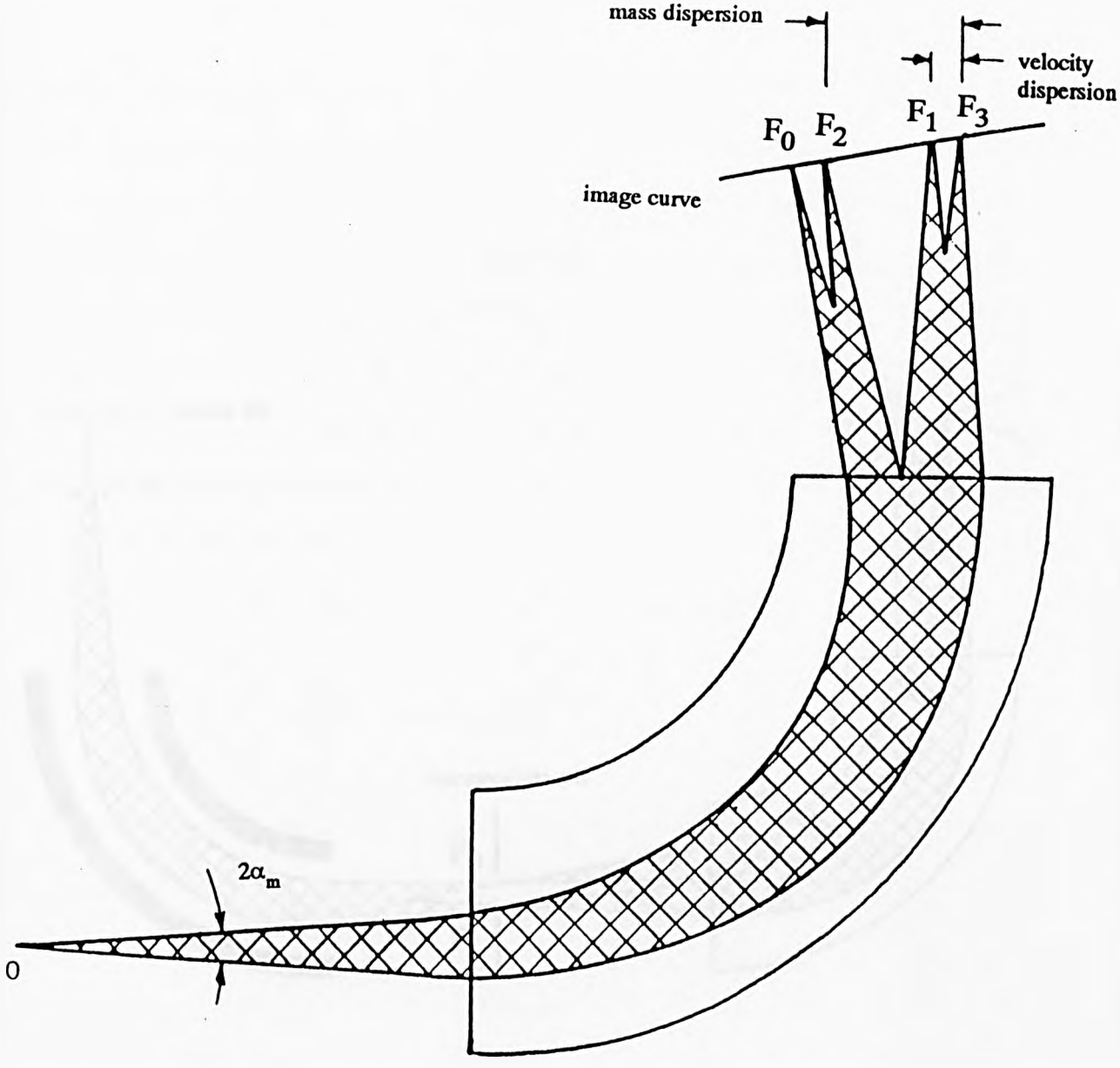

0 Points source for ions of mass M_0 and M_1 and velocity v_0 and v_1, with angular divergence of $2\alpha_m$ (where $M_1 > M_0$, $v_1 > v_0$ and $M_1v_0 > M_0v_1$).

F_0 Direction focus point for ions of mass M_0 and velocity v_0.

F_2 Direction focus point for ions of mass M_0 and velocity v_1.

F_1 Direction focus point for ions of mass M_1 and velocity v_0.

F_3 Direction focus point for ions of mass M_1 and velocity v_1.

Figure 1.2: Ion optics for a single focusing magnetic sector.

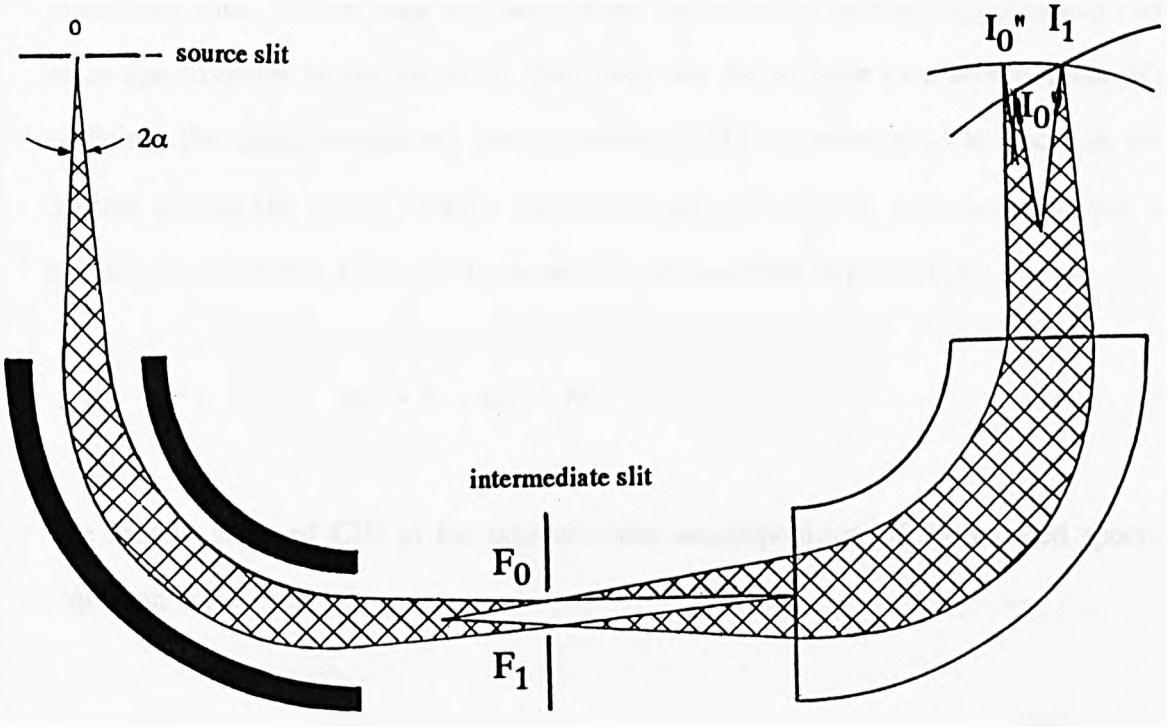

I_0' Velocity focus point for ions of mass M_0 and angular divergence $\alpha = 0$

I_0'' Direction focus point for monoenergetic ions of mass M_0 and angular divergence of 2α

I_1 Double-focusing point for ions of mass M_1.

Figure 1.3: The double-focusing principle.

1.3 Dynamics of Collision-Induced Dissociation.

Fragmentation of an ion, whether as a result of a collision or not, can occur at any point in a mass spectrometer. Ions which fragment directly after being formed, in the ion source, are described as unstable ions. Ions which decompose at some point after leaving the ion source but before reaching the detector are thought of as metastable ions. Stable ions will survive the full duration of their flight through the mass spectrometer to the detector. For ions that decompose as a direct result of a collision, the collision-induced decomposition (CID) is understood to occur in two distinct phases [49, 52-53]. Firstly collisional activation (CA), sometimes known as collisional excitation, gives rise to an excited intermediate (equation (7)).

$$m_1^+ + N \rightarrow m_1^{+*} + N' \qquad (7)$$

The second stage of CID is the unimolecular decomposition of the excited species (equation (8)).

$$m_1^{+*} \rightarrow m_2^+ + m_n \qquad (8)$$

The overall equation for the CID process is given in equation (9). This accounts for energy and mass,

$$m_1^+ + N + q \rightarrow m_2^+ + m_n + N' + T \qquad (9)$$

where m_1^+ is the parent ion and m_1^{+*} the excited parent ion, m_2^+ the fragment ion, N the pre-collisional state of the target gas and N' the post-collisional state of the target gas, q is the amount of translational energy of the colliding species that is converted into internal energy and T is the translational energy liberated in unimolecular dissociation.

1.3.1 Collisional Activation.

Collisional activation is a highly popular method for exciting ions in mass spectrometric experiments. Firstly the collisional cross-section for a multiatomic ion of around 1620 Da is 4 nm^2 [54]. Other characteristics of collisional activation to be considered are the amount of energy deposited into the ion, how it is distributed and how it can be varied. These characteristics can be controlled to some extent by choice of target gas and control of the local pressure of target gas in the collision region of the instrument. This localised pressure of target gas is achieved in mass spectrometers by differential pumping of the collision cell. The product ion beam emerging from the collision cell will not subsequently be affected by the target gas. Beer's law can then be applied to this type of beam experiment (equation (10)).

$$I = I_0 e^{-n\sigma l} \qquad (10)$$

I and I_0 represent ion beam intensity before and after attenuation with the target gas, n is the number density of the target gas, l is the length of the collision region and σ is the cross-section for all processes that bring about the loss of intensity of the parent ion beam. Such processes include decomposition of the collisionally activated species, charge exchange with the target gas or charge stripping and scattering of ions.

1.3.2 Unimolecular Dissociation.

Unimolecular dissociation of an excited species is deemed a separate stage to collisional activation in collision-induced decompositions, if the relative velocity of the ion and target gas is such that they separate before decomposition of the ion begins. The activated ion is, therefore, assumed to have no memory either of how it was formed in the source or how it was activated. The shortest bond-vibrational periods are 10^{-14} seconds, which sets the minimum limit on the duration of the fragmentation process [49]. An 8 keV ion of mass 100 Da, incident on a target gas, will have a

velocity of just over 10^7 cm/second, sufficient for the separation of the two stages of CID to be justified. Unimolecular dissociation, as well as being dependent on the rate coefficient of reaction, is also dependent on the internal energy distribution of the ion. The rates of dissociation for collisionally activated species have been described by the statistical models, Rice-Ramsperger-Kassel-Marcus (RRKM) theory [40, 55-56] and the quasiequilibrium theory [57-58], which are essentially the same as each other.

1.3.3 Mechanisms of Energy Transfer.

Classification of mechanisms of collisional energy transfer was discussed by Durup in 1970 [59-60]. Four possibilities were suggested: (i) electronic excitation, (ii) direct vibrational excitation, (iii) vibration involving a long-lived ion-molecule complex, (iv) perturbation of a highly excited species (including a transition to a repulsive electronic surface) and dissociation. For polyatomic species with high kinetic energies, Cooks *et al.* [42] have said that there is minimal transfer of momentum between collision partners, small scattering angles and mainly electronic interactions. For multiatomic species with lower kinetic energies the contact time for the collision partners is increased and so interactions resulting in a long-lived complex might occur. A guide to the dependence of the type of energy transition occurring upon interaction time is given by the Massey criterion [61-62]. For a given translational energy, the velocity of an ion will be lower when the mass is higher and so the interaction time between the collision partners will be longer. Organic ions smaller than 100 Da with keV translational energies will have interaction times of around 10^{-15} seconds, in which case electronic excitation is presumed to occur, followed by internal conversion of energy to leave the ion vibrationally excited. Multiatomic ions larger than 100 Da, with interaction times longer than 10^{-14} seconds, are often considered to be excited by direct vibrational transitions, *i.e.* direct momentum transfer of translational energy of the ion to its vibrational modes [54].

Many studies have been made on the collisions of multiatomic ions, and translational energy losses that result from their collisions [54, 63-64]. The translational

energy losses of multiatomic ions have been found to be as high as 10-100 eV [54, 65-68]. These translational energy losses have typically been determined from MIKE experiments, taking into account the '*Derrick*' shift, that is the error in mass assignment of fragment ions in MIKE spectra due to the translational energy loss of the parent ion [69]. Bricker *et al.* [70] observed that the translational energy loss of projectile ions decreased as the size of the inert collision gas employed increased from helium to krypton and explained their observations in terms of ionisation energies of the inert gases. This idea suggested that electronic excitation of the target gas and collisional activation were in competition with one another. Investigations by Alexander *et al.* [71] obtained results in contradiction to the findings of Bricker *et al.* [70]. Alexander *et al.* observed similar translational energy losses for helium and deuterium even though deuterium has an ionisation more comparable to argon than to helium [71, 81].

1.3.3.1 Mechanisms for Direct Momentum Transfer.

Two mechanisms have been proposed as a means of quantitatively estimating the internal energy uptake by an ion from a collision. The quasi-diatomic approximation [62-63, 72-73] considers a multiatomic ion, treated as an entity, and a monoatomic gas, hence quasi-diatomic. From conservation of momentum and energy, the internal energy uptake (Q) of an ion from a single collision is related to translational energy loss as follows:

$$Q = \left(\frac{m_i + m_g}{m_g}\right)\Delta E - \frac{2m_i E}{m_g}\left[1 - \left(\frac{E - \Delta E}{E}\right)^{\frac{1}{2}}\cos\varphi\right] \quad (11)$$

m_i is the mass of the ion, m_g is the mass of the gas, E is the translational energy of the ion, ΔE is the translational energy loss of the ion and φ is the scattering angle of the ion. The other mechanism does not consider the ion as a single entity. The target gas atom is considered to collide impulsively with a single atom of the ion, which gave rise

to the name impulsive collision transfer theory (ICT) [74-76]. The two colliding atoms are treated as hard spheres. The internal energy uptake is now given by,

$$Q = \left(\frac{\mu}{2\varepsilon}\right)\Delta E \qquad (12)$$

where

$$\mu = \frac{m_i\left(m_a + m_g\right)}{m_i\left(m_a + m_g\right) - m_a m_g} \qquad (13)$$

and

$$\varepsilon = \frac{m_i\left(m_a + m_g\right)}{2m_g\left(m_i - m_a\right)} \qquad (14)$$

m_a is the mass of the atom of the ion the undergoes the collision. In this thesis, in the case of a monoatomic gas the average values of μ and ε have been calculated for all the combinations of atoms in the ion colliding with the target gas atom. In the case of a molecular target gas, average values of μ and ε were calculated for all the combinations of atoms in the ion colliding with each of the constituent atoms of the gas.

ICT theory predicts:

(i) the average translational energy loss and the average internal energy uptake of the ion increases with increasing translational energy of the ion, *i.e.* internal energy uptake is directly proportional to the translational energy loss and this relationship between translational energy loss and internal energy uptake is independent of the scattering angle,

(ii) the greatest transfer efficiency of translational energy to internal energy is obtained when the mass of the gas equals the mass of the colliding atom of the ion,

(iii) internal energy increases as the mass of the gas increases, when all other factors are equal, as the centre-of-mass collision energy increases with the mass of the gas and (iv) scattering increases with the mass of the gas but decreases as the mass of the ion increases.

ICT theory has successfully been applied to collisions between both organic and inorganic ions with gas atoms [77-83].

1.3.3.2 Collision Gas Effects.

There are two factors to be considered with respect to the collision conditions. The first is the choice of gas, *i.e.* its mass, size (diameter), ionisation energy and the number of constituent atoms if a molecular gas is employed. The second is the pressure of the gas in the collision cell. In the keV range, Laramee *et al.* [84] reported that helium is the most efficient collision gas because of its high ionisation energy which prevents charge transfer occurring from the ion to the target gas. Helium has a small diameter and mass, so scattering of ions is minimal. A study with renin-substrate supported this finding [85]. These observations are supported by the ICT theory [75-76] as the '*mass-match*' between the constituent atoms of a peptide is better with helium than with argon. Results obtained by Bordas-Nagy *et al.* [86-87] showed argon to be more efficient at inducing decomposition than helium, an observation noted earlier by Neumann *et al.* [54]. Recent work by Vekey *et al.* [88-89] on inorganic cluster ions found that the translational energy losses were dependent on the centre-of-mass collision energy, such that there was an optimum collision energy for energy transfer, *i.e.* translational energy loss did not rise monatomically with respect to collision energy. However, the contributions to the centre-of-mass collision energy due to different translational energies were not separated from those due to different target gas masses.

The target gas pressure inside the collision cell can have significant effects on translational energy losses, the nature of which depend upon the fragmentation being studied. High-pressure, hence multiple collisions, has been found to affect translational

energy loss determined from measurements on small fragment ions. Translational energy losses determined from measurements on higher mass fragment ions, resulting primarily from single collisions, were not dependent on gas pressure [67, 80, 81].

1.3.4 Energy Considerations.

It is essential when dealing with conversions of translational energy to internal energy for the fragmentations of multiatomic ions to distinguish the different frames of reference absolutely clearly.

1.3.4.1 Centre-of-Mass Frame and Laboratory-Frame Coordinates.

For a singly charged projectile ion, travelling with energy equivalent to the ion accelerating potential, V_{acc}, entering a grounded collision cell the laboratory-frame collision energy E_{lab} is given by equation (15) if the gas is assumed to be stationary.

$$E_{lab} = V_{acc} e \qquad (15)$$

In the case of a collision cell floated at potential V_f, [44, 90] the laboratory-frame collision energy E_{lab} is given by equation (16),

$$E_{lab} = [V_{acc} - V_f] e \qquad (16)$$

When a projectile ion collides with a stationary neutral gas atom of mass m_g the maximum amount of translational energy transferable to internal energy of the collision partners is equal to the centre-of-mass frame collision energy E_{com} [91],

$$E_{com} = \frac{m_g}{m_g + m_i} \times E_{lab} \qquad (17)$$

m_i is the incident ion mass. There is an implicit assumption that the incident ion remains intact following the collision, *i.e.* the two-step model is implied. The centre-of-mass energy is a very important factor when considering the collision-induced decompositions of multiatomic ions, and has been shown in some other earlier experiments to limit the degree of fragmentation observed for massive ions [54]. It can be seen that for a fixed ion energy and a particular collision gas, say helium, E_{com} is inversely proportional to the mass of the ion and so will decrease as the mass of the ion increases. The centre-of-mass collision energy can be increased in one of two ways for an ion of mass m_i. The mass of the gas, m_g, can be increased or the translational energy of the ion can be increased by making E_{lab} greater.

If a collision complex forms, its kinetic energy will be reduced compared to that of the incident ion by an amount equal to the centre-of-mass collision energy. If following the collision, decomposition of the complex to a fragment ion occurs, the kinetic energy of the fragment ion, m_f, will be reduced still further compared to the incident ion energy as a consequence of partition of energy (18).

$$E_{def} = E_{lab} - \left[\frac{m_f}{m_g + m_i} \times (E_{lab} - E_{com}) \right] \qquad (18)$$

1.3.4.2 Translational Energy Losses.

Translational energy losses of incident ions in collisions can be determined from MIKE spectra. If for m_1^+ decomposing to m_2^+ (equation (4)), no translational energy is lost in the collision and the fragment ion will have the same velocity as the incident ion, given in equation (6). If translational energy is lost by the incident ion during a collision, the fragment ion will consequently arise from an incident ion of reduced energy and will itself have less energy, given by equation (19). V_2, V_2' and V_1 are electric sector potentials (see equation (6) and below).

$$V_2 - V_2' = \left(\frac{m_2}{m_1}\right)\left(\frac{\Delta E}{E_{lab}}\right)V_1 \qquad (19)$$

This can be rearranged to give the translational energy loss as,

$$\Delta E = \left(\frac{m_1}{m_2}\right)\left(\frac{V_2 - V_2'}{V_1}\right)E_{lab} \qquad (20)$$

In a MIKE spectrum, the difference between the electric sector potential required to pass a fragment ion in the absence of gas (V_2) and the electric sector potential (V_2') required to pass a fragment ion following a loss of translational energy by the parent ion from a collision with a gas is observed as a peak shift. If this shift is measured and the masses of the ion and fragment are known the translational energy loss ΔE can be determined.

For the metastable decomposition of m_1^+ to m_2^+ (equation (4)) in a field free region in front of a magnet, the metastable peak (m^*) would appear in a magnet scan at a mass-to-charge ratio given by equation (21),

$$m^* = \frac{m_2^2}{m_1} \qquad (21)$$

1.4 Introduction to Fullerenes.

In 1985 Kroto *et al.* [92] were carrying out laser/mass spectrometric experiments to study long chains of carbon molecules of the kind thought to be formed in interstellar space. Using one laser to vapourise carbon species from the surface of a solid graphite disk, a second laser for photoionisation of the carbon species and a time-of-flight mass spectrometer for analysis, Kroto *et al.* [92] observed a number of carbon clusters. Certain '*magic number*' peaks were observed, one of which corresponded to a sixty carbon-atom cluster. This species appeared to be superstable, a factor attributed to its structure which was proposed to be that of a truncated icosahedron [92]. This geodesic shape comprised twelve pentagonal rings and twenty hexagonal rings grouped together to form a three-dimensional hollow structure. Constructions by the architect and philosopher R. Buckminster Fuller with the same geodesic structure led to the naming of C_{60} as buckminsterfullerene or bucky-ball [93]. The structure of C_{60} was confirmed by x-ray crystallographic methods [94] and was shown to resemble the soccer ball initially suggested by Kroto *et al.* (figure 1.4) [92].

Soon other closed-cage carbon clusters also became known as fullerenes. The addition of ten more carbon atoms around the equator of C_{60} gives the next most common fullerene C_{70}, which resembles a rugby ball in shape (figure 1.4). There are twenty-five hexagonal rings and twelve pentagonal rings in the structure of C_{70}, and, as with its counterpart C_{60}, these are the only ring structures present in the carbon cage. In fact all fullerenes, C_n, comprised (n-20)/2 hexagonal rings and twelve pentagonal rings only. In order for the cage to close, or '*anneal*', the pentagons must not be adjacent to one another [95]. The growth of fullerenes arises in the gas phase from ion-molecule reactions. The presence of atomic carbon is thought to be necessary [95-96]. Linear long-chains of carbon link together to form graphite sheets, which curl around and anneal, tying up all loose surface bonds, to form a fullerene.

The hollow cage-like structures of fullerenes allow fullerenes to be derivatised in any one of three ways. Exohedral derivatives are formed from the addition of one

or more atoms or molecules to the outer surface of the fullerene cage. It was the formation of an exohedral osmium complex $C_{60}(OsO_4)$, which permitted confirmation of the structure of C_{60}. This osmium complex broke the pseudospherical symmetry of C_{60} to give order to the crystal structure [94]. Other species which have been attached onto the outer surface of fullerenes are the halogens [97], metals [98-100], oxygen [101-102] and small organic molecules [101, 103-106]. Reactions between oxygen and fullerenes produced an exohedral species whose structure was identified as an epoxide. Two isomers, one with oxygen bridging a 6-5 bond and the second oxygen bridging a 6-6 bond, were observed [107-110].

Endohedral derivatives are formed from the encapsulation of one or more atoms by the fullerene cage [111]. There are two ways in which these derivatives can be formed. Using lanthanum-impregnated graphite in the place of the normal graphite, laser-vapourisation produced C_{60} or C_{70} with one lanthanum attached [112]. The ability of this derivative to withstand further laser blasts suggested the lanthanum was in fact encapsulated by the fullerene cage. Support for this proposed structure came when two lanthanum atoms were attached to the fullerene cage from different experimental conditions. The two lanthanum atoms were removed from the fullerene cage by further laser treatment, suggesting that this particular species was exohedral [113]. Smalley *et al.* subsequently introduced a method of nomenclature in order to prevent confusion between exohedral and endohedral derivatives [114]. The term $M@C_n$ denoted atom M inside the C_n fullerene cage. Exohedral derivatives would be denoted MC_n, where the molecule or atom M was exohedrally bound to the outer surface of the fullerene, C_n, cage. Other species which have been encapsulated by fullerenes are alkali earth metals [115] and the noble gases [116-118]. The noble gases, helium, neon, argon, krypton and xenon, were inserted into the pre-formed fullerene cage by high-pressure experiments. Insertion into a pre-formed cage is the second general method for producing endohedral derivatives $M@C_n^{+\cdot}$ (M = Ar, Kr, Xe; n = 60 or 70). There is, however, a degree of controversy surrounding the endohedral derivatives. Pang *et al.* [119] calculated that, whilst helium and neon and possibly

argon could exist as endohedral derivatives, krypton and xenon would be unstable if endohedrally bound by $C_{60}^{+\cdot}$ or $C_{70}^{+\cdot}$ due to their sizes. In dispute with these calculations are the results by Son *et al.* [120], calculated using the same method as Pang *et al.* [119]. Son *et al.* [120] reported that helium, neon, argon and krypton would be more stable as endohedral derivatives than as exohedral derivatives. Xenon, they reported, would be more stable as an exohedral derivative.

Ab initio calculations on the electronic structure of endohedral derivatives suggest that an encapsulated atom would reside near the centre of the cage where it is able to spin freely [121]. C_{60} has a cavity diameter of 7.1Å [122-124]. The cage diameters for C_{70} are 7.96Å for the long axis and 7.12Å for the shorter axis [123-124].

Doped derivatives, often referred to as dopey-balls, are products formed from the substitution of one of the atoms in the cage by a heteroatom. The nomenclature used for these derivatives is $C_{n-1}M$, where one of the carbons in the fullerene C_n has been replaced by a heteroatom M. For a long time the most common form of dopey-ball was a boron doped fullerene [125-126], formed by laser vapourisation of boron nitride doped graphite. Only in the last year has nitrogen been shown to replace a carbon atom in C_{60} and C_{70} producing $C_{59}N^+$ and $C_{69}N^+$ species respectively [127]. This nitrogen doped fullerene was obtained from mass spectrometric fragmentation of regioselectively synthesized iminofullerene derivatives. Theoretical studies have been made on $C_{59}B$ and, at the time hypothetical, $C_{59}N$ [126]. It was proposed that these doped species would have widely different ionic and electronic properties from the C_{60} molecule, such that $C_{59}B$ would act as an electron acceptor and $C_{59}N$ an electron donor. Such properties suggest the potential use of these species in semiconductors, if they could be produced in adequate quantities.

Giant fullerenes have also been observed [128-130]. Structures known as bucky-tubes or nanotubes [131] which are essentially cylindrical tube with capped ends that seal off the tubes and hyperfullerenes ('*Russian eggs*' or '*bucky-onions*') [128, 132] which are fullerenes within fullerenes, present all sorts of interesting possibilities for the future of fullerene chemistry.

To date no commercial uses have been found for fullerenes although there are many different areas of science to which fullerene chemistry has been introduced with interesting prospects. The pharmaceutical industry [133-134], the materials industry [128] and the electronics industry [128] to name but a few are all beginning to patent new applications of fullerenes.

In 1996 Professors Harry W Kroto, Richard E Smalley and Robert F Curl were awarded the Nobel Prize for their discovery of C_{60}, buckminsterfullerene and for their achievements in the subsequent development of fullerene chemistry [135].

1.4.1 Mass Spectrometry of Fullerenes.

Mass spectrometry has played a key role in the investigation of fullerenes, beginning with their discovery [92]. Gas-phase experiments remained of the utmost importance in the study of fullerenes due to the limited quantity of sample that was available to scientists until 1990 [136]. Mass spectrometry has been responsible for providing a considerable proportion of the information on characterisation of fullerenes and fullerene derivatives [137].

Fullerenes can be ionised by all of the commonly employed ionisation techniques [137-141], the most common being electron impact ionisation [137]. Electron impact of a crude mixture of fullerenes gives rise to several ions: $C_{60}^{+\cdot}$, $C_{70}^{+\cdot}$, $C_{60}^{2+\cdot}$, $C_{70}^{2+\cdot}$, $C_{60}^{3+\cdot}$ and several fragmented fullerene ions. The negative ions $C_{60}^{-\cdot}$, $C_{70}^{-\cdot}$, $C_{60}^{2-\cdot}$, $C_{70}^{2-\cdot}$ have also been observed [142]. Fullerene ion fragmentation has been studied in more depth by tandem mass spectrometry [143-150]. Collision-induced processes were employed to study electron stripping of $C_{60}^{+\cdot}$ [151] and $C_{60}^{2-\cdot}$ and $C_{70}^{2-\cdot}$ [142]. High-energy collision-induced decomposition of multiply and singly charged fullerene ions were found to result in the loss of even numbers of carbon atoms from C_n ($n \geq 30$) [145, 149]. Similar observations were noted for the photodissociation of fullerene ions [151-152]. A proposal that the dissociation of these fullerenes was by the loss of C_{2n} as opposed to the consecutive loss of nC_2 from the

cage was only reported recently [149]. Fullerene derivatives have been observed to fragment in the same fashion [147, 153]. Experiments have shown that fullerene derivatives can be formed in the gas-phase from collisions in a mass spectrometer. This will be discussed later.

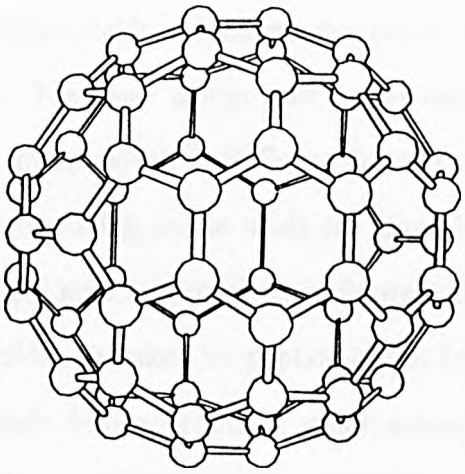

C_{60}

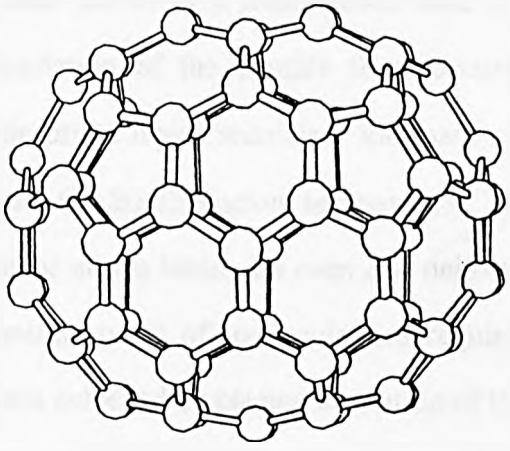

C_{70}

Figure 1.4: C_{60} and C_{70} fullerenes.

1.5 Introduction to Peptides.

Proteins are biologically active compounds of intense scientific interest in medical and pharmaceutical fields. Proteins are made up of small repeating units known as amino acids. The basic amino acid repeat unit is given in figure 1.5. R denotes the side-chain group which is different for the different amino acids. The twenty most commonly occurring amino acids are given in figure 1.6. Pyroglutamic acid, a less common amino acid, is also given in figure 1.6 as this amino acid features in this thesis. Amino acids are linked by peptide bonds (-NH-CO-) to form proteins. Cleavage of these peptide bonds produces small sub-units of proteins known as peptides. Some peptides are of a suitable mass (a few hundred to 4000 Da) to be studied by magnetic-sector mass spectrometry, however this limit is set by the ability to ionise peptides without causing their destruction. Magnetic-sector mass spectrometry has therefore played a key part in the study of this class of compound.

1.5.1 Mass Spectrometry of Peptides.

Peptides are often stored in a freeze-dried state at subzero temperatures in order to prevent degradation of the peptide from occurring. This solid form is incompatible with static-probe liquid secondary ion mass spectrometry (LSIMS) and fast atom bombardment (FAB) ionisation techniques. These methods rely on an impinging beam of ions or atoms hitting an even and uniform surface of the sample in order to create the constant beam of molecule-ions required for a steady signal. A uniform sample surface is achieved by placing a solution of the peptide on the probe tip and evaporating the solvent away. The problem here is that the nano or picomolar quantities used in mass spectrometry provide only a short-lived signal. The best results are obtained when the peptide is dissolved in a liquid matrix on the probe tip. The peptide must be able to diffuse throughout the matrix so as to arrive at the vacuum/matrix interface, where the impinging beam of ions will sputter the molecule-ions. The viscosity and depth of the liquid droplet on the probe tip ensures the sample

loading is constantly being refreshed with fresh layers of matrix/peptide solution. The main physical requirement of the matrix is its viscosity. The matrix must be relatively viscous as this ensures the probe loading remains on the probe, when it is inserted into the source (at 10^{-7} Torr), long enough for a continuous and constant signal to be produced.

LSIMS (and FAB) ionising techniques are quite 'soft' ionising methods, but they still impart a significant amount of energy into the molecule-ions. This internal energy is generally sufficient to induce a degree of fragmentation of a peptide ion. Observation of fragment ions in the mass spectra of peptides has been of great importance and use in discerning amino acid sequences of peptides. Other structural information can also be obtained for this class of compound, for example the presence of disulphide cross linkages and cyclic peptides. The fragmentation patterns observed in the high-energy collision-induced decomposition of peptides are significantly different to fragmentation observed in an ordinary mass spectra [154-155]. The complicated fragmentation spectra obtained require a simple and logical method of peak labelling.

1.5.2 Nomenclature of Peptide Fragment Ions.

Many conflicting and confusing methods of labelling the peaks on a mass spectrum of a peptide have been suggested over the years [156-158]. It was Roepstorff and Fohlman who initially proposed a standard scheme for naming the peptide fragments produced in mass spectrometry, regardless of the ionisation technique used. This scheme breaks the peptide backbone repeatedly in three different places and allowed the charge to be placed on either the N-terminal or C-terminal fragment (figure 1.7). When the charge resides on the N-terminal, a_n, b_n and c_n ions are produced and x_n, y_n and z_n ions are produced when the C-terminal retains the charge. To indicate the number of protons associated with the molecule-ion, Roepstorff and Fohlman [155] added primes (') to the left of the letter for proton loss and right of the letter for protons attached to the fragment. The number of primes indicates the

number of protons involved, for instance y_n ion plus two protons would be represented as y_n". This basic system was generally accepted although a few alterations have been made over the years to account for cyclic peptides or peptides with intramolecular disulphide bridges [158]. The most significant improvement was made by Biemann *et al.* [157] who accounted for side-chain fragmentations. They also replaced the prime and double prime method of indicating proton behaviour with +1, +2 or -1 and-2 for the addition and loss of protons [157]. Cleavage at the R-side-chain are common observations in mass spectrometry, especially from high-energy collision-induced decomposition. Fragment ions resulting from the loss of the side-chain fall into one of three categories. d_n ions are formed from the loss of the side-chain from an N-terminal fragment ion and v_n and w_n ions are formed from the loss of the side-chain from C-terminal fragment ions. There is evidence to suggest d_n ions are derived from a_n+1 ions, v_n from y_n+2 or x_n+1 precursor ions and w_n from z_n+1 precursor ions. This common nomenclature system is still widely used in mass spectrometry, and it is this process for labelling peptide fragments which is utilised by a computer program MACPROMASS [159]. MACPROMASS is a program that calculates all the fragments that could possibly form from a known linear peptide. It has been observed that y_n fragments always appear to have two protons attached to them, likewise with c_n fragments, presumably producing H_3N^+-CHR- (y_n+2) and -CO-NH_3^+ (c_n+2) respectively. Some reports [153] show these y_n+2 and c_n+2 fragments represented as y_n and c_n respectively to reduce crowding on a spectrum. The MACPROMASS software program lists what would be y_n+2 ions as y_n ions. This final adjustment can be very confusing and lead to misunderstandings when interpreting spectra. Therefore the system of peptide nomenclature used throughout this report is that described by Ashcroft and Derrick [160]. Here, if two protons are attached to a y_n or c_n ion, the format y_n+2 and c_n+2 has been used.

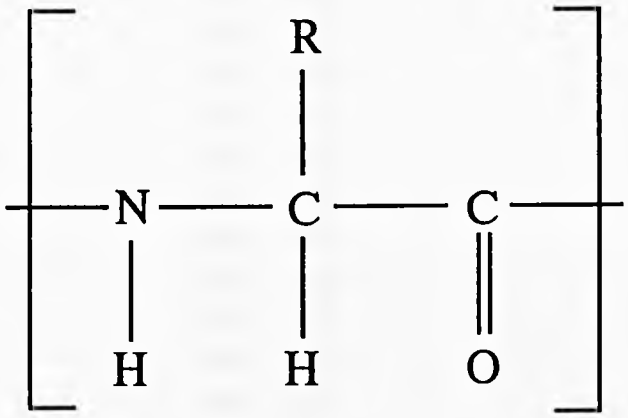

Figure 1.5: Basic amino acid repeat unit.

Name of amino acid	Abbrieviated codes		Elemental Composition
Alanine	Ala	(A)	C_3H_5NO
Arginine	Arg	(R)	$C_6H_{12}N_4O$
Asparagine	Asn	(N)	$C_4H_6N_2O_2$
Aspartic Acid	Asp	(D)	$C_4H_5NO_3$
Cysteine	Cys	(C)	C_3H_5NOS
Glutamic Acid	Glu	(E)	$C_5H_7NO_3$
Glutamine	Gln	(Q)	$C_5H_8N_20_2$
Glycine	Gly	(G)	C_2H_3NO
Histidine	His	(H)	$C_6H_7N_3O$
Isoleucine	Ile	(I)	$C_6H_{11}NO$
Leucine	Leu	(L)	$C_6H_{11}NO$
Lysine	Lys	(K)	$C_6H_{12}N_20$
Methionine	Met	(M)	C_5H_9NOS
Phenylalanine	Phe	(F)	C_9H_9NO
Proline	Pro	(P)	C_5H_7NO
Serine	Ser	(S)	$C_3H_5NO_2$
Threonine	Thr	(T)	$C_4H_7NO_2$
Tryptophan	Trp	(W)	$C_{11}H_{10}N_2O$
Tyrosine	Tyr	(Y)	$C_9H_9NO_2$
Valine	Val	(V)	C_5H_9NO
Pyroglutamic Acid	Pyr	-	$C_5H_5NO_2$

Figure 1.6: Summary of the twenty most common amino acids and one uncommon amino acid.

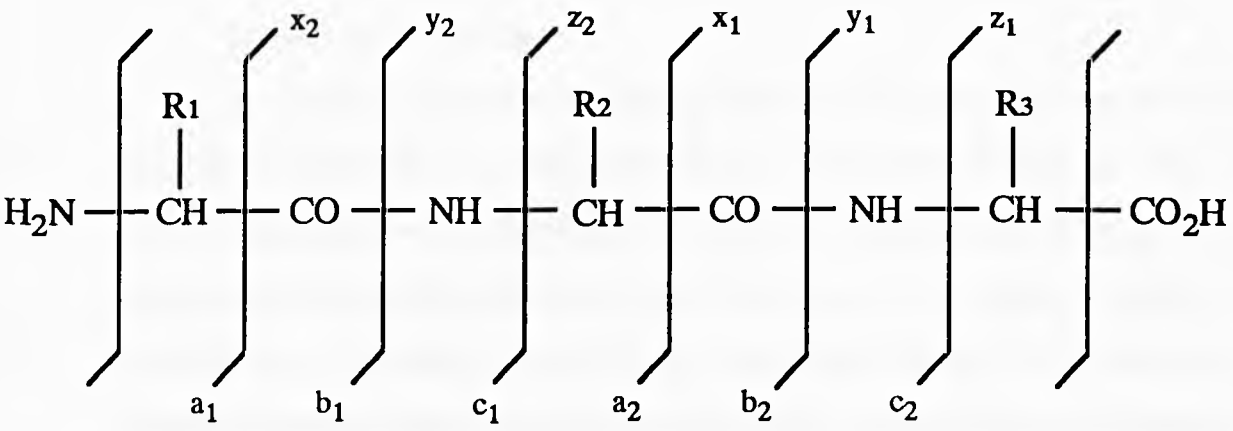

Backbone cleavages: N-terminal ions:

a_n	$H(NHCHRCO)_{n-1}\overset{+}{N}H=CHR$
b_n	$H(NHCHRCO)_{n-1}NH\text{-}CHR\text{-}C{\equiv}O^+$
c_n+2	$[H(NHCHRCO)_nNH_2]H^+$

C-terminal ions:

x_n	$^+O{\equiv}C(NHCHRCO)_nOH$
y_n+2	$[H(NHCHRCO)_nOH]H^+$
z_n+1	$[CHR\text{-}CO(NHCHRCO)_{n-1}OH]H^+$

Sidechain cleavages: N-terminal ions:

d_n	$[H(NHCHRCO)_{n-1}NH\text{-}CH+CHR']H^+$

C-terminal ions:

v_n	$[HN{=}CH\text{-}CO(NHCHRCO)_{n-1}OH]H^+$
w_n	$[R'CH{=}CH\text{-}CO(NHCHRCO)_{n-1}OH]H^+$

Figure 1.7: Nomenclature for common fragment ions observed in mass spectra of peptides.

1.6 Capture of Target Gases.

The possibility of an ion capturing a target gas during their collision was first proposed by Neumann *et al.* [54]. Neumann *et al.* [54] were studying the effect of internal energy uptake by ions and how the amount of internal energy uptake by an ion could result in either forward or backward scattering. It was logical, therefore, to presume that a cross-over point between forward and backward scattering could produce a complex, such that the ion and target gas would have the same laboratory-frame velocities. Such a complex would be stationary in the centre-of-mass frame and the ion/neutral complex would be detected as one entity provided the complex formed in the collision cell survived long enough. In the original paper by Neumann *et al.* [54] the effect of selecting ions with increasing masses with 8 keV ions incident on helium was proposed to result in a collision complex at 1500 Da.

The failure of an ion and a neutral gas to separate following their collision is the phenomena known as target-capture.

1.6.2 Target-Capture by Fullerenes.

Initial work in this field was carried out independently by Schwarz *et al.* [111] and Ross *et al.* [161]. Evidence was presented for the capture of helium by $C_{60}^{+\cdot}$ (and $C_{70}^{+\cdot}$ [111, 161]) from high-energy collisions. Fragmentation of a helium/$C_{60}^{+\cdot}$ complex by the loss of C_n (n = 2, 4, 6, 8) and not the loss of the helium atom led Schwarz *et al.* [111] and Ross *et al.* [161] to propose that the helium was endohedrally bound by the fullerene cage. Additional evidence for the existence of an endohedral structure He@$C_{60}^{+\cdot}$ arrived following neutralization-reionisation mass spectrometric experiments [162-163]. Expanding on this knowledge it was shown that the optimal laboratory-frame collision energy for the formation of He@$C_{60}^{+\cdot}$ was between 5 and 6 keV [161, 164]. Insertion of helium into doubly and triply charged buckminsterfullerene [164-165] and the injection of two helium atoms into $C_{60}^{+\cdot}$ and its fragment ions [166] was also observed. Subsequent to this, other noble gases were employed as target

species. Several reports gave evidence of a $Ne@C_{60}^{+\cdot}$ species where once more the observation of fragment ions $Ne@C_{60-n}^{+\cdot}$ (n = 2, 4, 6, 8, 10) suggested the structure of $Ne@C_{60}^{+\cdot}$ was endohedral [167-169]. Gross *et al.* also experimented with D_2 and argon, the latter experiment showed odd-numbered fragment ions $C_xAr^{+\cdot}$ (x = 55, 53, 51, 49) [167, 170]. These argon experiments have not been repeated. High-energy collisions on a reverse geometry four-sector mass spectrometer [171] and low-energy collisions on a quadrupole instrument [172] failed to produce any evidence of argon retained by $C_{60}^{+\cdot}$ fragments.

There are two proposed mechanisms by which entrapment of an atom by an intact fullerene could occur. Schwarz *et al.* [111], believing helium to be incorporated into the fullerene cage, calculated that helium would require less than 10 eV of energy to pass through a C_6H_6 or $C_6H_6^+$ plane. The high-energy collisions occurring in the mass spectrometer would provide more than enough kinetic energy for helium to pass through a hexagonal ring of the $C_{60}^{+\cdot}$ molecule. This '*squeeze through*' mechanism was supported by a study on collision energy dependence carried out by Spang *et al.* [173], who gave evidence for the passage of a helium atom through a pentagonal ring in the cage. The second mechanism considers the possibility that the atom may collide with a carbon-cage atom or between two carbon-cage atoms, breaking a carbon-carbon bond as opposed to hitting the centre of a ring. This '*smash through*' mechanism, in which enough bonds are broken to provide a hole or '*window*' large enough for the atom to pass through, is also known as the '*window*' mechanism. The fullerene cage would then be required to close up behind the atom to trap the atom inside the cavity. The '*window*' mechanism of entrapment was proposed following the encapsulation of helium and neon by neutral C_{60} from high-pressure and high-temperature experiments [116-118]. Using this method of entrapment krypton was encapsulated by C_{60} and then introduced into a mass spectrometer. High-energy collision with helium found that the C_{60} was able to retain both the krypton and incorporate a helium atom into its cage [174]. This was not the case when helium

underwent high-energy collisions with the exohedral derivative $C_{60}(H)CH_3^{+\cdot}$ [175]. In this instance, $He@C_{60}^{+\cdot}$ and $C_{60}^{+\cdot}$ were the only product ions observed.

A wide range of other fullerene derivatives have been formed from mass spectrometric studies. Unlike the mass spectrometry produced endohedral derivatives already mentioned, discussion of the structure of many derivatives has been scant. Small organic molecules have been found to form partial adducts with fullerene ions in the source [176-177] and from high-energy collisions [178]. For example, high-energy collisions between methane and $C_{60}^{+\cdot}$ produced the adducts $C_{60}CH_3^{+\cdot}$, $C_{60}CH_2^{+\cdot}$, $C_{60}CH^{+\cdot}$ and $C_{60}C^{+\cdot}$ [178]. A study of low-energy reactions with the neutral gases nitrogen, oxygen, methane, ammonia, heavy water, acetone, butene, and isobutene failed to give rise to any adduct ions [173]. Schwarz *et al.* [171] reported results from high-energy collisions with the gases D_2, H_2, O_2 and SF_6 which also failed to produce adduct ions. Gross *et al.* [170] failed to produce fullerene ion adducts with the gases N_2, NO and O_2 from high-energy collisions. Such collisions were seen to result in the loss of C_2 units from the fullerene cage. Christian *et al.* [179-180] observed reactions of O^+ with C_{60} to form $C_{59}O^+$ derivatives. This species, they suggested, could be either a dopey-ball or the endohedral derivative $CO@C_{58}^{+\cdot}$. Extending their study to the species N^+ and B^+ and other atomic cations, the species $C_{59}N^+$ was observed [181]. $C_{59}N^+$ was also observed by Cooper [182] from high-energy collisions between $C_{60}^{+\cdot}$ and nitrogen and $C_{60}^{+\cdot}$ nitric oxide. Cooper [182] also observed that collisions with nitrogen produced the species $C_{60}N_2^{+\cdot}$. The adducts $C_{60}NO^{+\cdot}$, $C_{60}N^{+\cdot}$ and $C_{60}O^{+\cdot}$ were seen from collisions with nitric oxide. $C_{60}O^{+\cdot}$ was also observed from collisions with oxygen and carbon monoxide. Collisions between carbon monoxide and $C_{60}^{+\cdot}$ was seen to give rise to the adducts $C_{60}CO^{+\cdot}$ and $C_{60}C^{+\cdot}$.

In this thesis, nomenclature of the form C_nM has been employed when the position of the heteroatom(s), M, relative to the fullerene cage, C_n, for a target captured species is not known.

1.6.1 Target-Capture by Peptides.

Fenselau *et al.* [183] presented evidence of target capture of hydrogen-containing gases with peptides from high-energy collisions. On colliding methane and ammonia with renin substrate, adduct peaks were observed at masses greater than the protonated peptide ($MH^+ = 1759$). These peaks were assigned as $[MH + CH_4 - 2H]^+$ when the collision gas was methane and $[MH + NH_3 - 2H]^+$ for ammonia. Isotope labelled target gases confirmed that one proton was lost from the target gas and one proton was eliminated from the peptide ion.

1.7 Project Aims.

Collision-induced dissociation of multiatomic ions is a very popular way of obtaining structural information on such ions. The process of CID is not fully understood and so cannot be used to its full potential. Ion-molecule reactions have been studied as a means to elucidate the mechanisms involved in CID. As already stated the process of CID is known to occur in two distinct phases, collisional activation which is separated in the time from unimolecular dissociation. For the case of a projectile ion colliding with a stationary neutral gas Neumann *et al.* [54] considered three possibilities. Firstly if there was not enough energy, involved in the collision, to excite an ion sufficiently, the ion and the gas would rebound from each other, an action Neumann *et al.* [63] termed backward scattering. The second possibility was the passage of the projectile ion seemingly through the gas (the gas would actually pass through the projectile ion). This outcome was termed forward scattering. The final consideration was the intermediate stage between forward and backward scattering whereby a neutral gas and a projectile ion remained together as a single entity. The term target capture was employed. The study of target capture features heavily in the thesis.

One objective of this thesis was the fragmentation of peptides by collision-induced decomposition with neutral gases. The aim was to study optimum collision conditions for peptides by varying collision gas mass and structure, translational energy of the incident ion and incident ion mass. These changes in the collision conditions were examined by measuring translational energy losses by the protonated peptides. Internal energy uptake by the protonated peptides from collisions were calculated, assuming the impulsive collision transfer (ICT) theory [75-76], as a means to gain further information on energy transfer during a collision. This study of energy transfer was then extended to a closer analysis of collision complexes. The aim was to control the collision conditions to allow target capture of methane by the peptides bombesin and alytesin to produce an isolated reaction system. The phenomenon of target

capture of peptides with the molecular gases methane and ammonia was originally studied by Fenselau *et al.* [183].

The study of target capture was then extended to fullerenes. Target capture by fullerenes was initially achieved with helium and neon [111, 161]. One objective of this project was to extend this study to the larger noble gases and to deduce where possible their structures. Molecular gases were employed as target gases in an attempt to induce capture of diatomic gases and small hydrocarbons by $C_{70}^{+\cdot}$. This included the target capture by fullerenes with methane as an extension to target capture by protonated peptides. The main aim was the formation and subsequent analysis of adducts formed from target capture of helium, neon, argon, krypton, xenon, carbon monoxide, nitric oxide, oxygen, nitrogen, methane, tetrafluoromethane, ethane, ethene, ethyne and propene gases by fullerene radical cations from high-energy collisions in a four-sector tandem mass spectrometer.

CHAPTER TWO: *Instrumentation and Experimental Methods.*

2.1 *Kratos Analytical* CONCEPT IIHH Four-Sector Tandem Mass Spectrometer.

The *Kratos Analytical* CONCEPT IIHH four-sector tandem mass spectrometer [184] is essentially two double-focusing magnetic-sector mass spectrometers connected in series. Both of the double-focusing mass spectrometers are of Nier-Johnson type geometry [185]. Ions were created from an ion source held in the source housing unit. Ions having a range of masses diverged from the source slit and entered the first stage of analysis, *i.e.* the first double-focusing mass spectrometer, MS-I. Ions could be collected after MS-I, or alternatively, the ions could be left to travel into the flexicell where they could undergo collisions. Collision products would be passed into the second stage of analysis, *i.e.* the second double-focusing mass spectrometer, MS-II. MS-I and MS-II were identical. Information on how the ions decomposed during their collisions was gained by collecting product ions at the end of MS-II. A schematic diagram of the *Kratos Analytical* CONCEPT IIHH is given in figure 2.1. All data was processed by the *Kratos Analytical* Mach3 [184] data system which was run on a *Sun Microsystems* Sparc station [186].

2.1.1 Ion Sources.

Ionisation took place in the ion source held in the source housing unit at the front of the instrument. Electron impact (EI) ionisation and liquid secondary ion mass spectrometry (LSIMS) ionisation were used to ionise samples. Both the EI and LSIMS ion sources were held at a potential of 7.9 keV. This meant that ions singly charged that diverged from the source slit, which was earthed, would be travelling with a mean energy of 7.9 keV. This potential difference through which ions were accelerated is termed the accelerating potential.

2.1.1.1 Electron Impact Ionisation.

Samples can be introduced as either a solid or as a vapour at low pressure into the EI source (figure 2.2). Electrons were produced from a resistively heated filament and were accelerated across the source by a potential difference of 70 V. These energetic electrons collided with the sample molecules stripping electrons from them, among other phenomena, resulting in a positive ion.

$$e^- + M \rightarrow M^+ + 2e^- \qquad (22)$$

The number of electrons traversing the source was monitored by an electron trap and kept constant by feedback to the filament. A small positive voltage applied to an ion repeller pushed the ion towards the ion exit slit. The whole of the source was held at 7.9 keV while the rest of the source region was earthed. The ions were then accelerated out of the source and into the analyser at 7.9 keV (in the case of singly charged ions).

2.1.1.2 Liquid Secondary Ion Mass Spectrometry Ionisation.

In LSIMS a beam of caesium ions was fired from a gun towards a probe tip containing the sample compound mixed with a matrix (figure 2.3). This beam of caesium ions hit the sample/matrix mixture to cause molecules to sputter from the liquid mixture and produce a dense gas phase just above the liquid mixture. This plasma contains positive and negative ions which were then selected according to positive or negative scan requirements. There was a 5 keV potential difference across the caesium gun and the entire gun was floated by a further 15 keV. The probe was held at 7.9 keV, therefore ions were sputtered from the sample surface from an impact of 12 keV of energy per caesium ion.

2.1.2 MS-I and MS-II Double-Focusing Mass Spectrometers.

MS-I and MS-II double-focusing mass spectrometers were identical. Each double-focusing mass spectrometer consisted of an electrostatic analyser followed by a magnetic analyser. These analysers are often referred to as electric sectors and magnetic sectors. The electrostatic analysers, E1 and E2, were comprised of two curved plates which had a sector angle of 90 degrees and a mean radius of 381 mm. A potential difference between the two plates focused the ions onto an image plane, according to ion energies, situated between the electric sector and the magnetic sector. The magnetic analysers, B1 and B2, focused the ions according to their masses on a collector slit. The magnetic fields for B1 and B2 were generated by two electromagnets. The strengths of the electromagnets were controlled by magnetic field measurements using a Hall probe. The electromagnets had sector angles of 60 degrees with a central radius of 686 mm. The shape of the electromagnet caused the ion beam to converge at a focal point, close to the exit of the magnet. β-slits situated at the image planes between E1 and B1 and between E2 and B2 were present to limit the energy spread of the ions that emerged from the electric sectors. Current shims on the magnet permitted the magnetic field to be finely adjusted slightly in order to improve peak shape and resolution if necessary. Hexapoles situated between E1 and B1 and between B1 and the MS-I collector slit corrected for any curvature and rotation of the ion beam brought about by the fringing field of the magnet. MS-II had identical hexapoles.

2.1.2.1 Modes of Operation.

MS-I was operated such that changing the field of the B1 while the E1 potential was kept constant brought ions of different mass-to-charge ratios to a focal point at the collector. Alternatively, doubly-focused ions could be mass-selected and passed into the flexicell.

MS-II was operated in any one of three ways in order to detect product ions that emerged from the flexicell. Ions that traversed E2 were separated according to their kinetic energies and collected between E2 and B2. The β-slit situated in the ion image plane between E2 and B2 was limited to reduce the energy spread of the ion beam and enhance resolution. A mass-analysed ion kinetic energy (MIKE) spectrum would result. Energy loss determinations were made from the MIKE spectra by measuring the shift in peak positions. MS-II was often operated such that collision products passed through E2, held at a fixed potential, and the magnetic field was scanned. The electric sector potential at E2 was generally reduced from that appropriate for the translational energy of the parent ion, in order to account for energy lost during a collision. Ions were focused on to the collector slit according to mass-to-charge ratio. Finally, in some cases, the B2 field and the E2 sector potential were scanned simultaneously such that the ratio of B/E remained constant. The output is termed a B/E linked scan.

2.1.3 The Flexicell.

The flexicell [184] comprised a series of focusing plates before and after the collision cell, which focused the ion beam into the collision cell and focused collision products that emerged, scattered from the cell. The input lens consisted of a resolving slit and several focusing plates which served to focus the ion beam from MS-I into the collision cell. A detector situated between two of the focusing plates allowed a spectrum to be recorded when MS-I was operated as a standard mass spectrometer. The collision cell was used for collision-induced decomposition of multiatomic ions. Neutral target gases were introduced into the collision cell at pressures controlled by monitoring the percentage reduction in the incident ion intensity as gas was added. A potential applied to the collision cell allowed control of the impact energy between the ions and the stationary neutral gas. The output lens focused the fragment ion beam from the collision cell onto the resolving slit of MS-II. A schematic of the flexicell is

given in figure 2.4. Another detector situated between two of the output lens plates was not used in any of the experiments described in this thesis.

2.1.4 Detection of Ions.

Two types of ion collector were used on the *Kratos Analytical* CONCEPT IIHH tandem mass spectrometer. These were four post-acceleration detectors (PAD), which are point detectors, and one array detector [187]. Both of these designs come under the category of multiplier detectors, that is electron multiplication enhanced the signal. This allowed single ion detection and rapid scanning of the ion beam.

The four PAD detectors were positioned such that PAD1 was in the flexicell housing unit before the collision cell and PAD2 (not in use) was also in the flexicell housing unit just after the collision cell. PAD3 was situated after E2 and PAD4 was placed at the exit of B2. The scanning array detector was positioned parallel to PAD4 such that these detectors could be interchanged quickly and easily. All ions collected after B2 were detected by the scanning array detector.

2.1.4.1 Post-acceleration Detectors.

Post-acceleration detectors (PAD), also known as point detectors, were comprised of a post-acceleration dynode, which had a highly polished aluminium surface, placed perpendicular to the ion beam. The ion beam was deflected, on passing through resolution slits at the detector entrance, onto the electrode. A highly negative potential applied to the electrode caused the ion beam to strike it, releasing secondary electrons which were attracted towards an electron multiplier. Figure 2.5 shows a diagram of a PAD detector.

There is one disadvantage in the way in which PAD detectors work. As the ion beam reaches the detector, a resolution slit allows only a limited number of ions through to the detector. The array detector is a design that has avoided this loss of ions as it does not require any resolving slits.

2.1.4.2 The Scanning Array Detector.

This detector collected all of the ions generated all of the time. No ions were lost at the detector's entrance because of a resolution slit. As all the ions reached the detector and were recorded, the sensitivities of resulting spectra were high.

The array detector (figure 2.6) on the CONCEPT IIHH functioned on a continuous scanning principle [187]. Two microchannel plates arranged such that the channel plates formed a chevron pattern ensured that the entrance face was in line with the focal plane of the mass spectrometer. A close proximity of the two plates was required in order to place a voltage across them. When an ion struck one of the channels, electrons leaving the rear of the second microchannel plate multiplier were accelerated on to an aluminium-coated phosphor screen, which was the face plate to a bundle of fibre optic wires. When the electron hit the phosphorus screen, it became illuminated and photons were transmitted through the fibre optic wires onto a charge coupled device (CCD). Each channel converted the photon signal into a charge which was integrated and stored electronically. Originally the array detectors on instruments of this type collected data through a 4% (of the mass range) window before moving onto the next 4% window. The array detector on the CONCEPT IIHH scanned the whole mass range continuously, albeit in 4% window as opposed to 4% 'snapshots', hence this detector was termed a scanning array detector.

2.1.5 The Vacuum System.

The high vacuum required in the CONCEPT IIHH was achieved through a series of pumps. Four two-stage rotary backing pumps and seven turbomolecular pumps were used with thermocouple gauges to indicate the vacuum given by the rotary pumps and ion gauges to monitor the vacuum in the various housing units of the mass spectrometer. The flow of gas through these pumps and housing units was controlled by a selection of valves: diaphragm ball, isolation and solenoid operated valves. Typical pressures for the sector instrument were of the order of 10^{-7} Torr for the source and the flexicell housing units, although this was variable due to the inlet of

the sample into the source and a collision gas into the flexicell. The analysers functioned at around 10^{-8} Torr.

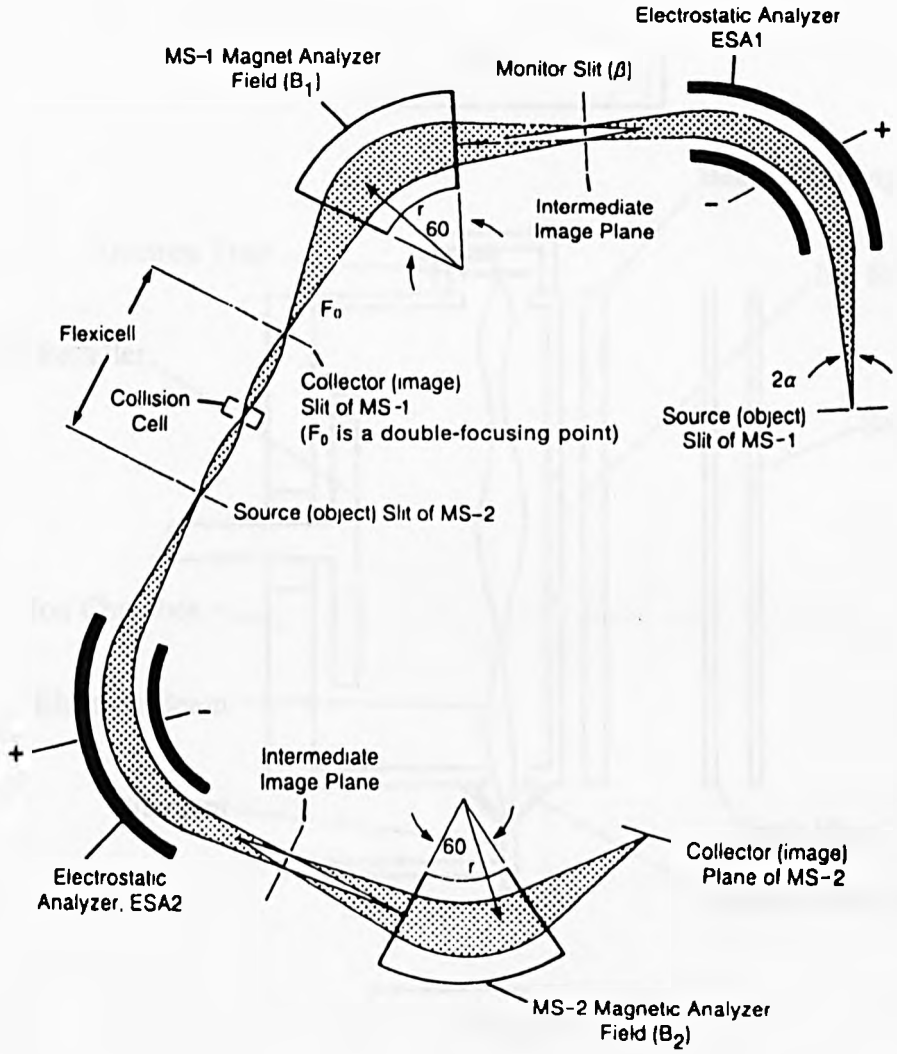

Figure 2.1: Ion optics of the *Kratos Analytical* CONCEPT IIHH mass spectrometer.

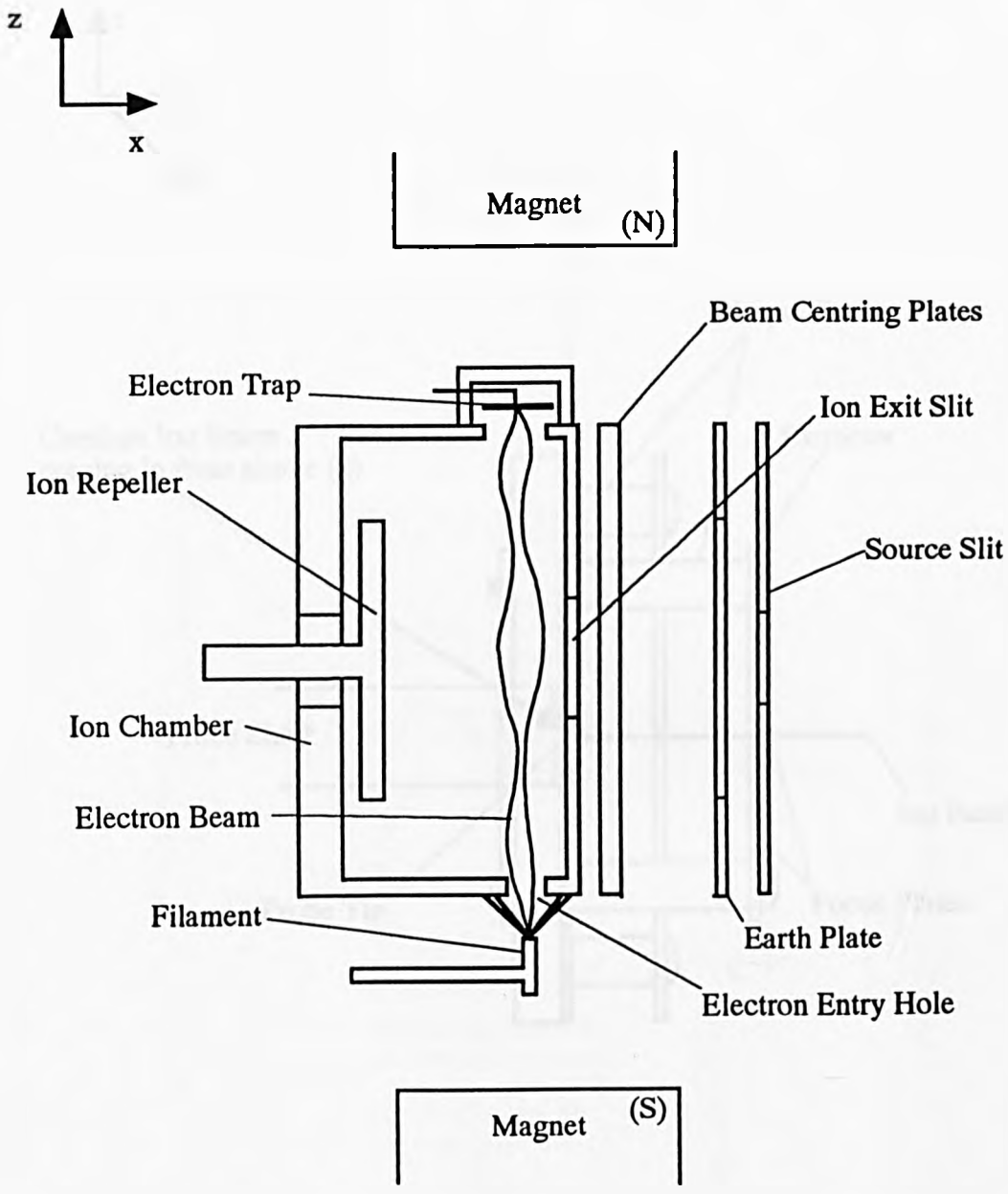

Figure 2.2: Schematic diagram of the electron impact ionisation source.

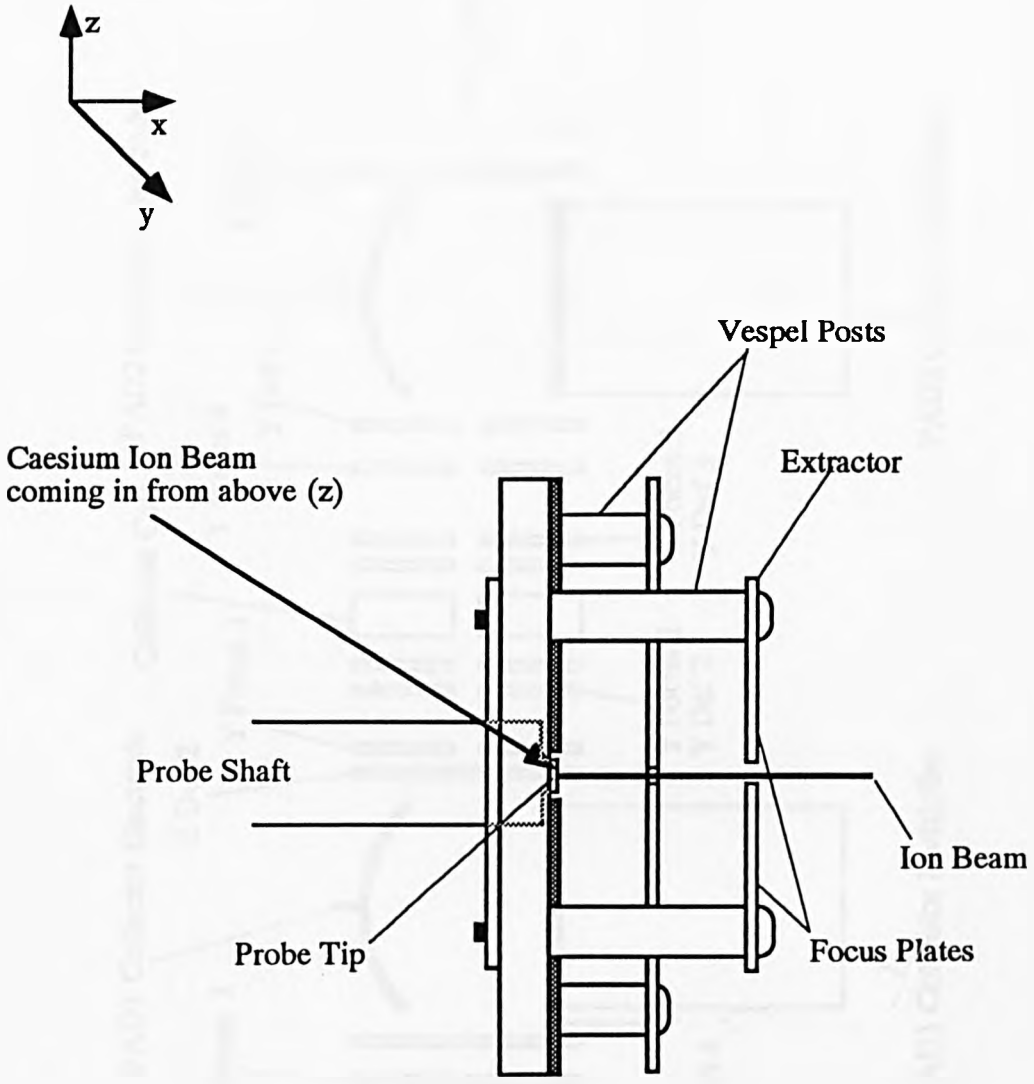

Figure 2.3: Schematic diagram of the liquid secondary ion mass spectrometry ionisation source.

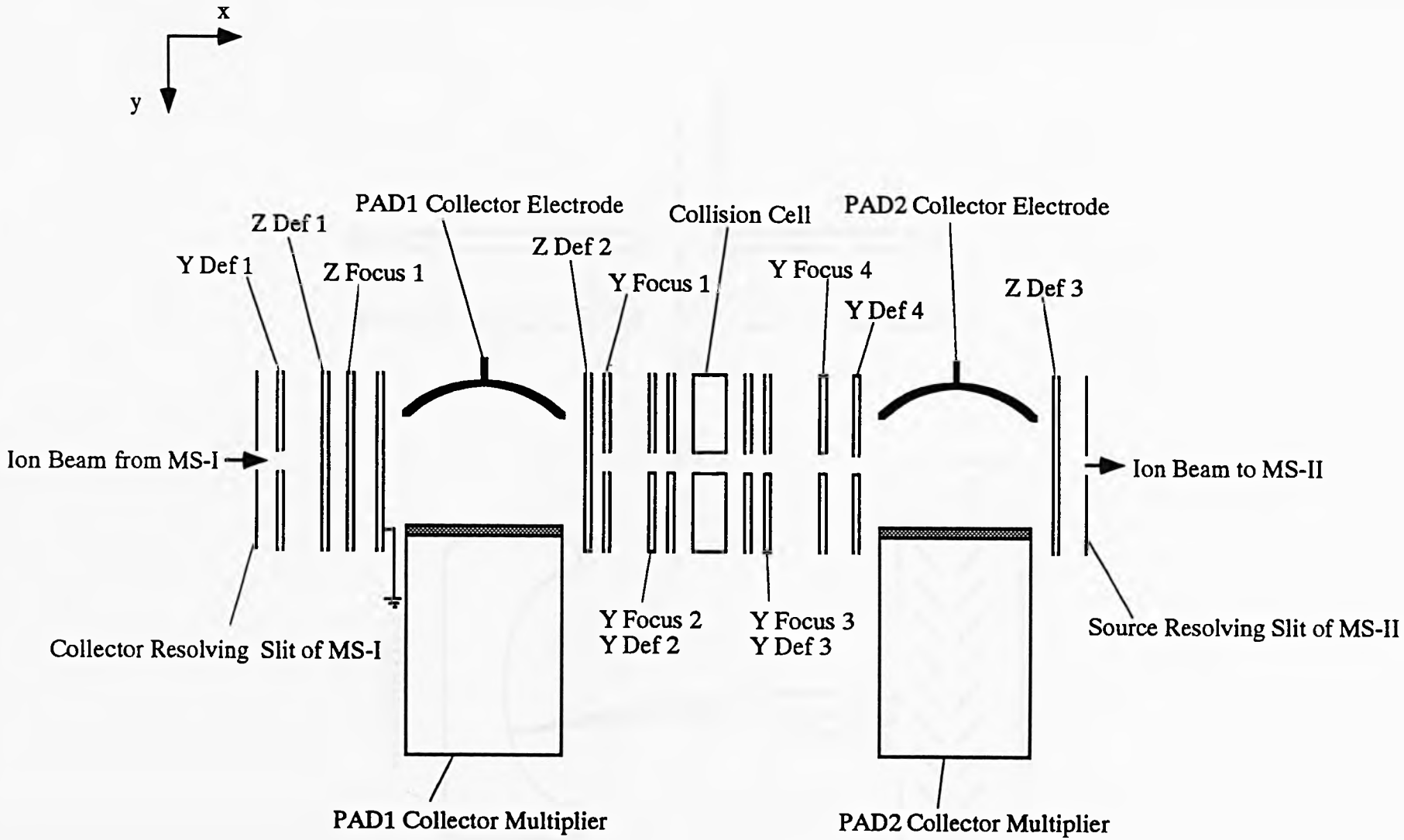

Figure 2.4: Arrangement of slit plates and PAD collectors in the flexicell.

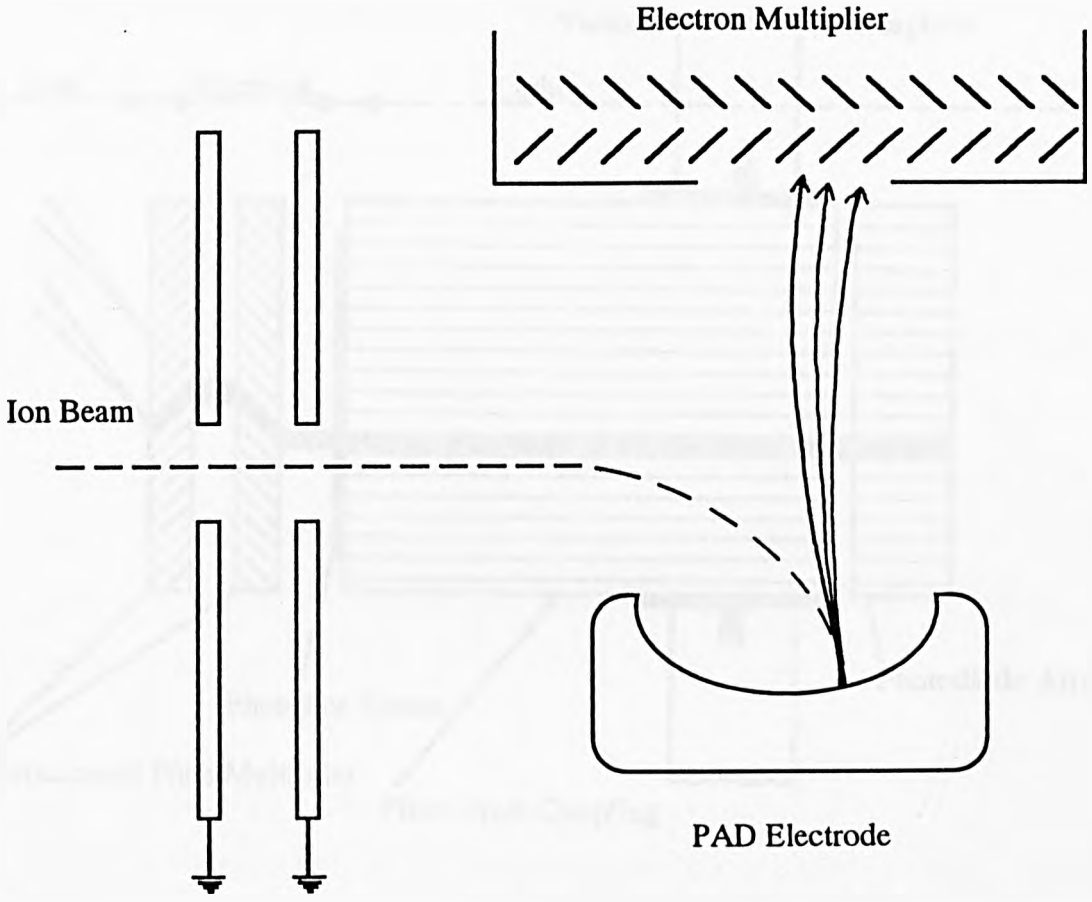

Figure 2.5: Schematic diagram of a post-acceleration detector.

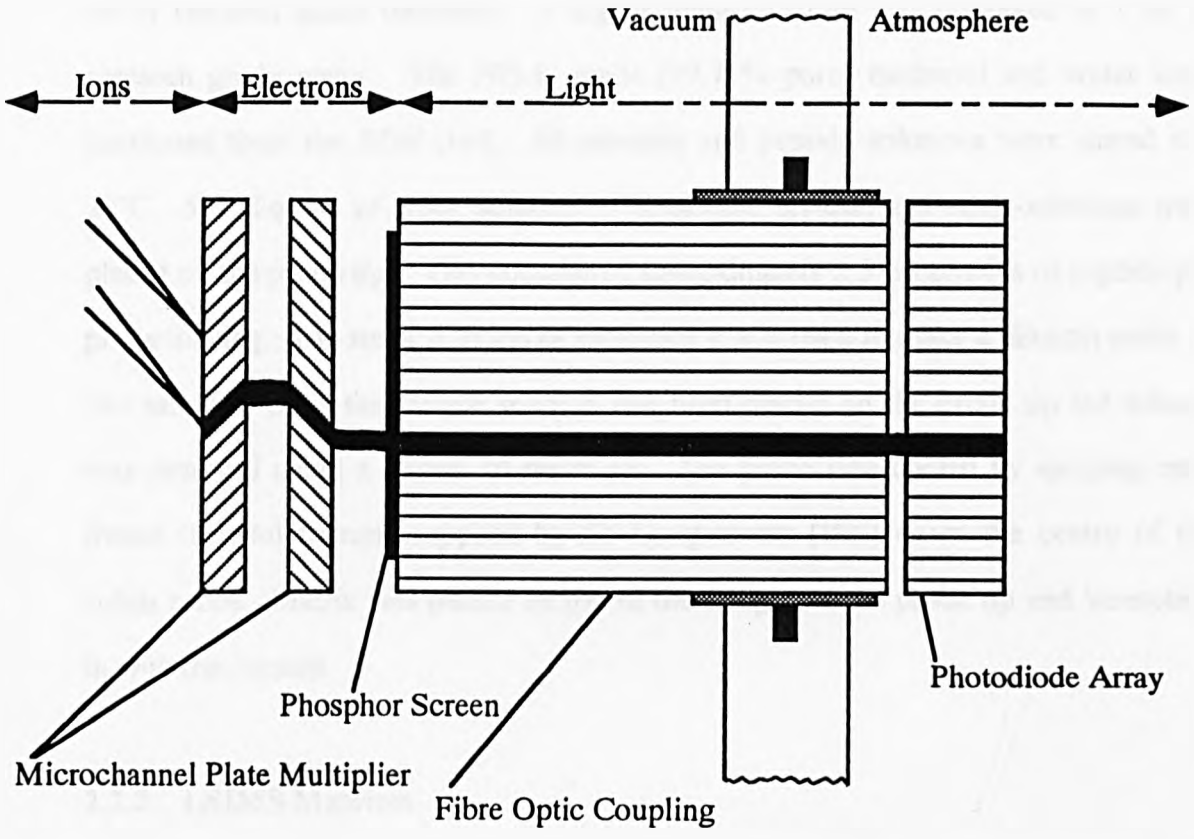

Figure 2.6: Schematic diagram of the scanning array detector.

2.2 Materials and Sample Preparation.

2.2.1 Peptides.

The peptides bombesin, alytesin, substance P and renin-substrate were supplied by *Sigma-Aldrich Chemical Company* [188]. The peptide content in 1 mg of sample purchased was between 76 % and 86 % of the total content. This was taken into account when calculating the concentration of the peptide in solution. Stock solutions of bombesin, alytesin and substance P were made up by dissolving 1 mg of peptide in 1 ml of research grade methanol. 1 mg of renin-substrate was dissolved in 1 ml of research grade water. The HPLC grade (99.7 % pure) methanol and water were purchased from the *BDH* [189]. All peptides and peptide solutions were stored at -28°C. 5µl aliquots of stock solution of bombesin, alytesin and renin-substrate were placed on the probe tip. This constituted approximately 2.5 nanomoles of peptide per probe loading. The stock solution of substance P was used to make a dilution series of this sample. Once the sample solution had been placed on the probe tip the solvent was removed using a stream of warm air. The probe was cooled by spraying anti-freeze (aerosol freezer, supplied by *RS Components* [190]) down the centre of the solids probe. Matrix was placed on top of the sample on the probe tip and 'scratched' in with the peptide.

2.2.2 LSIMS Matrices.

The matrix used for bombesin, alytesin and substance P was a mixture of glycerol and thioglycerol (1:1) plus 1 % trifluoroacetic acid [191]. Glycerol, thioglycerol and trifluoroacetic acid were supplied by *Fisons* [190]. They were 99.0 %, 99.0 % and 99.5 % pure respectively. An improved signal was obtained for renin-substrate when a matrix known as *magic bullet* was used [193]. *Magic bullet* is a mixture of dithiothreitol and dithioerythritol in a 5:1 ratio. Dithiothreitol and dithioerythritol were both powders, but when they were heated together at 50°C they melted, mixed and remained as a viscous liquid at room temperature. Dithiothreitol

and dithioerythritol were supplied by *Sigma-Aldrich Chemical Company* [188] and were both 99.0 % pure respectively.

2.2.3 Fullerenes.

A crude sample of mixed fullerenes was provided by *Dr M Wilson of CSIRO*, Australia [194]. This was loaded into a glass capillary and inserted into the EI solid state sample probe. The probe was heated to 250°C and the EI source was heated to 250°C for experiments with $C_{60}^{+\cdot}$ and 300°C for experiments with $C_{70}^{+\cdot}$.

2.2.4 Collision Gases.

All collision gases employed in this research were supplied by *BOC Special Gases* [195] with the exception of $C^{13}H_4$, CD_4, CF_4 and $C^{13}O$ which were purchased from *Fluorochem* [196]. All gases were of research grade purity.

CHAPTER THREE: *Target Capture of Noble Gases by $C_{60}^{+\cdot}$ and $C_{70}^{+\cdot}$ Radical Cations.*

3.1 Introduction.

Noble gases are most commonly employed as collision gases for collision-induced decomposition (CID) of multiatomic ions in tandem mass spectrometry. As the mechanism of CID is not well understood, ion-molecule reactions of noble gas atoms are of great interest. Target capture of noble gases had been studied previously [111, 161-175] with the conclusion reached being that helium and neon [111, 161] could be encapsulated by fullerene cages. It was also concluded that incorporation of krypton and xenon by fullerene radical ions was not possible in mass spectrometric experiments [170]. Inclusion of krypton and xenon, as well as argon, neon and helium was, however, achieved from high-pressure experiments with neutral C_{60} [116-118]. This chapter describes studies of the energetics of $He@C_{60}^{+\cdot}$, $He@C_{70}^{+\cdot}$, $Ne@C_{60}^{+\cdot}$ and $Ne@C_{70}^{+\cdot}$ adduct ions and contains evidence of encapsulation of argon by both $C_{60}^{+\cdot}$ and $C_{70}^{+\cdot}$ radical cations. Evidence to suggest possible incorporation of krypton and xenon by these ions is also given.

3.1.1 Experimental Conditions.

Electron impact ionisation was used to produce $C_{60}^{+\cdot}$ and $C_{70}^{+\cdot}$ radical cations from the crude fullerene sample. The desired fullerene ion was mass-selected using MS-I and subsequently focused into the collision cell. The collision cell was floated at potentials chosen so as to set desired laboratory-frame collision energies. Collision gases were introduced into the collision cell and their pressures were monitored as percentage decrease in the incident ion signal intensity following the increase in gas pressure inside the collision cell. MS-II was operated so as to analyse product ions resulting from collisions between the fullerene radical cation and target gas. As a portion of translational energy would be lost during collisions between an ion and a

stationary neutral, the second electric sector (E2) potential was reduced appropriately so as to transmit species of reduced kinetic energy. The β-slit situated at the exit of E2 was used to optimise the energy resolution of products exiting E2. The second magnet (B2) was scanned and spectra were recorded using a scanning array detector.

3.2 Target Capture of Helium and Neon by $C_{60}^{+\cdot}$ and $C_{70}^{+\cdot}$ Radical Cations.

Encapsulation of helium and neon by $C_{60}^{+\cdot}$ and $C_{70}^{+\cdot}$ radical cations has been reported previously [111, 161] and as a starting point these experiments were repeated. Figures 3.1(a) and 3.1(b) show $He@C_{60}^{+\cdot}$ and $He@C_{70}^{+\cdot}$ adducts. These spectra were measured at laboratory-frame collision energies of 5000 eV. Neon adducts, $Ne@C_{60}^{+\cdot}$ (figure 3.2(a)) and $Ne@C_{70}^{+\cdot}$ (figure 3.2(b)) were formed at laboratory-frame collision energies of 1500 eV and 2000 eV respectively. Neon has two isotopes. Ne^{20} (90.9%) and Ne^{22} (8.8%). The mass for neon used in calculating centre-of-mass collision energies was 20 Da. The spectra in figures 3.1 and 3.2 were obtained with E2 set to transmit those ions with an energy deficit equal to the centre-of-mass collision energy. The β-slit width was narrow in these experiments. The target gases were introduced at pressures sufficient to reduce parent ion signal to 50% of its original intensity.

3.2.1 Investigation of Collision Energies.

Once evidence for the $He@C_{60}^{+\cdot}$, $He@C_{70}^{+\cdot}$, $Ne@C_{60}^{+\cdot}$ and $Ne@C_{70}^{+\cdot}$ adducts had been established, experiments were carried out whereby the relationships between the abundances of these adducts and energy deficits were investigated by reducing the E2 potential in 2 V intervals. The areas of the adduct peaks were measured as a function of energy deficit. Resulting graphs are displayed in figures 3.3 to 3.6 inclusively. It can be seen from table 3.1 that in each case the abundances of the full adducts maximised at energy deficits equivalent to their centre-of-mass collision energies.

Following these experiments an investigation was undertaken to find the dependences of abundances of $He@C_{60}^{+\cdot}$, $He@C_{70}^{+\cdot}$, $Ne@C_{60}^{+\cdot}$ and $Ne@C_{70}^{+\cdot}$ on laboratory-frame collision energy. In this set of experiments, E2 was set to transmit ions with an energy deficit equal to the centre-of-mass collision energy for each laboratory-frame collision energy employed. Figures 3.7 to 3.10 inclusively show the areas of the adduct peaks relative to the areas of the parent ion peaks for different laboratory-frame collision energies. The formation of $He@C_{60}^{+\cdot}$ was found to be most probable at a range of laboratory-frame collision energy of 5600 ± 500 eV, corresponding to centre-of-mass collision energies of 31 ± 3 eV. Other workers have reported that the formation of $He@C_{60}^{+\cdot}$ was optimised between laboratory-frame collision energies of 5 keV and 6 keV [161]. Formation of $He@C_{70}^{+\cdot}$ was most probable for a centre-of-mass collision energy of 34 ± 3 eV (E_{lab} = 7200 ± 600 eV). Formation of the adduct $Ne@C_{60}^{+\cdot}$ was found to be most probable at E_{com} = 41 ± 3 eV (E_{lab} = 1500 ± 100 eV) and the adduct $Ne@C_{70}^{+\cdot}$ was observed over the range E_{com} = 42 ± 3 eV (E_{lab} = 1800 ± 150 eV). These results are summarised in table 3.2. In conclusion, helium and neon both formed adducts with $C_{60}^{+\cdot}$ at lower centre-of-mass collision energies than with $C_{70}^{+\cdot}$. In addition, helium formed adducts at a lower centre-of-mass collision energy than neon for a particular fullerene ion.

3.2.2 Investigation of Fragment Ions produced from Helium/$C_{70}^{+\cdot}$ Collisions.

Gross *et al.*[167, 170] reported association of two helium atoms with even-numbered $C_{70}^{+\cdot}$ fragment ions. They used a B/E linked scan to obtain a spectrum showing weak evidence for the series of species $C_{52}He_2^{+\cdot}$ to $C_{64}He_2^{+\cdot}$. An experiment aimed at reproducing these observations was carried out using a magnet (B2) scan. Multiple collisions would be required to trap more than one helium atom, so for this experiment the helium pressure used was sufficient to reduce the parent ion intensity to 20% of its original value. The β-slit was opened to its maximum width as interest lay in the observation of peaks at m/z = 8 above $C_{70}^{+\cdot}$ fragment peaks. Figure 3.11 shows the spectrum obtained when $C_{70}^{+\cdot}$ collided with helium at a

laboratory-frame collision energy of 7.9 keV. The E2 potential was adjusted for the energy deficit, predicted on the basis that $C_{70}He_2^{+\cdot}$ was formed and subsequently decomposed to $C_{62}He_2^{+\cdot}$. Species observed in this spectrum are $C_{60}^{+\cdot}$, $C_{60}He^{+\cdot}$, $C_{60}He_2^{+\cdot}$, $C_{62}^{+\cdot}$, $C_{62}He^{+\cdot}$, $C_{62}He_2^{+\cdot}$, $C_{64}^{+\cdot}$, $C_{64}He^{+\cdot}$ and $C_{66}^{+\cdot}$. On increasing E2 so as to transmit ions with the energy deficit expected on the basis that $C_{70}He_2^{+\cdot}$ was formed and then decomposed to $C_{60}He_2^{+\cdot}$ (figure 3.12), the $C_{60}He_2^{+\cdot}$ peak became more abundant relative to $C_{60}^{+\cdot}$. $C_{60}He^{+\cdot}$ was still observed, and $C_{62}^{+\cdot}$, $C_{62}He^{+\cdot}$ and $C_{64}^{+\cdot}$ remained as intense peaks. In summary, a series of helium/$C_{70}^{+\cdot}$ fragment ions were observed: $C_{62}He_2^{+\cdot}$ to $C_{56}He_2^{+\cdot}$ inclusive (table 3.3).

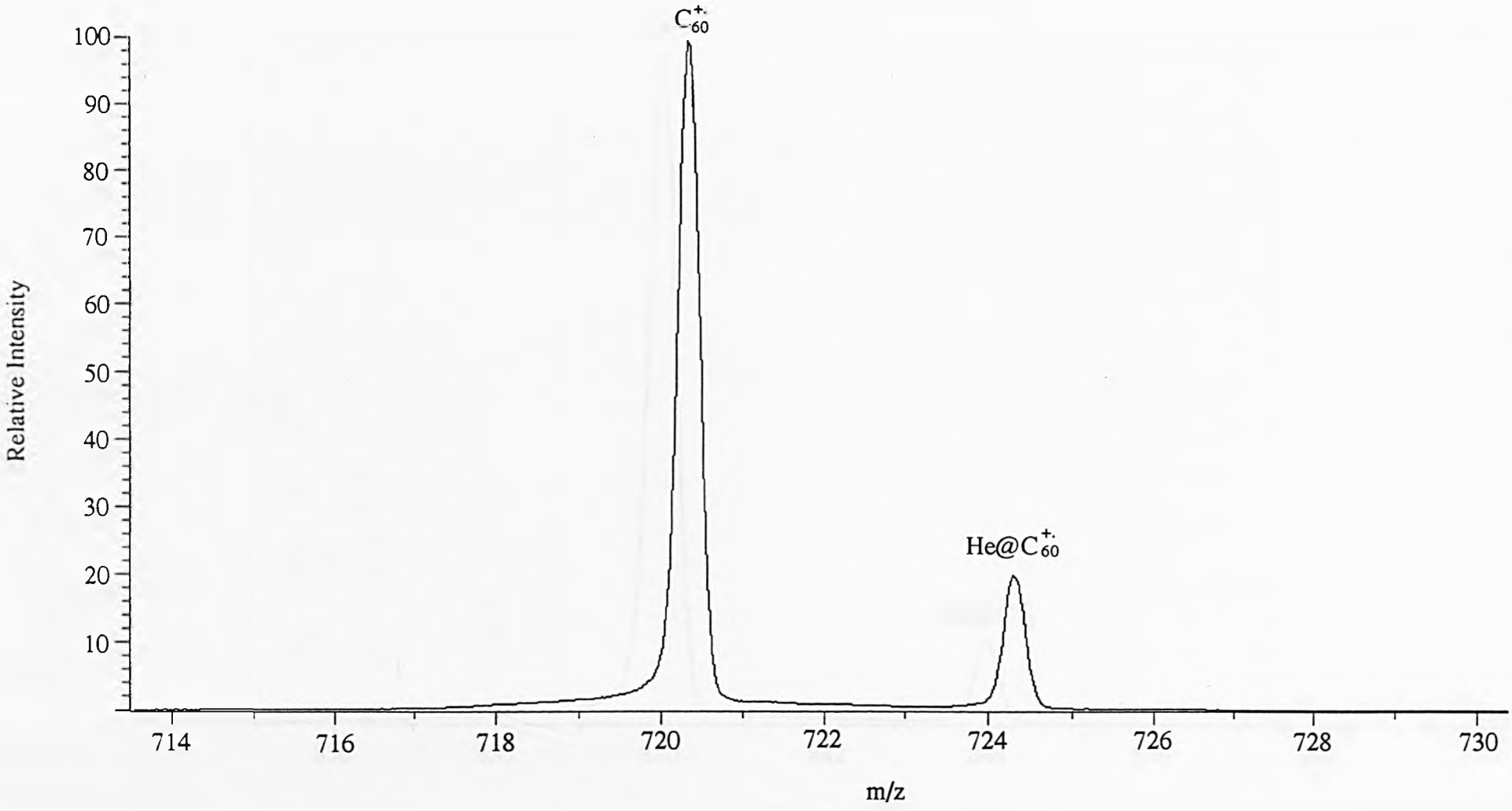

Figure 3.1(a): Magnet scan of $C_{60}^{+\cdot}$ and helium at E_{lab} = 5.0 keV.

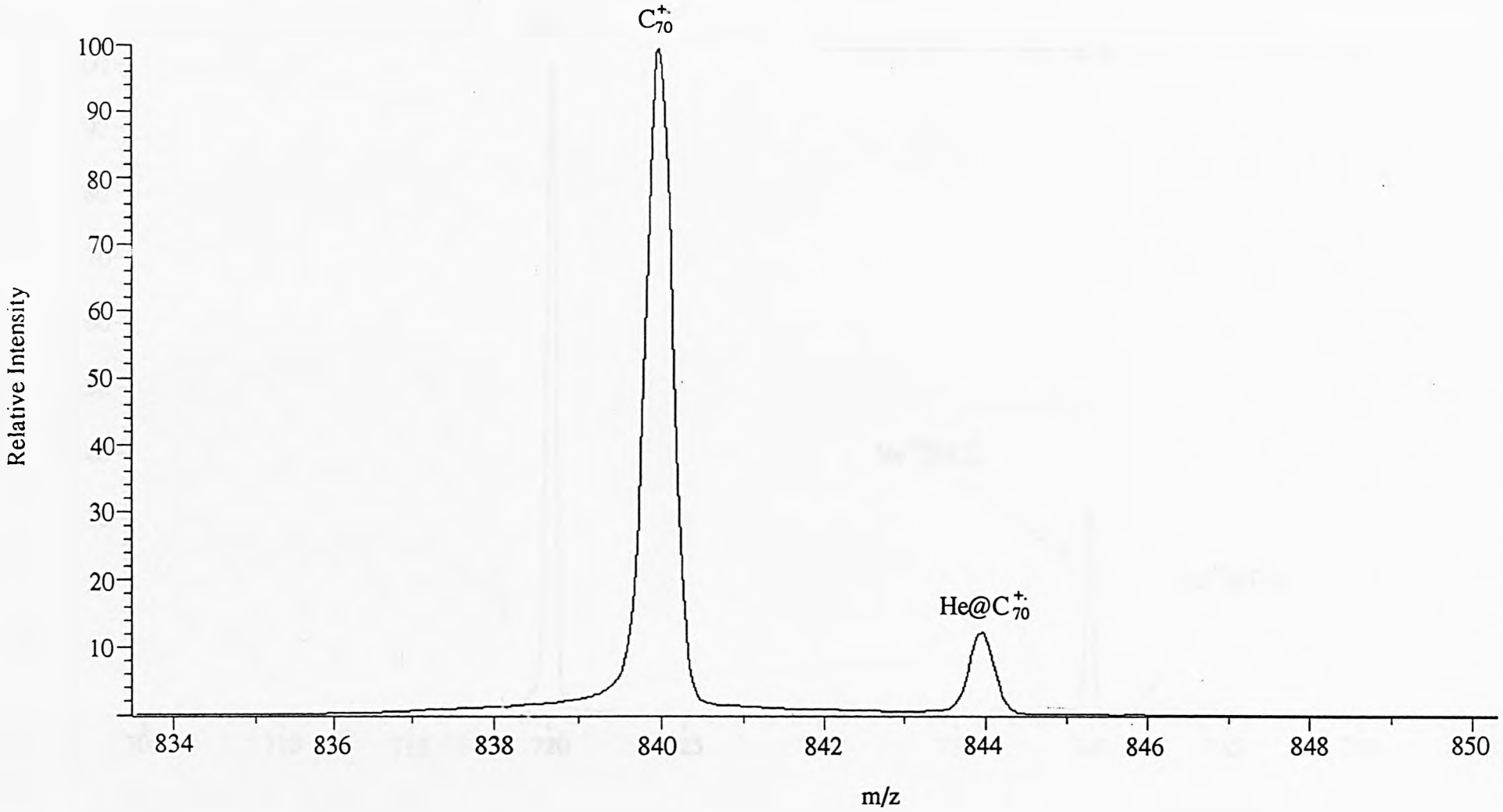

Figure 3.1(b): Magnet scan of $C_{70}^{+\cdot}$ and helium at E_{lab} = 5.0 keV.

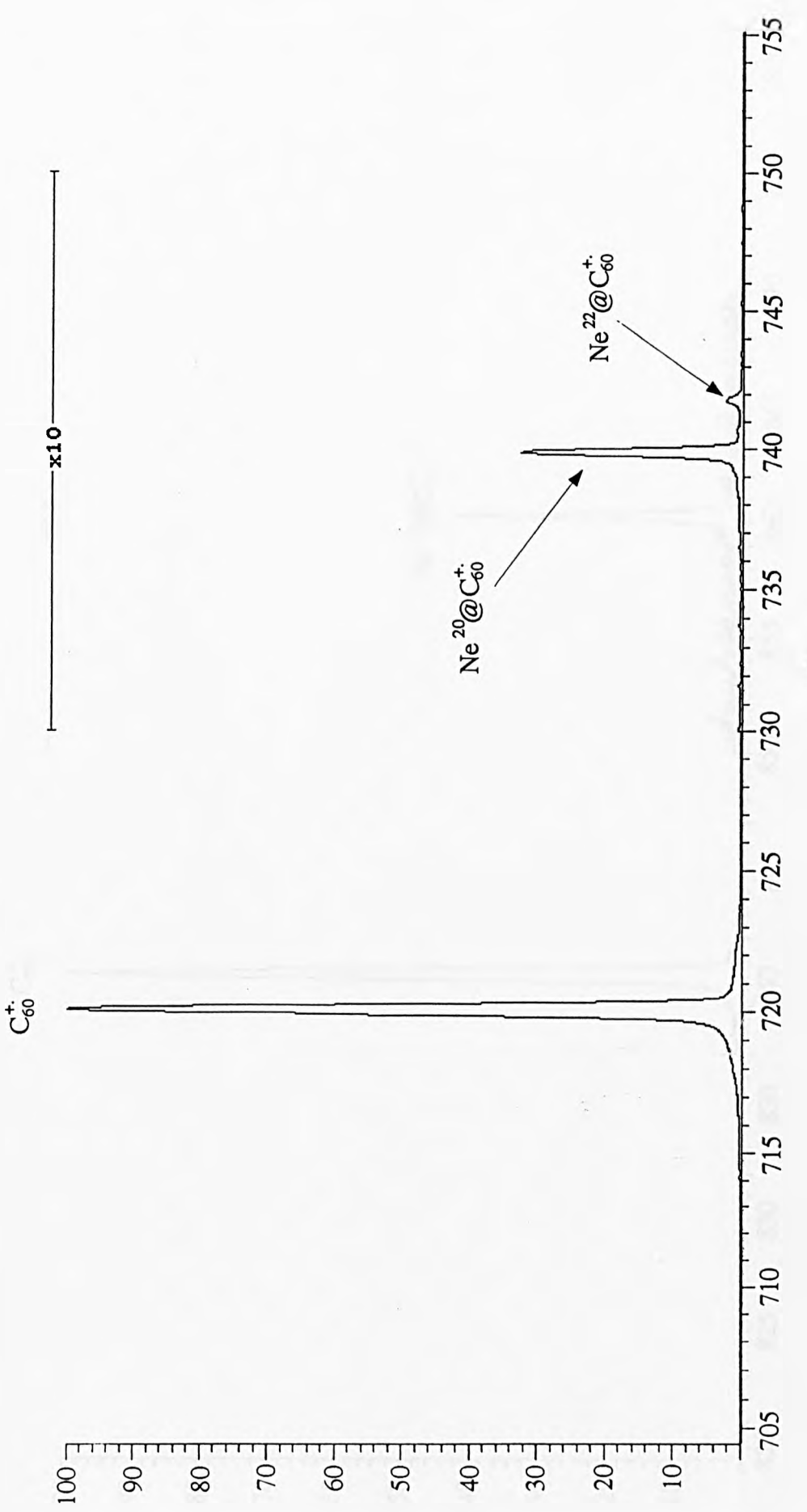

Figure 3.2(a): Magnet scan of $C_{60}^{+\cdot}$ and neon at E_{lab} = 1.5 keV.

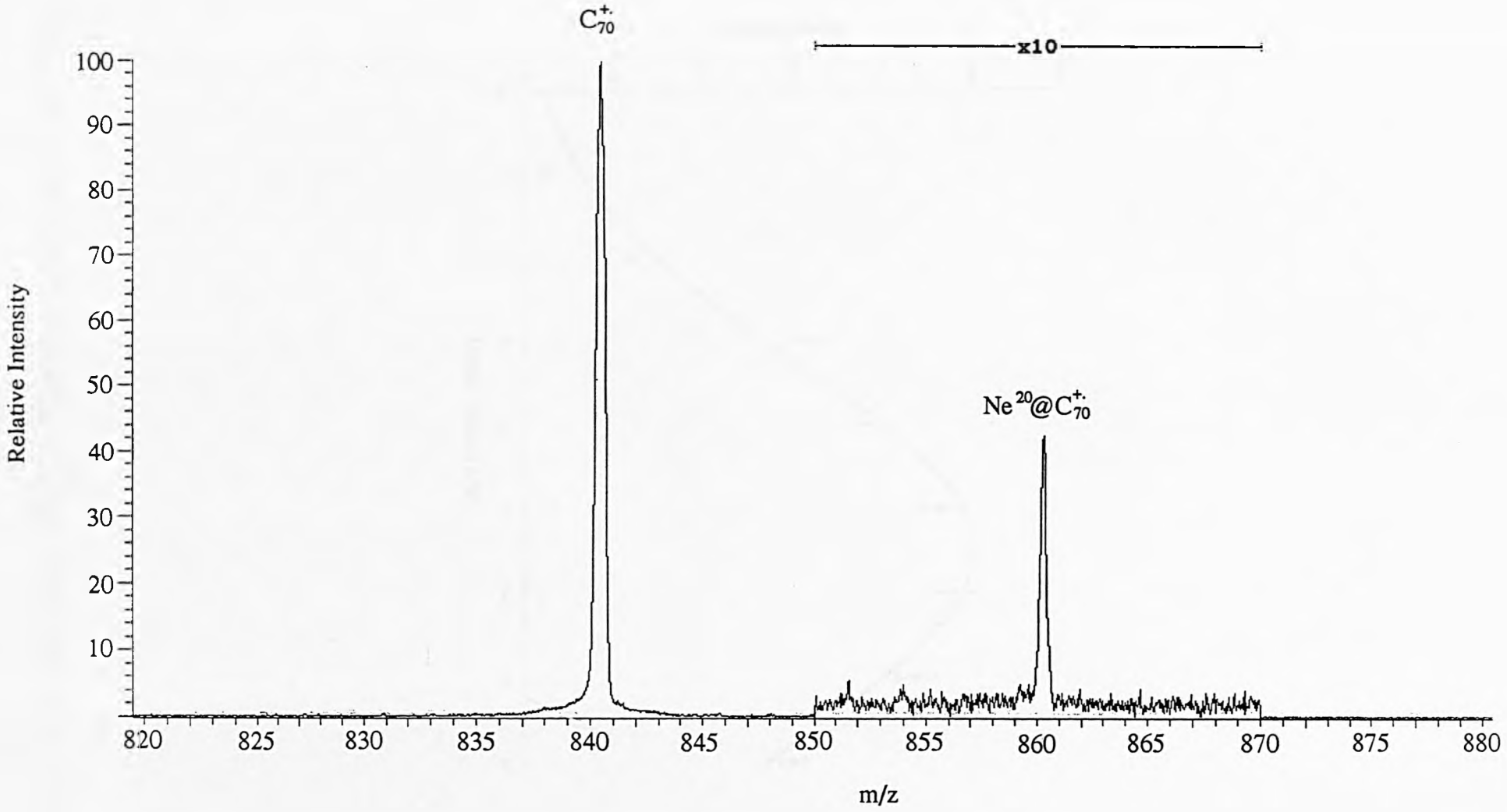

Figure 3.2(b): Magnet scan of $C_{70}^{+\cdot}$ and neon at E_{lab} = 2.0 keV.

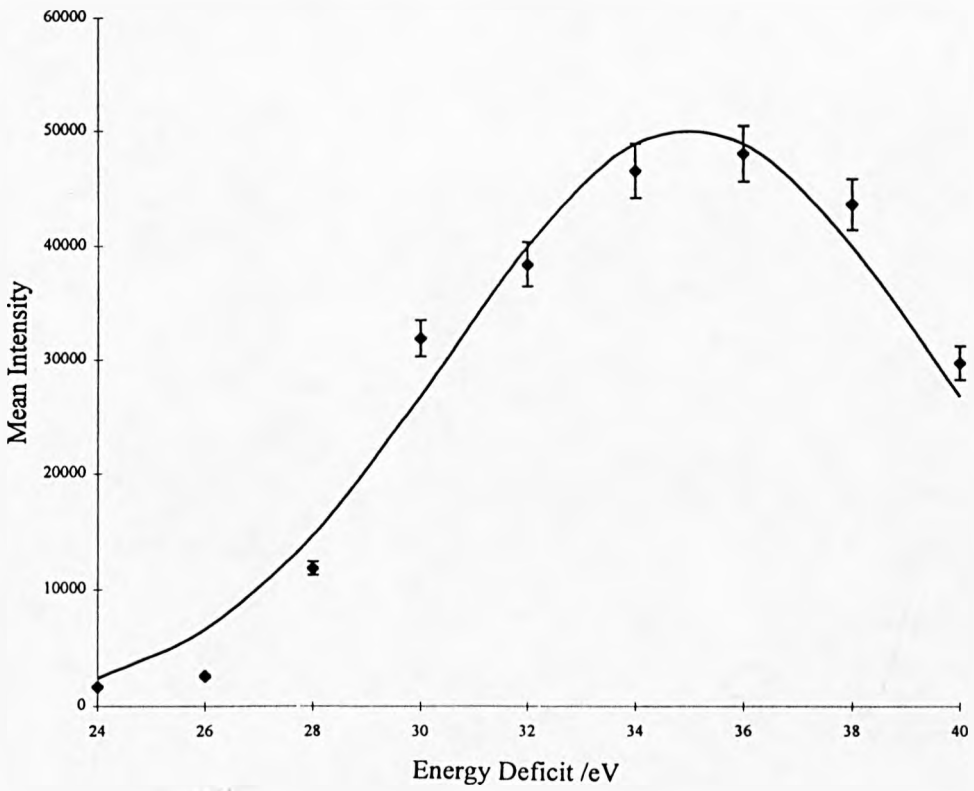

Figure 3.3: Mean intensity of $He@C_{60}^{+\cdot}$ against energy deficit at E_{lab} = 5750 eV.

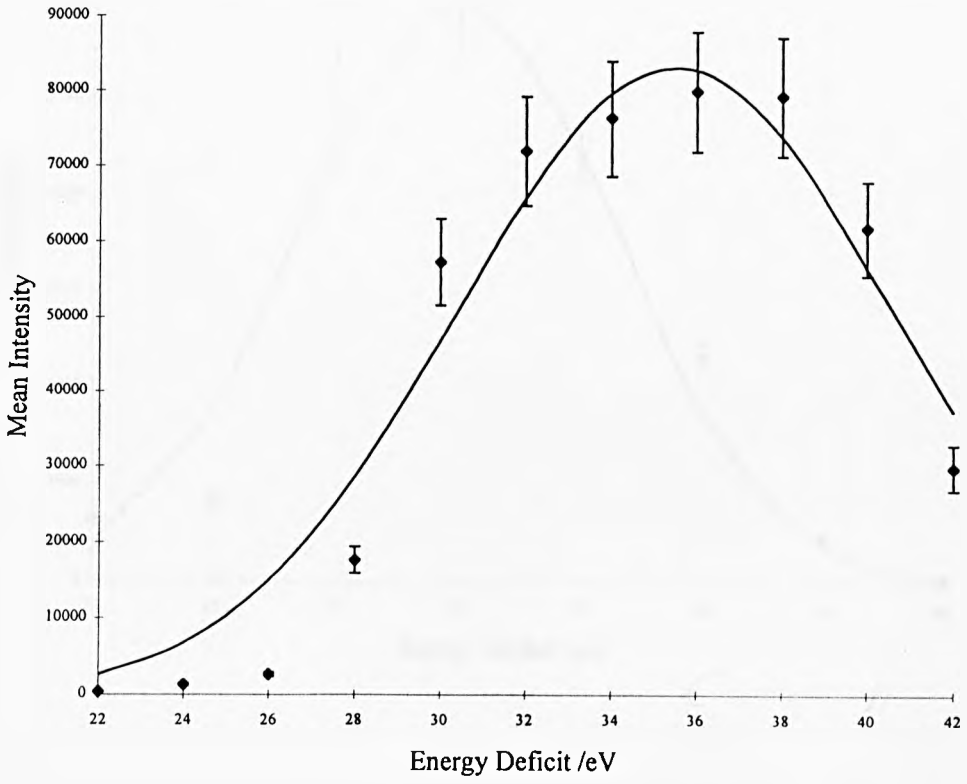

Figure 3.4: Mean intensity of $He@C_{70}^{+\cdot}$ against energy deficit at E_{lab} = 7000 eV.

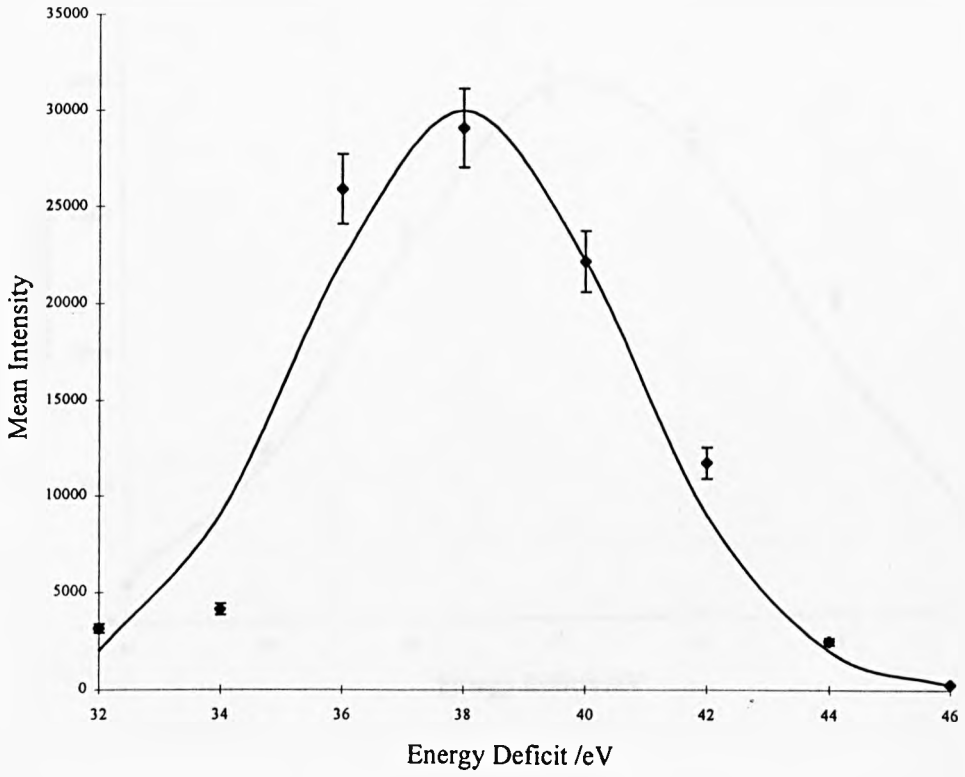

Figure 3.5: Mean intensity of $Ne@C_{60}^{+\cdot}$ against energy deficit at E_{lab} = 1500 eV.

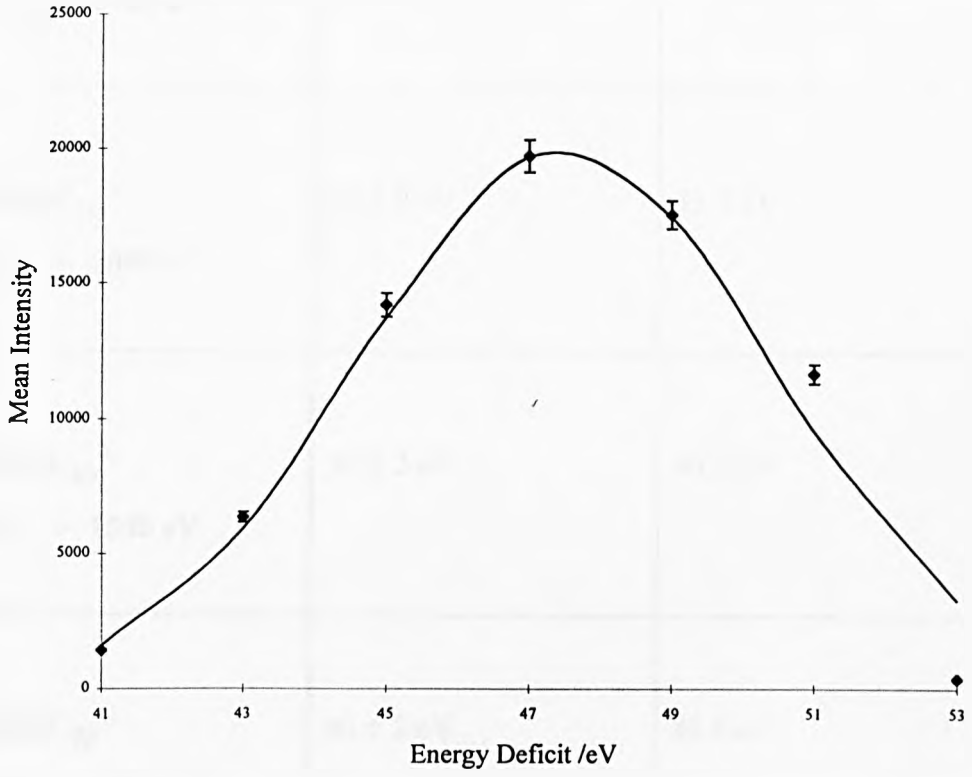

Figure 3.6: Mean intensity of $Ne@C_{70}^{+\cdot}$ against energy deficit at E_{lab} = 2000 eV.

	Energy deficit /eV	**E_{com} /eV**
$He@C_{60}^{+\cdot}$ **E_{lab} = 5750 eV**	35 ± 2 eV	31.8 eV
$He@C_{70}^{+\cdot}$ **E_{lab} = 7000 eV**	35 ± 2 eV	33.2 eV
$Ne@C_{60}^{+\cdot}$ **E_{lab} = 1500 eV**	39 ± 2 eV	40.5 eV
$Ne@C_{70}^{+\cdot}$ **E_{lab} = 2000 eV**	46 ± 2 eV	46.5 eV

Table 3.1: Comparison of experimental energy deficit settings with centre-of-mass collision energies for the formation of $He@C_{60}^{+\cdot}$, $He@C_{70}^{+\cdot}$, $Ne@C_{60}^{+\cdot}$ and $Ne@C_{70}^{+\cdot}$.

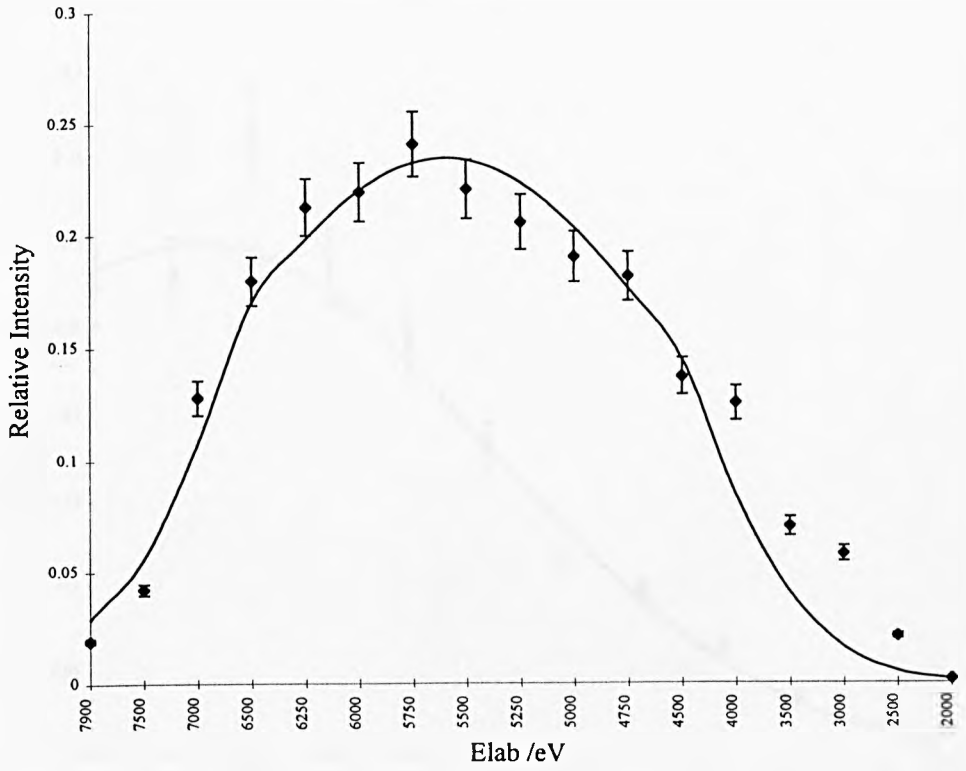

Figure 3.7: Relative intensity of $He@C_{60}^{+\cdot}$ against laboratory-frame collision energy.

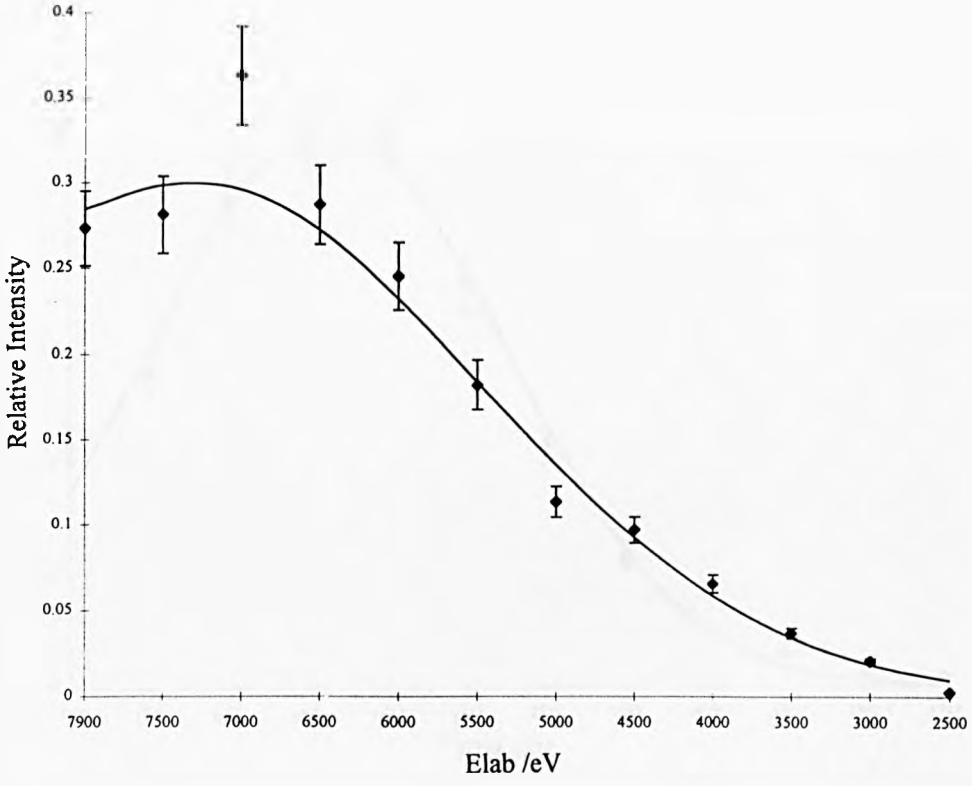

Figure 3.8: Relative intensity of $He@C_{70}^{+\cdot}$ against laboratory-frame collision energy.

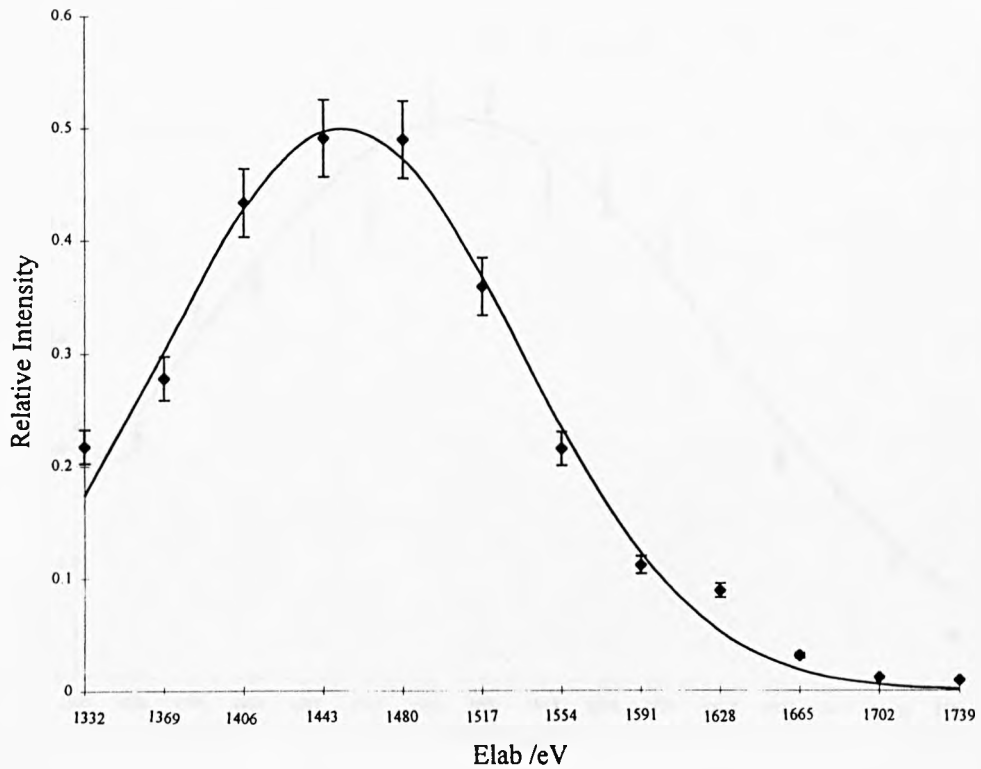

Figure 3.9: Relative intensity $Ne@C_{60}^{+\cdot}$ against laboratory-frame collision energy.

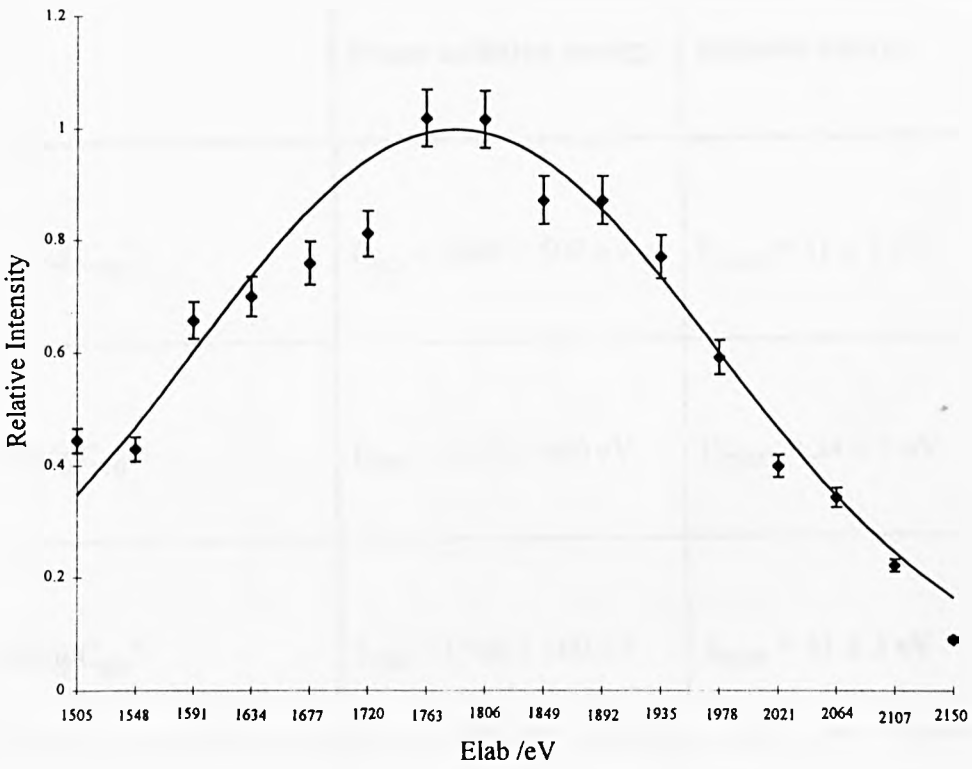

Figure 3.10: Relative intensity of $Ne@C_{70}^{+\cdot}$ against laboratory-frame collision energy.

	Optimum laboratory-frame collision energy	**Centre-of-mass frame collision energy**
He@$C_{60}^{+\cdot}$	E_{lab} = 5600 ± 500 eV	E_{com} = 31 ± 3 eV
He@$C_{70}^{+\cdot}$	E_{lab} = 7200 ± 600 eV	E_{com} = 34 ± 3 eV
Ne@$C_{60}^{+\cdot}$	E_{lab} = 1500 ± 100 eV	E_{com} = 41 ± 3 eV
Ne@$C_{70}^{+\cdot}$	E_{lab} = 1800 ± 150 eV	E_{com} = 42 ± 3 eV

Table 3.2: Summary of optimum laboratory-frame and centre-of-mass frame collision energies for the formation of He@$C_{60}^{+\cdot}$, He@$C_{70}^{+\cdot}$, Ne@$C_{60}^{+\cdot}$ and Ne@$C_{70}^{+\cdot}$.

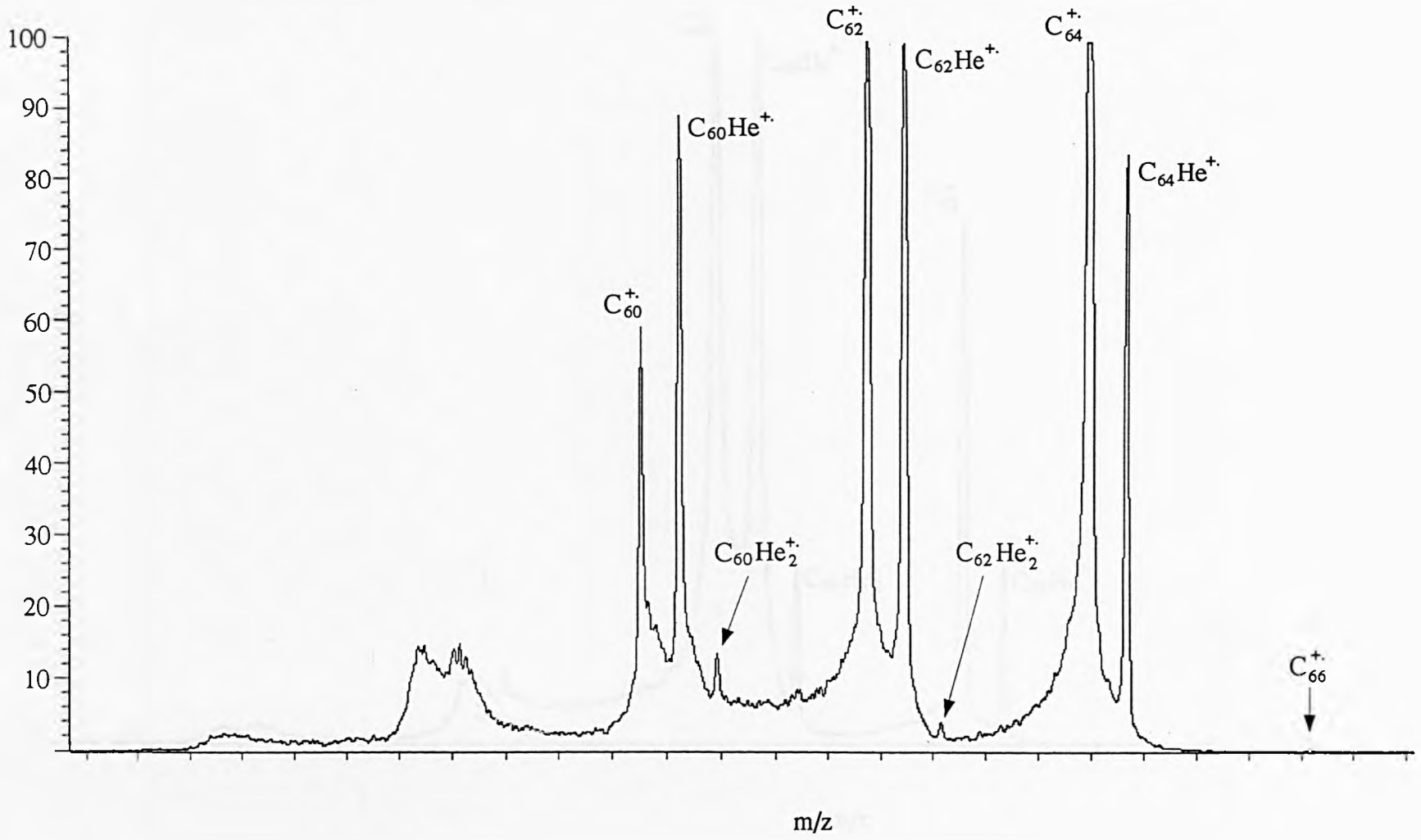

Fig 3.11: Magnet scan of $C_{70}^{+\cdot}$ and helium at E_{lab} = 7.9 keV, E_{def} = 961 eV.

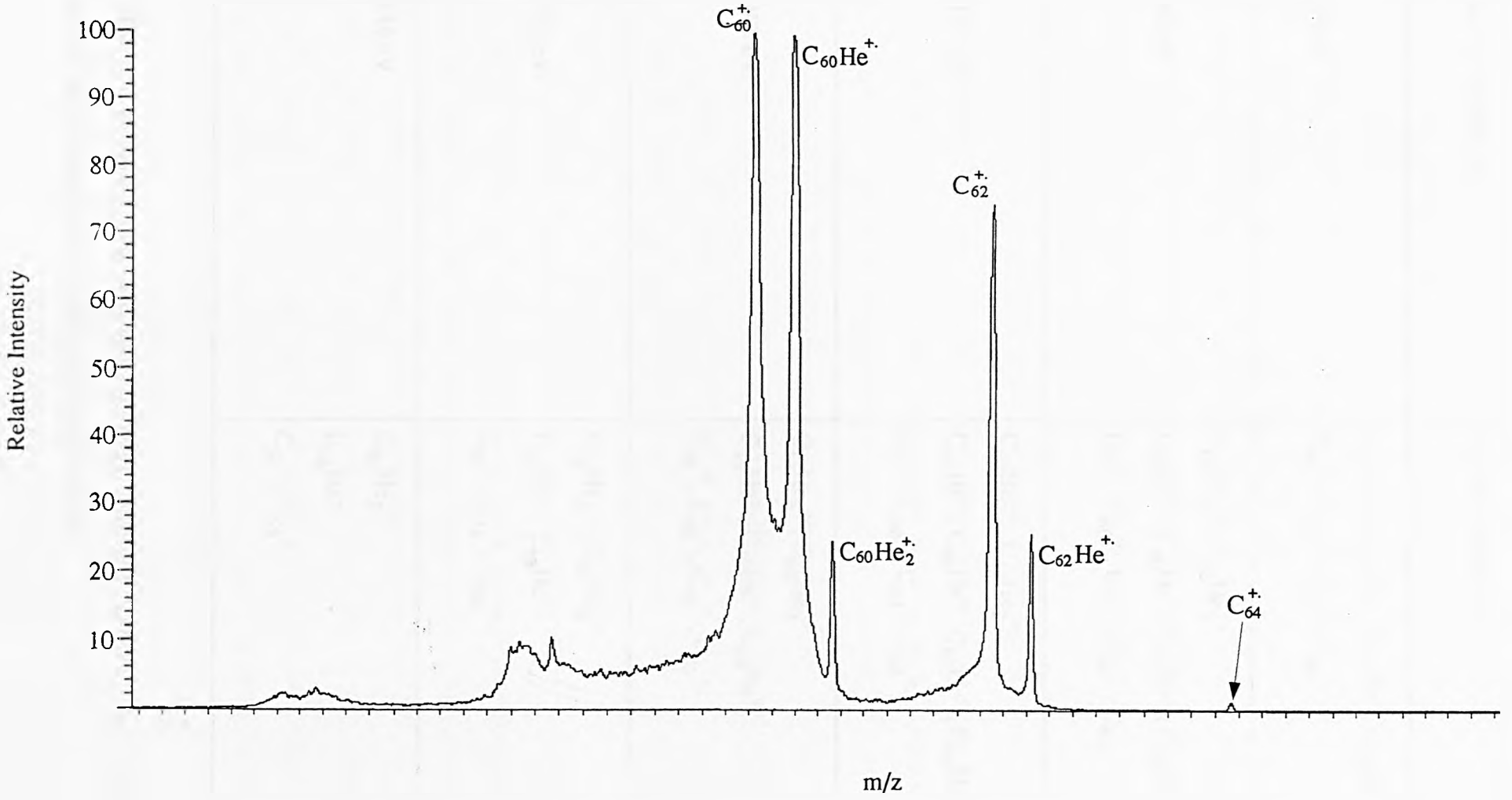

Figure 3.12: Magnet scan of $C_{70}^{+\cdot}$ and helium at E_{lab} = 7.9 keV, E_{def} = 1182 eV.

Energy deficit /eV	**Species observed**
739 eV	$C_{60}He^{+\cdot}$, $C_{62}He^{+\cdot}$, $C_{64}He^{+\cdot}$, $C_{66}He^{+\cdot}$ $C_{60}^{+\cdot}$, $C_{62}^{+\cdot}$, $C_{64}^{+\cdot}$, $C_{66}^{+\cdot}$
960 eV	$C_{60}He_2^{+\cdot}$, $C_{62}He_2^{+\cdot}$ $C_{58}He^{+\cdot}$, $C_{60}He^{+\cdot}$, $C_{62}He^{+\cdot}$, $C_{64}He^{+\cdot}$ $C_{58}^{+\cdot}$, $C_{60}^{+\cdot}$, $C_{62}^{+\cdot}$, $C_{64}^{+\cdot}$, $C_{66}^{+\cdot}$
1182 eV	$C_{60}He_2^{+\cdot}$, $C_{62}He_2^{+\cdot}$ $C_{58}He^{+\cdot}$, $C_{60}He^{+\cdot}$, $C_{62}He^{+\cdot}$, $C_{64}He^{+\cdot}$ $C_{58}^{+\cdot}$, $C_{60}^{+\cdot}$, $C_{62}^{+\cdot}$, $C_{64}^{+\cdot}$
1403 eV	$C_{58}He_2^{+\cdot}$, $C_{60}He_2^{+\cdot}$ $C_{56}He^{+\cdot}$, $C_{58}He^{+\cdot}$, $C_{60}He^{+\cdot}$ $C_{56}^{+\cdot}$, $C_{58}^{+\cdot}$, $C_{60}^{+\cdot}$, $C_{62}^{+\cdot}$
1625 eV	$C_{56}He_2^{+\cdot}$, $C_{58}He_2^{+\cdot}$ $C_{56}He^{+\cdot}$, $C_{58}He^{+\cdot}$ $C_{56}^{+\cdot}$, $C_{58}^{+\cdot}$, $C_{60}^{+\cdot}$
1846 eV	$C_{56}He_2^{+\cdot}$ $C_{56}He^{+\cdot}$ $C_{56}^{+\cdot}$, $C_{58}^{+\cdot}$

Table 3.3: Fragment ions observed following collisions between $C_{70}^{+\cdot}$ and helium with E2 set to transmit ions with large energy deficits.

3.3 Target Capture of Argon, Krypton and Xenon by $C_{60}^{+\cdot}$ and $C_{70}^{+\cdot}$ Radical Cations.

Prior to the undertaking of this research, it was firmly believed that atomic gases larger then neon could not be trapped by fullerene ions under mass spectrometric conditions [170]. It had been reported that argon formed adduct ions consisting of odd-numbered carbon clusters plus argon following reactive collisions with $C_{70}^{+\cdot}$ in a mass spectrometer [170]. All the inert gases have, however, been shown to form endohedral compounds with fullerene using other experimental techniques [116-118], so the question of whether or not argon, krypton and xenon would physically fit inside C_{60} or C_{70} fullerene cages does not seem to arise.

Argon was introduced into the collision cell at a pressure sufficient to reduce the parent ion intensity to 50% of its original value. The second electric sector potential was reduced by an amount equivalent to the centre-of-mass collision energy. Figure 3.13 shows a peak at m/z = 760 corresponding to argon trapped by $C_{60}^{+\cdot}$. Similarly figure 3.14 shows trapping of argon by $C_{70}^{+\cdot}$. The spectrum given in figure 3.13 was obtained at E_{lab} = 800 eV and that in figure 3.14 was obtained at E_{lab} = 1000 eV.

Krypton has five isotopes greater than 1% abundance: Kr^{84} = 56.9%, Kr^{86} = 17.4%, Kr^{82} = 11.6%, Kr^{83} = 11.6% and Kr^{80} = 2.3%. The average mass of krypton (83.8 Da) was used for all collision-energy calculations. Xenon has seven isotopes with an abundance greater than 1%: Xe^{132} = 26.9%, Xe^{129} = 26.4%, Xe^{131} = 21.2%, Xe^{134} = 10.4% and Xe^{136} = 8.9%, Xe^{130} = 4.1% and Xe^{128} = 1.9%. The average mass of xenon (131.3 Da) was used for all collision-energy calculations. As full krypton or xenon adducts would be so far removed in mass from the parent ion, the β-slit after E2 was set wider than in previous experiments with helium, neon or argon. Krypton and xenon, like argon, were introduced into the collision cell at pressures sufficient to reduce the parent ion signal to 50% of its original intensity. Figures 3.15 and 3.16 show evidence to suggest that krypton was captured by $C_{60}^{+\cdot}$ and $C_{70}^{+\cdot}$

respectively. The peak at m/z = 804 (figure 3.15) is tentatively assigned as the full $C_{60}Kr^{+\cdot}$ adduct ion. The peak at m/z = 924 (figure 3.16) is tentatively assigned as full $C_{70}Kr^{+\cdot}$. The observation of a single isotope of krypton associated with $C_{60}^{+\cdot}$ and $C_{70}^{+\cdot}$ would have to be attributed to reducing the potential of E2 by the amount appropriate for the average mass of krypton, which is closer to Kr^{84} than Kr^{86}.

Due to the β-slit not being reduced in width as much as in previous experiments with helium, neon or argon, additional peaks were observed between the parent ion and the putative $C_{60}Kr^{+\cdot}$ adduct peak. Figure 3.15 contains two clusters of peaks 24 Da and 48 Da less than the peak assigned as the full adduct ion. Each cluster of peaks show an intensity distribution which corresponds to the relative abundances of krypton's isotopes. Hence the clusters have been assigned as $C_{58}Kr^{+\cdot}$ and $C_{56}Kr^{+\cdot}$ ions. Corresponding fragment ions were absent from figure 3.16 when the incident ion was $C_{70}^{+\cdot}$. Possibly, the adduct with the larger fullerene is more stable.

Figures 3.17 and 3.18 show spectra containing evidence of capture of xenon by $C_{60}^{+\cdot}$ and $C_{70}^{+\cdot}$ respectively. Once more the adduct peaks were of low intensities, and it was the observation of the isotope pattern of xenon that supports assignment of the cluster of peaks at m/z = 848 to 855 to the full xenon/$C_{60}^{+\cdot}$ adduct. There was a discrepancy in the mass-assignment made by the computer in the case of $C_{70}^{+\cdot}$. The cluster of peaks fitting the isotope pattern of xenon were 1 Da less in mass than would be expected for a $C_{70}Xe^{+\cdot}$ adduct. This cannot be explained, only to say the most intense peak in this cluster corresponds to an addition of 131.5 Da which is approximately the average mass of xenon (131.3 Da) as used in calculating the energy deficit (equal to the centre-of-mass collision energy) for the E2 setting. Two clusters of peaks were observed between $C_{60}^{+\cdot}$ and the full adduct peak. These have been assigned as $XeC_{58}^{+\cdot}$ and $XeC_{56}^{+\cdot}$. When $C_{70}^{+\cdot}$ was the incident ion, three clusters of peaks were observed between the incident ion peak and the cluster of peaks assigned as the full xenon/$C_{70}^{+\cdot}$ adduct. These three clusters of peaks are assigned as $XeC_{64}^{+\cdot}$, $XeC_{66}^{+\cdot}$ and $XeC_{68}^{+\cdot}$ species. The peaks at at m/z = 724 in figure 3.17 and m/z = 844

in figure 3.18 could not be assigned. These peaks, both about 4 Da above the particular parent ions, may be due to a helium impurity in the xenon.

3.3.1 Investigation of Collision Energies.

Argon was found to form an adduct with $C_{60}^{+\cdot}$, which was observed over the range of centre-of-mass collision energies from 40 eV to 45 eV. Laboratory-frame collision energies of 760 eV to 855 eV correspond to this range. A $C_{70}Ar^{+\cdot}$ species was observed at centre-of-mass collision energies of 42 eV to 47 eV (laboratory-frame collision energies of 924 eV to 1034 eV). Evidence for $C_{60}Kr^{+\cdot}$ was only obtained with a centre-of-mass collision energy of 46 eV (*i.e.* laboratory-frame collision energy of 440 eV). Evidence for krypton associated with $C_{70}^{+\cdot}$ was observed at a centre-of-mass collision energy of 45 eV only (laboratory-frame collision energy of 500 eV). Collisions between xenon and $C_{60}^{+\cdot}$ produced a $C_{60}Xe^{+\cdot}$ species at a centre-of-mass collision energy of 42 eV (E_{lab} = 270 eV). $C_{70}^{+\cdot}$ reacted with xenon to give a tenuous $C_{70}Xe^{+\cdot}$ adduct at centre-of-mass collision energy of 45 eV (E_{lab} = 330 eV). These results are summarised in tables 3.4(a), (b) and (c) for argon, krypton and xenon respectively. Centre-of-mass collision energies ranging between 40 and 47 eV were required to form argon, and possibly krypton and xenon adducts with fullerene ions. Neon also formed adducts with $C_{60}^{+\cdot}$ and $C_{70}^{+\cdot}$ within this limit. Helium formed adducts with $C_{60}^{+\cdot}$ and $C_{70}^{+\cdot}$ at significantly lower centre-of-mass collision energies, ranging between 28 and 37 eV.

3.3.2 Fragmented Adduct Ions.

Two helium atoms associated with $C_n^{+\cdot}$ (n = 62 to 56 inclusive) fragment ions of $C_{70}^{+\cdot}$ have been observed by different experimental methods in previous studies and in this study (figures 3.11 and 3.12). Evidence for $C_{58}Xe^{+\cdot}$ and $C_{56}Xe^{+\cdot}$, $C_{68}Xe^{+\cdot}$, $C_{66}Xe^{+\cdot}$ and $C_{64}Xe^{+\cdot}$ and $C_{58}Kr^{+\cdot}$ and $C_{56}Kr^{+\cdot}$ was noted when the β-slit was wider than typically used for this type of experiment (figures 3.15, 3.17 and

3.18). By adjusting the E2 setting to transmit ions with a greater energy deficit than an amount equal to the centre-of-mass collision energy, a whole range of fullerene fragment ions with noble gas atoms in association were observed. The β-slit width was reduced so as to optimise energy resolution of these fragment ions. The full adduct was no longer observed. E2 was set to transmit ions with energy deficits calculated on the basis that the full adduct was formed and decomposed. Figure 3.19 shows the spectrum obtained from when E2 was set to transmit ions with an energy deficit calculated on the basis that ten carbon atoms were lost from $C_{60}Ar^{+\cdot}$. $C_{50}Ar^{+\cdot}$, $C_{52}Ar^{+\cdot}$, $C_{54}Ar^{+\cdot}$ and $C_{56}Ar^{+\cdot}$ peaks were observed. $C_{50}^{+\cdot}$, $C_{52}^{+\cdot}$, $C_{54}^{+\cdot}$ and $C_{56}^{+\cdot}$ peaks were also observed. Broad signals at m/z = 576 and 600 are tentatively assigned as $C_{48}^{+\cdot}$ and $C_{50}^{+\cdot}$, presumed to be unfocused due to the restrictions set by the β-slit. Odd-numbered carbon-cluster ions with argon atoms in association were not observed [170]. For reactive collisions between krypton and $C_{60}^{+\cdot}$, when E2 was set for an energy deficit calculated on the basis that ten carbon atoms are lost from the closed fullerene cage, peaks assigned as $C_{56}^{+\cdot}$, $C_{58}^{+\cdot}$ and $C_{60}^{+\cdot}$ were observed (figure 3.20). Fragment ions $C_{50}Kr^{+\cdot}$, $C_{52}Kr^{+\cdot}$, $C_{54}Kr^{+\cdot}$ and $C_{56}Kr^{+\cdot}$ were observed as clusters of peaks whose intensities corresponded to relative abundances of the various isotopes of krypton. Broad signals at m/z = 624 and 648, possibly $C_{52}^{+\cdot}$ and $C_{54}^{+\cdot}$ were also observed. On changing the target gas to xenon and adjusting the E2 setting to transmit ions with an energy deficit equivalent to an amount calculated on the basis that ten carbon atoms were lost from $C_{60}Xe^{+\cdot}$, the spectrum in figure 3.21(a) was observed. $C_{60}^{+\cdot}$ was observed, as were the fragment ions $C_{54}^{+\cdot}$, $C_{56}^{+\cdot}$ and $C_{58}^{+\cdot}$. Peaks at m/z = 600 and 624, assigned as $C_{50}^{+\cdot}$ and $C_{52}^{+\cdot}$, were presumed to be unfocused. Peaks representing xenon associated with $C_{60}^{+\cdot}$ fragment ions were identified as $C_{52}Xe^{+\cdot}$, $C_{54}Xe^{+\cdot}$ and $C_{56}Xe^{+\cdot}$ due to these clusters of peaks showing intensity distributions identical to the relative abundances of the xenon isotopes. Broad signals around m/z = 707 and 731, possibly due to unfocused $C_{48}Xe^{+\cdot}$ and $C_{50}Xe^{+\cdot}$ species, were also present in the spectrum (figure 3.21(a)). Figure 3.21(b), an expanded portion of figure 3.21(a), shows $C_{52}Xe^{+\cdot}$ and $C_{54}Xe^{+\cdot}$ in more detail.

Tables 3.5(a) and (b) show for argon, krypton and xenon, the fullerene fragment ions retaining these noble gases which were observed when E2 was set to transmit ions with energy deficits calculated for the loss of 2, 4, 6, 8 and 10 carbon atoms from (a) $C_{60}^{+\cdot}$ and (b) $C_{70}^{+\cdot}$ fullerene cages respectively.

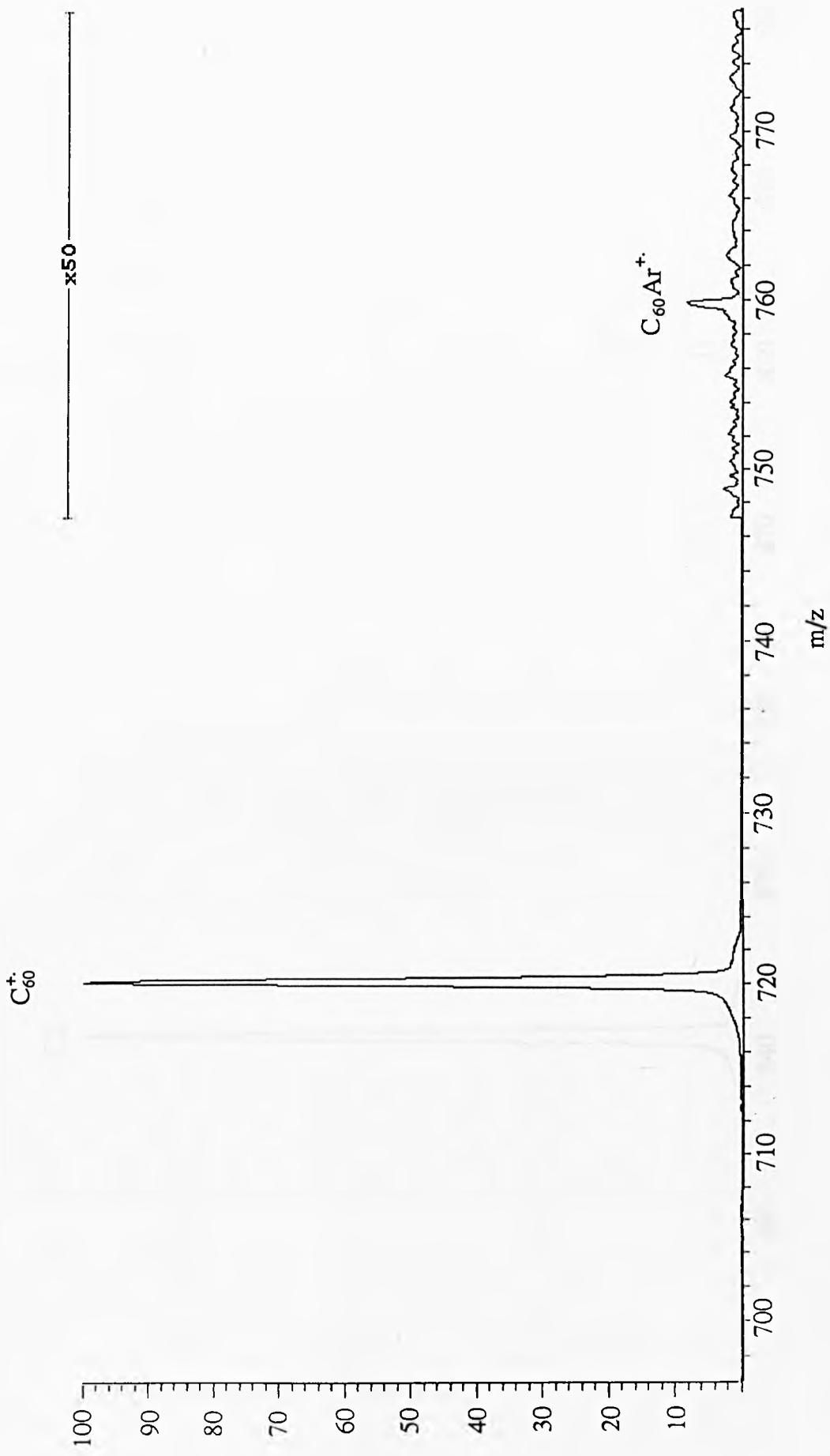

Figure 3.13: Magnet scan of $C_{60}^{+\cdot}$ and argon at E_{lab} = 800 eV.

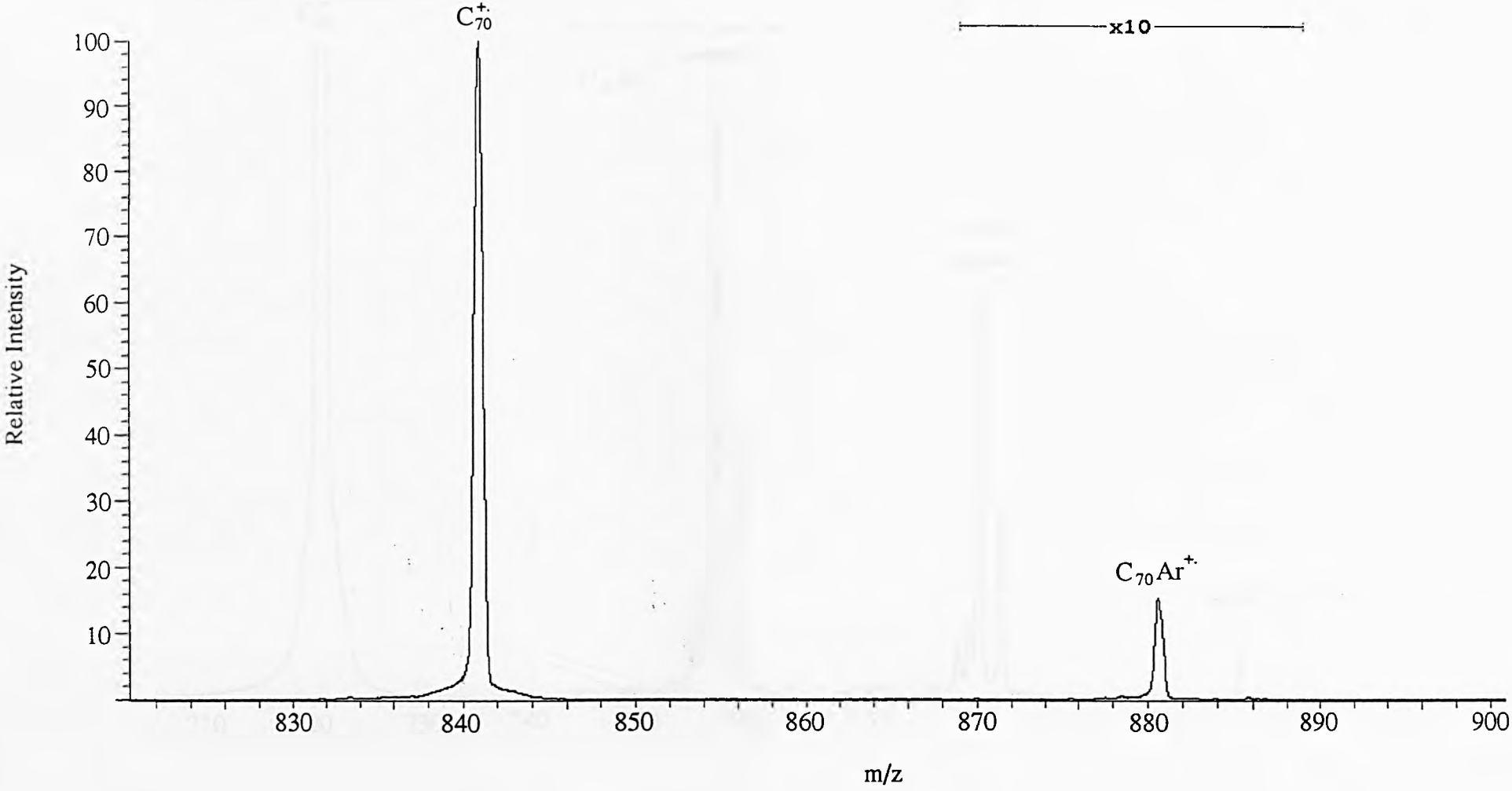

Figure 3.14: Magnet scan of $C_{70}^{+\cdot}$ and argon at E_{lab} = 1000 eV.

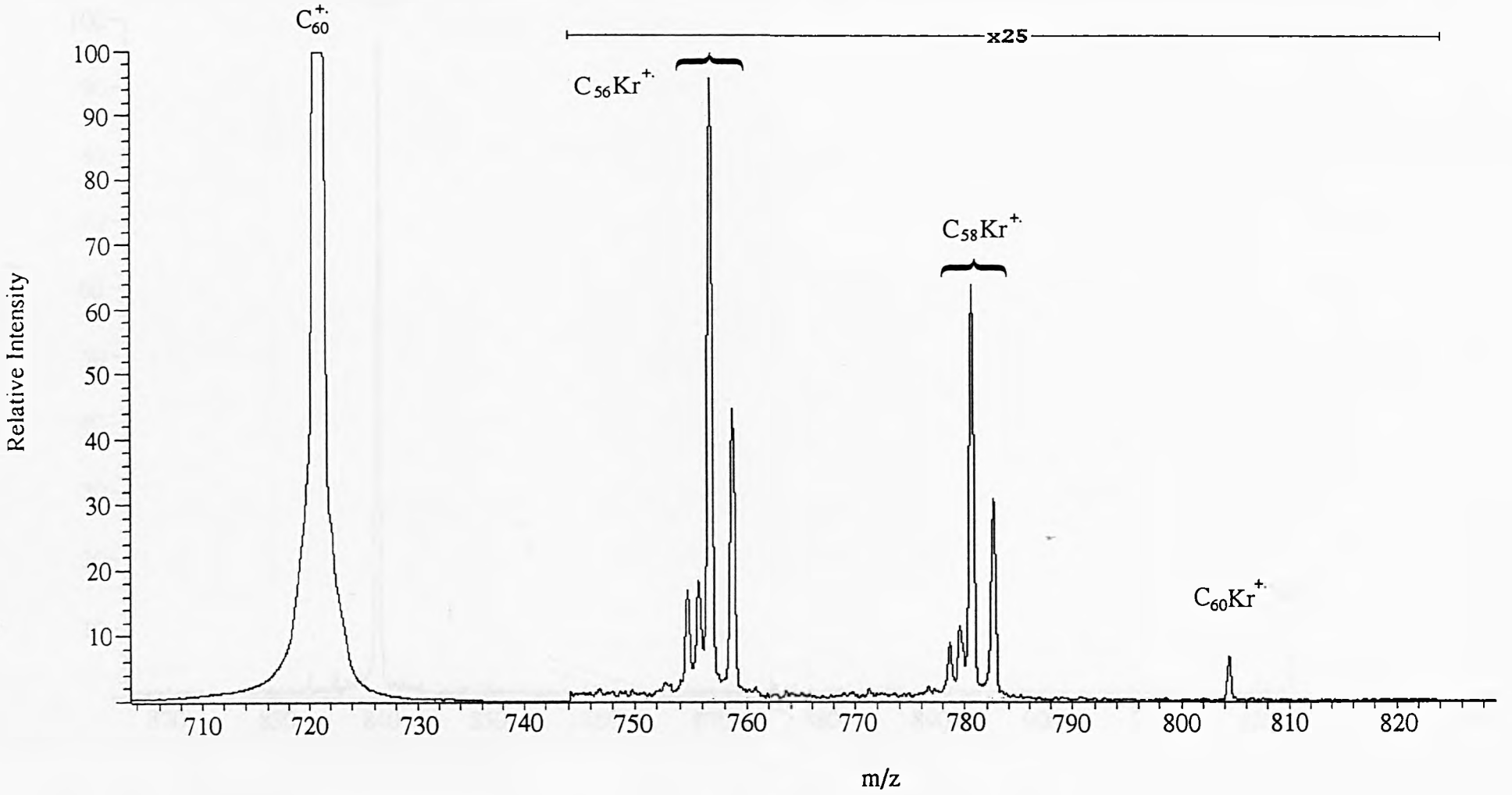

Figure 3.15: Magnet scan of $C_{60}^{+\cdot}$ and krypton at E_{lab} = 440 eV.

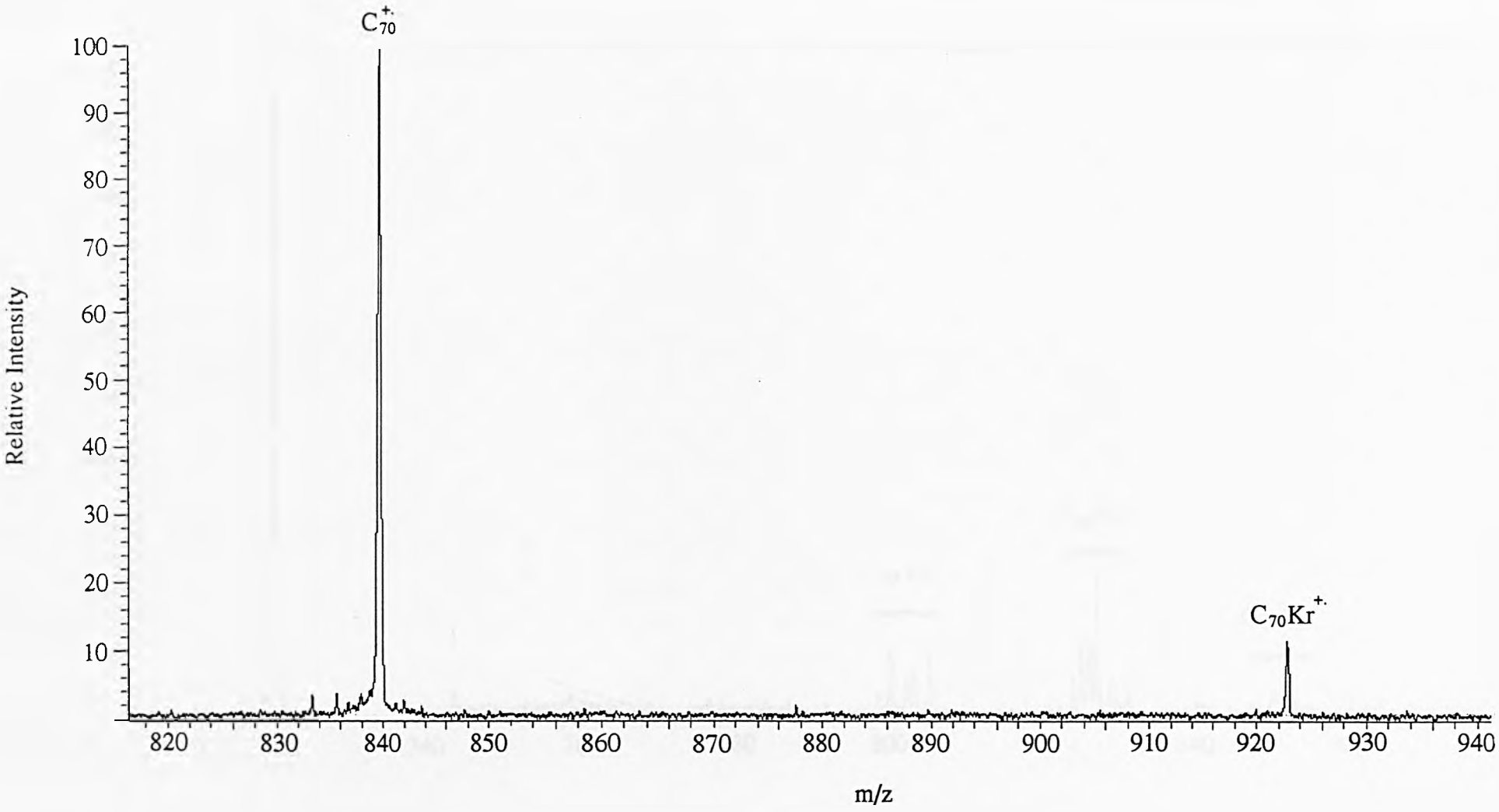

Figure 3.16: Magnet scan of $C_{70}^{+\cdot}$ and krypton at E_{iab} = 500 eV.

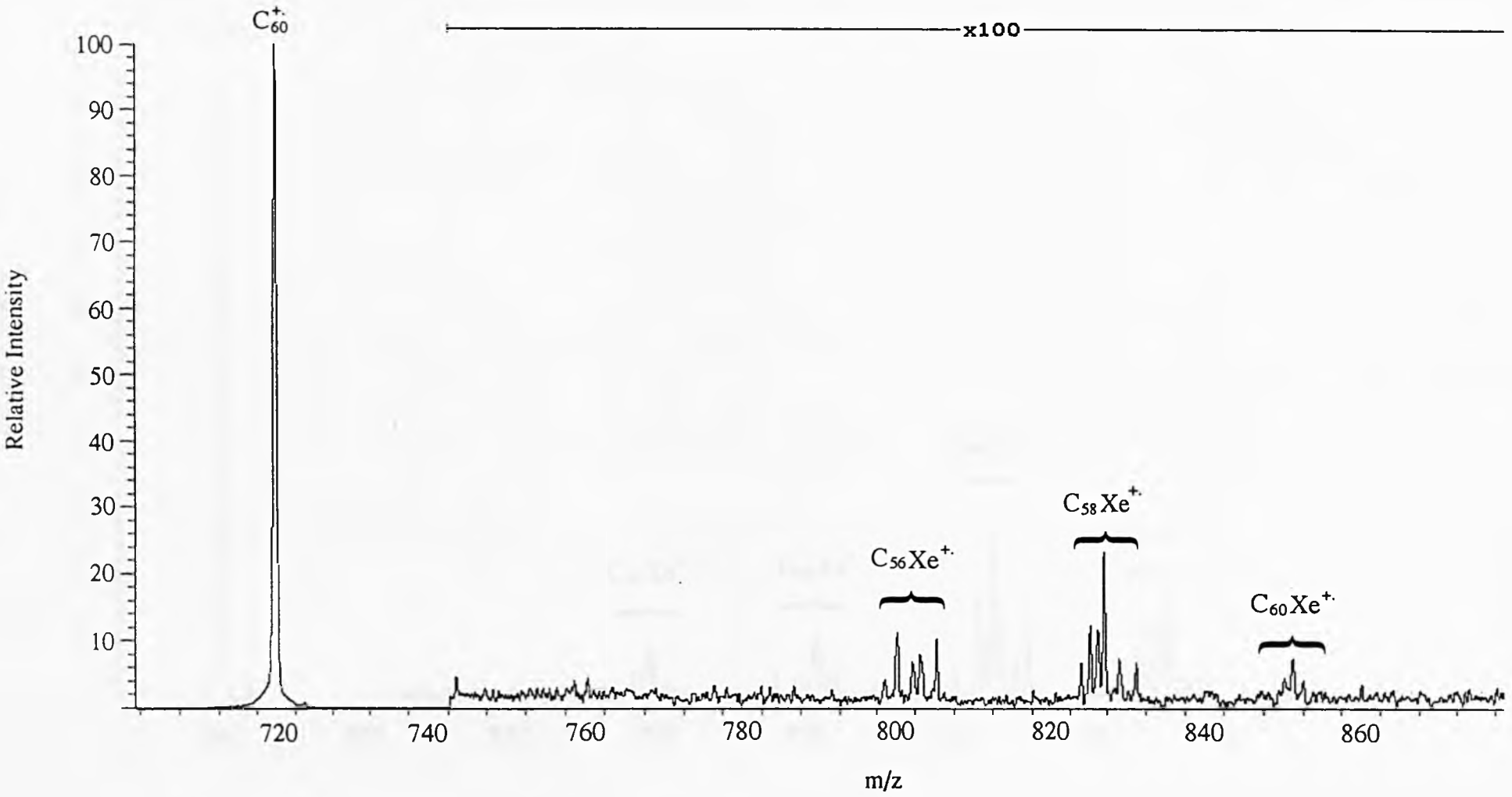

Figure 3.17: Magnet scan of $C_{60}^{+\cdot}$ and xenon at E_{lab} = 270 eV.

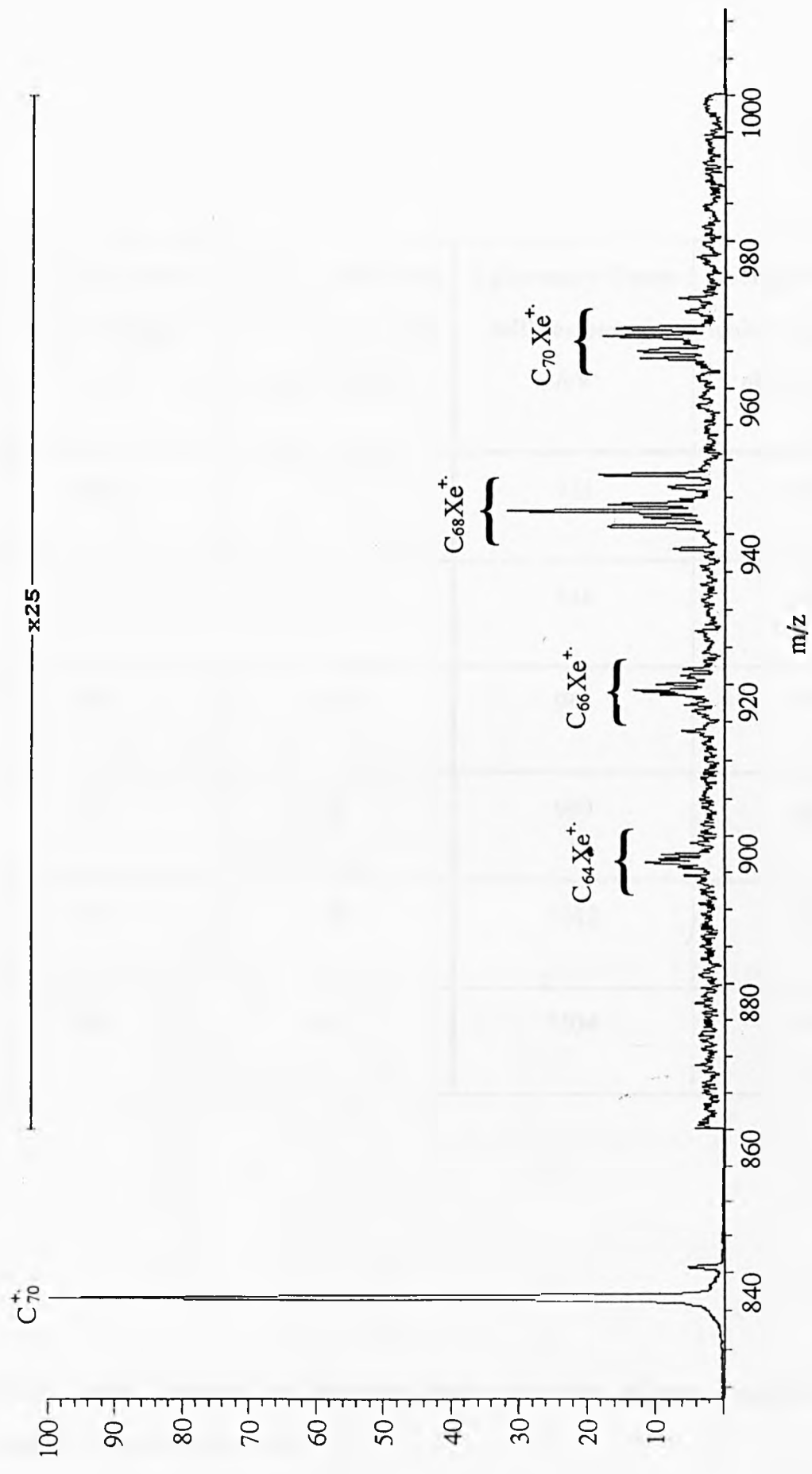

Figure 3.18: Magnet scan of $C_{70}^{+\cdot}$ and xenon at E_{lab} = 330 eV.

Laboratory-frame collision energy /eV	**Energy deficit with which $C_{60}Ar^{+\cdot}$ was observed /eV**	**Laboratory-frame collision energy /eV**	**Energy deficit with which $C_{70}Ar^{+\cdot}$ was observed /eV**
760	40	924	42
779	41	946	43
898	42	968	44
817	43	990	45
836	44	1012	46
855	45	1034	47

Table 3.4(a): Summary of laboratory-frame and centre-of-mass frame collision energies for argon adduct ions.

Laboratory-frame collision energy /eV	**Energy deficit with which $C_{60}Kr^{+\cdot}$ was observed /eV**	**Laboratory-frame collision energy /eV**	**Energy deficit with which $C_{70}Kr^{+\cdot}$ was observed /eV**
440	46	500	45

Table 3.4(b): Summary of laboratory-frame and centre-of-mass frame collision energies for krypton adduct ions.

Laboratory-frame collision energy /eV	**Energy deficit with which $C_{60}Xe^{+\cdot}$ was observed /eV**	**Laboratory-frame collision energy /eV**	**Energy deficit with which $C_{70}Xe^{+\cdot}$ was observed /eV**
270	42	330	45

Table 3.4(c): Summary of laboratory-frame and centre-of-mass frame collision energies for xenon adduct ions.

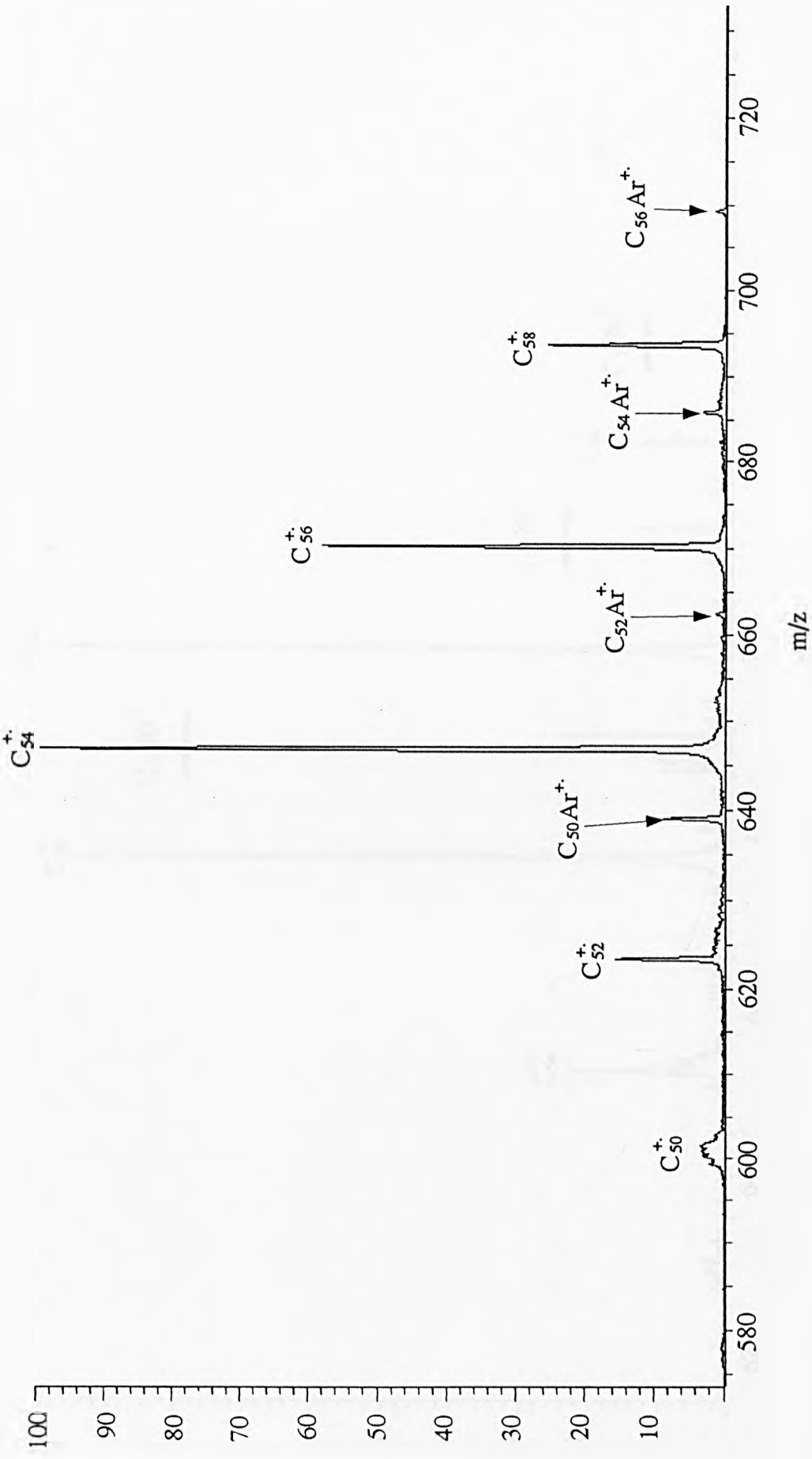

Figure 3.19: Magnet scan of $C_{60}^{+\cdot}$ and argon at E_{lab} = 1000 eV, E_{def} = 202 eV.

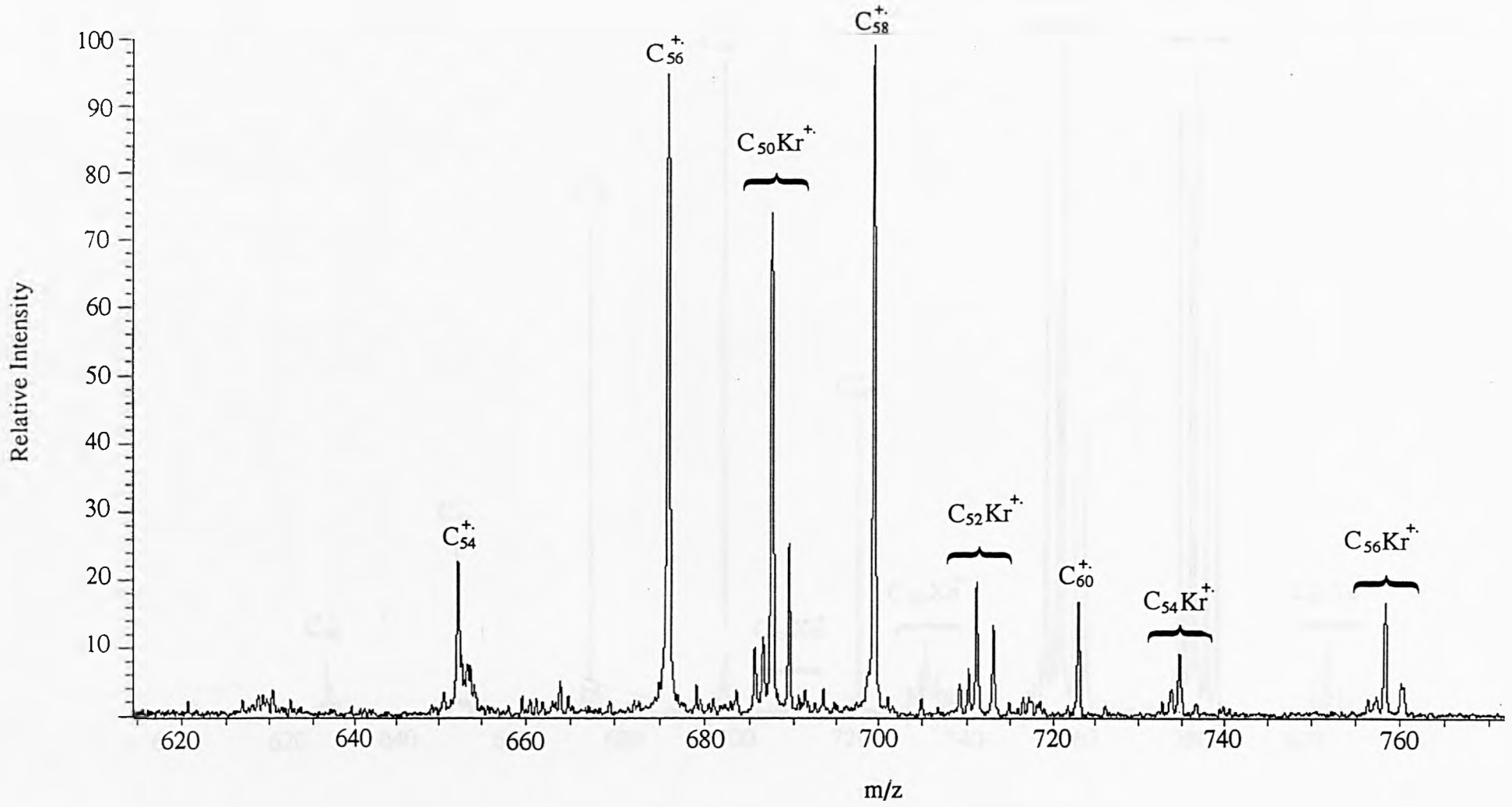

Figure 3.20: Magnet scan of $C_{60}^{+\cdot}$ and krypton at E_{lab} = 500 eV, E_{def} = 119 eV.

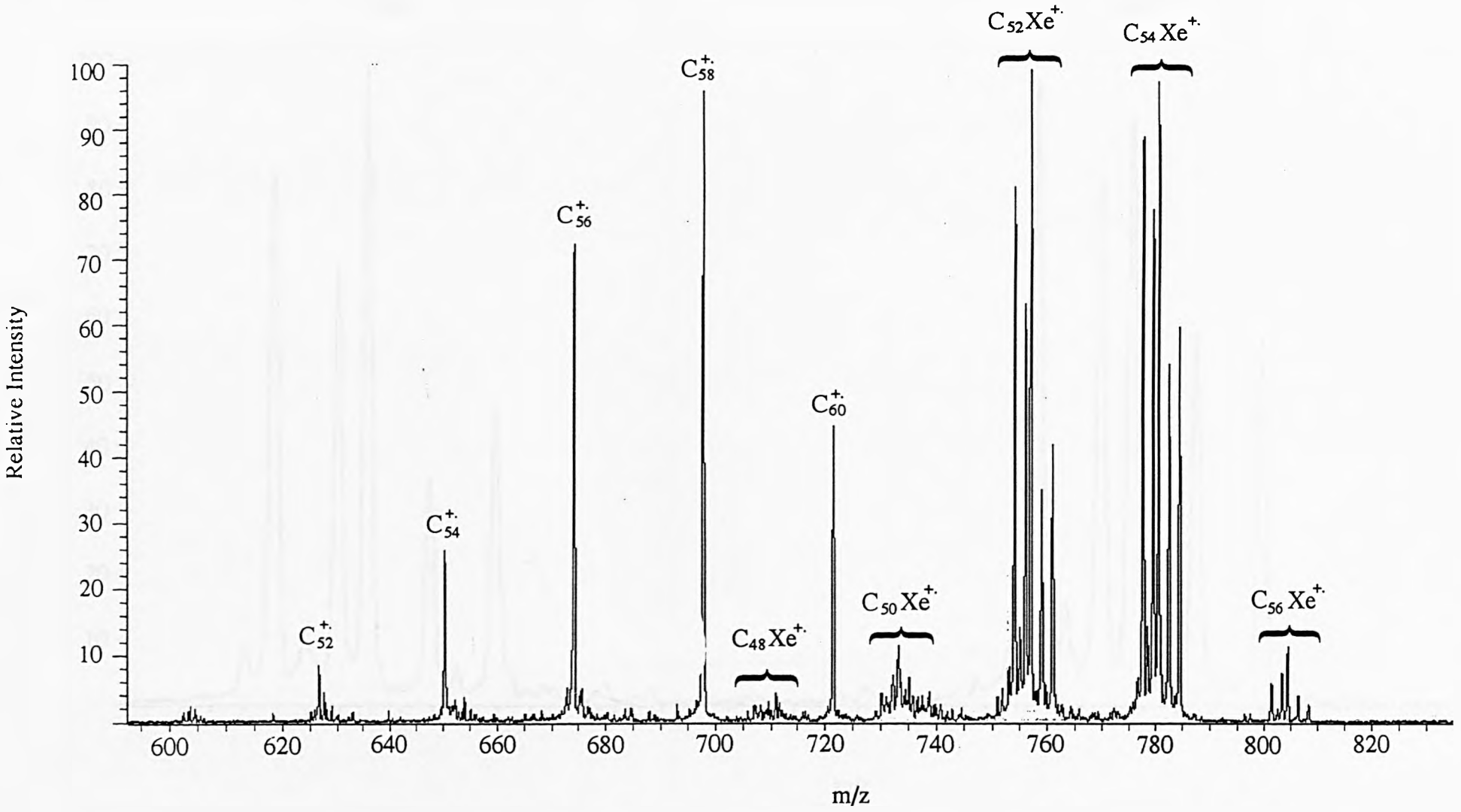

Figure 3.21(a): Magnet scan of $C_{60}^{+\cdot}$ and xenon at E_{lab} = 350 eV, E_{def} = 85 eV.

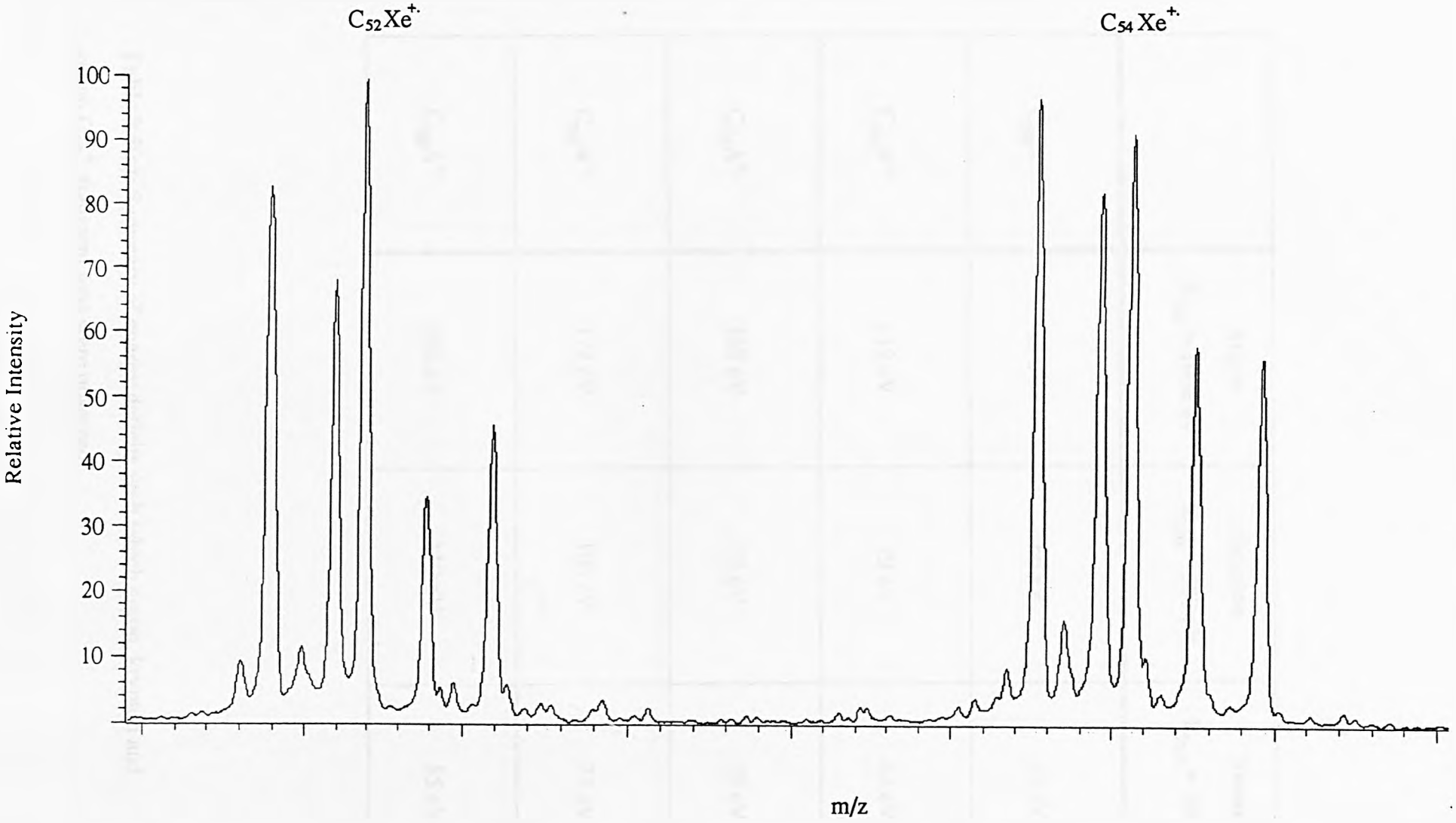

Figure 3.21(b): Magnet scan of $C_{60}^{+\cdot}$ and xenon at E_{lab} = 350 eV, E_{def} = 85, m/z = 750 - 790 region of figure 3.21(a) expanded.

	Argon E_{lab} **= 1000 eV**	**Krypton** E_{lab} **= 500 eV**	**Xenon** E_{lab} **= 350 eV**
$C_{58}A^{+\cdot}$	83 eV	66 eV	55 eV
$C_{56}A^{+\cdot}$	112 eV	79 eV	62 eV
$C_{54}A^{+\cdot}$	142 eV	92 eV	70 eV
$C_{52}A^{+\cdot}$	172 eV	106 eV	77 eV
$C_{50}A^{+\cdot}$	202 eV	119 eV	85 eV

Table 3.5(a): Summary of energy deficits with which argon, krypton and xenon $C_{60}^{+\cdot}$ fragment ions were observed.

	Argon E_{lab} **= 1000 eV**	**Krypton** E_{lab} **= 500 eV**	**Xenon** E_{lab} **= 350 eV**
$C_{68}A^{+\cdot}$	72 eV	57 eV	62 eV
$C_{66}A^{+\cdot}$	98 eV	69 eV	71 eV
$C_{64}A^{+\cdot}$	124 eV	81 eV	79 eV
$C_{62}A^{+\cdot}$	150 eV	93 eV	87 eV
$C_{60}A^{+\cdot}$	176 eV	105 eV	96 eV

Table 3.5(b): Summary of energy deficits with which argon, krypton and xenon $C_{70}^{+\cdot}$ fragment ions were observed.

CHAPTER FOUR: *Target Capture of Diatomic Gases by $C_{70}^{+\cdot}$ Radical Cations.*

4.1 Introduction.

The action of fullerenes under oxidative conditions is of the utmost importance if this new allotrope of carbon is to be of use outside the laboratory. Many studies have been made of the reactions of the closed-cage fullerene ions, $C_{60}^{+\cdot}$ and $C_{70}^{+\cdot}$ with oxygen [107-110, 170, 179-180, 182]. Detailed descriptions of progress already made in the field were given in chapter one of this thesis. The work in this chapter was aimed at expanding the knowledge of interactions between certain atmospheric gases, some of which contain oxygen, and the C_{70} radical cation, before going on to study oxygen/$C_{70}^{+\cdot}$ interactions. Such work also expands on research carried out in the previous chapter where the gas phase reactions of monoatomic collision gases with $C_{60}^{+\cdot}$ and $C_{70}^{+\cdot}$ were studied and the complexes formed were concluded to be endohedral fullerene derivatives.

4.1.1 Experimental Conditions.

A range of laboratory-frame collision energies was employed for all of the diatomic collision gases studied: 300 eV, 500 eV, 750 eV, 1000 eV, 1250 eV and 1500 eV. Each diatomic gas was introduced into the collision cell such that the parent ion signal was reduced to 50% of its original transmission. The β-slit situated at the focal point between E2 and B2 (the second magnet) was reduced in width to enhance the energy resolution. As mentioned before the second magnet B2 was scanned and spectra recorded using the scanning array detector.

4.2 Target Capture of Carbon Monoxide by $C_{70}^{+\cdot}$ Radical Cations.

Carbon monoxide was made to collide with $C_{70}^{+\cdot}$ at the laboratory-frame collision energies previously mentioned. E2 energy deficits were equivalent to the

centre-of-mass collision energy unless otherwise stated. Adduct species were only observed at laboratory-frame collision energies of 750 eV and above. Figure 4.1 shows how there is no apparent reaction between CO and $C_{70}^{+\cdot}$ at E_{lab} = 500 eV. When the laboratory-frame collision energy was increased to 750 eV, peaks corresponding to the adducts $[M + 12]^+$, $[M + 16]^+$ and $[M + 28]^{+\cdot}$ were observed as shown in figure 4.2. These adduct ions are assigned as $C_{70}C^{+\cdot}$, $C_{70}O^{+\cdot}$ and $C_{70}CO^{+\cdot}$ respectively. $C_{68}^{+\cdot}$ was also observed. This is a known fragmentation product resulting from CID of $C_{70}^{+\cdot}$ [145]. Some, but not always all, of these adduct peaks were observed at higher laboratory-frame collision energies and the intensities of these adduct peaks relative to each other changed as the laboratory-frame collision energy changed suggesting different adducts were produced preferentially at certain energies. This can be seen by comparing figures 4.2 and 4.3 which show the results at laboratory-frame collision energies of 750 eV and 1000 eV respectively. In the 1000 eV spectrum the peak corresponding to the full adduct, $C_{70}CO^{+\cdot}$, had increased in intensity relative to the $C_{70}C^{+\cdot}$ and $C_{70}O^{+\cdot}$ ions. At a laboratory-frame collision energy of 1250 eV (figure 4.4) the atomic adducts, $C_{70}C^{+\cdot}$ and $C_{70}O^{+\cdot}$ completely disappeared and only the full adduct, $C_{70}CO^{+\cdot}$, remained. The $C_{70}CO^{+\cdot}$ adduct fell in intensity as the laboratory-frame collision energy was increased to 1500 eV (figure 4.5). From these results it appears that the full adduct, $C_{70}CO^{+\cdot}$, was produced preferentially at higher laboratory-frame collision energies. The atomic adducts, $C_{70}C^{+\cdot}$ and $C_{70}O^{+\cdot}$, were more abundant at the lower collision energies. These two statements seem to be counter-intuitive as higher collision energies might have been expected to induce fragmentation of the full adduct into smaller species and the lower energies to stabilise the full adduct.

In all of the experiments so far, the E2 potential energy deficits were equivalent to the centre-of-mass collision energy. If the E2 potentials were reduced beyond this value, a peak at $[M + 4]^+$ was observed (figures 4.6). The E2 potential energy deficit was adjusted so as to optimise the $[M + 4]^+$ peak intensity. At this maximum peak intensity, the E2 potential energy deficits were noted and a spectrum

was recorded. $[M + 4]^+$, tentatively assigned as $C_{69}O^{+\cdot}$ optimised with an energy deficit of 75± 4 eV (at the laboratory-frame collision energy of 1250 eV). This energy deficit of 75± 4 eV is within experimental error of the theoretical value (see equation (18)) calculated on the basis that the full adduct $[M + CO]^+$ forms and decomposes to $[M + 4]^+$ (see table 4.1).

If the full adduct is formed before decomposing into fragments, the question which must be asked is what are the structures of these adduct ions and how are they formed? In the case of $C_{69}O^{+\cdot}$, two carbon atoms would appear to have been lost from the full $C_{70}CO^{+\cdot}$ adduct. One of the carbon atoms must have originated from the fullerene cage, but the second carbon atom could have come from either the fullerene cage or the collision gas. It is known that high-energy collision-induced decomposition of fullerene cages results in the loss of 2n carbon atoms (n = 1,2,3...) [145]. To probe this question, ^{13}CO was employed as the collision gas. ^{13}CO, as expected, gave very similar results to CO in experiments where the energy deficits transmitted were equal to the centre-of-mass collision energies. Results are displayed in figures 4.7 to 4.10. All spectra showed $C_{68}^{+\cdot}$, presumably a decomposition product of the parent ion. $C_{70}^{+\cdot}$ showed no reaction with ^{13}CO at E_{lab} = 500 eV. On increasing the laboratory-frame collision energy to 750 eV, $[M + 13]^+$ and $[M + 16]^+$ peaks corresponding to $C_{70}{}^{13}C^{+\cdot}$ and $C_{70}O^{+\cdot}$ adduct ions were observed (figure 4.7). $C_{70}{}^{13}CO^{+\cdot}$ was only just visible . At E_{lab} = 1000 eV, (figure 4.8) the full adduct $C_{70}{}^{13}CO^{+\cdot}$ was more intense than the atomic adducts $C_{70}{}^{13}C^{+\cdot}$ and $C_{70}O^{+\cdot}$, the latter adduct being only just visible above the base line. An unexpected peak at higher mass was observed at E_{lab} = 1000 eV and E_{lab} = 1250 eV , (see figure 4.8 and 4.9). This $[M + 31]^+$ peak could be consistent with $^{13}C^{18}O$ present in the cylinder of ^{13}CO, however assignment of this peak would be very tenuous. The adduct $C_{70}{}^{13}CO^{+\cdot}$ was less intense at E_{lab} = 1250 eV, consistent with the results for CO. At a laboratory-frame collision energy of 1000 eV there was a peak at m/z = 841, *i.e.* $[M + 1]^+$. This peak increased in intensity as the laboratory-frame collision energy was raised to 1250 eV and 1500 eV. At E_{lab} = 1500 eV (shown in figure 4.10) with the energy deficit

transmitted equal to the centre-of-mass collision energy, no adducts other than $[M + 1]^+$ were observed. At E_{lab} = 1250 eV with the E2 potential reduced by 60 eV, only the adducts $[M + 1]^+$, $[M + 4]^+$, $[M + 5]^+$, $[M + 6]^+$ and $[M + 7]^+$ were observed (figure 4.11). Due to a low pressure in the cylinder of ^{13}CO this experiment could not be repeated satisfactorily. $[M + 4]^+$ and $[M + 5]^+$ suggest a carbon atom could be lost from either the gas or the fullerene cage. An EI spectrum of the contents of the cylinder showed the intensity of $^{13}C^{18}O$, relative to $^{13}C^{16}O$, was 14%. The appearance of a peak at m/z = 828 at E_{lab} = 1500 eV suggested fragmentation by the loss of one carbon atom from the fullerene cage to form $C_{69}^{+\cdot}$. $C_{59}^{+\cdot}$ has been observed with oxygen/$C_{60}^{+\cdot}$ collisions [179] and nitrogen/$C_{60}^{+\cdot}$ collisions [180].

Collisions with CO produced an adduct at m/z = 844 assigned as $C_{69}O^{+\cdot}$, whose intensity optimised at the E2 potentials appropriate for the formation of the full adduct, $C_{70}O^{+\cdot}$, followed by decomposition to $C_{69}O^{+\cdot}$. The observation of $[M + 1]^+$ with ^{13}CO suggested that it was also possible for the full adduct to decompose by the loss of CO *i.e.* a fullerene cage carbon atom and the target gas oxygen atom. The optimum intensity of $[M + 1]^+$ (corresponding to $C_{69}{}^{13}C^{+\cdot}$) was found by adjusting E2 potentials and a spectrum was recorded (figure 4.12). For E_{lab} = 1000 eV, the $C_{69}{}^{13}C^{+\cdot}$ species optimised at an E2 potential equivalent to an energy deficit of 64 ± 1 eV. This value corresponds quite closely to the theoretical value (E_{def} (theoretical) = 64.5 eV) calculated for the formation of the full adduct, followed by the loss of ^{12}C and O atoms. A similar energy experiment was carried out for the formation of the full adducts. In both cases ($C_{70}{}^{13}CO^{+\cdot}$ and $C_{70}CO^{+\cdot}$), peaks optimised at E2 potentials equivalent to energy deficits equal to the centre-of-mass collision energies.

Two aspects of these results suggest that the full adducts are created before decomposition. Firstly the E2 potentials at which the various fragments were observed correspond to the theoretical values, and secondly a combination of carbon-cage atoms and target gas atoms are lost in fragmentations suggesting significant degrees of interaction between the diatomic gas and the fullerene.

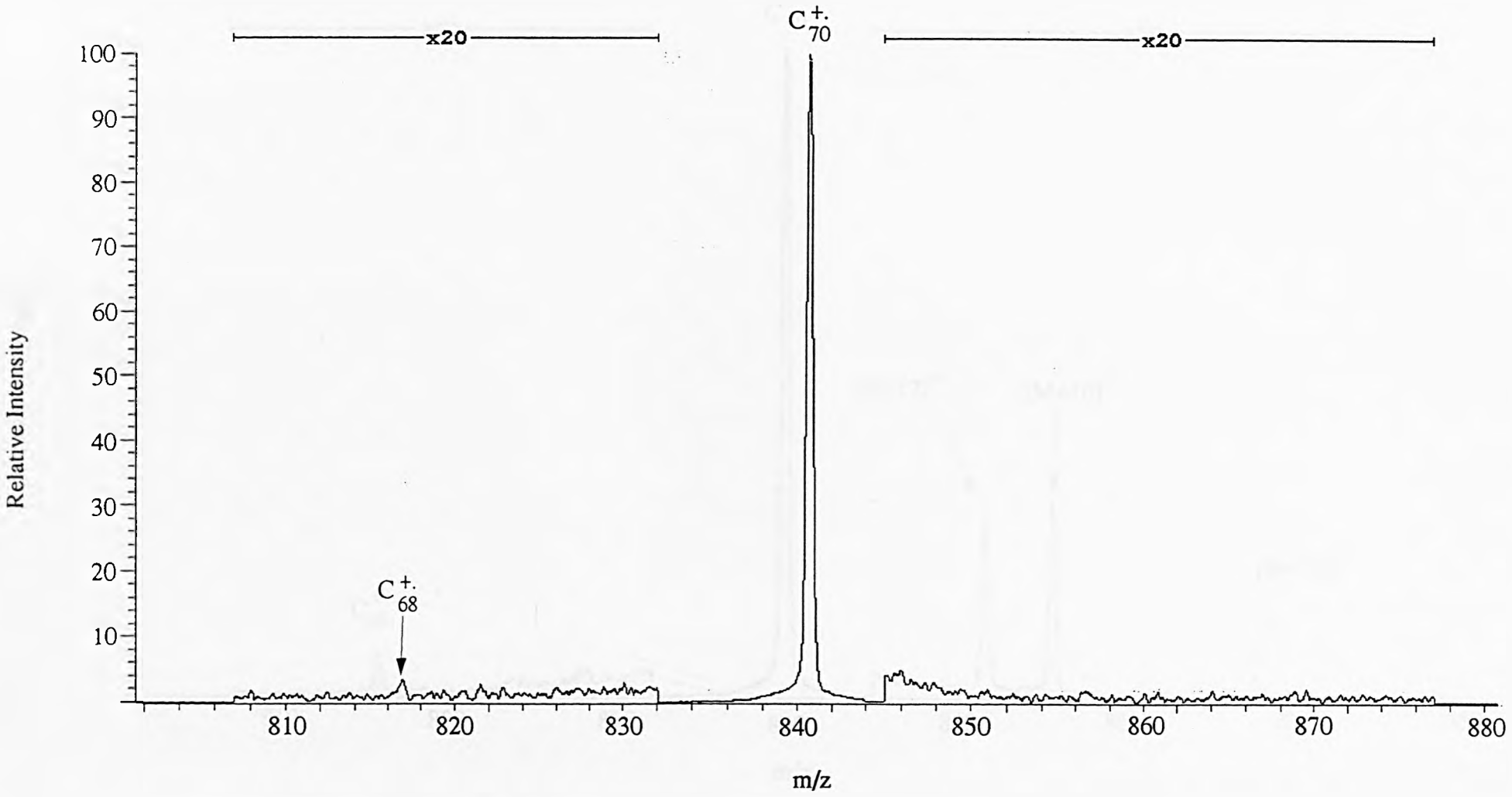

Figure 4.1: Magnet scan of $C_{70}^{+\cdot}$ and carbon monoxide at E_{lab} = 500 eV.

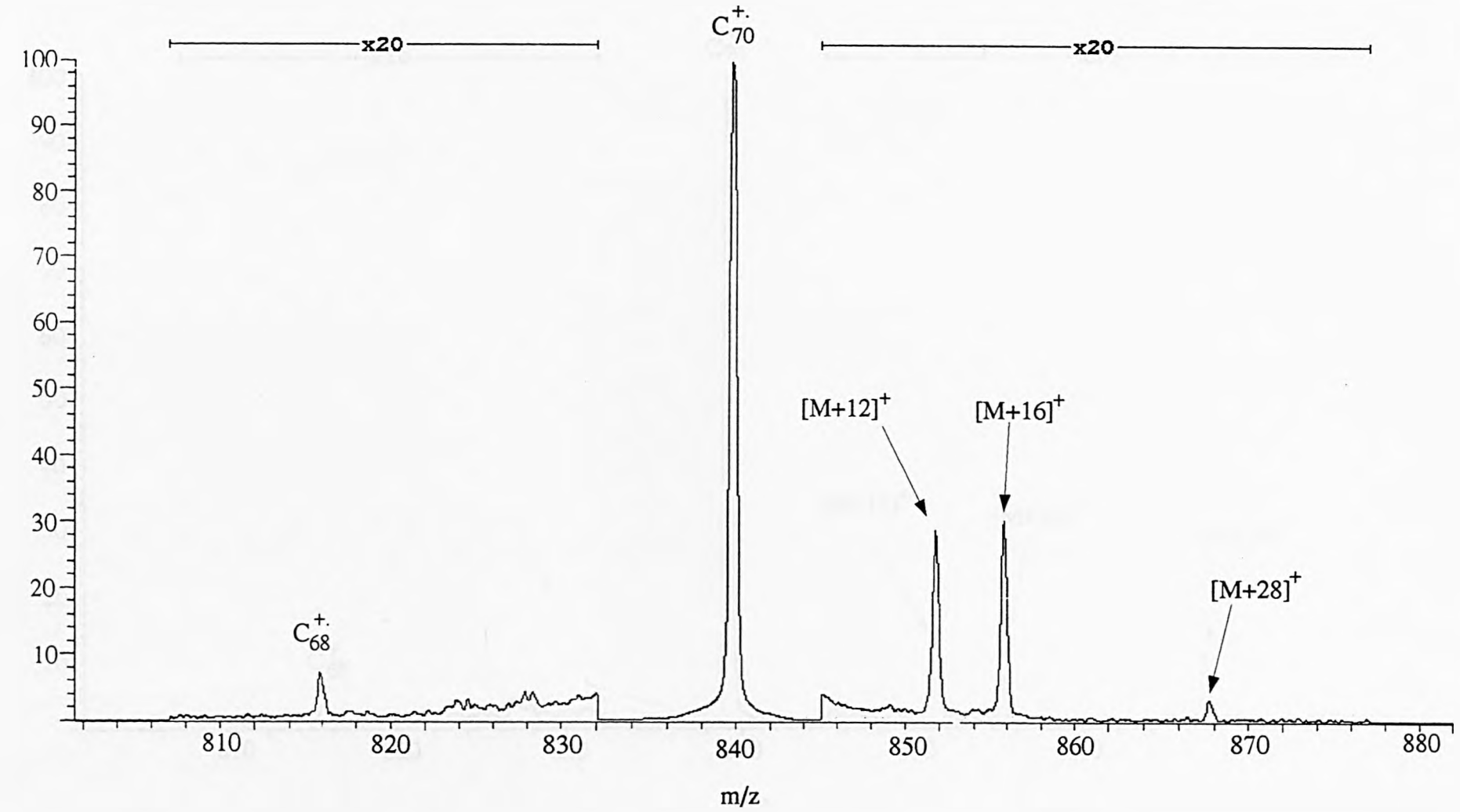

Figure 4.2: Magnet scan of $C_{70}^{+\cdot}$ and carbon monoxide at E_{lab} = 750 eV.

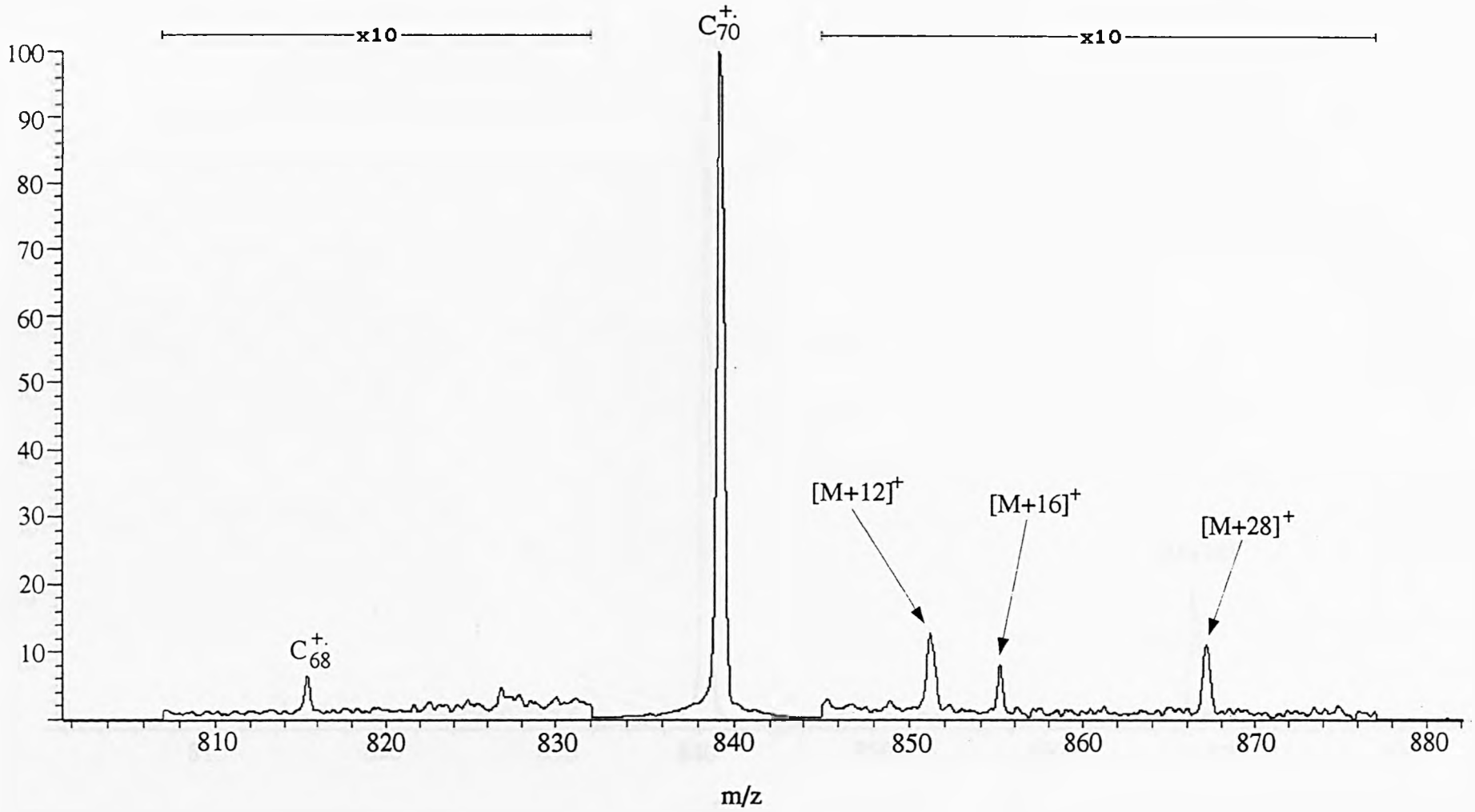

Figure 4.3: Magnet scan of $C_{70}^{+\cdot}$ and carbon monoxide at E_{lab} = 1000 eV.

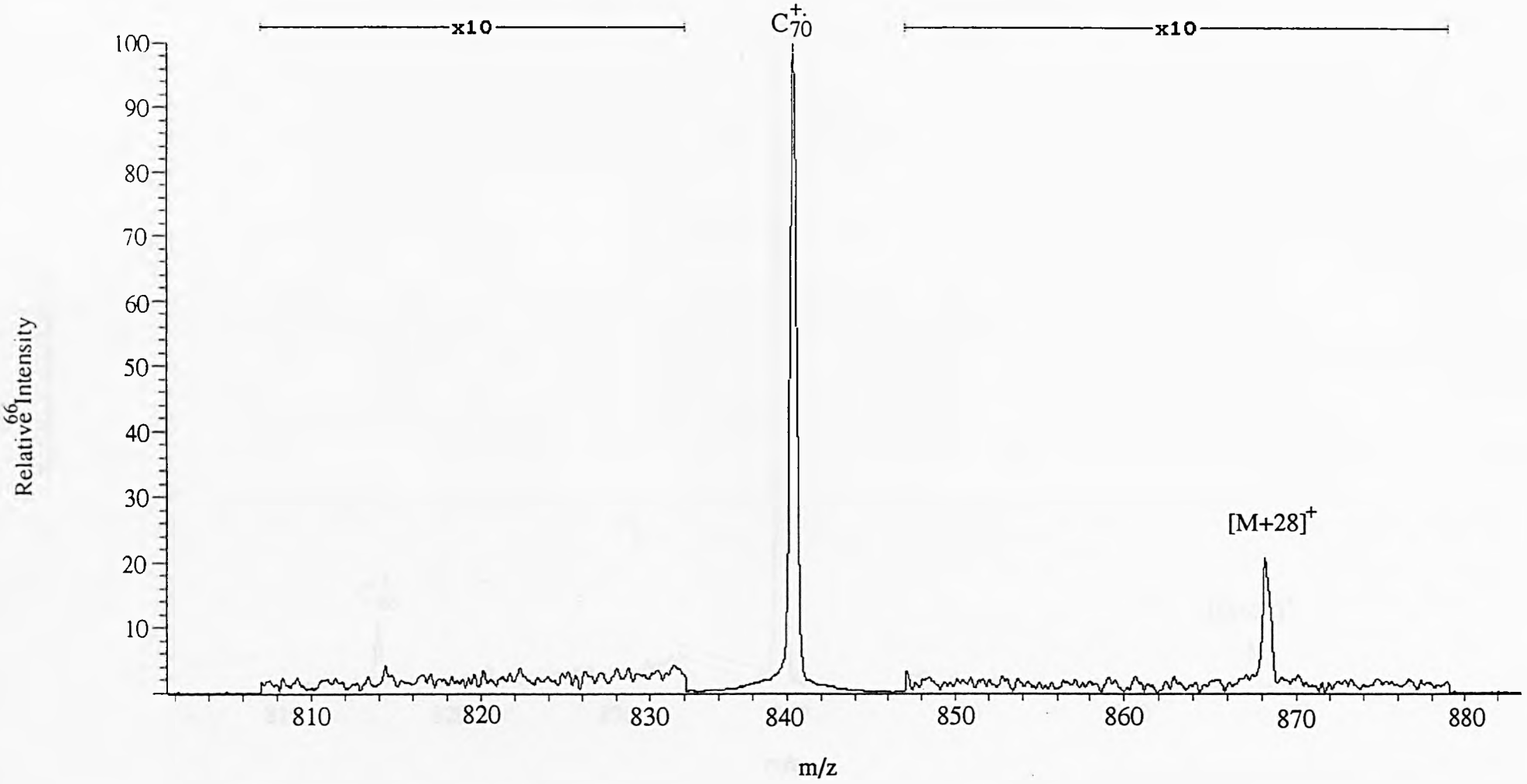

Figure 4.4: Magnet scan of $C_{70}^{+\cdot}$ and carbon monoxide at E_{lab} = 1250 eV.

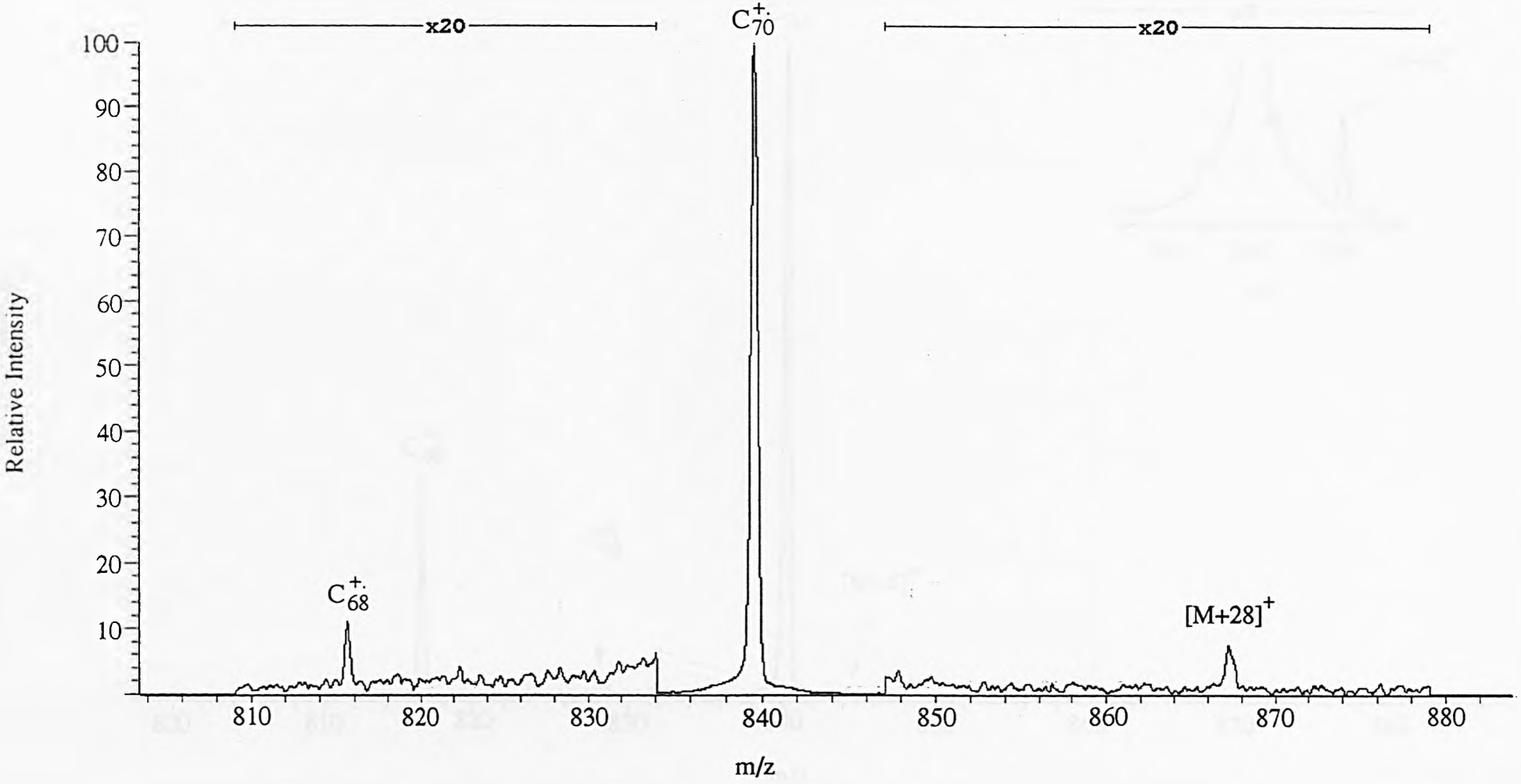

Figure 4.5: Magnet scan of $C_{70}^{+\cdot}$ and carbon monoxide at E_{lab} = 1500 eV.

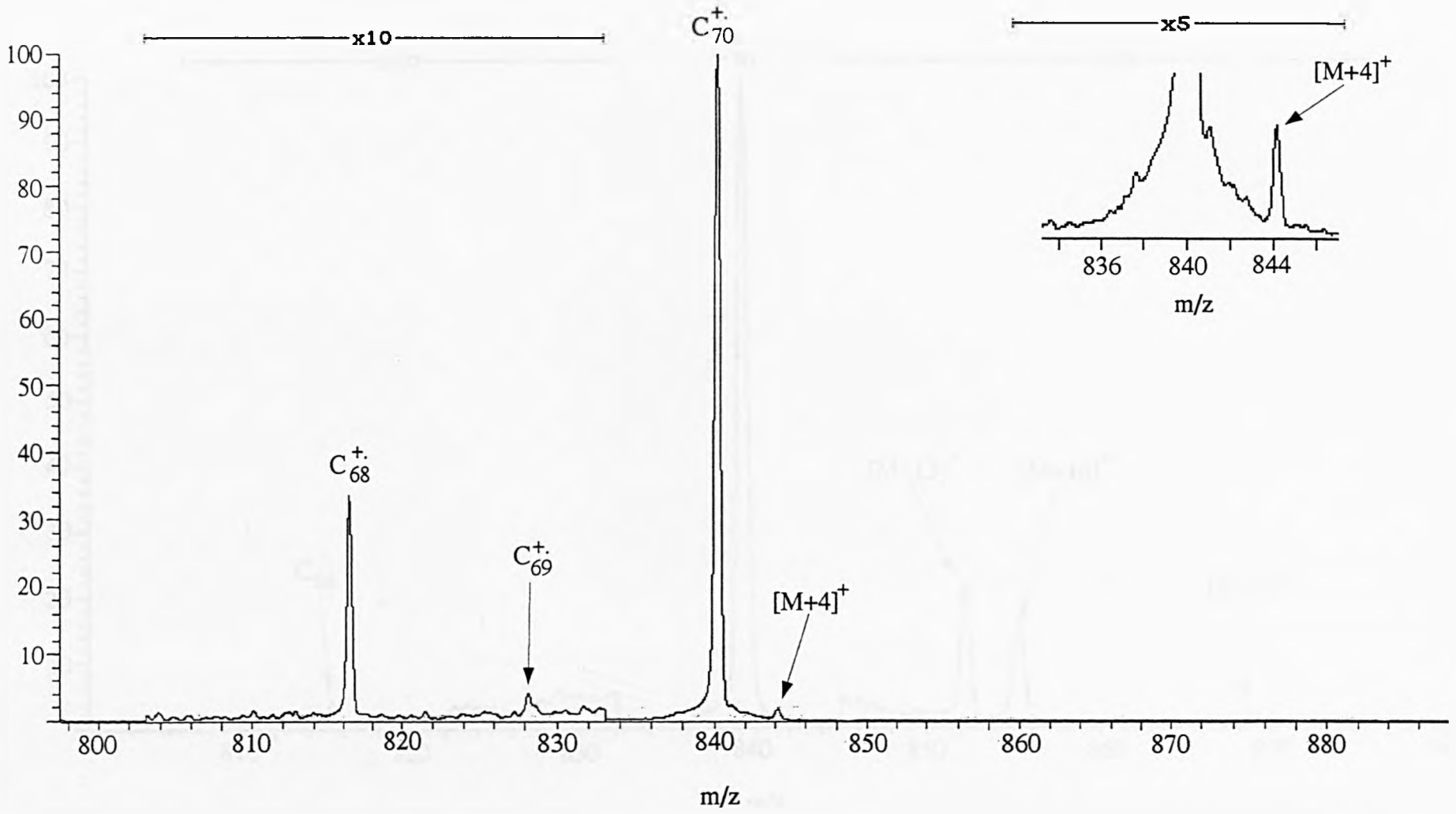

Figure 4.6: Magnet scan of $C_{70}^{+\cdot}$ and carbon monoxide at E_{lab} = 1250 eV, E2 potential adjusted so as to maximise the intensity of $[M + 4]^+$.

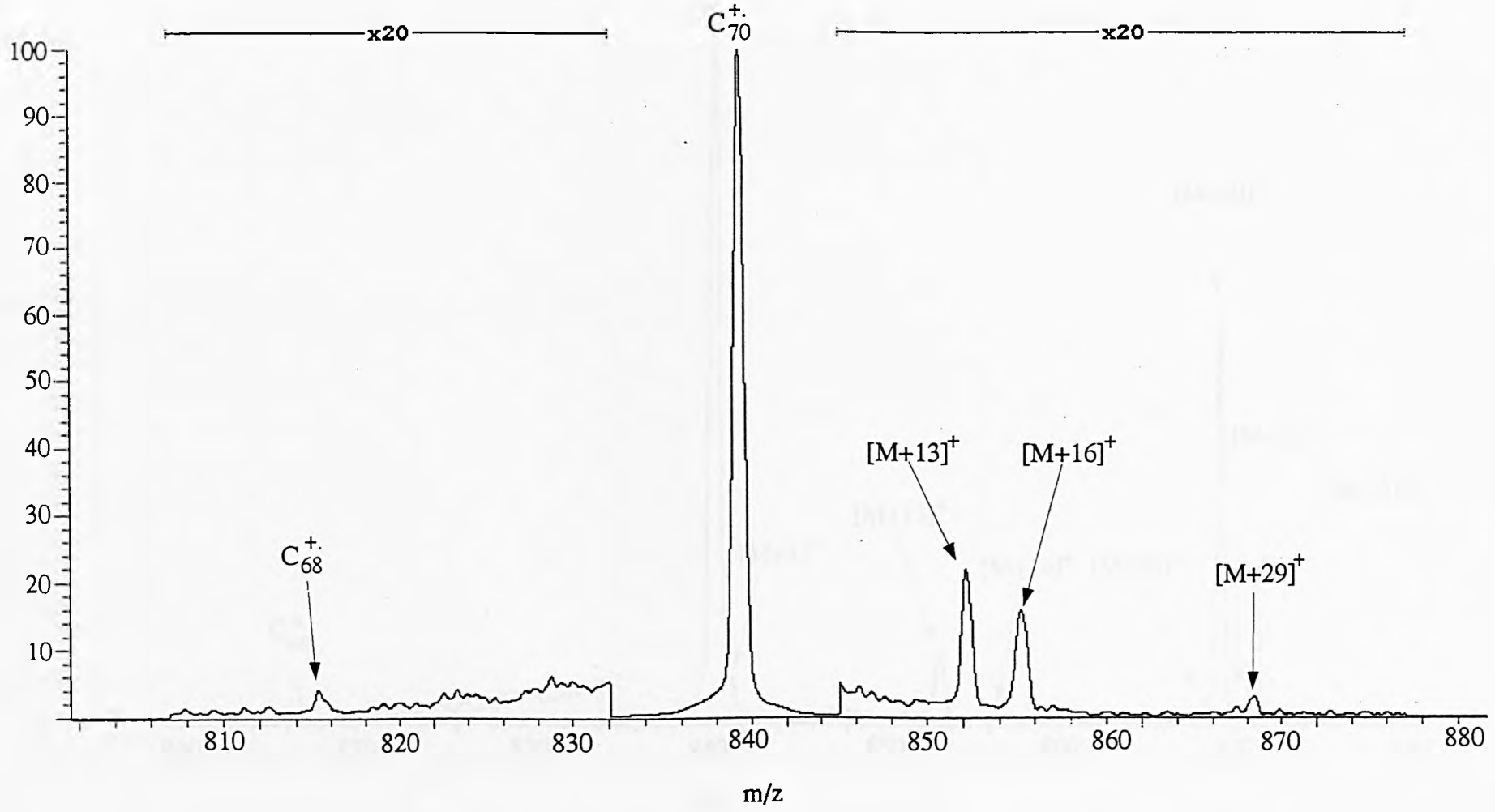

Figure 4.7: Magnet scan of $C_{70}^{+\cdot}$ and ^{13} carbon monoxide at E_{lab} = 750 eV.

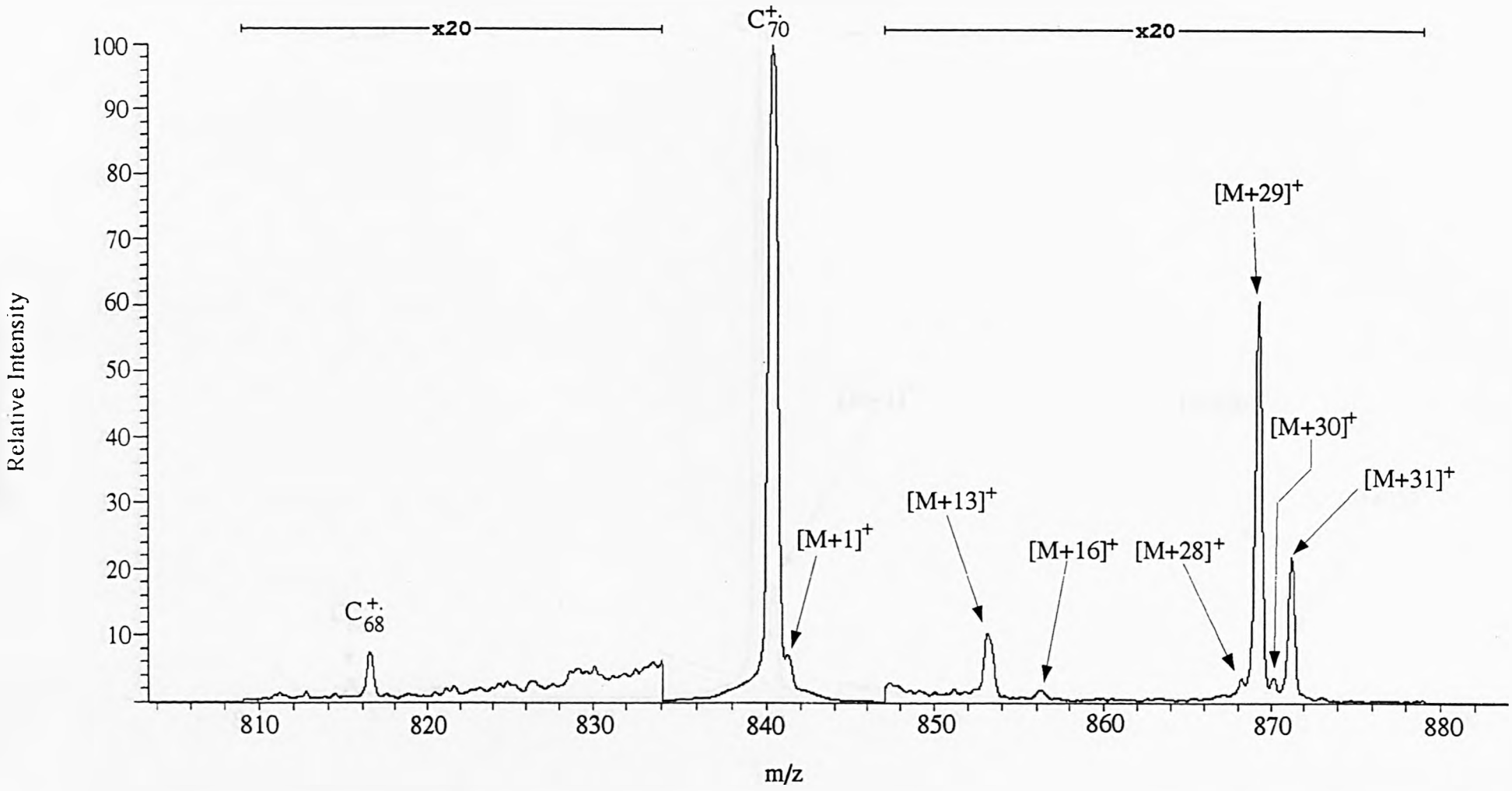

Figure 4.8: Magnet scan of $C_{70}^{+\cdot}$ and ^{13} carbon monoxide at E_{lab} = 1000 eV.

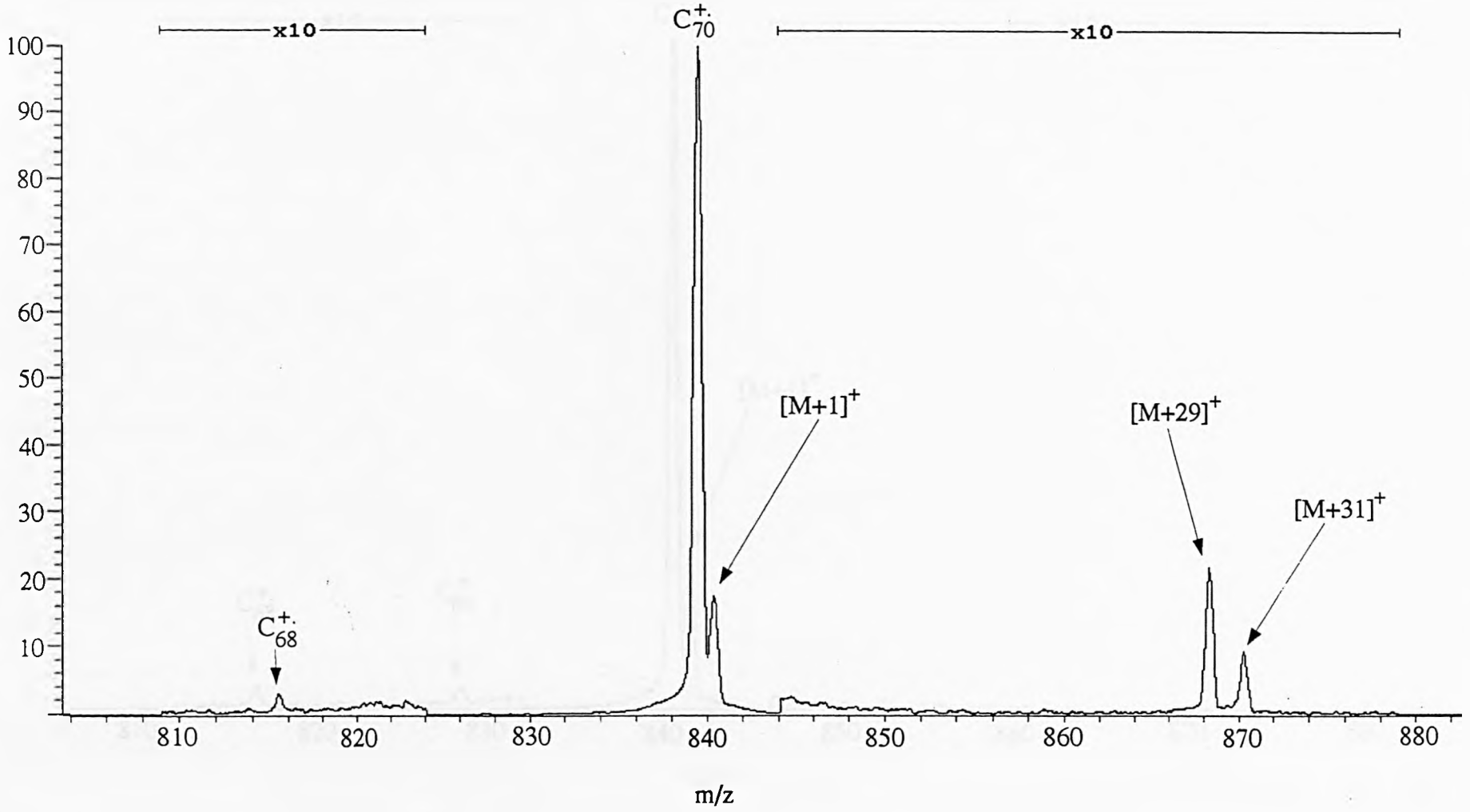

Figure 4.9: Magnet scan of $C_{70}^{+\cdot}$ and ^{13} carbon monoxide at E_{lab} = 1250 eV.

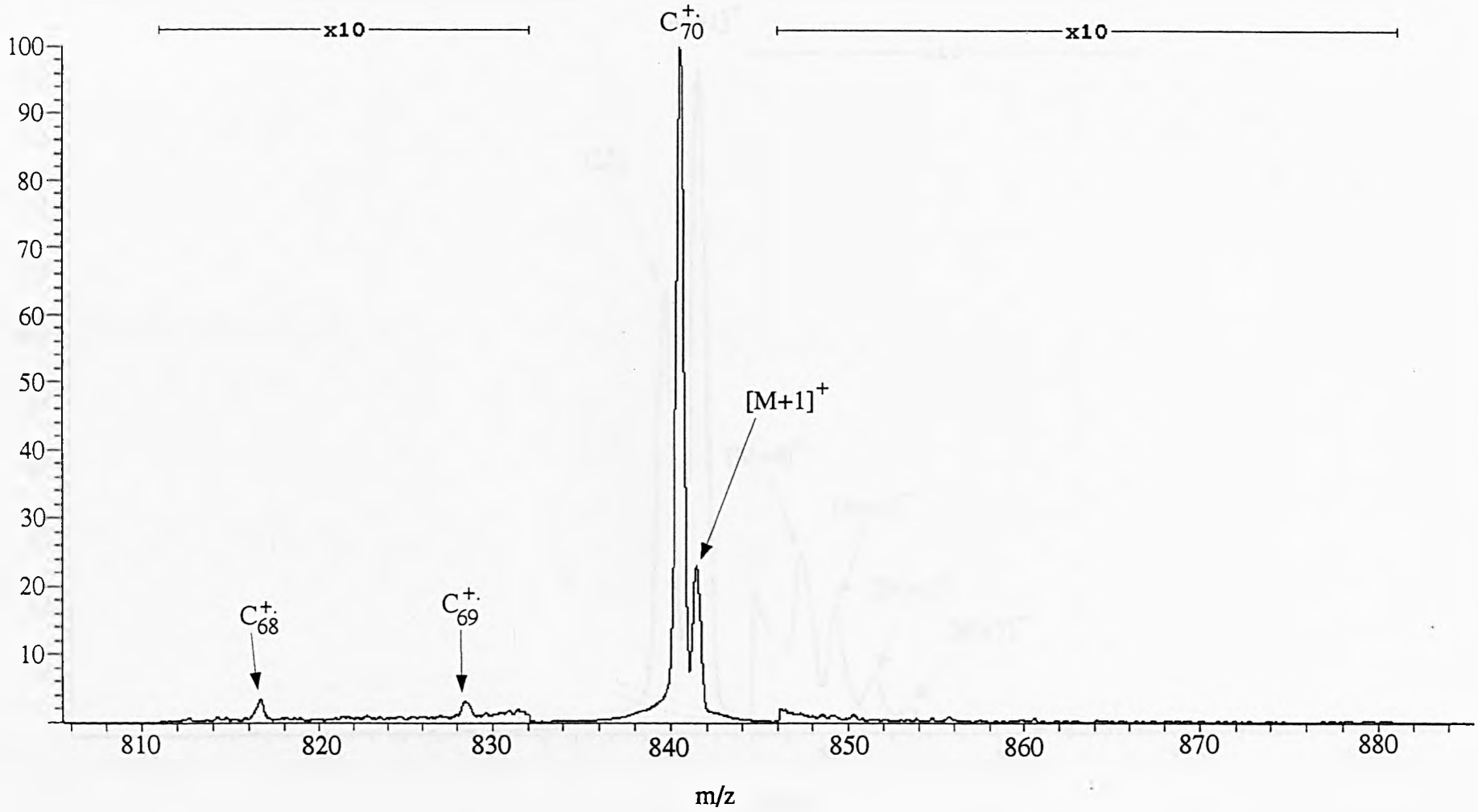

Figure 4.10: Magnet scan of $C_{70}^{+\cdot}$ and ^{13} carbon monoxide at E_{lab} = 1500 eV.

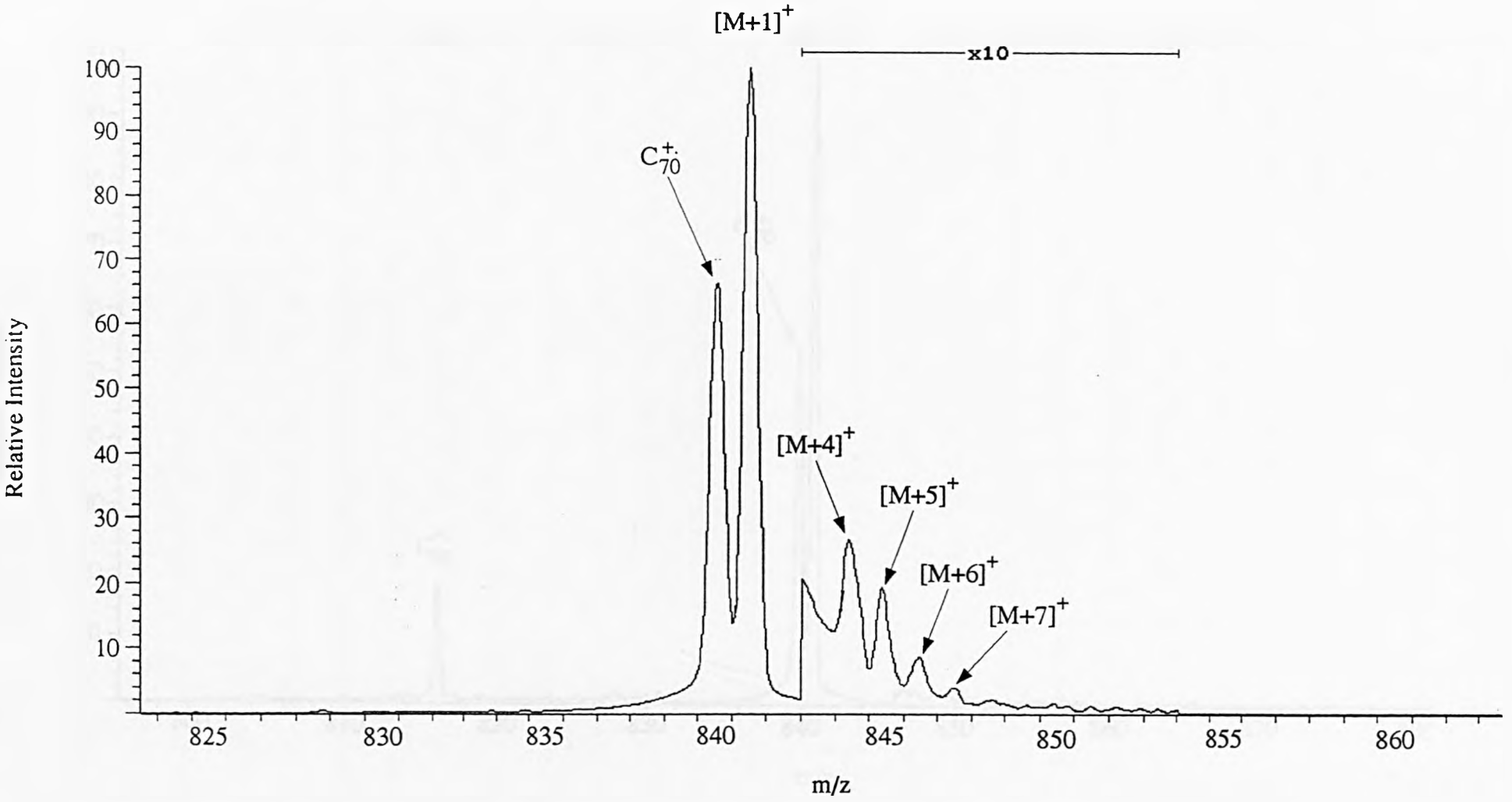

Figure 4.11: Magnet scan of $C_{70}^{+\cdot}$ and ^{13} carbon monoxide at E_{lab} = 1250 eV, E2 potential reduced by 60 eV.

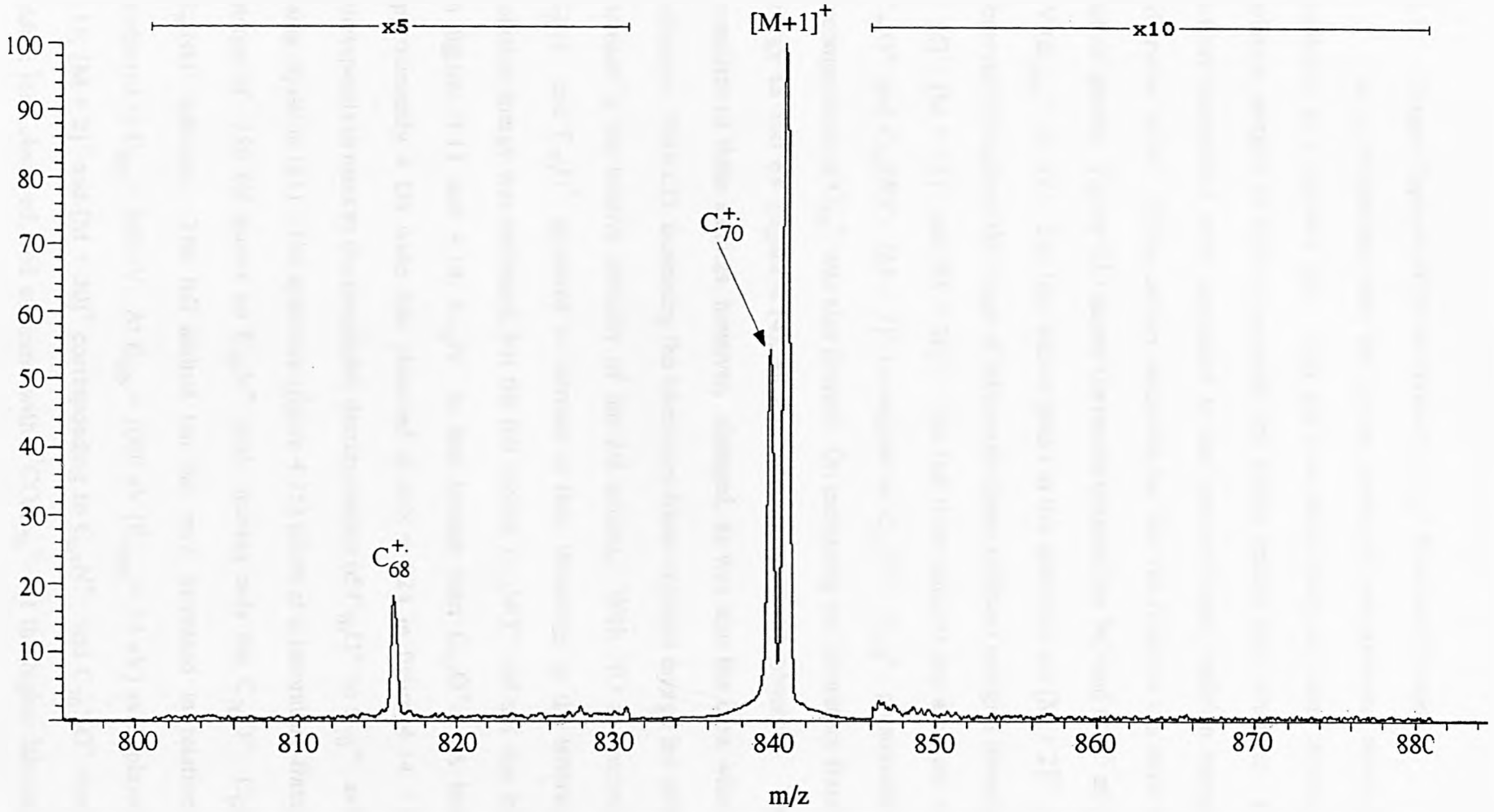

Figure 4.12: Magnet scan of $C_{70}^{+\cdot}$ and ^{13} carbon monoxide at E_{lab} = 1000 eV, E2 potential adjusted so as to maximise the intensity of $[M + 1]^+$.

4.3 Target Capture of Nitric Oxide by $C_{70}^{+\cdot}$ Radical Cations.

As a comparison with the carbon monoxide experiments, nitric oxide was employed as a collision gas. This gas was tested over the same laboratory-frame collision energies as carbon monoxide and similar results were obtained. The energy deficits transmitted were equivalent to the centre-of-mass collision energies unless otherwise stated. Unlike carbon monoxide but like the fullerene ion nitric oxide is a radical species. Figure 4.13 shows the results obtained for NO and $C_{70}^{+\cdot}$ at E_{lab} = 300 eV (E_{com} = 10 eV). The four adduct peaks in this spectrum are $[M + 2]^+$, which was observed throughout the range of laboratory-frame collision energies investigated, $[M + 14]^+$, $[M + 16]^+$ and $[M + 30]^+$. The last three adducts are assigned as $C_{70}N^{+\cdot}$, $C_{70}O^{+\cdot}$ and $C_{70}NO^+$. $[M + 2]^+$ is assigned as $C_{69}N^{+\cdot}$. $C_{68}^{+\cdot}$, presumably from the decomposition of $C_{70}^{+\cdot}$ was also formed. On increasing the laboratory-frame collision energy to 500 eV (figure 4.14), all four adducts were still observed. The relative intensities of these adducts, however, changed, as was also the case with $CO/C_{70}^{+\cdot}$ collisions. With CO, increasing the laboratory-frame collision energy led initially to an increase in the relative intensity of the full adduct. With NO the atomic adducts $C_{70}N^{+\cdot}$ and $C_{70}O^{+\cdot}$ appeared to increase in their intensities as the laboratory-frame collision energy was increased, but the full adduct, $C_{70}NO^+$, did not rise in intensity. In figures 4.13 and 4.14, $C_{70}N^{+\cdot}$ is less intense than $C_{70}O^{+\cdot}$. A broad peak, approximately 4 Da wide was observed at m/z = 824 in figure 4.14. This peak corresponds in mass to the metastable decomposition of $C_{70}O^{+\cdot}$ to $C_{70}^{+\cdot}$, as calculated using equation (21). The spectrum (figure 4.15) taken at a laboratory-frame collision energy of 750 eV shows no $C_{70}N^{+\cdot}$ peak, leaving only the $C_{70}O^{+\cdot}$, $C_{69}N^{+\cdot}$ and $C_{70}NO^+$ adducts. The full adduct ion has now increased in relative intensity, compared to E_{lab} = 500 eV. At E_{lab} = 1000 eV (E_{com} = 34 eV) as displayed in figure 4.16, $[M + 2]^+$ and $[M + 30]^+$ corresponding to $C_{69}N^{+\cdot}$ and $C_{70}NO^+$ were the only adduct ions observed, and as found with $^{13}CO/C_{70}^{+\cdot}$ at the higher laboratory-frame

collision energies, the appearance of $C_{69}^{+\cdot}$ was noted. There was little change on increasing the laboratory-frame collision energy to 1250 eV (figure 4.17).

Two points must be noted at this time. Firstly the $C_{70}O^{+\cdot}$ adduct when formed from collisions with carbon monoxide was observed at E_{lab} = 750 eV and E_{lab} = 1000 eV (E_{com} = 24.2 eV and E_{com} = 32.3 eV respectively). When NO was introduced as the collision gas, the $C_{70}O^{+\cdot}$ adduct was observed only at lower collision energies (from E_{lab} = 300 eV (E_{com} = 10.3 eV) to E_{lab} = 750 eV (E_{com} = 25.9 eV)). Secondly, $C_{69}N^{+\cdot}$ from collision with NO appeared more abundant than $C_{69}{}^{13}C^{+\cdot}$ from ^{13}CO collisions.

The observation of $C_{69}O^{+\cdot}$ from collisions between $C_{70}^{+\cdot}$ and CO prompted a search for similar ions resulting from collisions between $C_{70}^{+\cdot}$ and NO. $[M + 2]^+$, $[M + 4]^+$ and $[M + 6]^+$ peaks were observed with NO. The translational energies of these ions was investigated by adjusting the E2 potentials until the $[M + 2]^+$, $[M + 4]^+$ or $[M + 6]^+$peak reached its maximum intensity. $[M + 2]^+$ is assigned as $C_{69}N^{+\cdot}$, $[M + 4]^+$ is assigned as $C_{69}O^{+\cdot}$ and $[M + 6]^+$ is assigned as $C_{68}NO^{+\cdot}$. At a laboratory-frame collision energy of 1250 eV the $[M + 2]^+$ peak intensity was maximised at an energy deficit of 83 ± 5 eV, $[M + 4]^+$ at an energy deficit of 80 ± 5 eV and $[M + 6]^+$ at an energy deficit of 78 ± 5 eV (these results can be seen in figures 4.18 to 4.20 respectively). Energy deficits, calculated using equation (18) on the basis that the full adduct is formed and decomposes to products, gave values in agreement with the experimental energy deficits for $C_{69}N^{+\cdot}$, $C_{69}O^{+\cdot}$ and $C_{68}NO^{+\cdot}$ (table 4.1). This satisfactory agreement suggests that the full adduct $C_{70}NO^{+\cdot}$ forms then decomposes to $C_{69}N^{+\cdot}$, $C_{69}O^{+\cdot}$ and $C_{68}NO^{+\cdot}$. $C_{69}N^{+\cdot}$ represents CO loss and $C_{69}O^{+\cdot}$ represents CN loss [180]. The $C_{68}NO^{+\cdot}$ represents loss of two carbon atoms from the fullerene cage and their replacement by NO.

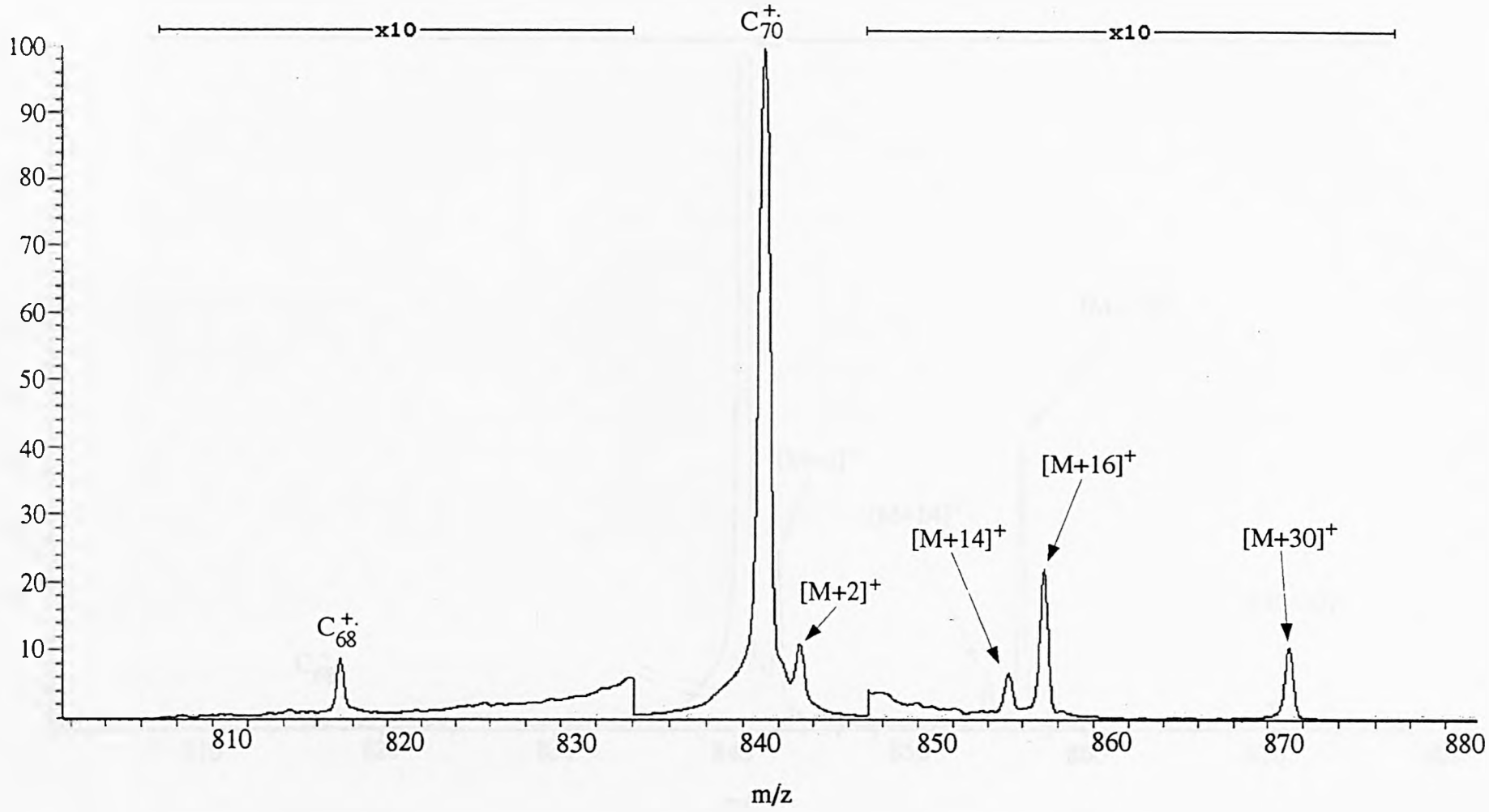

Figure 4.13: Magnet scan of $C_{70}^{+\cdot}$ and nitric oxide at E_{lab} = 300 eV.

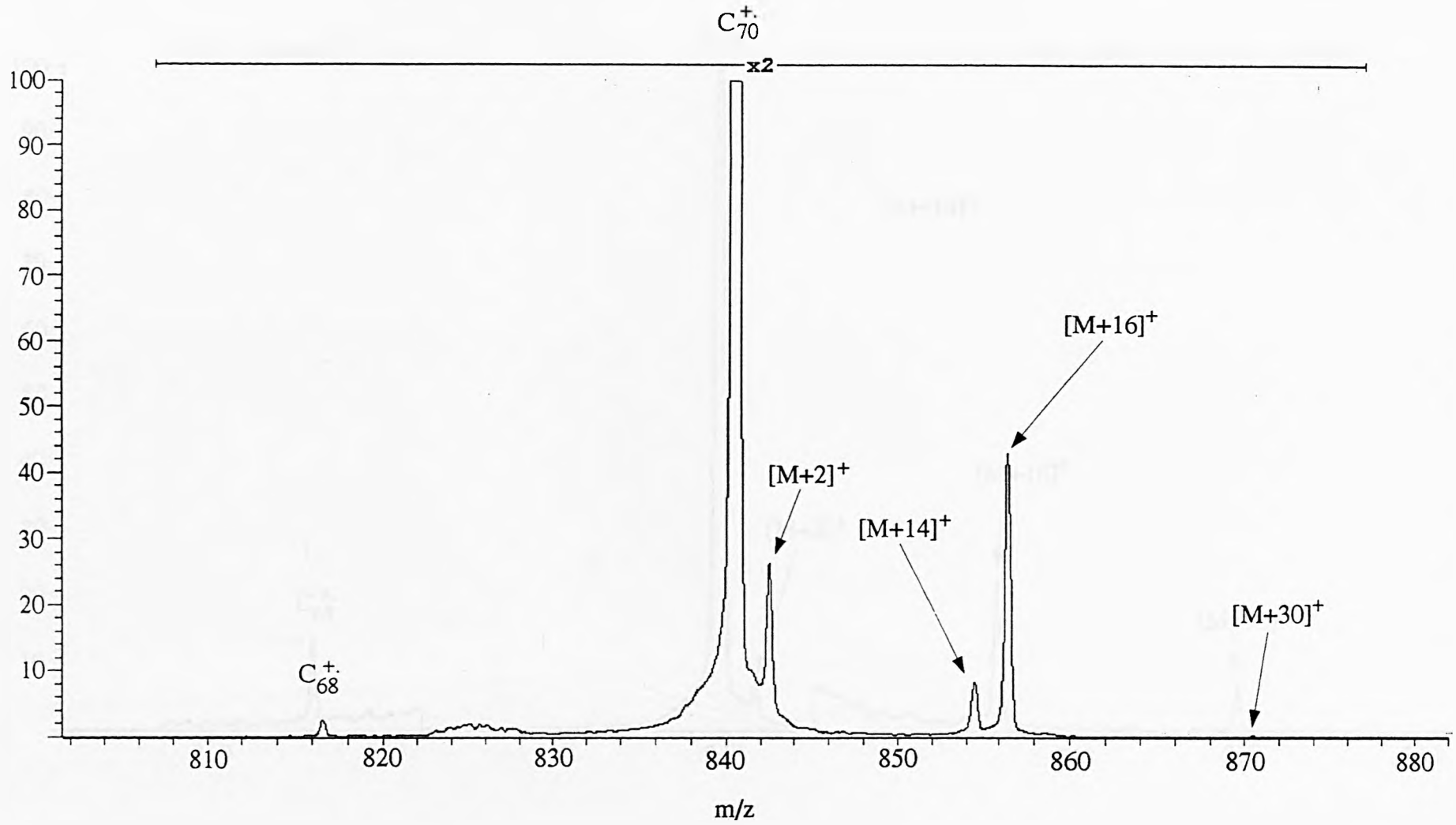

Figure 4.14: Magnet scan of $C_{70}^{+\cdot}$ and nitric oxide at E_{lab} = 500 eV.

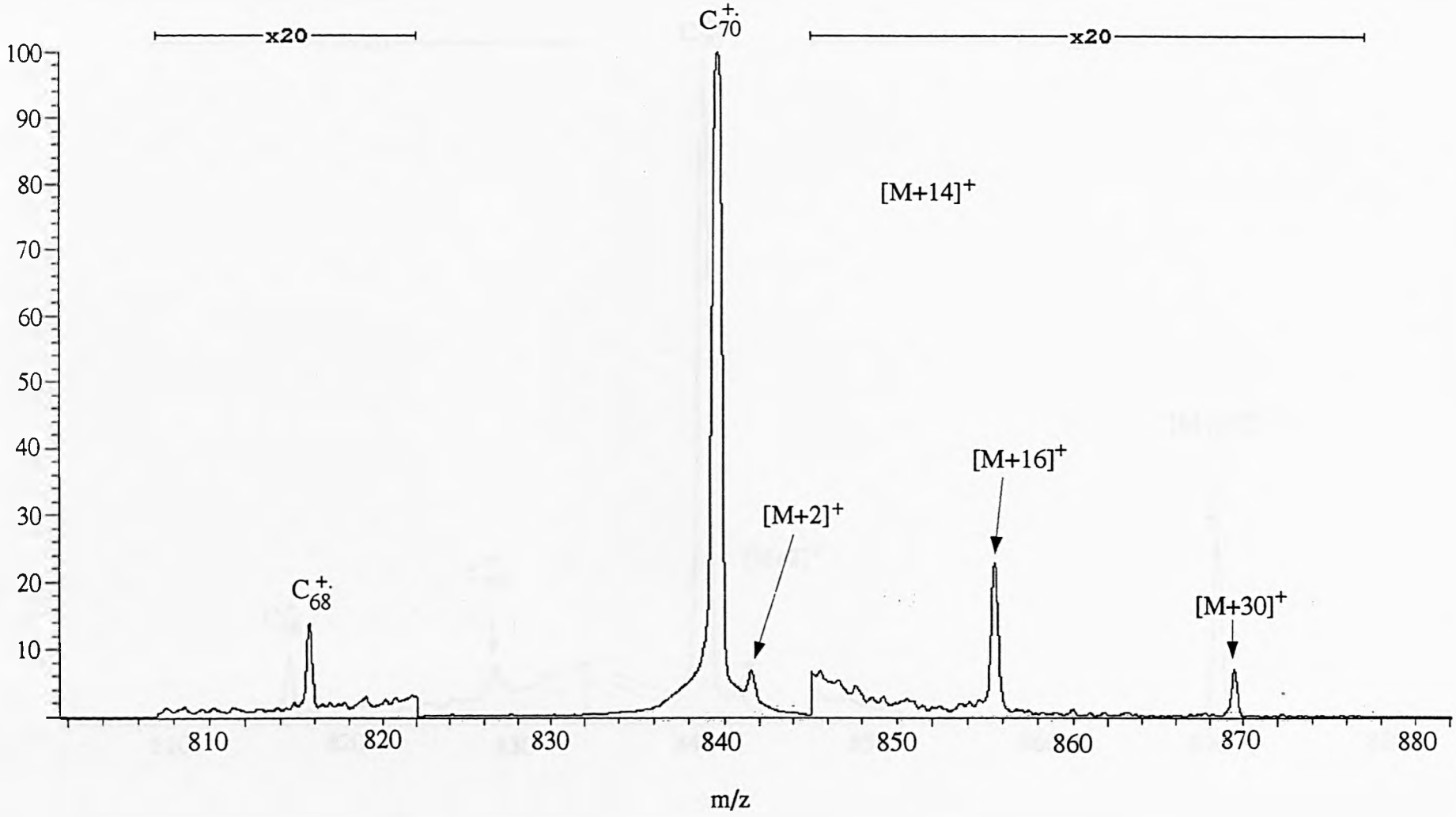

Figure 4.15: Magnet scan of $C_{70}^{+\cdot}$ and nitric oxide at E_{lab} = 750 eV.

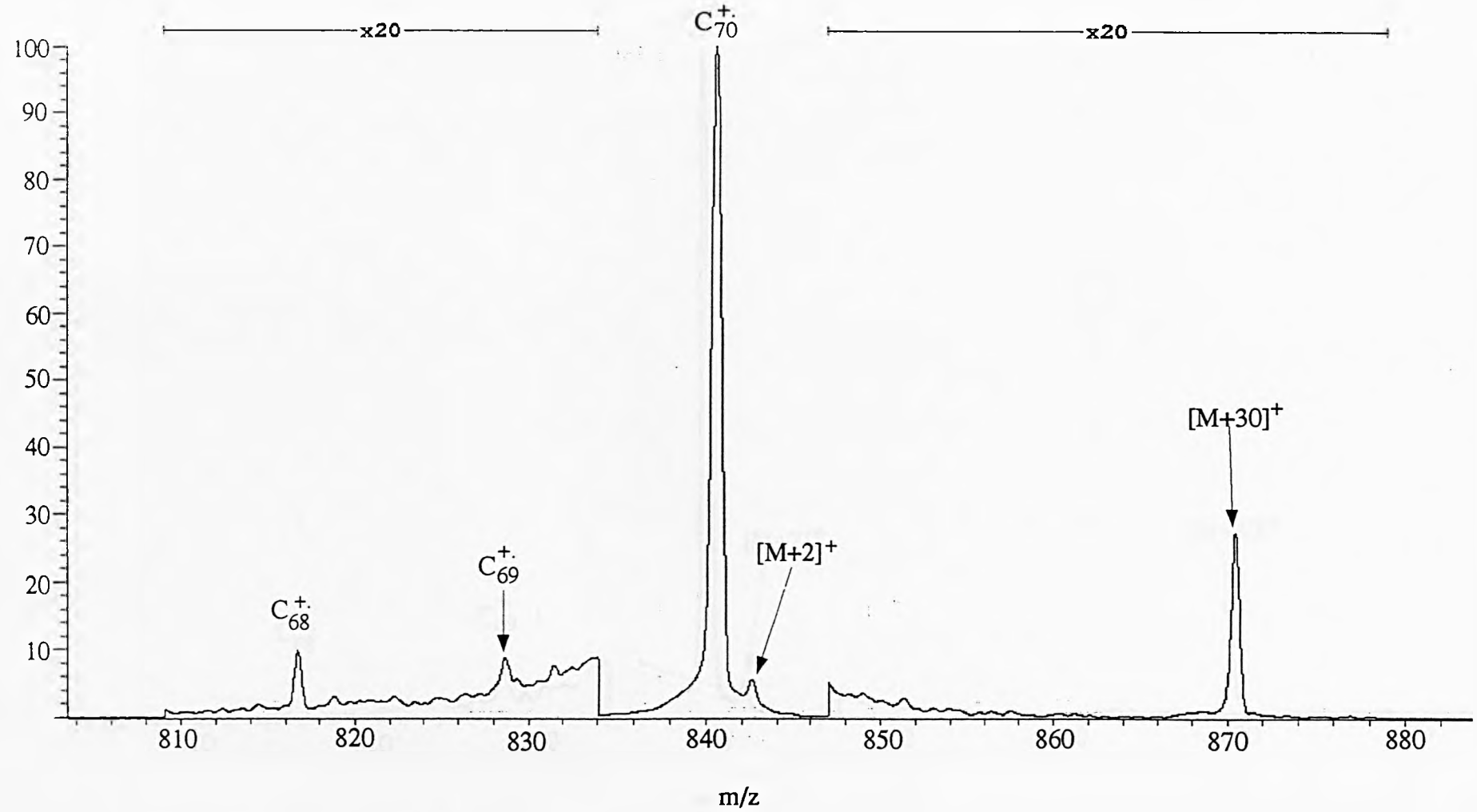

Figure 4.16: Magnet scan of $C_{70}^{+\cdot}$ and nitric oxide at E_{lab} = 1000 eV.

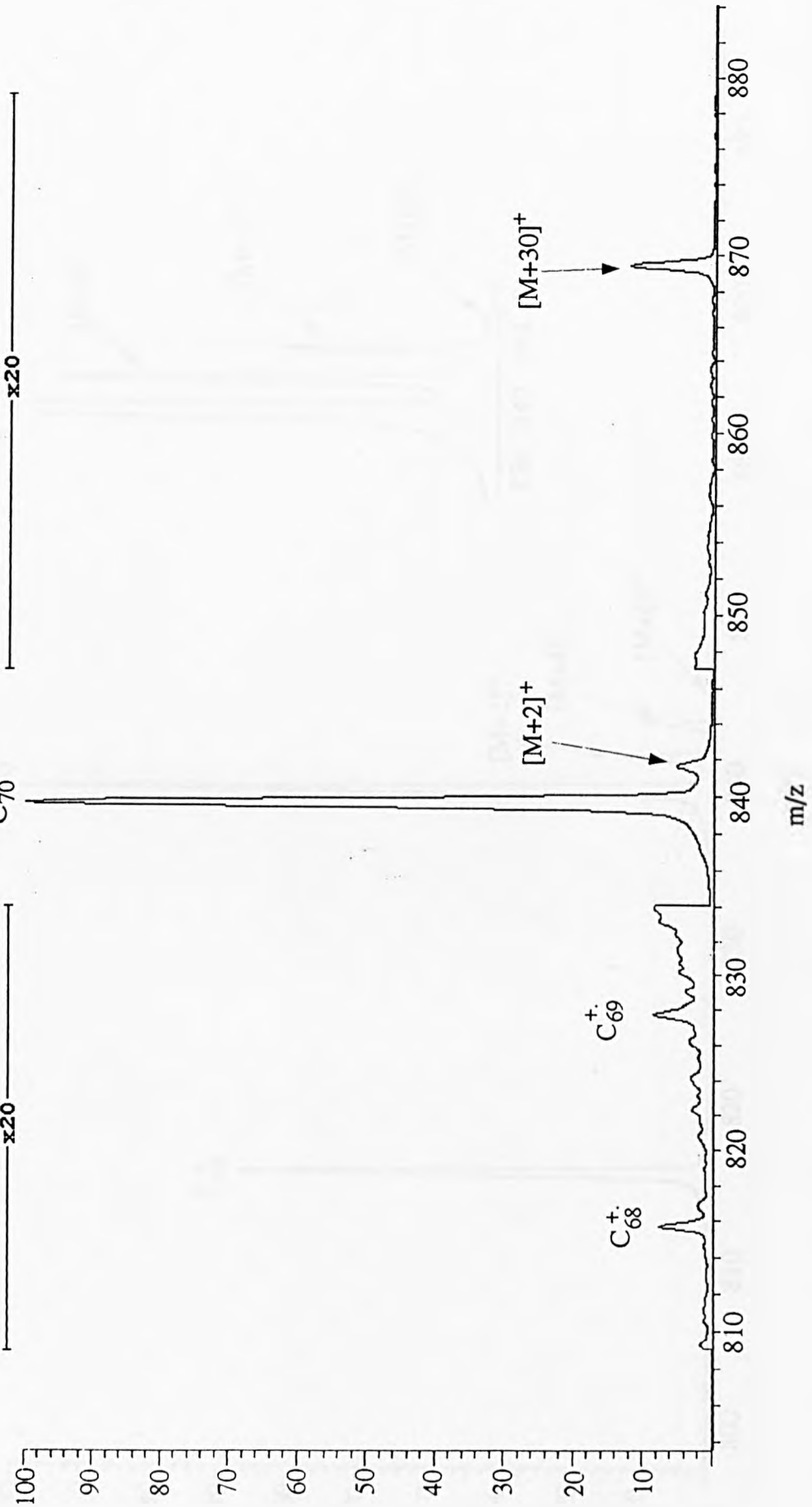

Figure 4.17: Magnet scan of $C_{70}^{+\cdot}$ and nitric oxide at E_{lab} = 1250 eV.

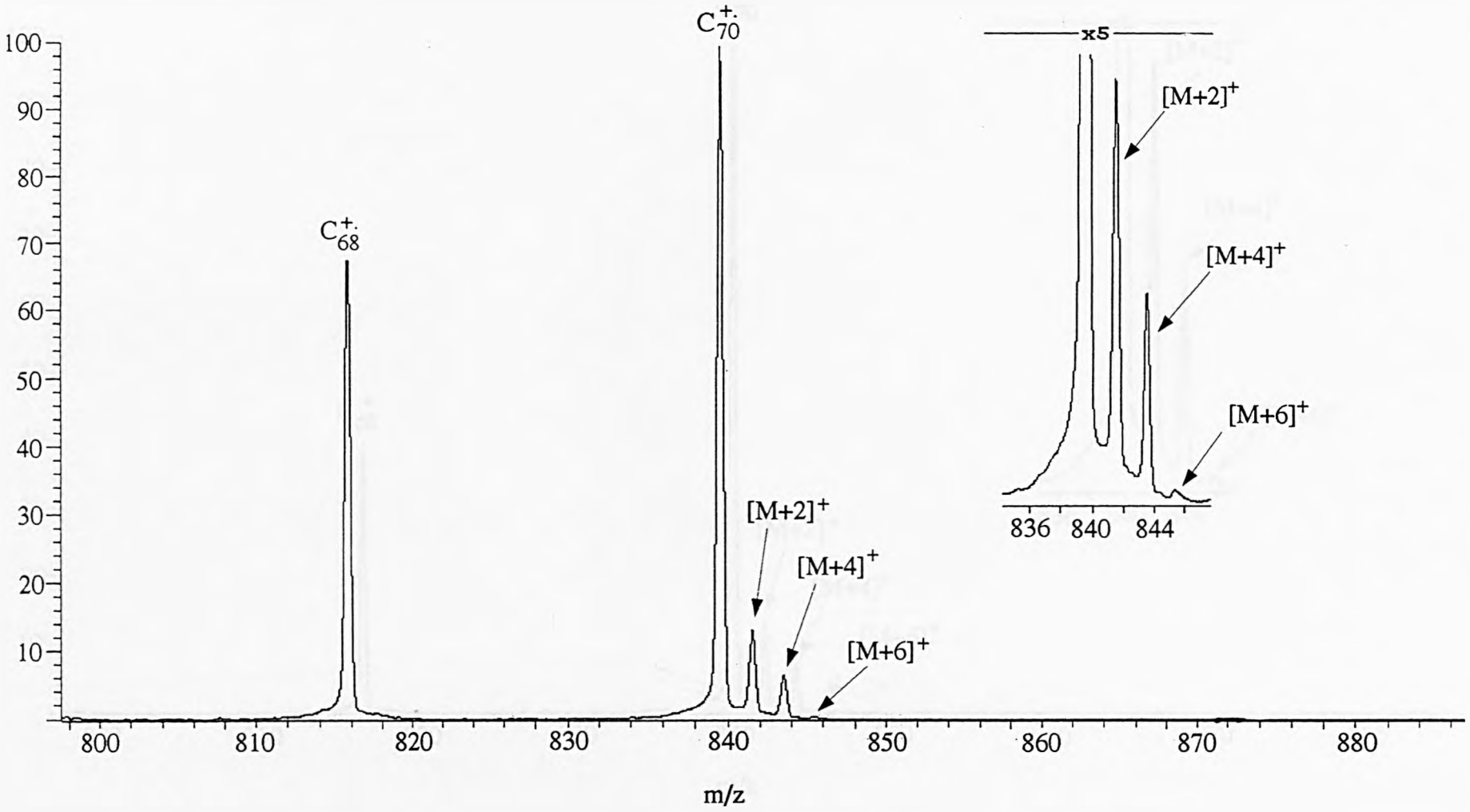

Figure 4.18: Magnet scan of $C_{70}^{+\cdot}$ and nitric oxide at E_{lab} = 1250 eV, E2 potential adjusted so as to maximise the intensity of $[M + 2]^{+}$.

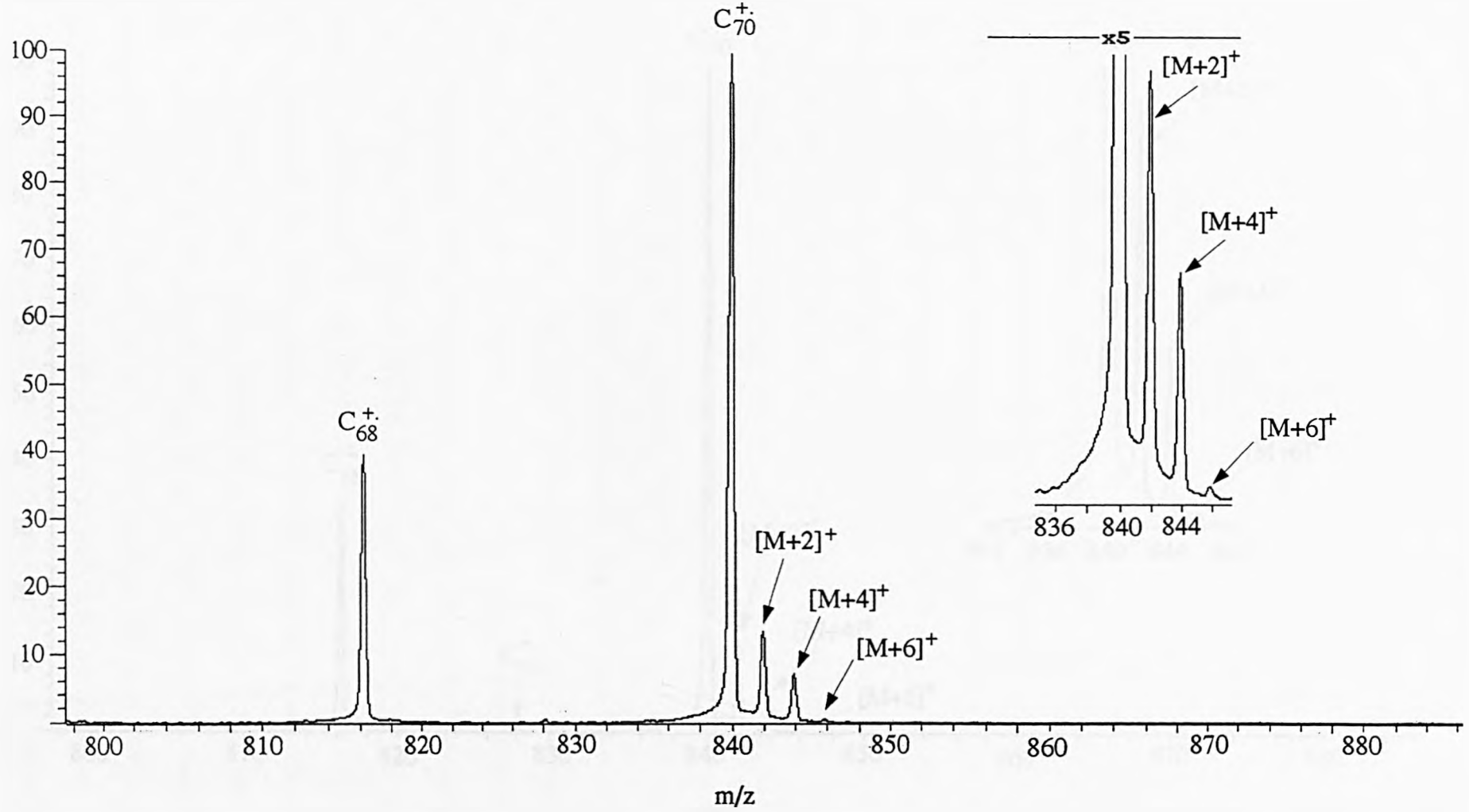

Figure 4.19: Magnet scan of $C_{70}^{+\cdot}$ and nitric oxide at E_{lab} = 1250 eV, E2 potential adjusted so as to maximise the intensity of $[M + 4]^{+}$.

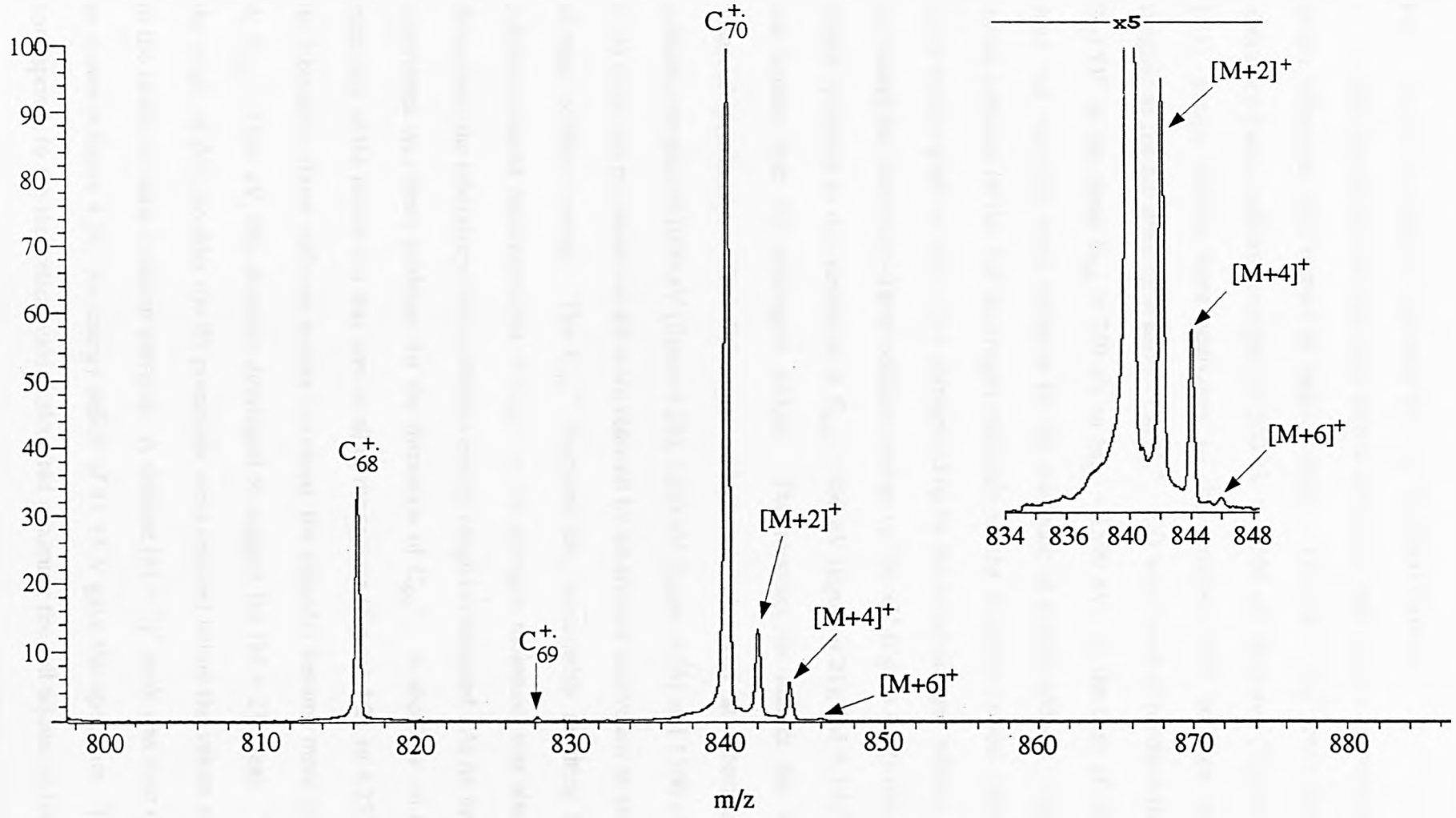

Figure 4.20: Magnet scan of $C_{70}^{+\cdot}$ and nitric oxide at E_{lab} = 1250 eV, E2 potential adjusted so as to maximise the intensity of $[M + 6]^+$.

4.4 Target Capture of Nitrogen by $C_{70}^{+\cdot}$ Radical Cations.

Nitrogen is isoelectronic with carbon monoxide and in some respects displayed similar behaviour with respect to target capture. The $[M + 28]^+$ peak observed at laboratory-frame collision energies of 500 eV to 1500 eV inclusive (figures 4.21 to 4.25), energy deficits were equivalent to the centre-of-mass collision energy, is assigned as the full dinitrogen adduct $C_{70}N_2^{+\cdot}$. CO was found to produce the adduct $C_{70}CO^{+\cdot}$ in the range E_{lab} = 750 eV to E_{lab} = 1500 eV. In the case of dinitrogen, there was only very weak evidence for the existence of atomic adducts. Figure 4.21 shows addition of the full dinitrogen molecule to the fullerene radical cation and a much weaker peak at m/z = 854 corresponding to the mononitrogen adduct, $C_{70}N^{+\cdot}$. Increasing the laboratory-frame collision energy to 750 eV (figure 4.22) resulted in a similar spectrum to that measured at E_{lab} = 500 eV (figure 4.21); $[M + 14]^+$ was far less intense than the dinitrogen adduct. The monoatomic adduct has not been observed previously. The dinitrogen adduct was observed at laboratory-frame collision energies of 1000 eV (figure 4.23), 1250 eV (figure 4.24) and 1500 eV (figure 4.25) when the potentials on E2 were reduced by an amount equivalent to the centre-of-mass collision energy. The $C_{68}^{+\cdot}$ fragment ion, presumably resulting from the collision-induced decomposition of $C_{70}^{+\cdot}$ by the nitrogen molecule, was also present throughout the laboratory-frame collision energy range investigated. At no time in this experiment was there evidence for the formation of $C_{69}^{+\cdot}$. A shoulder on the high-mass side of the parent ion was seen in all of the spectra (figures 4.21 to 4.25), and, as the laboratory-frame collision energy increased, the shoulder became more prominent. At E_{lab} = 1500 eV, this shoulder developed to suggest the $[M + 2]^+$ peak. To probe the origin of this shoulder the E2 potentials were reduced below the values equivalent to the centre-of-mass collision energies. A definite $[M + 2]^+$ peak was then observed, as shown in figure 4.26. An energy deficit of 81 ±5 V gave this spectrum. This value corresponds to the theoretical value calculated assuming the full adduct is formed and decomposes to $C_{69}N^{+\cdot}$. The spectrum in figure 4.26 was obtained at a laboratory-

frame collision energy of 1250 eV, and the energy deficit 81±5 eV was the energy deficit at which the $[M + 2]^+$ peak was optimised. Theoretical and experimental energy deficits are compared in table 4.1. The question then arose of whether $C_{68}N_2^{+\cdot}$ existed, given that the species $C_{68}NO^{+\cdot}$ was seen with NO. Evidence for the formation of $C_{68}N_2^{+\cdot}$ is shown in figure 4.27. A peak at $[M-22]^+$ is evidence for the species $C_{67}N^{+\cdot}$ (figure 4.27). The $[M + 4]^+$ peak is clearly visible in this spectrum. The experimental energy deficit was 76 ± 5 eV. Agreement with the calculated energy deficit is satisfactory (table 4.1).

As was found with carbon monoxide and nitric oxide, the full adduct $C_{70}N_2^{+\cdot}$ appeared to be more stable than the $C_{70}N^+$ adduct as the collision energy was increased. This is the first reported evidence of a $C_{70}N^+$ species. The dependence of the abundance of $C_{70}N_2^{+\cdot}$ on energy deficit was investigated. The area of the adduct peak was measured relative to that of the parent ion at 2 eV intervals in energy deficit. Results are shown in figures 4.28 and 4.29 for laboratory-frame collision energies of 500 eV and 750 eV. The relative intensity of the full adduct, $C_{70}N_2^{+\cdot}$, maximised at an energy deficit equal to the centre-of-mass collision energy. The comparison is given in table 4.2. The same experiments were carried out for the mononitrogen adduct $C_{70}N^+$. $C_{70}N^+$ was observed over a narrow energy range, which included the value calculated for the formation of this species from the decomposition of the molecular adduct at E_{lab} = 750 eV. At E_{lab} = 500 eV, the $C_{70}N^+$ adduct was not observed.

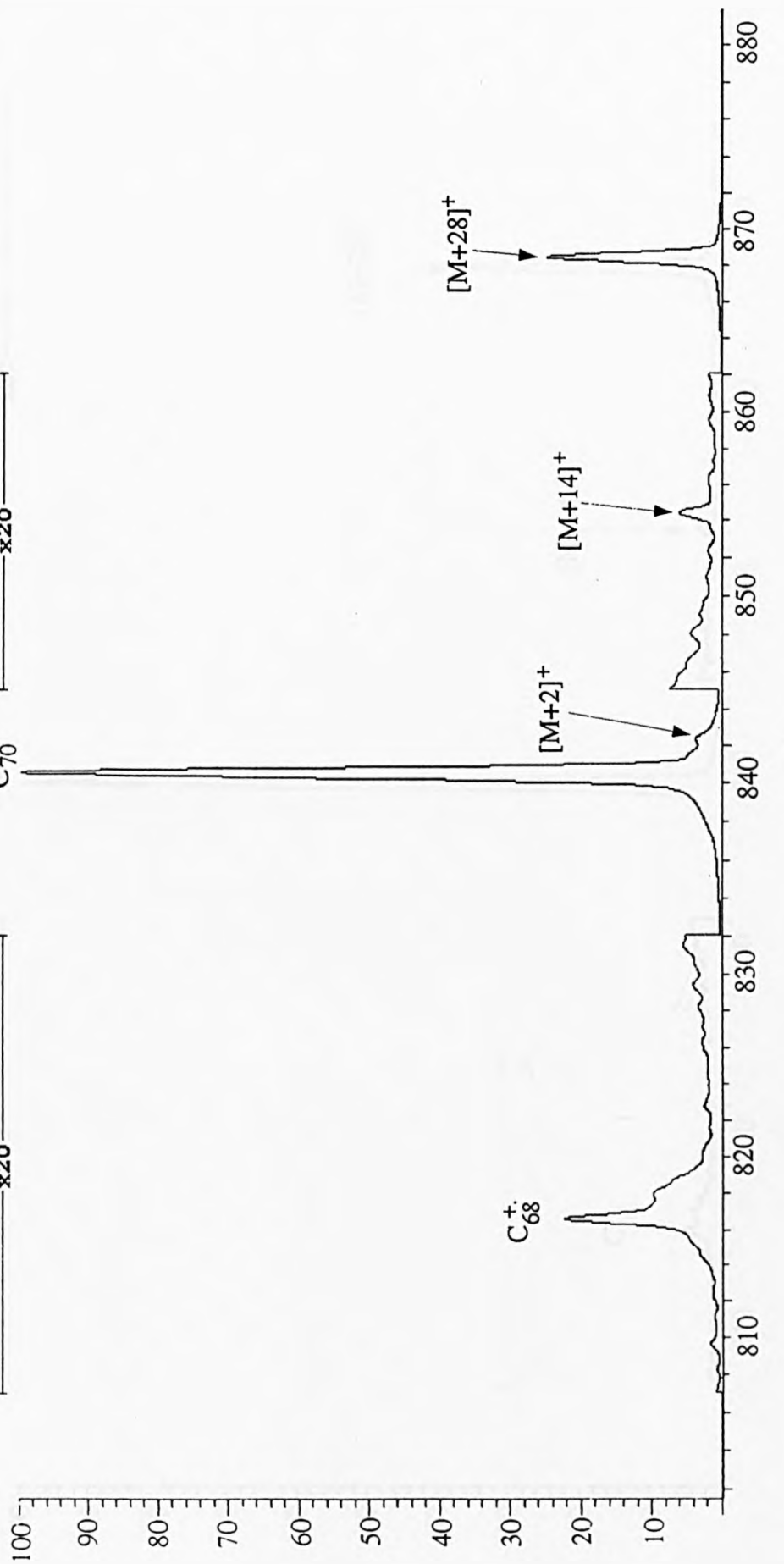

Figure 4.21: Magnet scan of $C_{70}^{+\cdot}$ and nitrogen at E_{lab} = 500 eV.

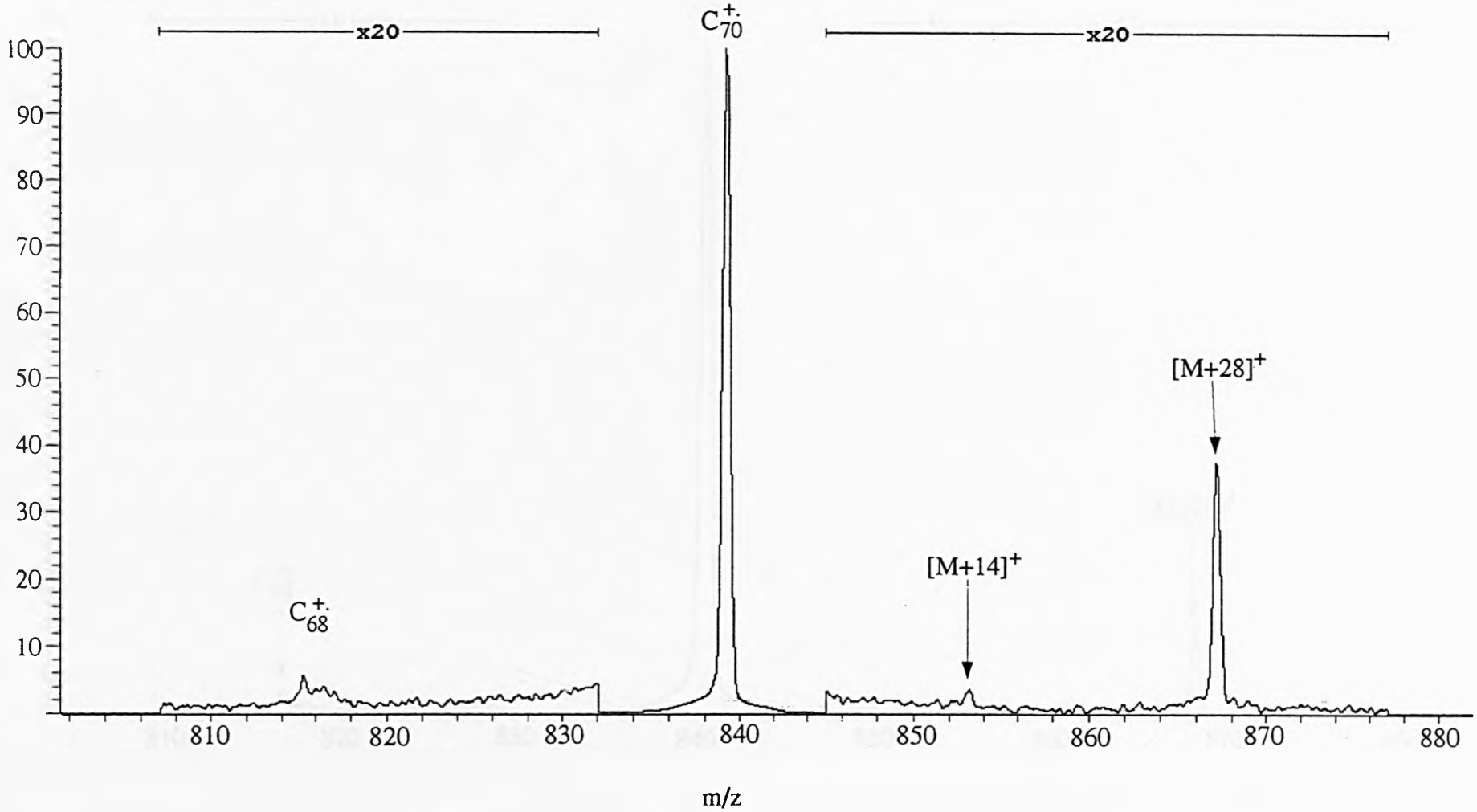

Figure 4.22: Magnet scan of $C_{70}^{+\cdot}$ and nitrogen at E_{lab} = 750 eV.

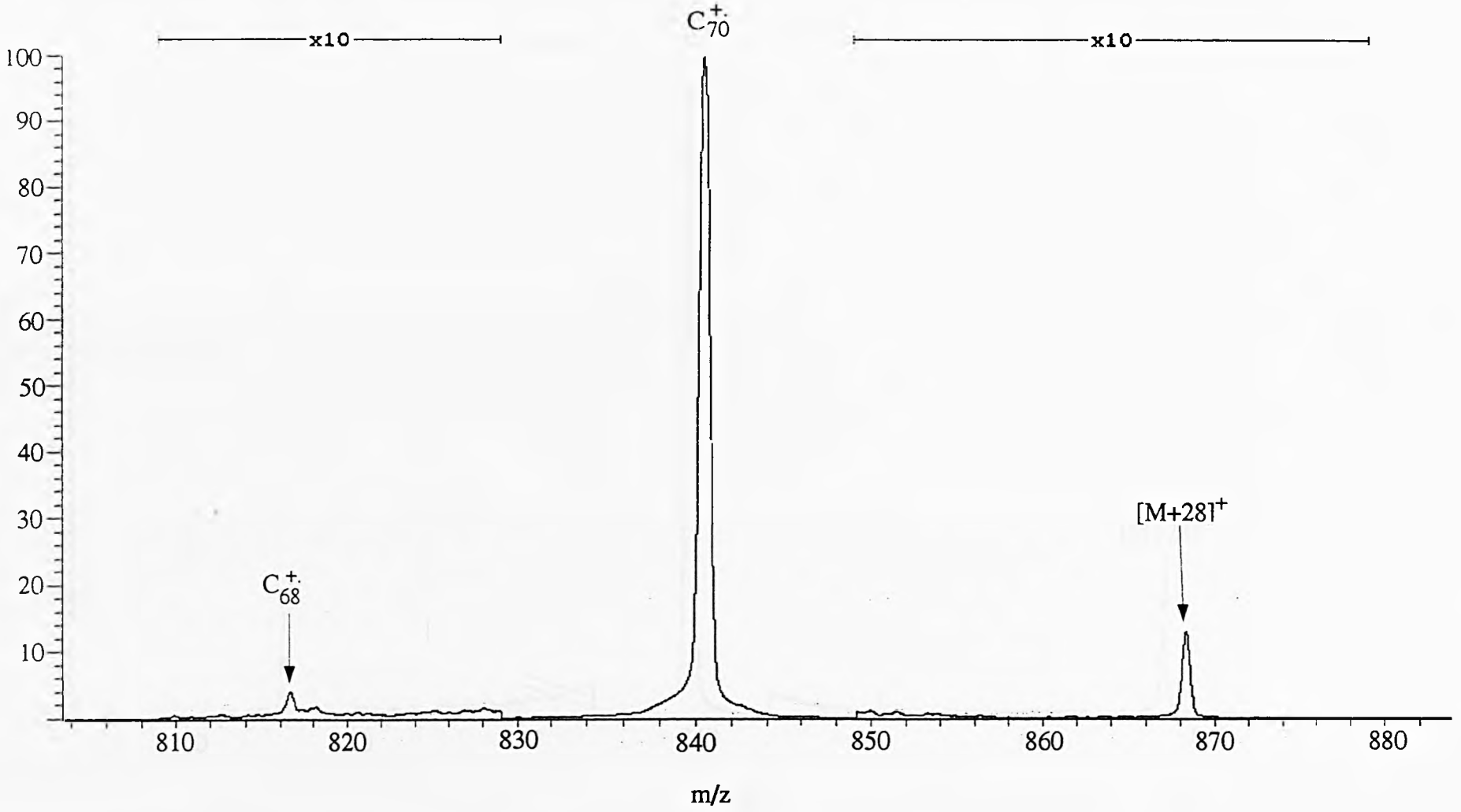

Figure 4.23: Magnet scan of $C_{70}^{+\cdot}$ and nitrogen at E_{lab} = 1000 eV.

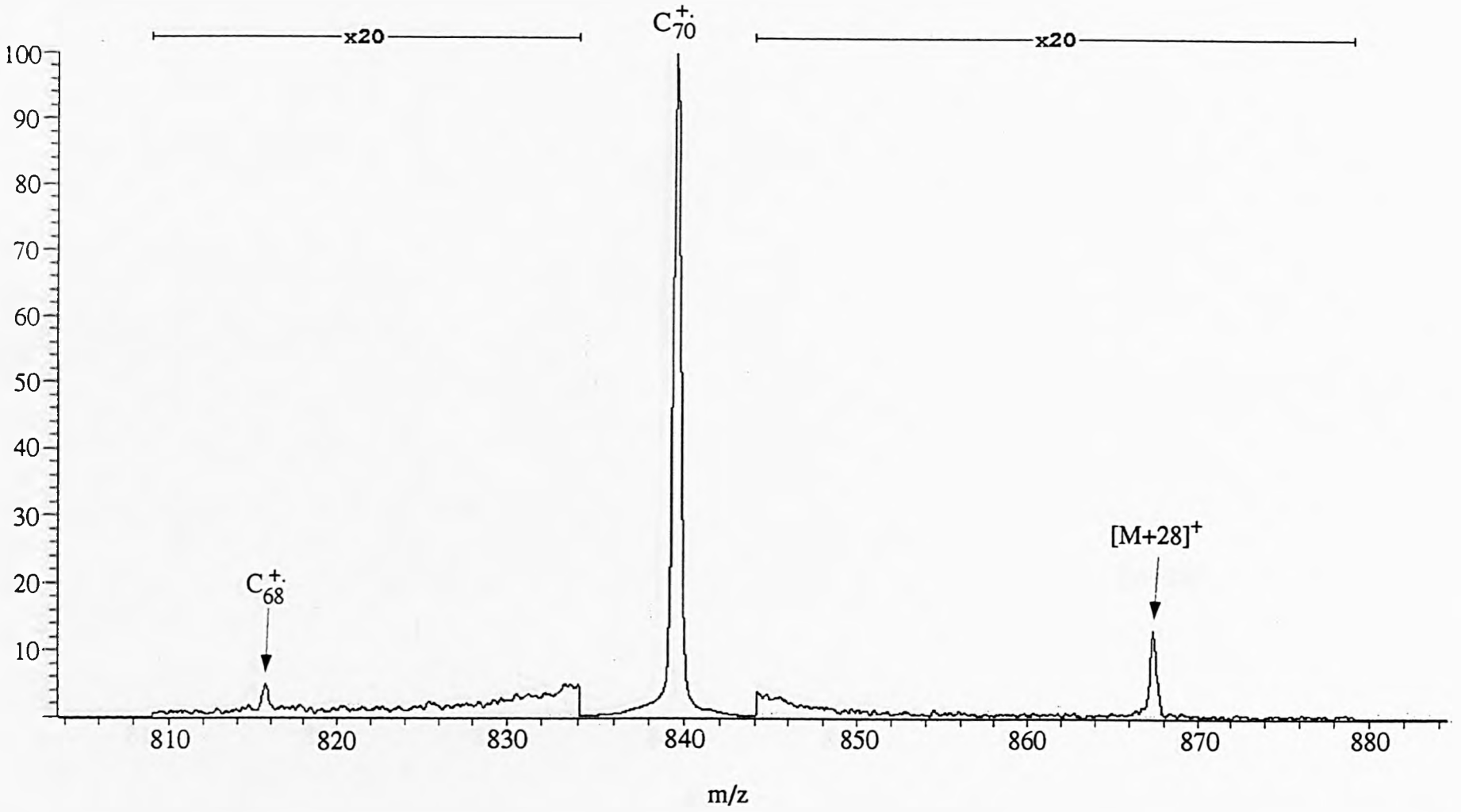

Figure 4.24: Magnet scan of $C_{70}^{+\cdot}$ and nitrogen at E_{lab} = 1250 eV.

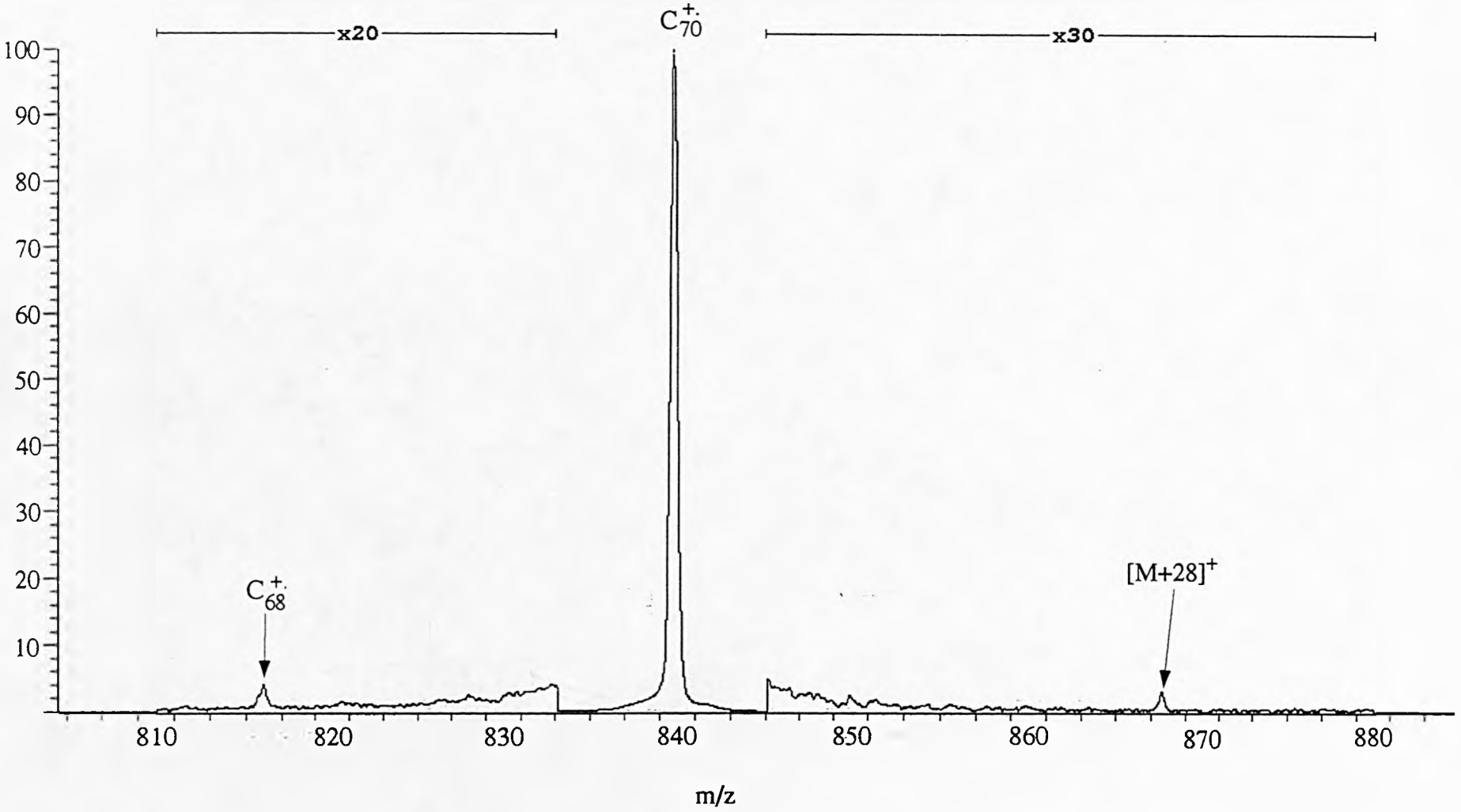

Figure 4.25: Magnet scan of $C_{70}^{+\cdot}$ and nitrogen at E_{lab} = 1500 eV.

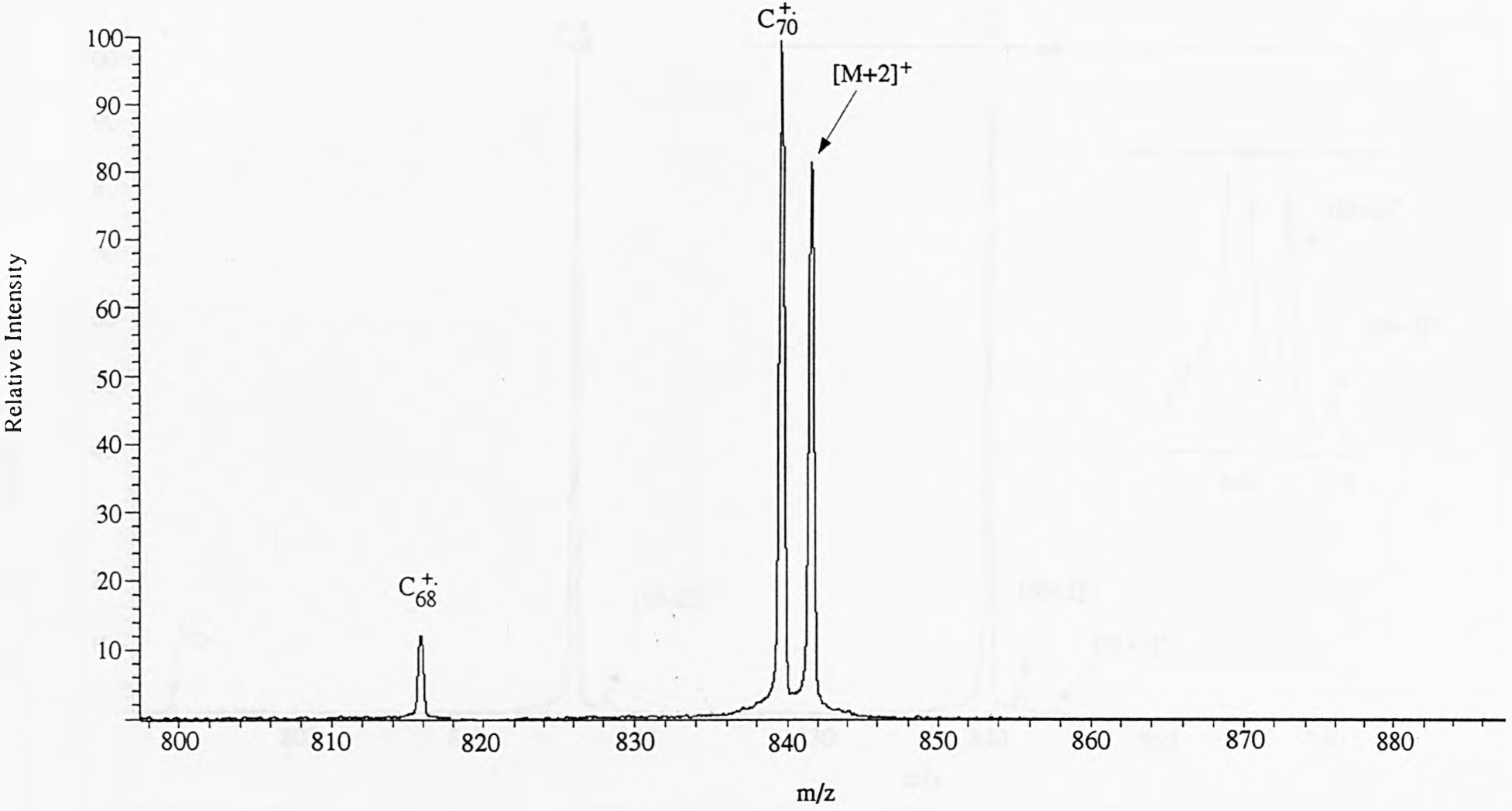

Figure 4.26: Magnet scan of $C_{70}^{+\cdot}$ and nitrogen at E_{lab} = 1250 eV, E2 potential adjusted so as to maximise the intensity of $[M + 2]^{+\cdot}$.

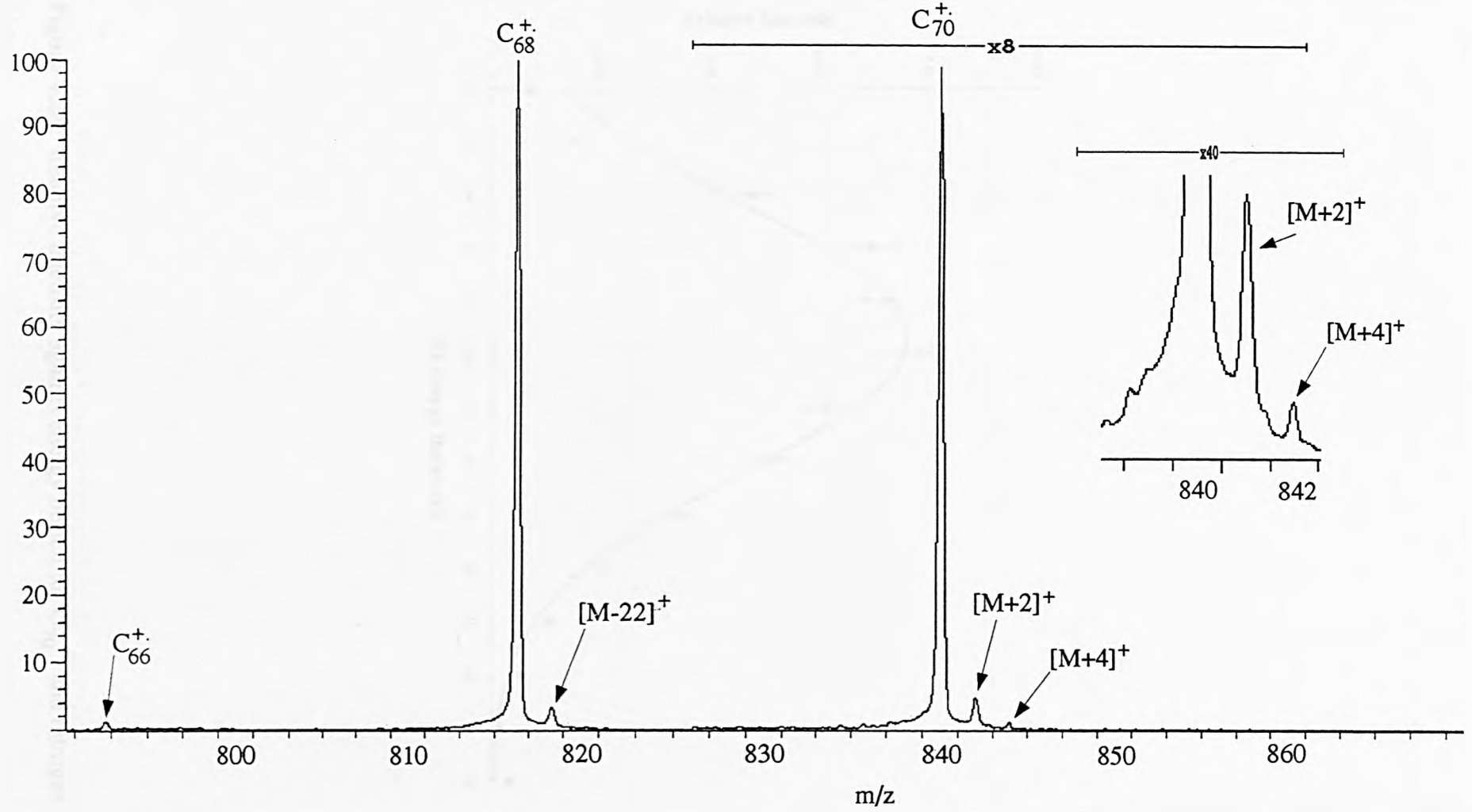

Figure 4.27: Magnet scan of $C_{70}^{+\cdot}$ and nitrogen at E_{lab} = 1250 eV, E2 potential adjusted so as to maximise the intensity of $[M + 4]^{+}$.

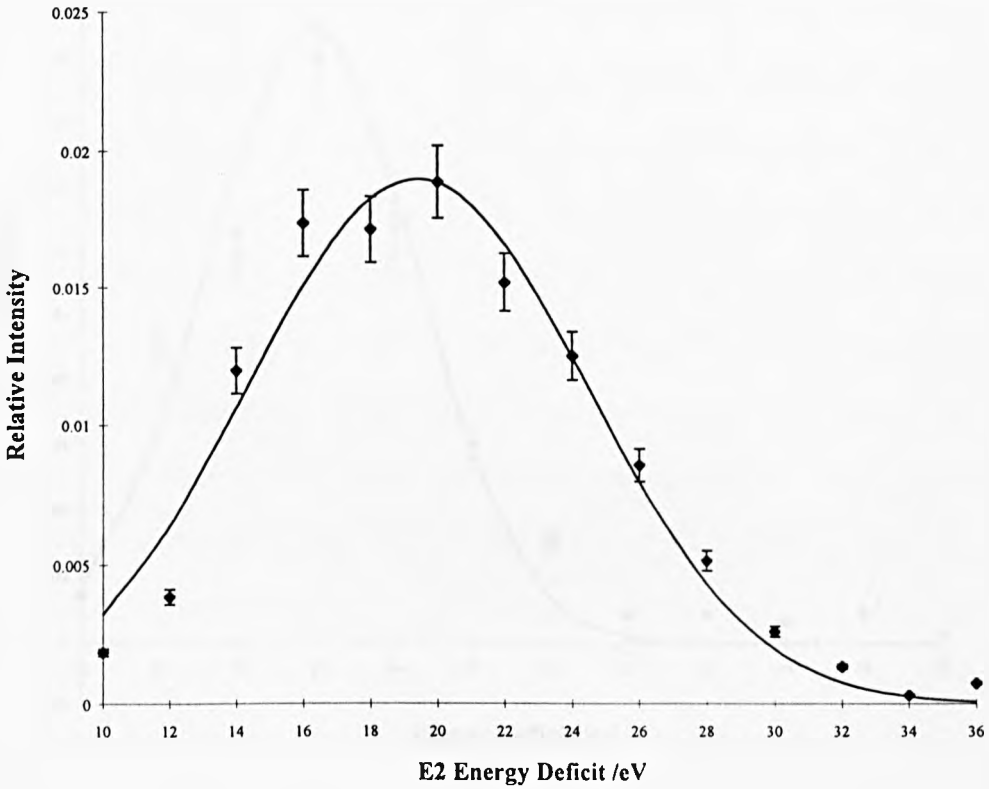

Figure 4.28: Relative intensity against energy deficit for $C_{70}^{+\cdot}$ and nitrogen at Elab = 500 eV.

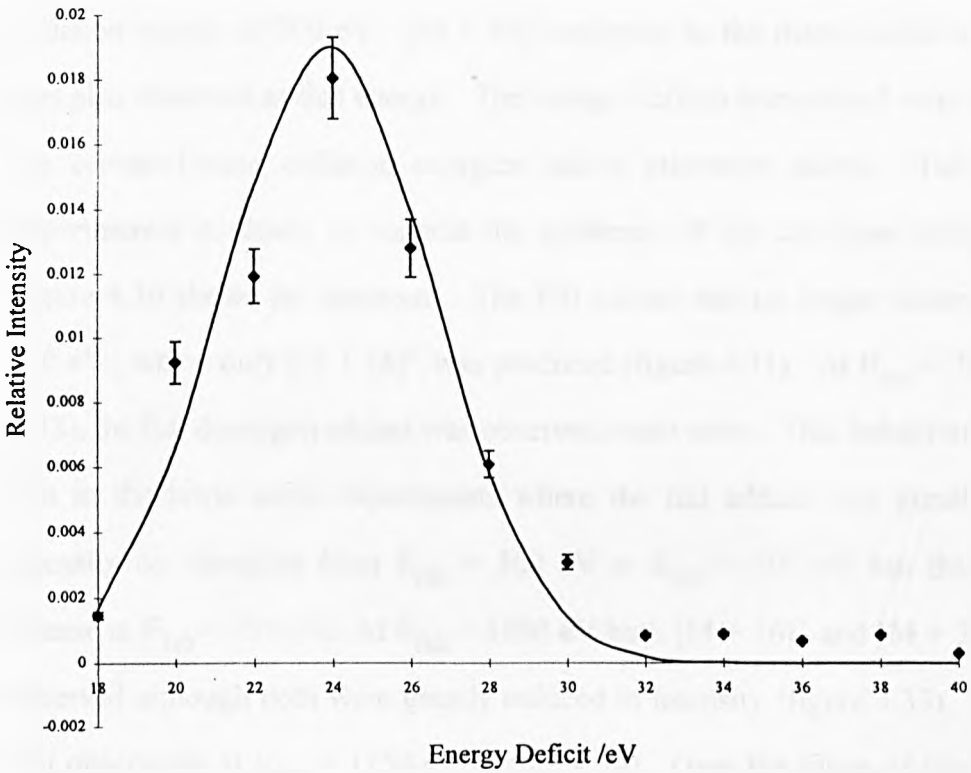

Figure 4.29: Relative intensity against energy deficit for $C_{70}^{+\cdot}$ and nitrogen at Elab = 750 eV.

4.5 Target Capture of Oxygen by $C_{70}^{+\cdot}$ Radical Cations.

The remaining diatomic collision gas studied was oxygen. Oxygen, like nitric oxide, is a paramagnetic gas and as such was expected to be relatively reactive on colliding with the radical species $C_{70}^{+\cdot}$. The importance of oxidative reactions has been the reason behind so many studies on the outcome, under different experimental conditions, of reactions between oxygen and fullerenes [107-110, 170, 179-180, 182]. Like nitric oxide, oxygen produced a full adduct ($C_{70}O_2^{+\cdot}$) at a laboratory-frame collision energy of 300 eV. $[M + 16]^+$ assigned as the monoatomic adduct $C_{70}O^{+\cdot}$ was also observed at this energy. The energy deficits transmitted were equivalent to the centre-of-mass collision energies unless otherwise stated. This is the first experimental evidence to suggest the existence of the dioxygen adduct of $C_{70}^{+\cdot}$. Figure 4.30 shows the spectrum. The full adduct was no longer observed at E_{lab} = 500 eV , where only $[M + 16]^+$ was produced (figure 4.31). At E_{lab} = 750 eV (figure 4.32), the full dioxygen adduct was observed, once more. This behaviour is similar to that in the nitric oxide experiments where the full adduct was greatly reduced in intensity on changing from E_{lab} = 300 eV to E_{lab} = 500 eV but then grew more intense at E_{lab} = 750 eV. At E_{lab} = 1000 eV both $[M + 16]^+$ and $[M + 32]^+$ were still observed although both were greatly reduced in intensity (figure 4.33). $C_{70}O_2^{+\cdot}$ was still observable at E_{lab} = 1250 eV (figure 4.34). Over the range of laboratory-frame collision energies investigated, the fragment ion $C_{68}^{+\cdot}$ was always observed. In addition the fragment ion $C_{69}^{+\cdot}$ was observed. This fragment was produced in the experiments with ^{13}CO and NO. A broad peak, approximately 5 Da wide was observed at m/z = 824 (see figures 4.30, 4.31 and 4.32). A peak at this mass, of the same shape, was observed following collisions with nitric oxide and assigned as the metastable decay of $C_{70}O^{+\cdot}$ to $C_{70}^{+\cdot}$. The same conclusion can be drawn for oxygen.

The observation of $C_{69}O^{+\cdot}$ from collisions between $C_{70}^{+\cdot}$ and NO promoted a search for a $[M + 4]^+$ peak from $C_{70}^{+\cdot}$ collisions with molecular oxygen. At a laboratory-frame collision energy of 1250 eV, $[M + 4]^+$ was observed when the E2

potentials was reduced below the value equivalent to the centre-of-mass collision energy (figure 4.35). Assigned as $C_{69}O^{+\cdot}$, the intensity of this peak was found to be maximised at an energy deficit of 86±4 eV. This value is within experimental error of the theoretical value E_{def} = 84.5 eV, calculated on the basis of formation of $C_{70}O_2^{+\cdot}$ and decomposition to $C_{69}O^{+\cdot}$. There was no evidence for the existence of $C_{68}O_2^{+\cdot}$ at E_{lab} = 1250 eV.

The dependences of the abundances of $C_{70}O_2^{+\cdot}$ and $C_{70}O^{+}$ on energy deficit was investigated. The areas of these adduct peaks relative to the parent ion peak were measured at laboratory-frame collision energies of 300 eV and 1000 eV for a range energy deficits at 2 eV intervals. The results are shown in figures 4.36 and 4.37 respectively. Comparison with theoretical values is given in table 4.3. The full molecular adduct was observed over a range of energy deficits which included the value equal to the centre-of-mass collision energy. At E_{lab} = 300 eV the $C_{70}O^{+}$ adduct ion was observed at an energy deficit corresponding to that calculated on the basis of formation of the full adduct and decomposition to $C_{70}O^{+}$. This is in contrast with the finding at E_{lab} = 1000 eV, where the energy deficit corresponded to the value calculated on the basis that one atom of the collision gas was stripped from the diatomic molecule and captured by the fullerene ion.

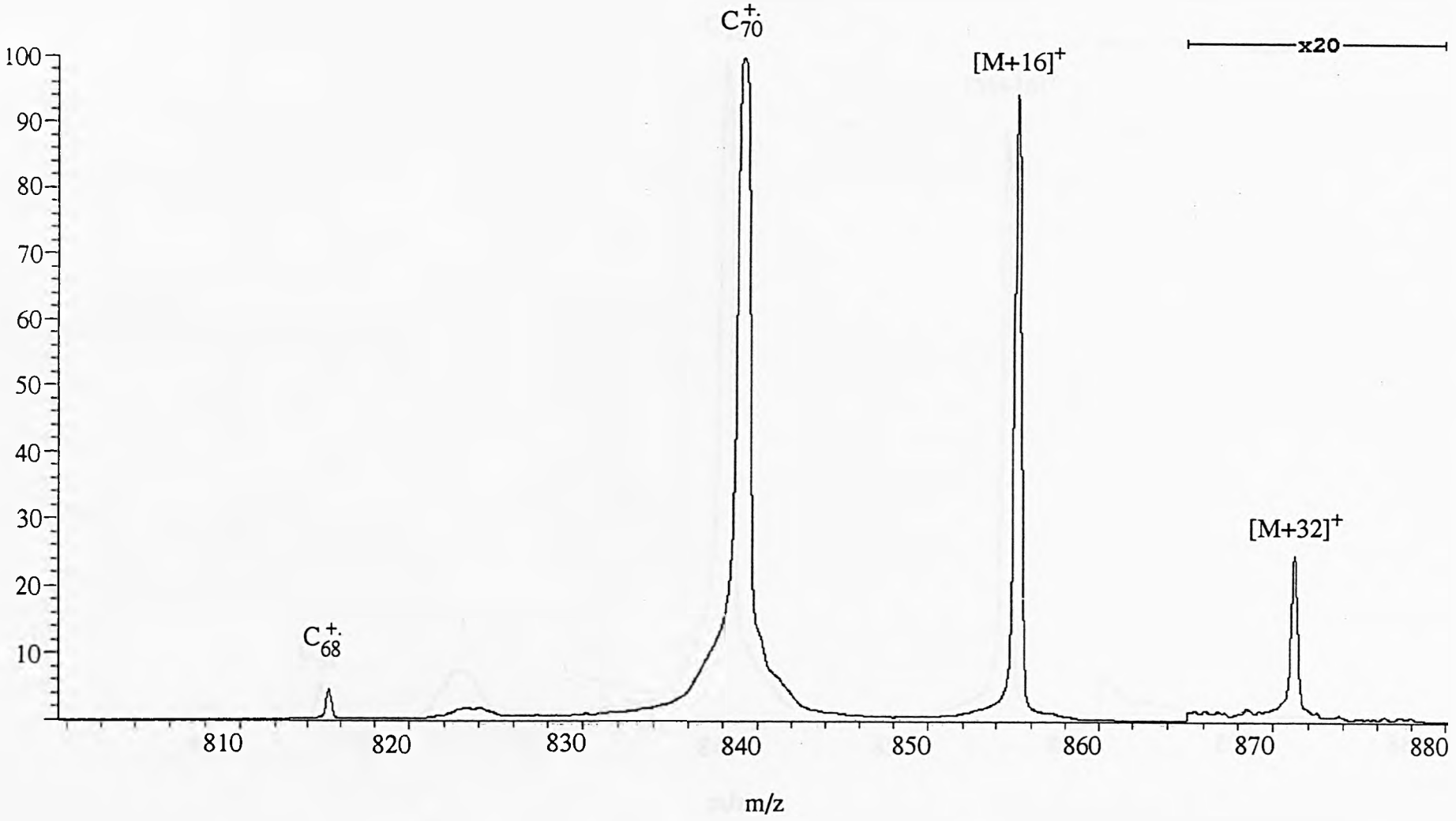

Figure 4.30: Magnet scan of $C_{70}^{+\cdot}$ and oxygen at E_{lab} = 300 eV.

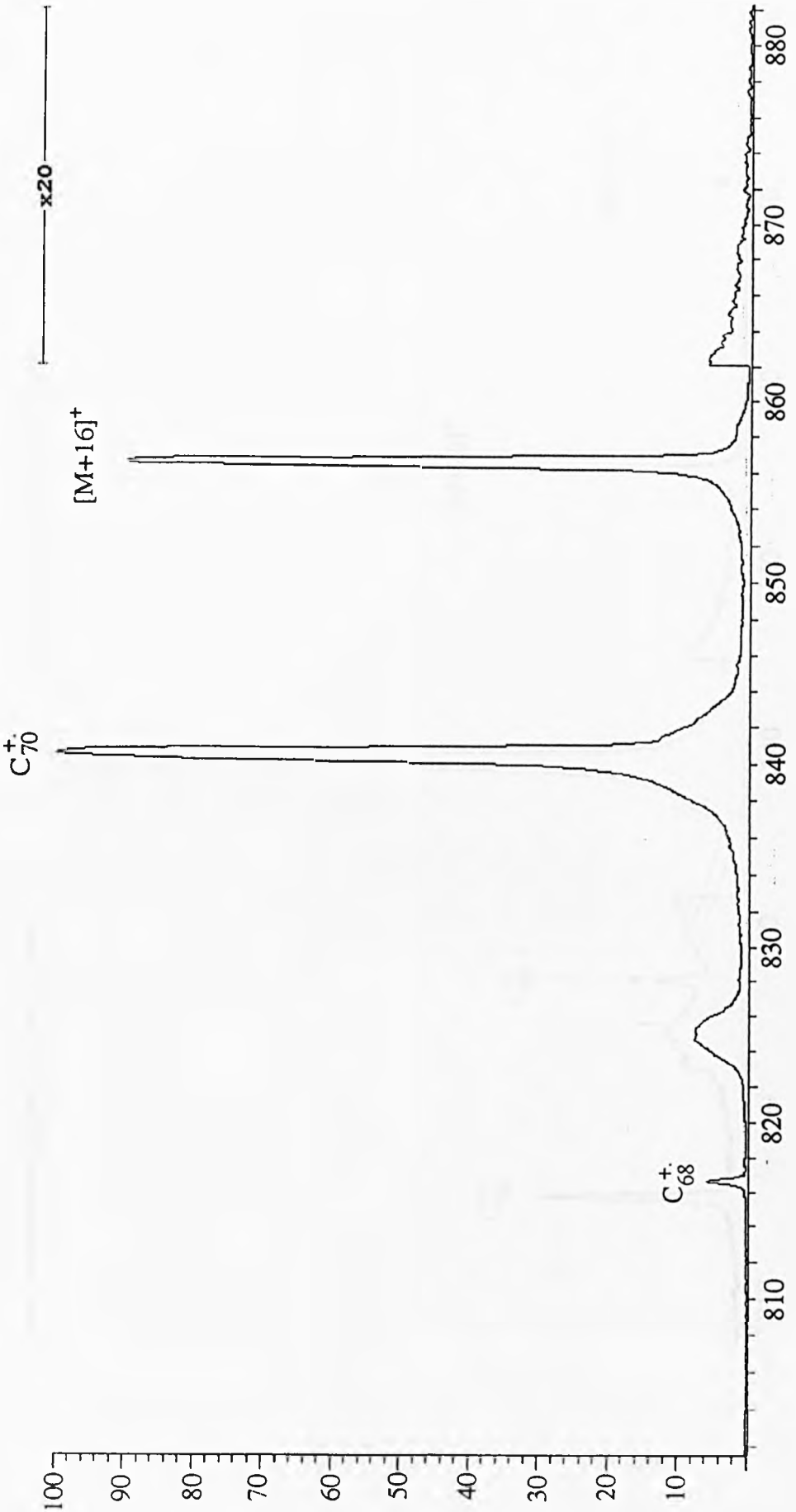

Figure 4.31: Magnet scan of $C_{70}^{+\cdot}$ and oxygen at E_{lab} = 500 eV.

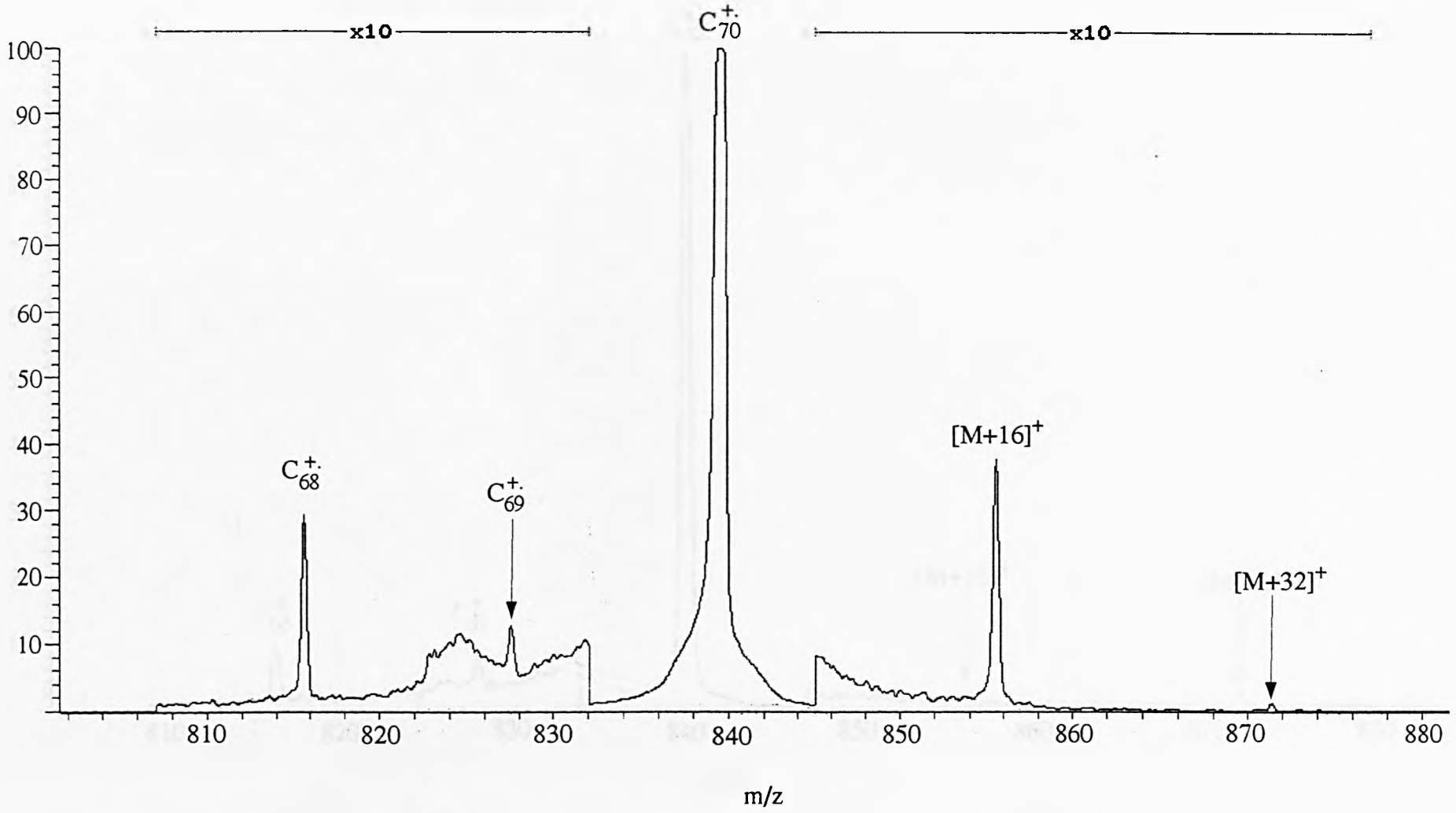

Figure 4.32: Magnet scan of $C_{70}^{+\cdot}$ and oxygen at E_{lab} = 750 eV.

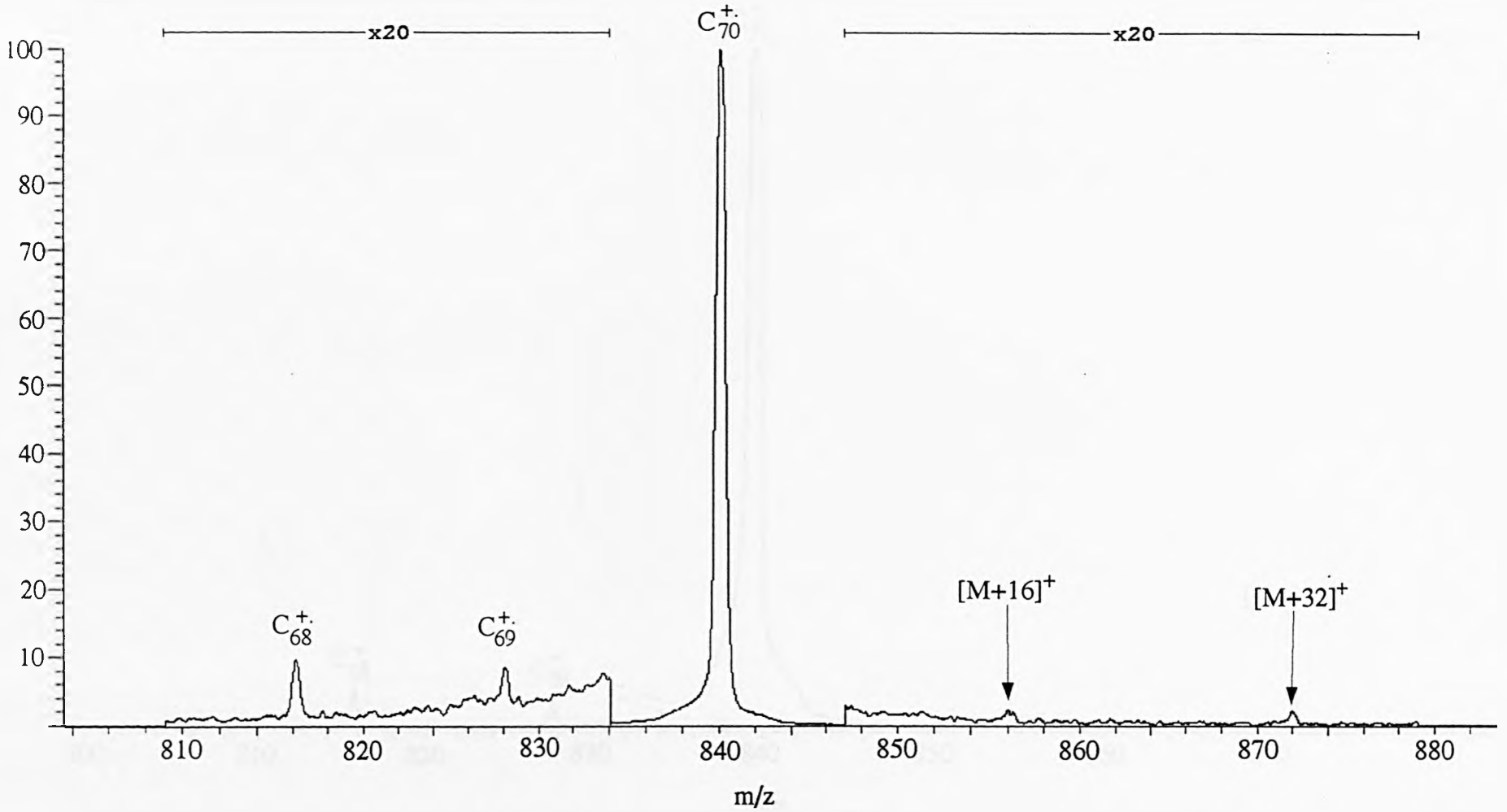

Figure 4.33: Magnet scan of $C_{70}^{+\cdot}$ and oxygen at E_{lab} = 1000 eV.

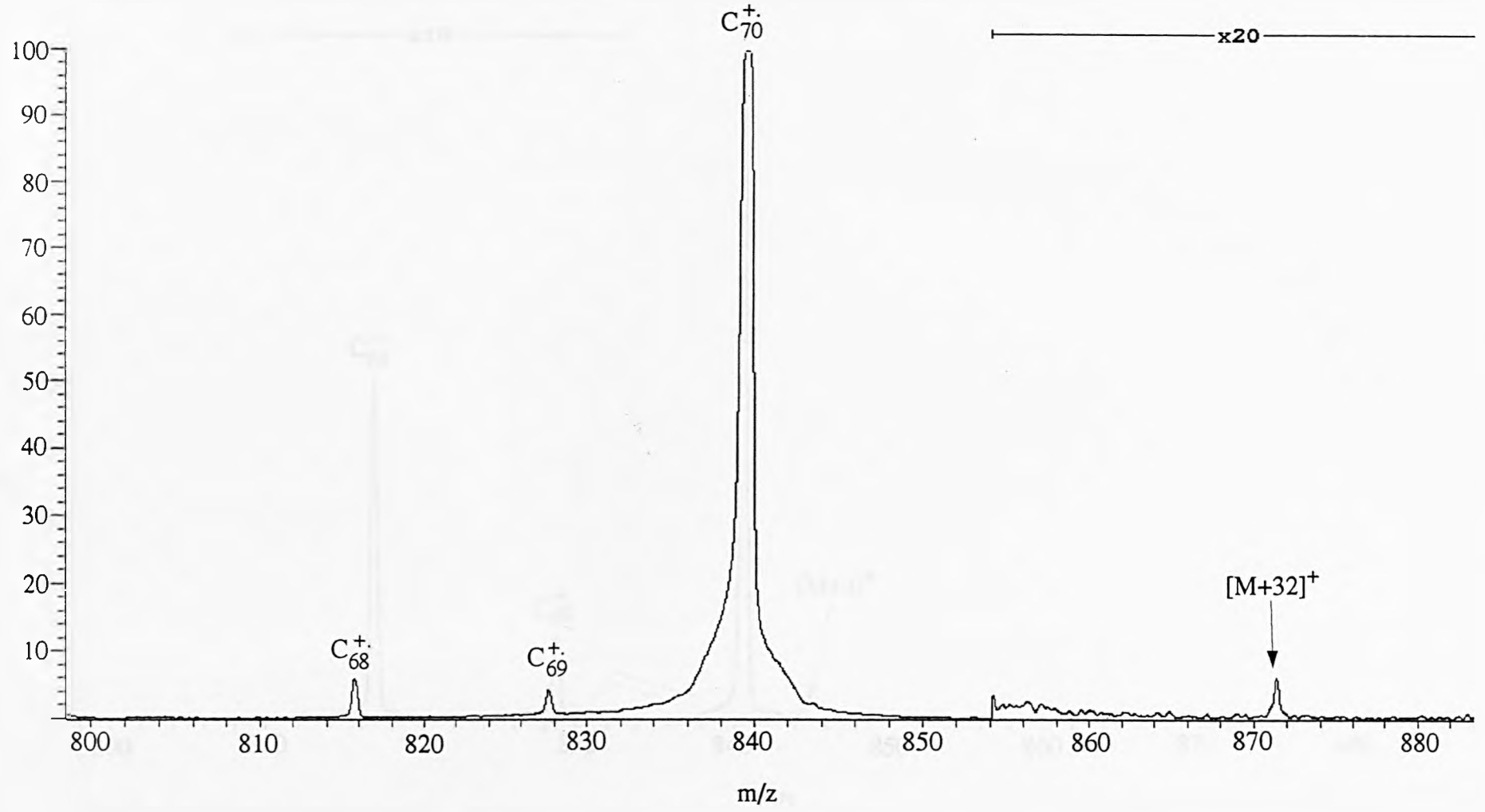

Figure 4.34: Magnet scan of $C_{70}^{+\cdot}$ and oxygen at E_{lab} = 1250 eV.

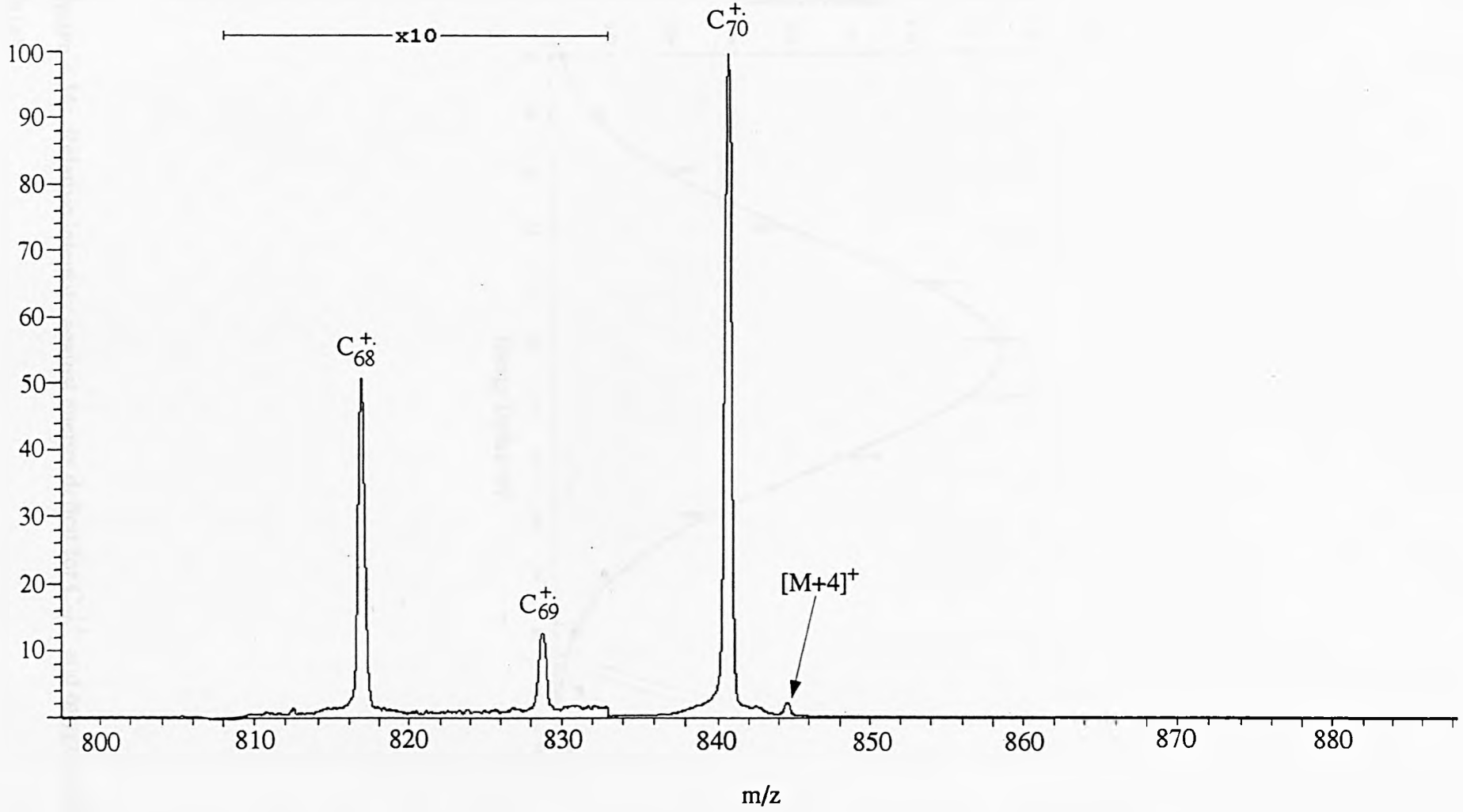

Figure 4.35: Magnet scan of $C_{70}^{+\cdot}$ and oxygen at E_{lab} = 1250 eV, E2 potential adjusted so as to maximise the intensity of $[M + 4]^{+\cdot}$.

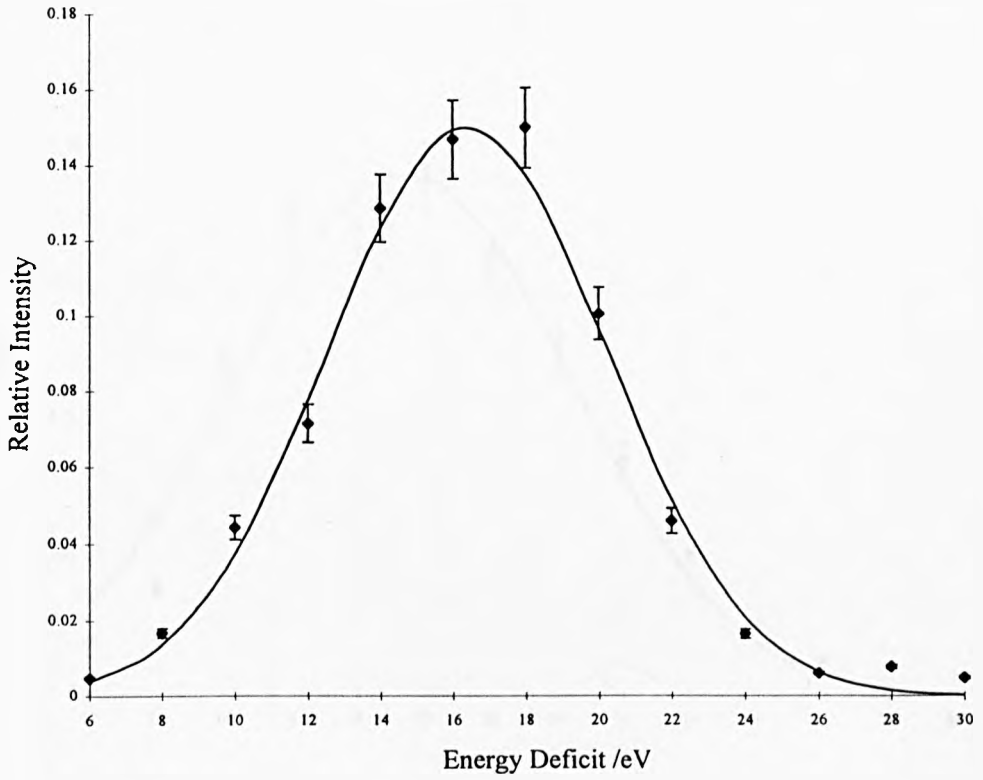

Figure 4.36: Relative intensity against energy deficit for $C_{70}^{+\cdot}$ and oxygen at Elab = 300 eV.

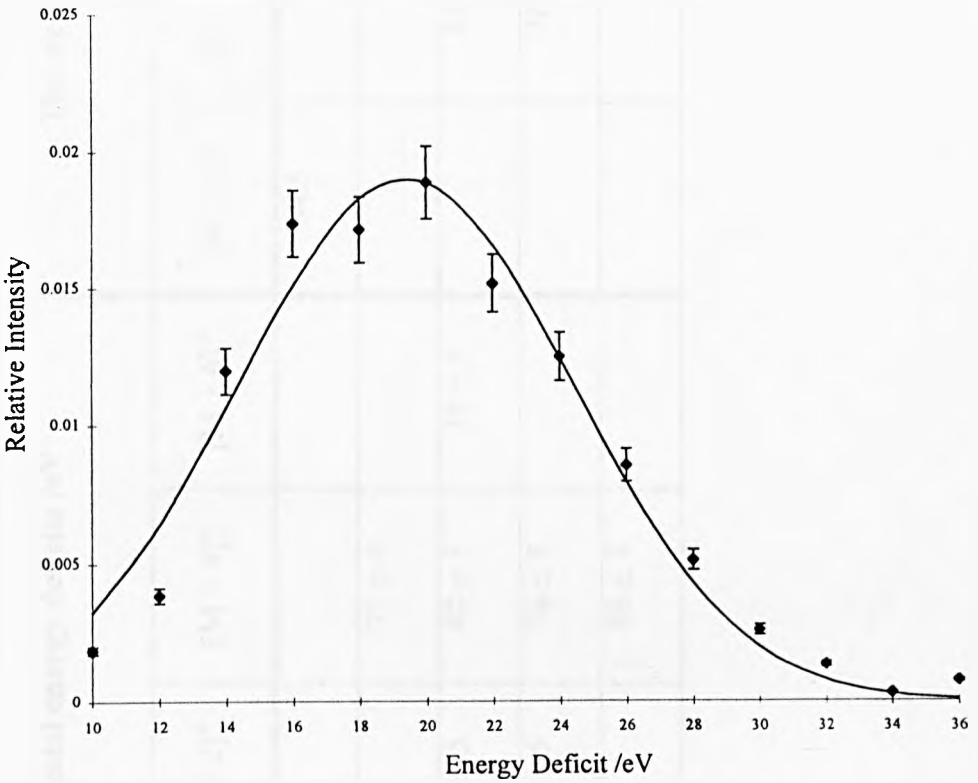

Figure 4.37: Relative intensity against energy deficit for $C_{70}^{+\cdot}$ and oxygen at Elab = 1000 eV.

Collision gas	E_{lab} /eV	Experimental energy deficits /eV				Theoretical energy deficits /eV			
		$[M + 1]^+$	$[M + 2]^+$	$[M + 4]^+$	$[M + 6]^+$	$[M + 1]^+$	$[M + 2]^+$	$[M + 4]^+$	$[M + 6]^+$
^{13}Carbon monoxide	1000	64 ± 1				64.5			
Carbon monoxide	1250			75 ± 4				73.8	
Nitric oxide	1250		83 ± 5	80 ± 5	78 ± 5		81.9	79.2	76.4
nitrogen	1250		81 ± 5	76 ± 5			76.6	73.8	
oxygen	1250			86 ± 4				84.5	

Table 4.1: Comparison of experimental energy deficits with theoretical energy deficits, calculated assuming full adduct formation prior to decomposition into fragment adduct ions.

E_{lab} /eV	Experimental energy deficits /eV		Theoretical energy deficits /eV		
	$C_{70}N_2^{+\cdot}$	$C_{70}N^{+\cdot}$	$C_{70}N_2^{+\cdot}$	Decomposition of $C_{70}N_2^{+\cdot}$ to $C_{70}N^{+\cdot}$	Removal and capture of N from N_2 by $C_{70}^{+\cdot}$ forming $C_{70}N^{+\cdot}$
500	15 ± 2	not observed	16.1	23.9	6.2
750	23 ± 2	32 ± 8	24.2	35.9	12.3

Table 4.2: Comparison of experimental and theoretical energy deficits for the formation of the full dinitrogen adduct and the mononitrogen adduct from collisions of $C_{70}^{+\cdot}$ with N_2.

E_{lab} /eV	Experimental energy deficits /eV		Theoretical energy deficits /eV		
	$C_{70}O_2^{+\cdot}$	$C_{70}O^{+\cdot}$	$C_{70}O_2^{+\cdot}$	Dissociation of $C_{70}O_2^{+\cdot}$ to $C_{70}O^{+\cdot}$	Removal and capture of O from O_2 by $C_{70}^{+\cdot}$ forming $C_{70}O^{+\cdot}$
300	11 ± 5	17 ± 1	11.0	16.3	5.6
1000	36 ± 4	19 ± 1	36.7	54.4	18.7

Table 4.3: Comparison of experimental and theoretical energy deficits for the formation of the full dioxygen adduct and the monooxygen adduct from collisions of $C_{70}^{+\cdot}$ with O_2.

CHAPTER FIVE: *Target Capture of Multiatomic Gases by $C_{70}^{+\cdot}$ Radical Cations.*

5.1 Introduction.

This chapter focuses on studies made on reactive collisions between $C_{70}^{+\cdot}$ and a range of neutral hydrocarbons gases. Hydrocarbon gases investigated included methane, ethane, ethene, ethyne and propene. Reactive collisions between methane and $C_{60}^{+\cdot}$ have been studied previously [178, 182]. It was concluded that the full methane/$C_{60}^{+\cdot}$ adduct was formed as a transient species only and decomposed almost instantaneously into methane/$C_{60}^{+\cdot}$ fragment ions. Ethene, ethyne and propene have been found to form doubly charged, full adducts when collided with $C_{60}^{2+\cdot}$ in selected-ion flow tube studies; no reaction products were found for $C_{60}^{2+\cdot}$ and methane or ethane collisions [177].

5.2 Target Capture of Methane by $C_{70}^{+\cdot}$ Radical Cations.

Reactive collisions of $C_{70}^{+\cdot}$ with CH_4 and the isotopomers CD_4 and $^{13}CH_4$ were investigated. In all cases the gas pressure was sufficient to reduce the parent ion signal to 50% of its original intensity. In all of the experiments, the second electric sector (E2) was set to transmit ions with an energy deficit equal to the centre-of-mass collision energy. At a laboratory-frame collision energy of 300 eV, the only peak observed in the m/z range above m/z = 840 was at m/z = 854 (figure 5.1). This peak is assigned as $C_{70}CH_2^{+\cdot}$. On increasing the laboratory-frame collision energy to 500 eV $[M + 1]^+$, proposed to be $C_{70}H^+$ was produced. This species was observed from a laboratory-frame collision energy of 500 eV to 1250 eV inclusively. Three other adduct peaks were also observed at the laboratory-frame collision energy to 500 eV (table 5.1). These peaks, $[M + 12]^+$, $[M + 13]^+$ and $[M + 15]^+$ were proposed to be $C_{70}C^{+\cdot}$, $C_{70}CH^+$ and $C_{70}CH_3^+$ respectively. $[M + 14]^+$ was the most intense adduct peak in this spectrum. At E_{lab} = 750 eV, $[M + 14]^+$ remained the most intense adduct

(figure 5.2) and only $[M + 13]^+$ and $[M + 15]^+$ were seen in addition to this $C_{70}CH_2^{+\cdot}$ species. For E_{lab} = 1000 eV, $[M + 13]^+$ and $[M + 14]^+$ were approximately equal in intensity, but $[M + 13]^+$ became slightly more abundant than $[M + 14]^+$ at E_{lab} = 1250 eV and 1500 eV. Results for laboratory-frame collision energies of 1000 eV, 1250 eV and 1500 eV are displayed in figure 5.3, 5.4 and 5.5 respectively. Above a laboratory-frame collision energy of 1500 eV, (E_{lab} = 1750 eV or 2000 eV), $[M + 13]^+$ was the only adduct to result as a product of $CH_4/C_{70}^{+\cdot}$ collisions. It would appear that increasing the laboratory-frame collision energy caused a $C_{70}CH^+$ species to be produced preferentially to the larger $C_{70}CH_2^{+\cdot}$ species. A summary of adducts observed for the laboratory-frame collision energies investigated is given in table 5.1. There was no evidence of $[M + 16]^+$, corresponding to a full methane adduct, $C_{70}CH_4^{+\cdot}$. The adducts that were observed could have been the result of one of two possible reaction mechanisms. The fullerene could acquire a fragment of the methane molecule as the fullerene ion collides with the stationary neutral gas. Alternatively a collision between methane and the fullerene ion may produce a short lived $C_{70}CH_4^{+\cdot}$ species, which could decompose into fragment ions. Evidence for the existence of a transient $C_{60}CH_4^{+\cdot}$ complex has been previously reported by Cooper *et al.* [178].

To elucidate the reaction mechanism CD_4 and $^{13}CH_4$ were employed as collision gases. For collisions between $^{13}CH_4$ and $C_{70}^{+\cdot}$ at a laboratory-frame collision energy of 300 eV, the only adduct observed was $[M + 15]^+$. Assigned as $C_{70}{}^{13}CH_2^{+\cdot}$, this result was consistent with that obtained with CH_4. Increasing the laboratory-frame collision energy to 500 eV introduced $[M + 13]^+$, $[M + 14]^+$ and $[M + 16]^+$ peaks. Identified as $C_{70}{}^{13}C^+$, $C_{70}{}^{13}CH^+$ and $C_{70}{}^{13}CH_3^+$, these peaks were also observed at E_{lab} = 750 eV and E_{lab} = 1000 eV (figures 5.7 and 5.8). At a laboratory-frame collision energy of 1250 eV, $[M + 14]^+$ and $[M + 15]^+$ ($C_{70}{}^{13}CH^+$ and $C_{70}{}^{13}CH_2^{+\cdot}$) were observed; at E_{lab} = 1500 eV and 1750 eV $[M + 14]^+$ ($C_{70}{}^{13}CH^+$) alone was produced as an adduct. Above E_{lab} = 1750 eV, no adducts were observed (table 5.2). These results mimic the observations with CH_4. $[M + 1]^+$ from collisions between $^{13}CH_4$ and $C_{70}^{+\cdot}$ could be assigned as either $C_{70}H^+$ or

$C_{69}{}^{13}C^+$. $[M + 1]^+$ from CH_4 collisions could be assigned only as $C_{70}H^+$. The assignment, $C_{69}{}^{13}C^+$, represents the substitution of one atom from the fullerene cage by the ^{13}C atom from methane. High mass-resolution would be required to differentiate between $C_{70}H^+$ (m/z = 841.0078) and $C_{69}{}^{13}C^+$ (m/z = 841.0034). A peak at m/z =842, suggestive of $C_{69}{}^{13}CH^+$, was present at E_{lab} = 1000 eV (figure 5.2), so $C_{69}{}^{13}C^+$ is certainly a possibility. Absence of $[M + 2]^+$ with $C_{70}^{+\cdot}/CH_4$ collisions suggests that $C_{70}H_2^{+\cdot}$ is not a collision product. Both $C_{70}H^+$ and $C_{69}{}^{13}C^+$ may contribute to $[M + 1]^+$ with $^{13}CH_4$. The intensity change in $[M + 1]^+$ relative to $M^{+\cdot}$ as the collision gas was changed from CH_4 to $^{13}CH_4$ was not substantial enough to further the situation. No evidence for the full $C_{70}{}^{13}CH_4^{+\cdot}$ adduct was obtained under any of the collision conditions examined. Similar observations have been recorded previously [178, 182].

Deuterated methane gave collision products with $C_{70}^{+\cdot}$ analogous to those obtained with CH_4 and $^{13}CH_4$. A summary of these results is given in table 5.3. A peak observed at m/z = 842, for laboratory-frame collision energies of 750 eV to 1500 eV inclusively, was assigned as $C_{70}D^+$. Figures 5.8, 5.9 and 5.10 show spectra recorded at laboratory-frame collision energies of 500 eV, 1000 eV and 1250 eV respectively. The $[M + 16]^+$ adduct peak, assigned as $C_{70}CD_2^{+\cdot}$ was the most intense at laboratory-frame collision energies of 500 eV and 1000 eV. At a laboratory-frame collision energy of 300 eV, this was the only adduct peak observed. For laboratory-frame collision energies of 1250 eV and above, this peak was no longer the most intense in the spectrum (figure 5.10). $[M + 14]^+$ assigned as $C_{70}CD^+$ gave a stronger signal at these energies. At E_{lab} = 750 eV and E_{lab} = 1000 eV, $[M + 12]^+$ and $[M + 18]^+$ assigned as $C_{70}C^+$ and $C_{70}CD_3^+$ respectively were observed, in addition to $[M + 14]^+$ and $[M + 16]^+$ (figure 5.9). At a laboratory-frame collision energy of 1500 eV, only the $[M + 14]^+$ peak was observed. These results mimic those obtained with the other methane collision gases. At higher collision energies, there was no evidence of any adducts. As with the other two collision gases, CD_4 showed no indication of

forming the full $C_{70}CD_4^{+\cdot}$ adduct ion. These results observed here are analogous to those observed by Cooper *et al.* [178, 182].

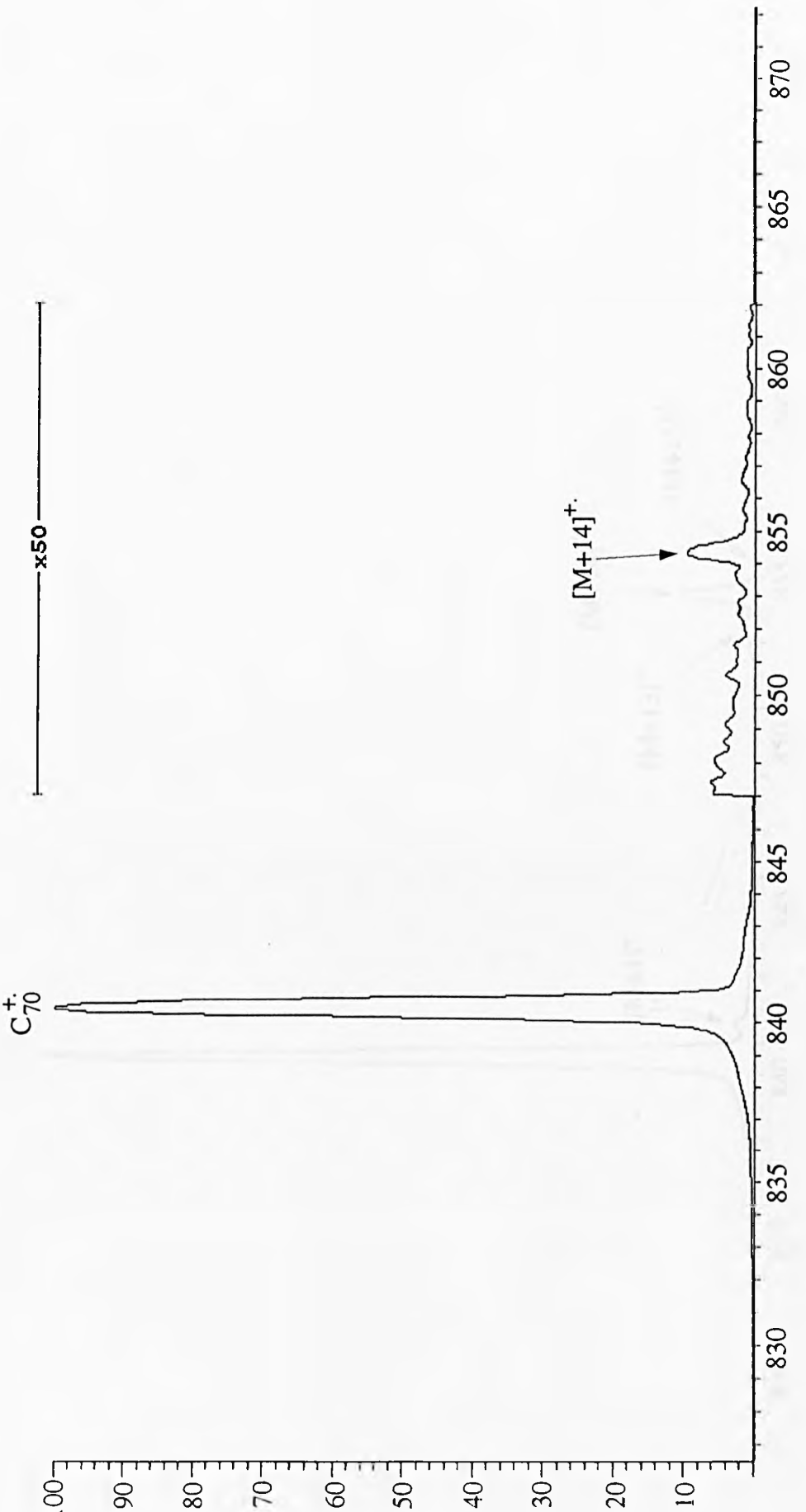

Figure 5.1: Magnet scan of $C_{70}^{+\cdot}$ and methane at E_{lab} = 300 eV.

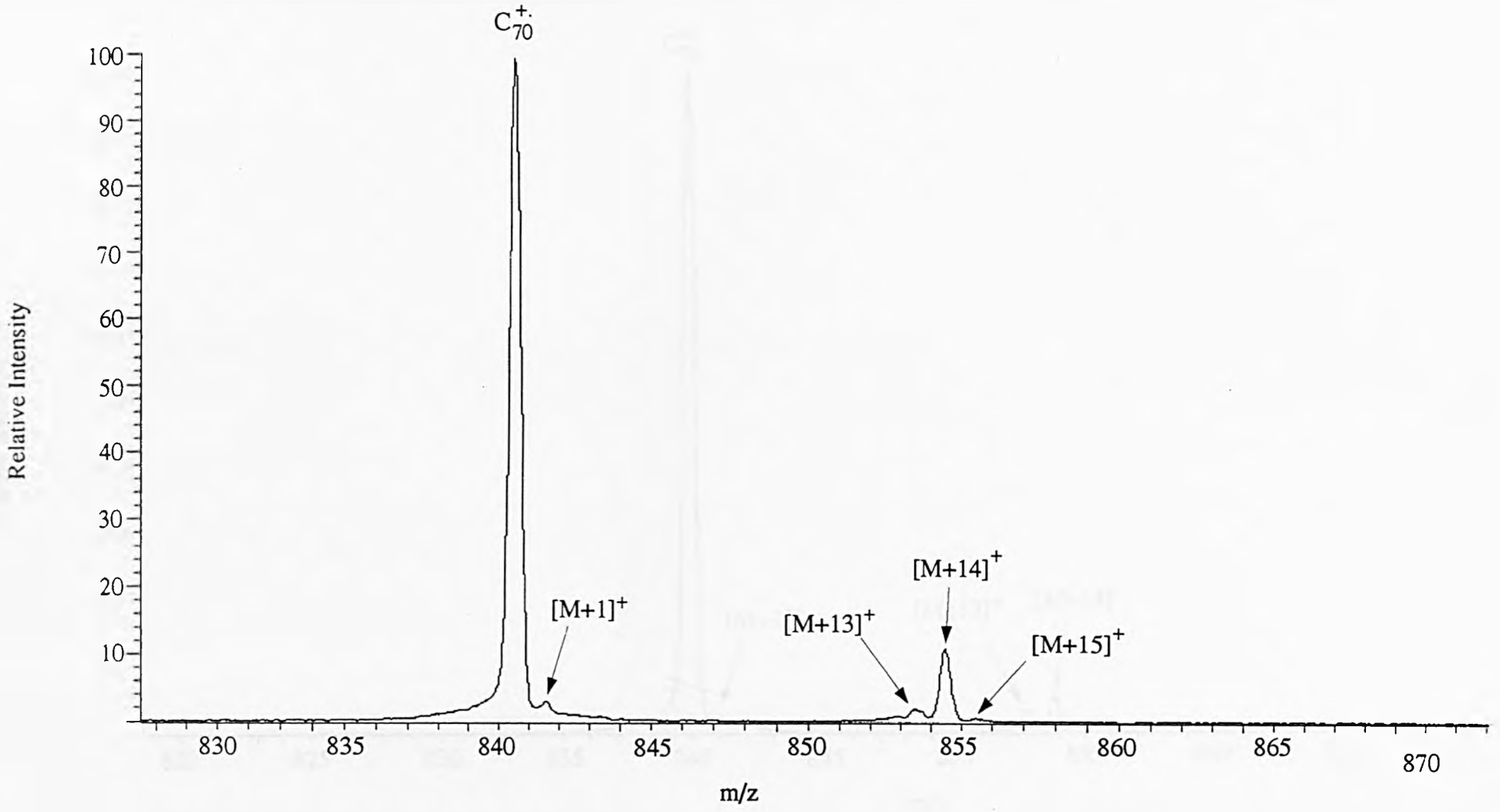

Figure 5.2: Magnet scan of $C_{70}^{+\cdot}$ and methane at E_{lab} = 750 eV.

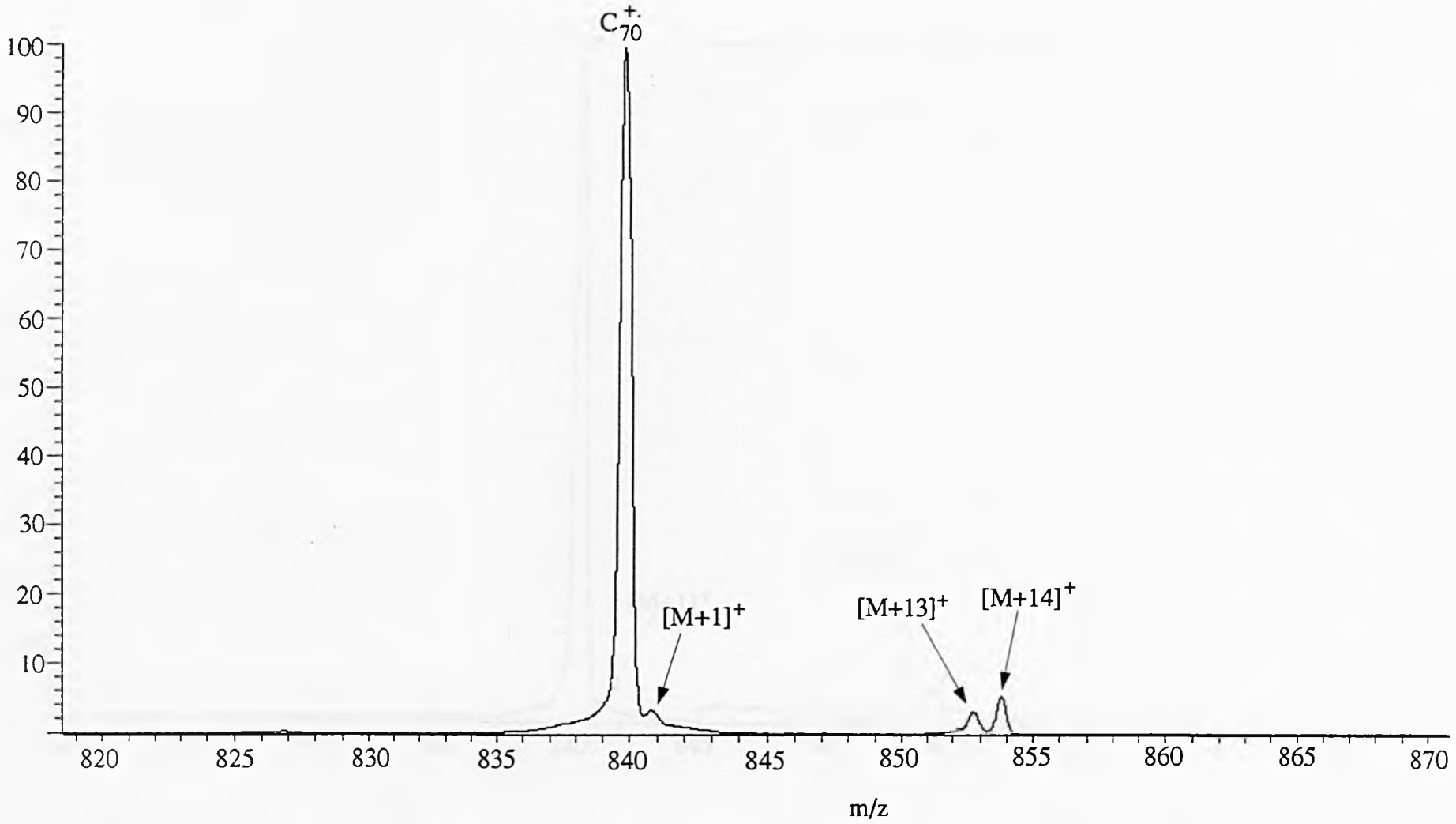

Figure 5.3: Magnet scan of $C_{70}^{+\cdot}$ and methane at E_{lab} = 1000 eV.

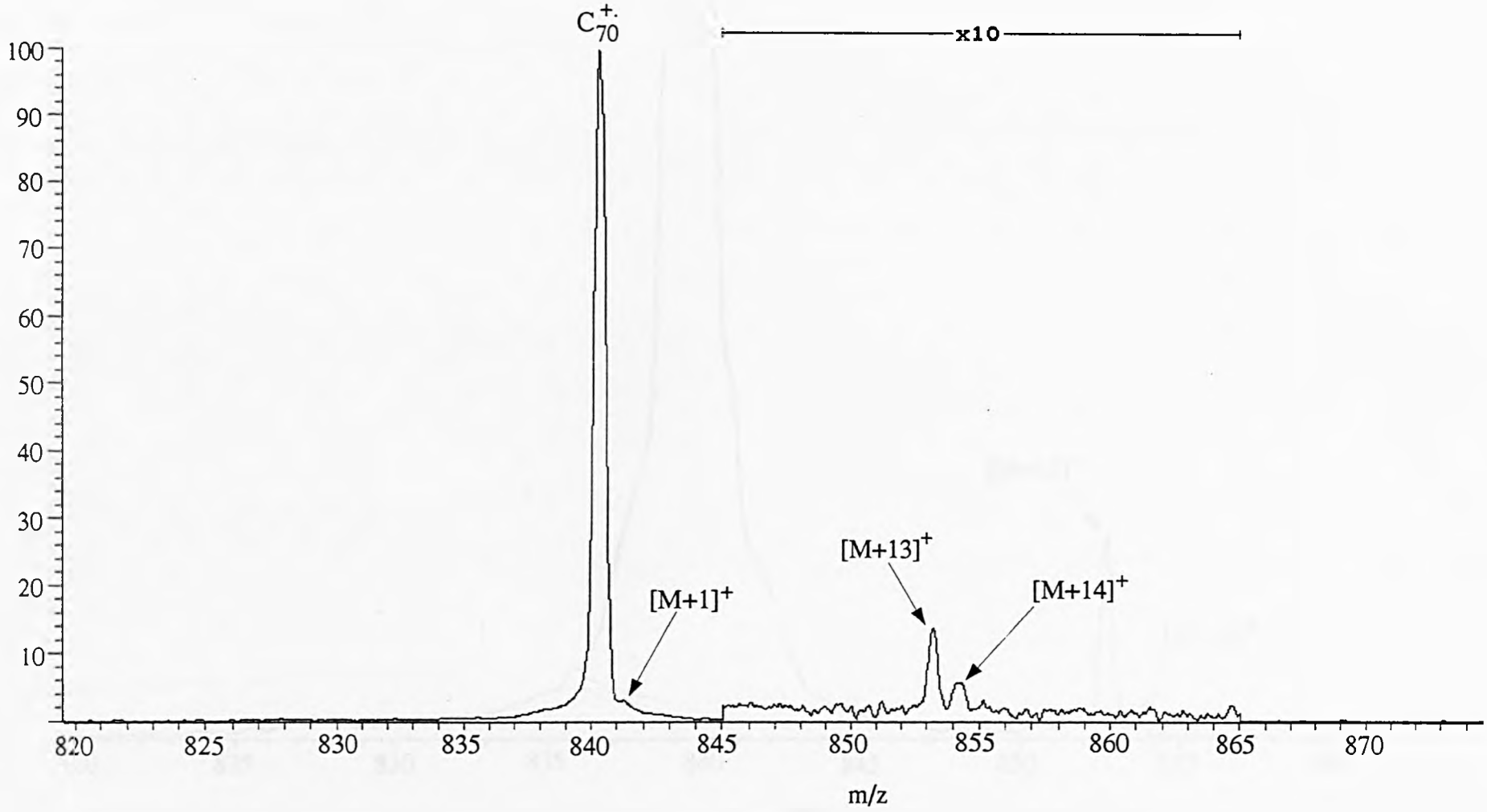

Figure 5.4: Magnet scan of $C_{70}^{+\cdot}$ and methane at E_{lab} = 1250 eV.

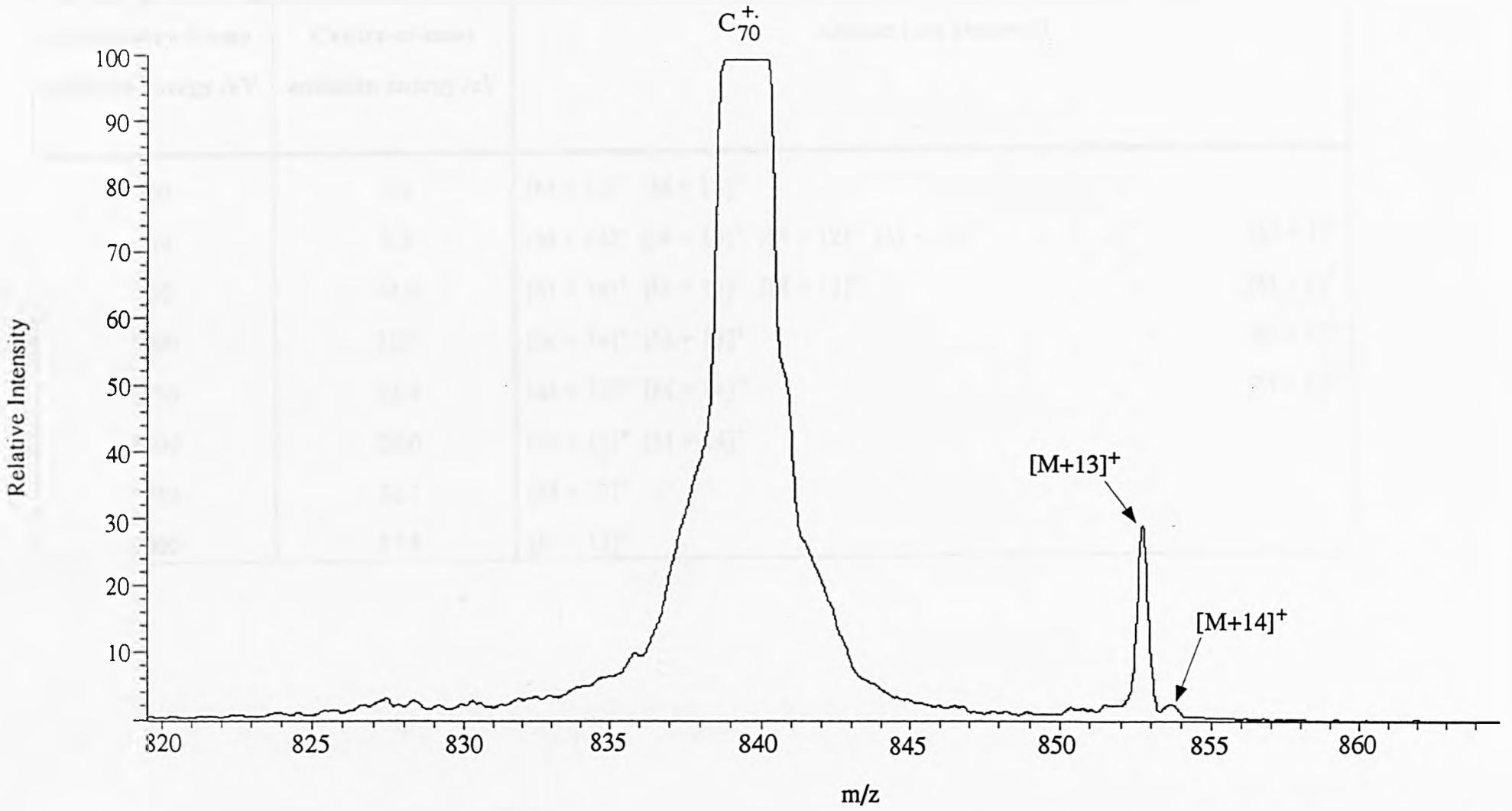

Figure 5.5: Magnet scan of $C_{70}^{+\cdot}$ and methane at E_{lab} = 1500 eV.

Laboratory-frame collision energy /eV	Centre-of-mass collision energy /eV	Adduct ions observed
300	5.6	$[M + 14]^+$ $[M + 13]^+$
500	9.3	$[M + 14]^+$ $[M + 13]^+$ $[M + 12]^+$ $[M + 15]^+$ $[M + 1]^+$
750	14.0	$[M + 14]^+$ $[M + 13]^+$ $[M + 15]^+$ $[M + 1]^+$
1000	18.7	$[M + 14]^+$ $[M + 13]^+$ $[M + 1]^+$
1250	23.4	$[M + 13]^+$ $[M + 14]^+$ $[M + 1]^+$
1500	28.0	$[M + 13]^+$ $[M + 14]^+$
1750	32.7	$[M + 13]^+$
2000	37.4	$[M + 13]^+$

Table 5.1: Laboratory-frame and centre-of-mass frame collision energies at which $C_{70}^{+\cdot}$/methane adducts were observed.

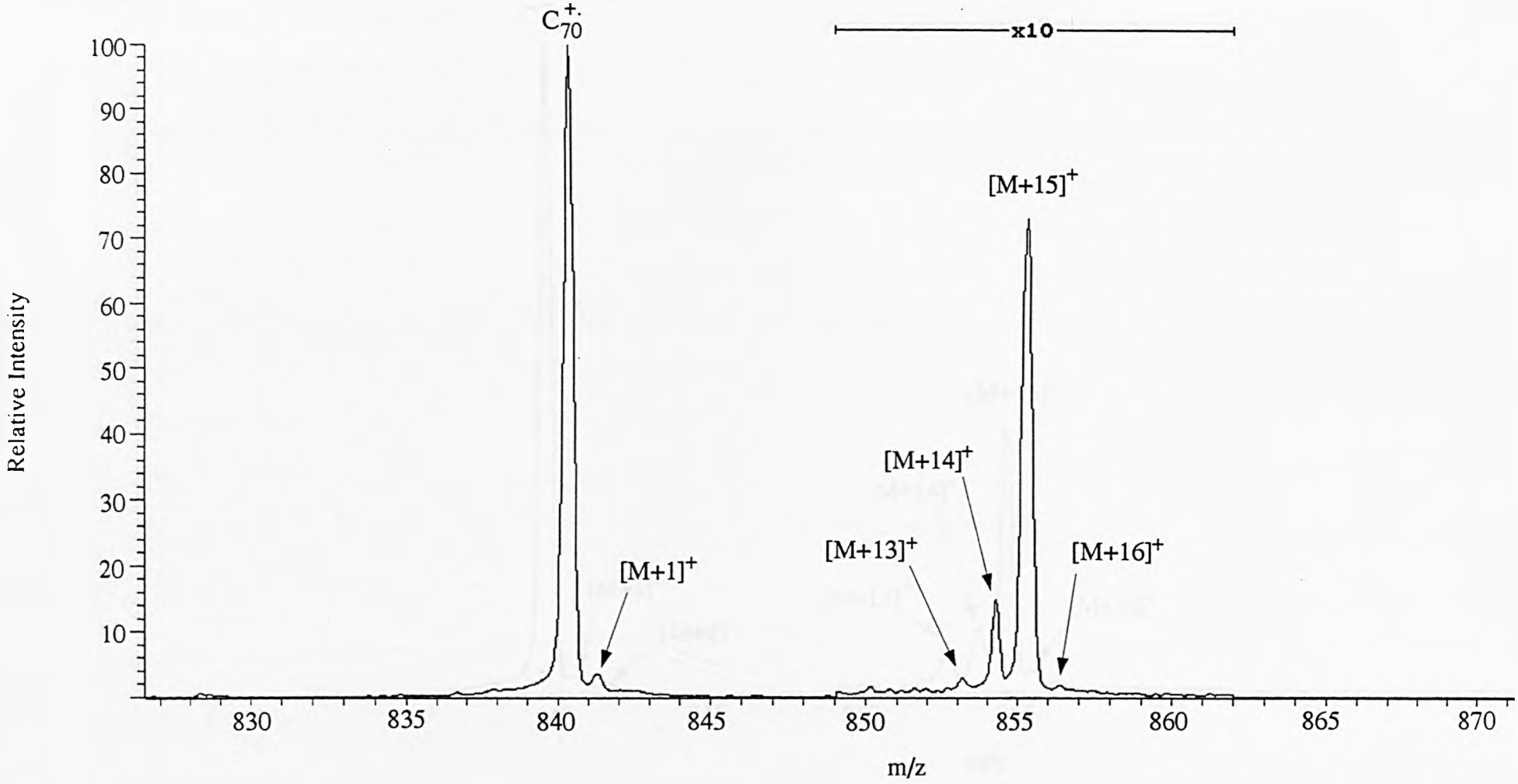

Figure 5.6: Magnet scan of $C_{70}^{+\cdot}$ and ^{13} carbon methane at E_{lab} = 750 eV.

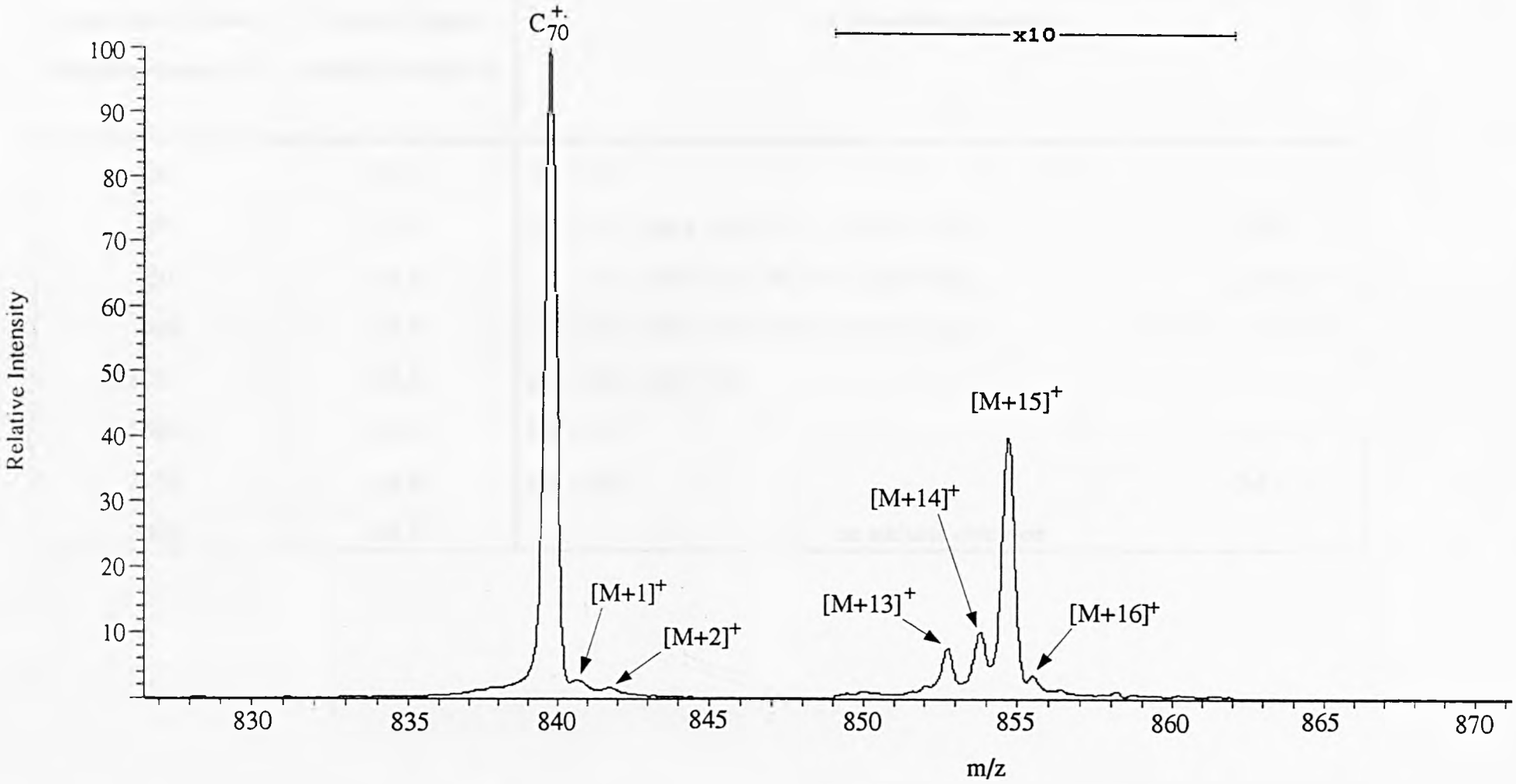

Figure 5.7: Magnet scan of $C_{70}^{+\cdot}$ and ^{13} carbon methane at E_{lab} = 1000 eV.

Laboratory-frame collision energy /eV	Centre-of-mass collision energy /eV	Adduct ions observed
300	6.0	$[M + 15]^+$
500	9.9	$[M + 15]^+$ $[M + 14]^+$ $[M + 13]^+$ $[M + 16]^+$ $[M + 1]^+$
750	14.9	$[M + 15]^+$ $[M + 14]^+$ $[M + 13]^+$ $[M + 16]^+$ $[M + 1]^+$
1000	19.9	$[M + 14]^+$ $[M + 15]^+$ $[M + 13]^+$ $[M + 16]^+$ $[M + 1]^+$ $[M + 2]^+$
1250	24.8	$[M + 14]^+$ $[M + 15]^+$ $[M + 1]^+$
1500	29.8	$[M + 14]^+$ $[M + 1]^+$
1750	34.8	$[M + 14]^+$ $[M + 1]^+$
2000	39.7	no adducts observed

Table 5.2: Laboratory-frame and centre-of-mass frame collision energies at which $C_{70}^{+\cdot}$/^{13}carbon methane adducts were observed.

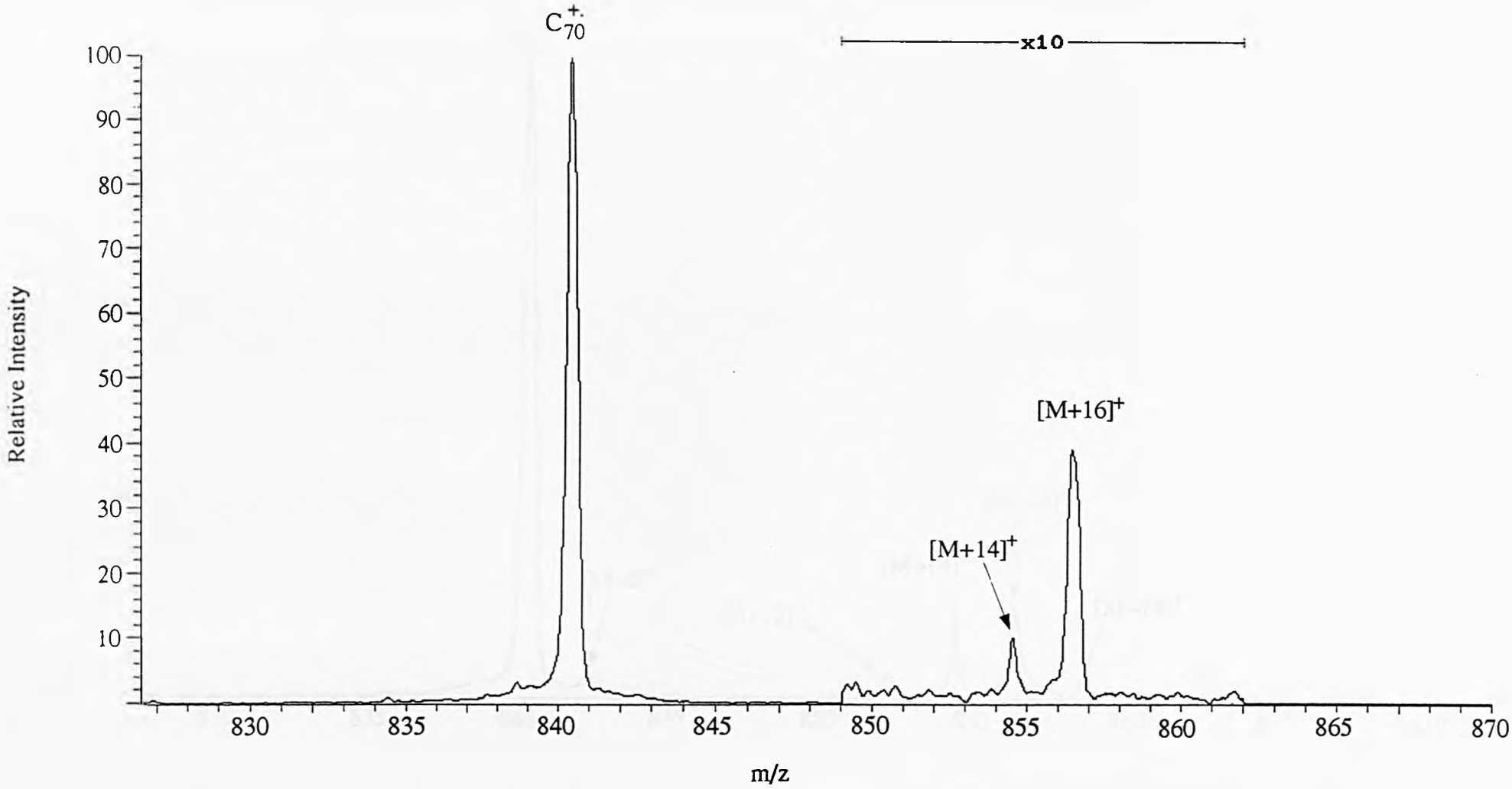

Figure 5.8: Magnet scan of $C_{70}^{+\cdot}$ and deuterated methane at E_{lab} = 500 eV.

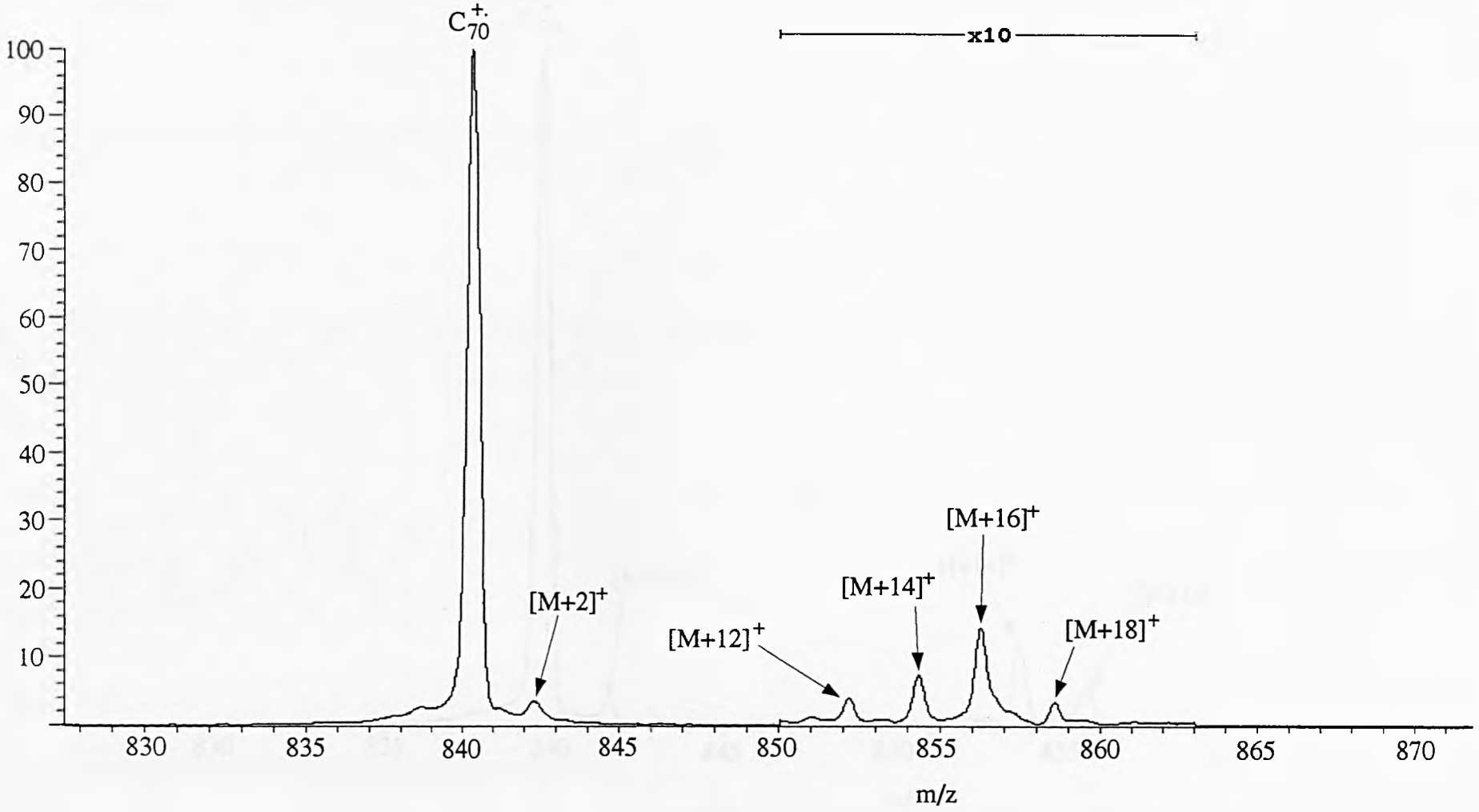

Figure 5.9: Magnet scan of $C_{70}^{+\cdot}$ and deuterated methane at E_{lab} = 1000 eV.

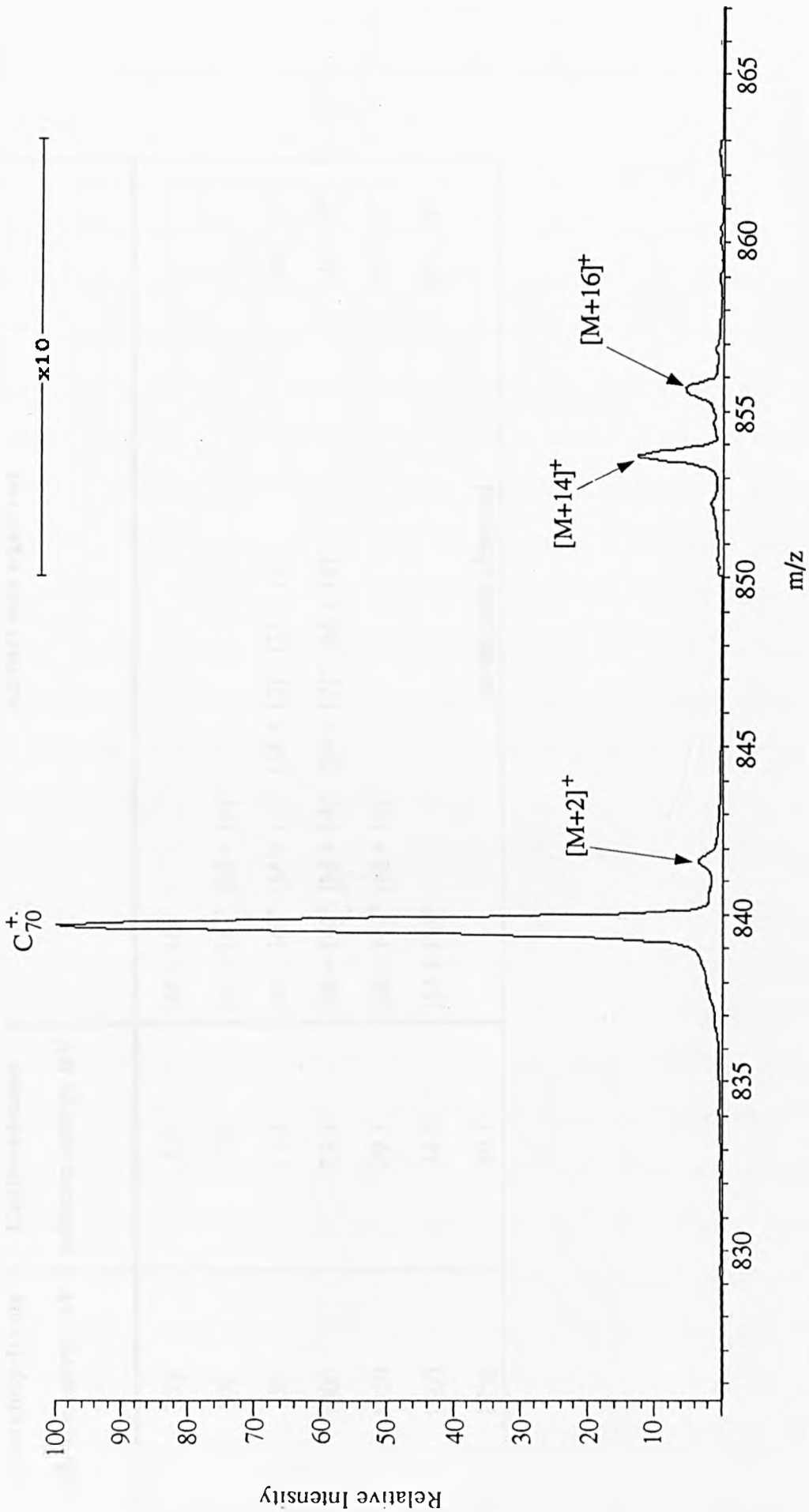

Figure 5.10: Magnet scan of $C_{70}^{+\cdot}$ and deuterated methane at E_{lab} = 1250 eV.

Laboratory-frame collision energy /eV	Centre-of-mass collision energy /eV	Adduct ions observed
300	7.0	$[M + 16]^+$
500	11.6	$[M + 16]^+$ $[M + 14]^+$
750	17.4	$[M + 16]^+$ $[M + 14]^+$ $[M + 12]^+$ $[M + 18]^+$ $[M + 2]^+$
1000	23.3	$[M + 16]^+$ $[M + 14]^+$ $[M + 12]^+$ $[M + 18]^+$ $[M + 2]^+$
1250	29.1	$[M + 14]^+$ $[M + 16]^+$ $[M + 2]^+$
1500	34.9	$[M + 14]^+$ $[M + 2]^+$
1750	40.7	no adducts observed

Table 5.3: Laboratory-frame and centre-of-mass frame collision energies at which $C_{70}^{+\cdot}$/deuterated methane adducts were observed.

5.2.1 Investigation of Collisions between Tetrafluoromethane and $C_{70}^{+\cdot}$ Radical Cations.

Tetrafluoromethane is considerably larger than methane in size, as well as mass. C-F bonds (CF_3-F = 125±4 kcal mol^{-1}) of tetrafluoromethane are also much stronger than C-H (CH_3-H = 30 kcal mol^{-1}) bonds of methane, thus making CF_4 a relatively inert species. Tetrafluoromethane is close in mass to the inert gas krypton, which is known from this work to form full endohedral adducts from reactive collisions with $C_{70}^{+\cdot}$. Initial experiments were carried out at laboratory-frame collision energies of 100 eV, 500 eV, 1000 eV, 1500 eV and 2000 eV. E2 was set to transmit ions with a range of calculated energy deficits. The first E2 energy deficit investigated was equivalent to the centre-of-mass collision energy. The E2 energy deficit was then increased, in stages, on the basis that the full $C_{70}CF_4^{+\cdot}$ adduct formed and decomposed with the loss one, two, three and finally four fluorine atoms. The β-slit was opened to its maximum width. Results are summarised in table 5.4(a). Collisions between tetrafluromethane and $C_{70}^{+\cdot}$ gave no evidence of any peaks in the m/z range above m/z = 840. Spectra from $CF_4/C_{70}^{+\cdot}$ collisions at a laboratory-frame collision energy of 500 eV are displayed in figures 5.11 and 5.12. Figure 5.11 represents the result obtained when E2 was set to transmit ions with an energy deficit equal to the centre-of-mass collision energy. No adduct ions were observed. As the E2 setting was lowered to transmit ions with larger energy deficits, a broad signal approximately 40 m/z wide was observed beginning about 50 m/z higher than the parent ion. The spectrum in figure 5.12 was acquired with E2 set for an energy deficit calculated on the basis that a transient $C_{70}CF_4^{+\cdot}$ complex decompose to lose all four fluorine atoms. (*i.e.* E_{def} = 84 eV). No sharp peaks were observed for any combination of collision energy and E2 setting tested. The broad peak could be due to the metastable decay of $C_{70}CF_4^{+\cdot}$ to either $C_{70}CF_3^{+\cdot}$ or $C_{70}CF_2^{+\cdot}$, or the decomposition of $C_{70}CF_3^{+\cdot}$ to $C_{70}CF_2^{+\cdot}$, as calculated using equation (21). Any

measurements made on this peak must be treated with caution as the large width of the peak (40 Da) introduces a degree of uncertainty.

In order to assess the possibility that the broad signal observed was due in some way to poor focusing, the β-slit was reduced in width. Laboratory-frame collision energies of 300 eV, 500 eV, 475 eV, 750 eV, 1000 eV and 2000 eV were employed; results are given in table 5.4(b). A laboratory-frame collision energy of 475 eV represents a centre-of-mass collision energy of 45 eV, which is the centre-of-mass collision energy found to be required to insert krypton (average m/z = 84) into $C_{70}^{+\cdot}$. At settings of E2 approximate for energy deficits equivalent to the centre-of-mass collision energy, no adducts were observed (see example in figure 5.13).

Sharp, well defined peaks representing fragment ions formed by consecutive C_2 losses from the fullerene cage were observed at all laboratory-frame collision energies and E2 settings investigated. A greater degree of fragmentation was observed when the β-slit was fully open. These fragment peaks were quite intense for tetrafluoromethane, compared to methane. It is concluded that $C_{70}^{+\cdot}$ underwent collision-induced decomposition following collisions with tetrafluoromethane and that target capture of this gas was not achieved.

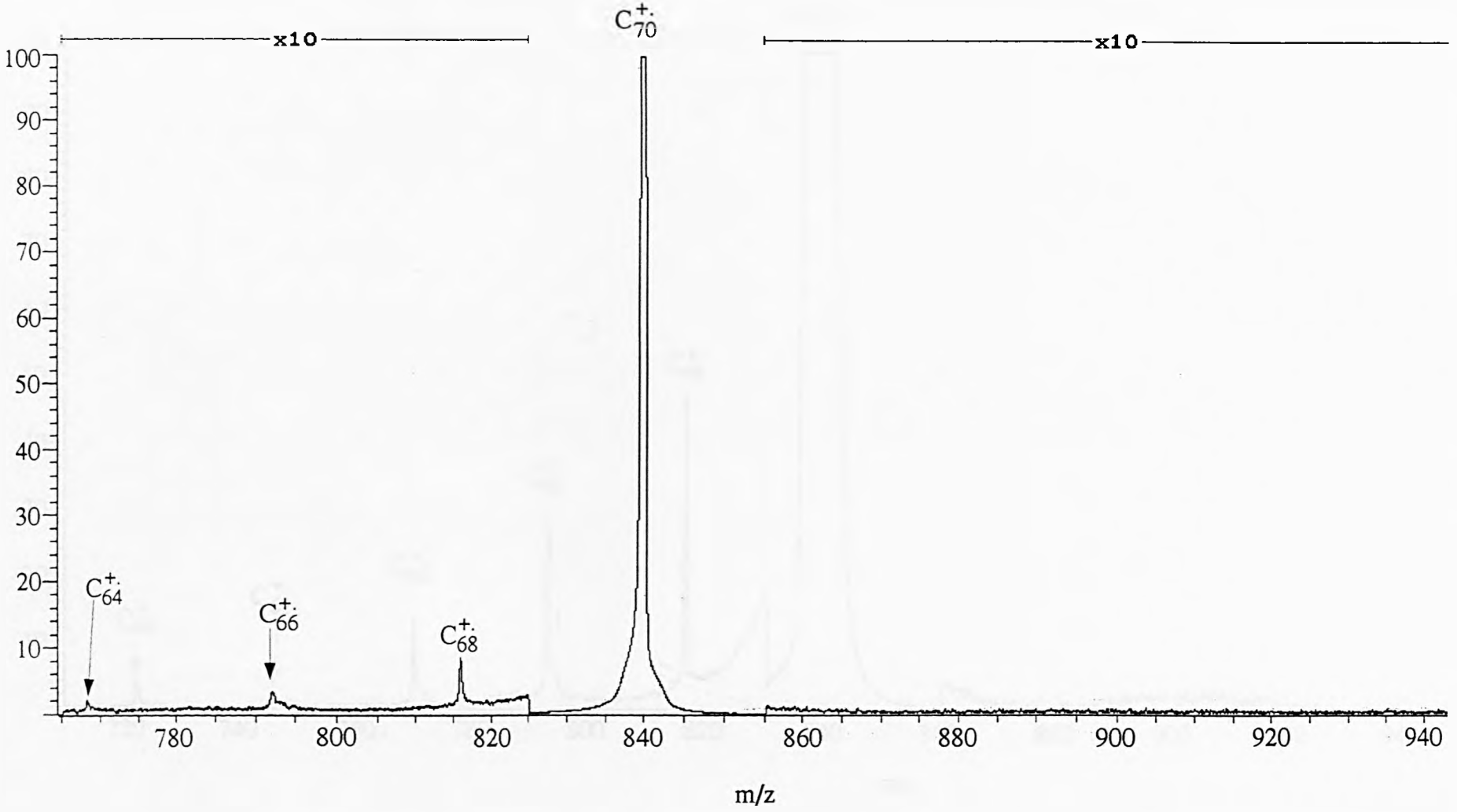

Figure 5.11: Magnet scan of $C_{70}^{+\cdot}$ and tetrafluoromethane at E_{lab} = 500 eV, β - slit fully opened. E_{def} = 47 eV.

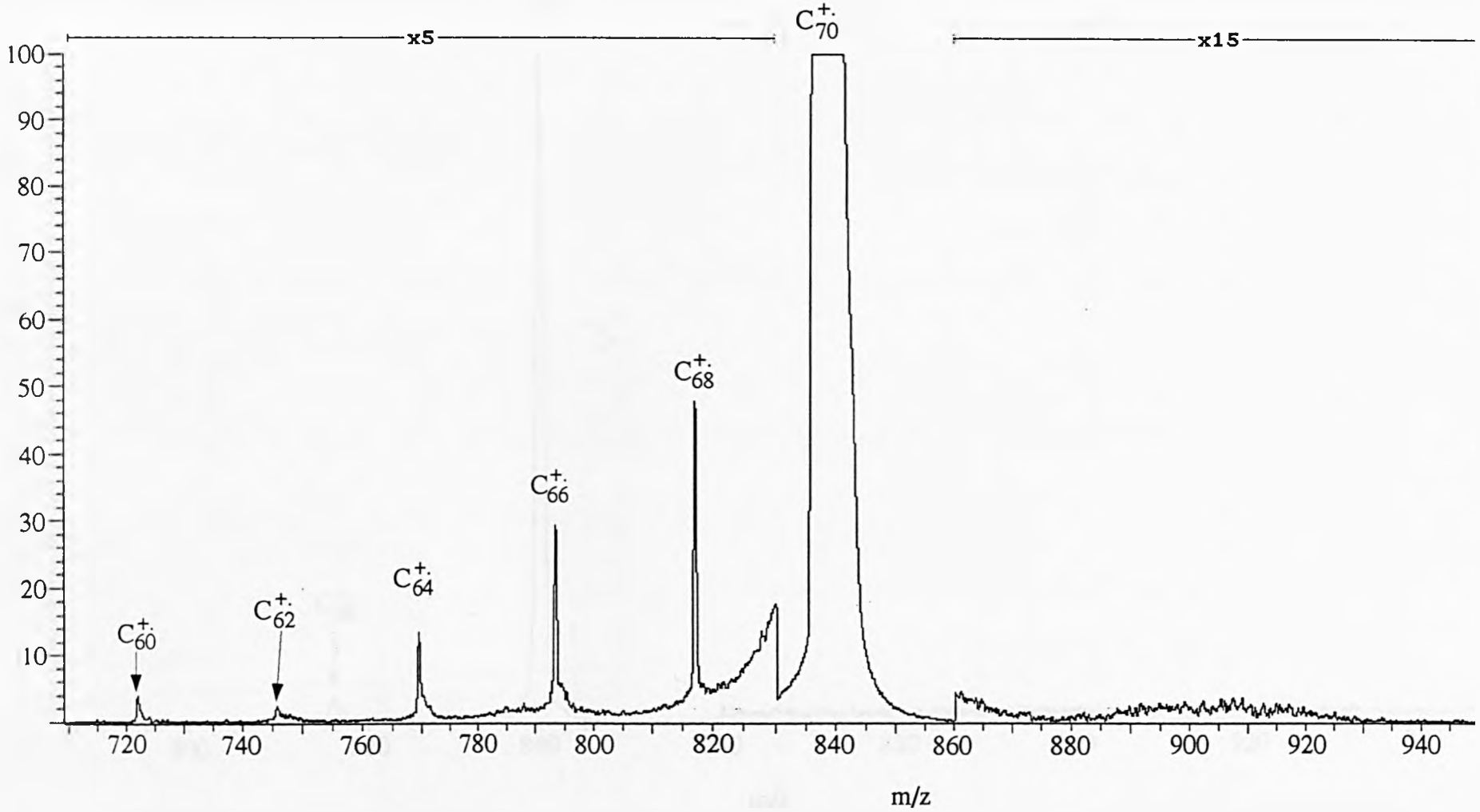

Figure 5.12: Magnet scan of $C_{70}^{+\cdot}$ and tetrafluoromethane at E_{lab} = 500 eV, β - slit fully opened. E_{def} = 47 eV.

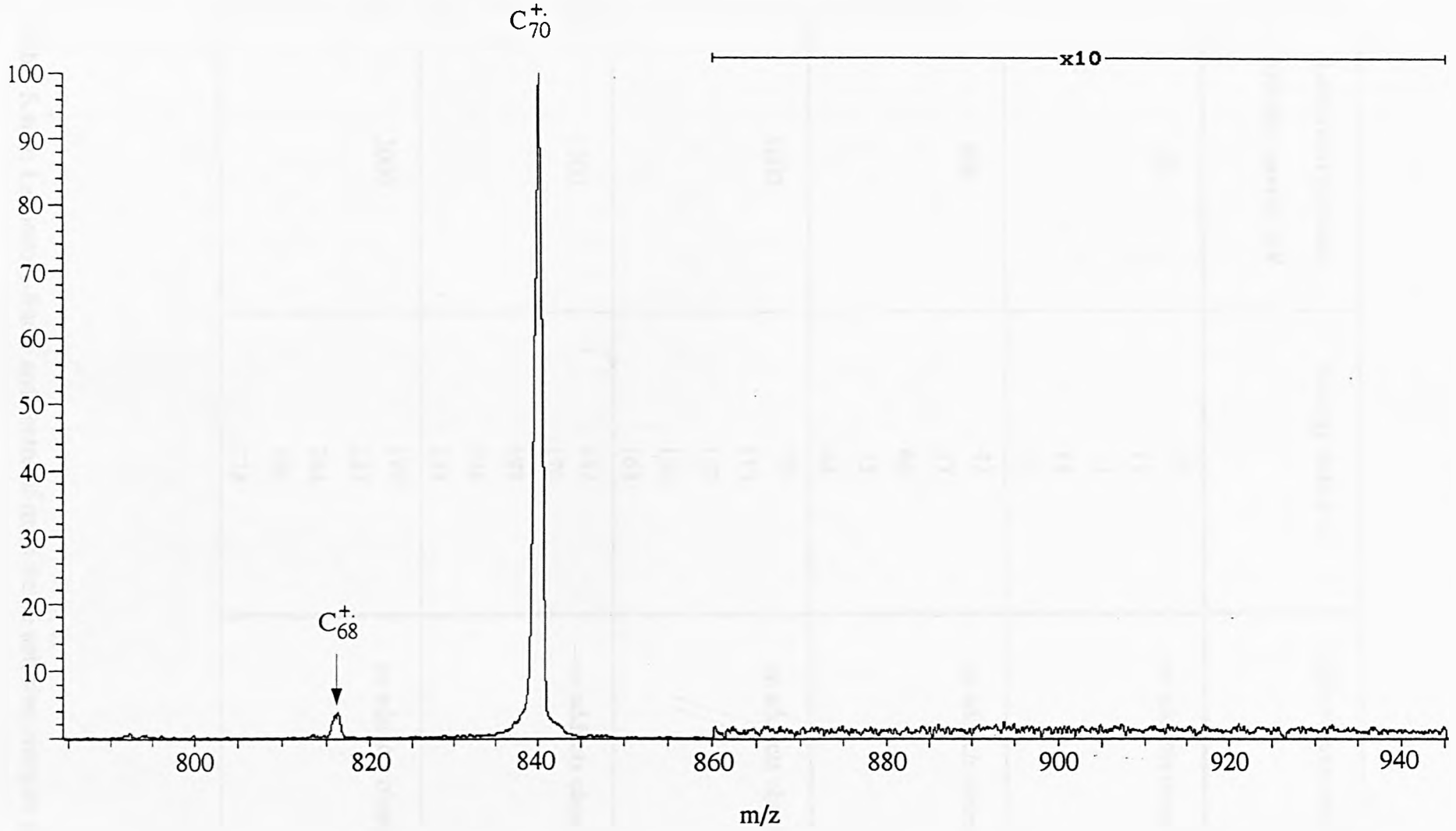

Figure 5.13: Magnet scan of $C_{70}^{+\cdot}$ and tetrafluoromethane at E_{lab} = 500 eV, narrowβ - slit. E_{def} = 47 eV.

Laboratory-frame collision energy /eV	**Energy deficit /eV**	**Adduct ions observed**
100	10 11 13 15 17	no adducts observed
500	47 57 66 75 84	no adducts observed
1000	95 113 132 150 168	no adducts observed
1500	142 170 198 226 233	no adducts observed
2000	190 227 264 301 338	no adducts observed

Table 5.4(a): Laboratory-frame and centre-of-mass frame collision energies at which measurements were made. β-slit fully open.

Laboratory-frame collision energy /eV	Centre-of-mass collision energy /eV	Adduct ions observed
300	29	no adducts observed
500	47	no adducts observed
475	45	no adducts observed
750	71	no adducts observed
1000	95	no adducts observed
2000	190	no adducts observed

Table 5.4(b): Laboratory-frame and centre-of-mass frame collision energies at which measurements were made. Narrow β-slit.

5.3 Investigation of Collisions between Ethane and $C_{70}^{+\cdot}$ Radical Cations.

Methane has been found to form fragmented adduct ions with $C_{70}^{+\cdot}$ and $C_{60}^{+\cdot}$ [178], but the full adduct has not been observed. The question here is whether larger hydrocarbons produce the same fragmented species as methane? Ethane was introduced into the collision cell so as to reduce the parent ion signal intensity by 50%. The E2 setting was for an energy deficit equal to the centre-of-mass collision energy. At a laboratory-frame collision energy of 300 eV, one adduct was observed, $[M + 16]^+$ (figure 5.14). A hydrocarbon adduct peak at $[M + 16]^+$ was a novel observation. The mass would be consistent with CH_4 attached to the fullerene cage, however in the light of the experiments with methane this was thought improbable. As the laboratory-frame collision energy with ethane was increased, more adducts were observed (see table 5.5). At E_{lab} = 500 eV , in addition to $[M + 16]^+$, $[M + 14]^+$ was seen. $[M + 16]^+$ was the more abundant of these two adducts. It was evident from these observations that the carbon-carbon bond had been ruptured. Two larger adducts were also observed at this energy, $[M + 28]^+$ and $[M + 29]^+$. $[M + 28]^+$ was by far the more intense of these two peaks. At E_{lab} = 750 eV $[M + 29]^+$ was no longer observed (figures 5.15). At E_{lab} = 1000 eV $[M + 13]^+$ was present (figure 5.16). $[M + 16]^+$ remained intense compared to $[M + 14]^+$ and $[M + 13]^+$ at these energies. At E_{lab} = 750 eV, $[M + 1]^+$ $[M + 2]^+$ satellite peaks were observed. Evidence for the $[M + 2]^+$ peak, assigned as $C_{70}H_2^{+\cdot}$, remained at laboratory-frame collision energies of 1000 eV and 1250 eV (figures 5.16 and 5.17).

$[M + 13]^+$ and $[M + 14]^+$ were assigned as $C_{70}CH^+$ and $C_{70}CH_2^{+\cdot}$ respectively, in accordance with assignments made for methane collision experiments. Of the lower-mass cluster of adduct peaks produced with ethane, $[M + 16]^+$ was the most intense. As $[M + 14]^+$ was quite abundant in both ethane and methane experiments, it is tempting to propose that $[M + 16]^+$ represents addition of CH_2 and H_2 species to the fullerene cage producing a $C_{70}H_2CH_2^{+\cdot}$ species. Evidence for $[M + 2]^+$, *i.e.* $C_{70}H_2^{+\cdot}$, was observed at laboratory-frame collision energies of 750 eV and

1250 eV. There was no evidence of a $[M + 15]^+$ peak following collisions with ethane, so addition of $CH_3\cdot$ and $H\cdot$ species to the fullerene cage producing a $C_{70}HCH_3^{+\cdot}$ species was considered to be less likely. Two explanations were equally possible for the assignment of $[M + 28]^+$. This peak could correspond to the addition of C_2H_4 or to the addition of two CH_2 fragments. The same uncertainty applies to $[M + 29]^+$ which could be either $C_{70}C_2H_5^+$ or $C_{70}H_2CH_3^+$ species. In conclusion, $[M + 14]^+$ and $[M + 16]^+$ were produced in greater abundance at lower laboratory-frame collision energies and $[M + 28]^+$ at higher laboratory-frame collision energies.

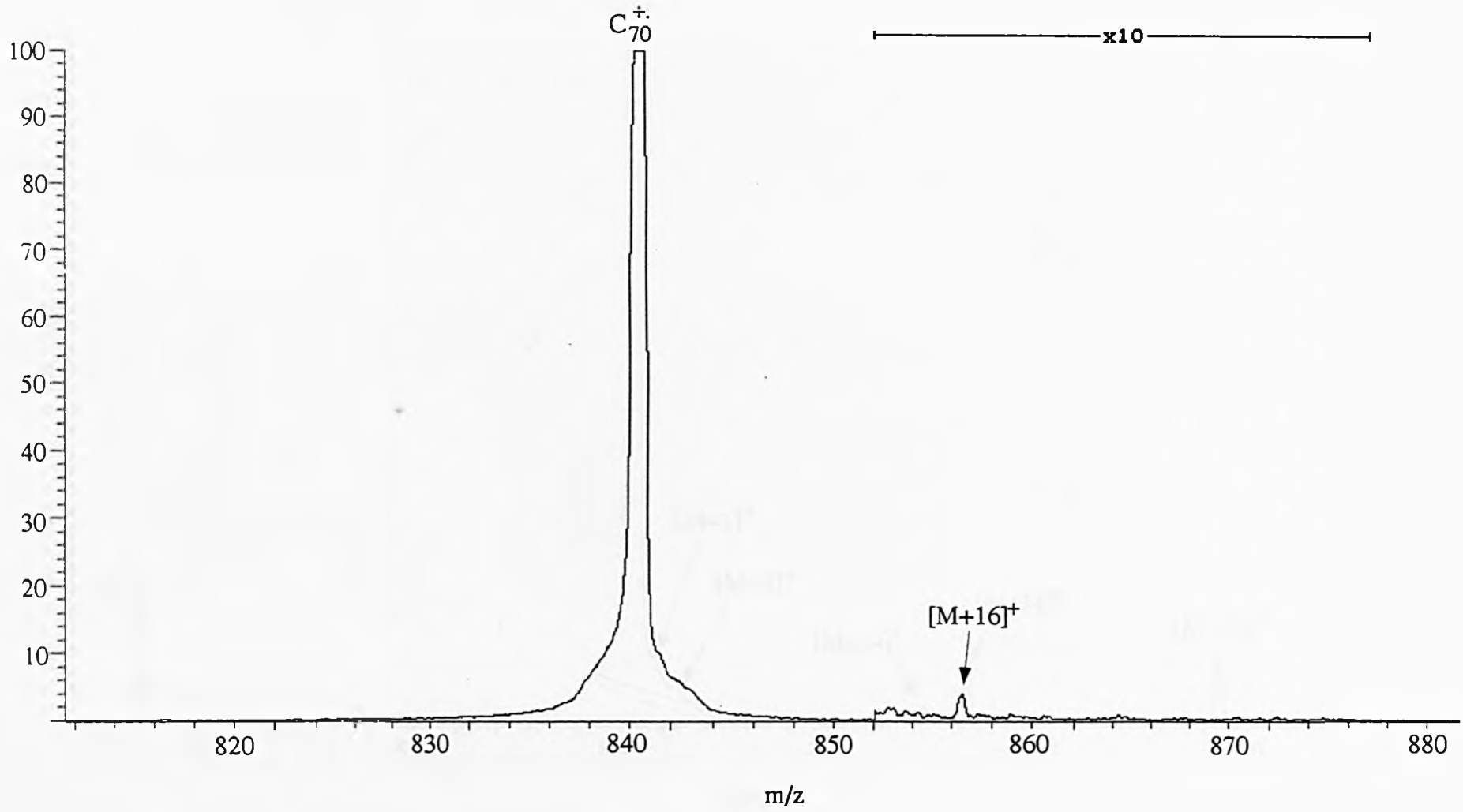

Figure 5.14: Magnet scan of $C_{70}^{+\cdot}$ and ethane at E_{lab} = 300 eV.

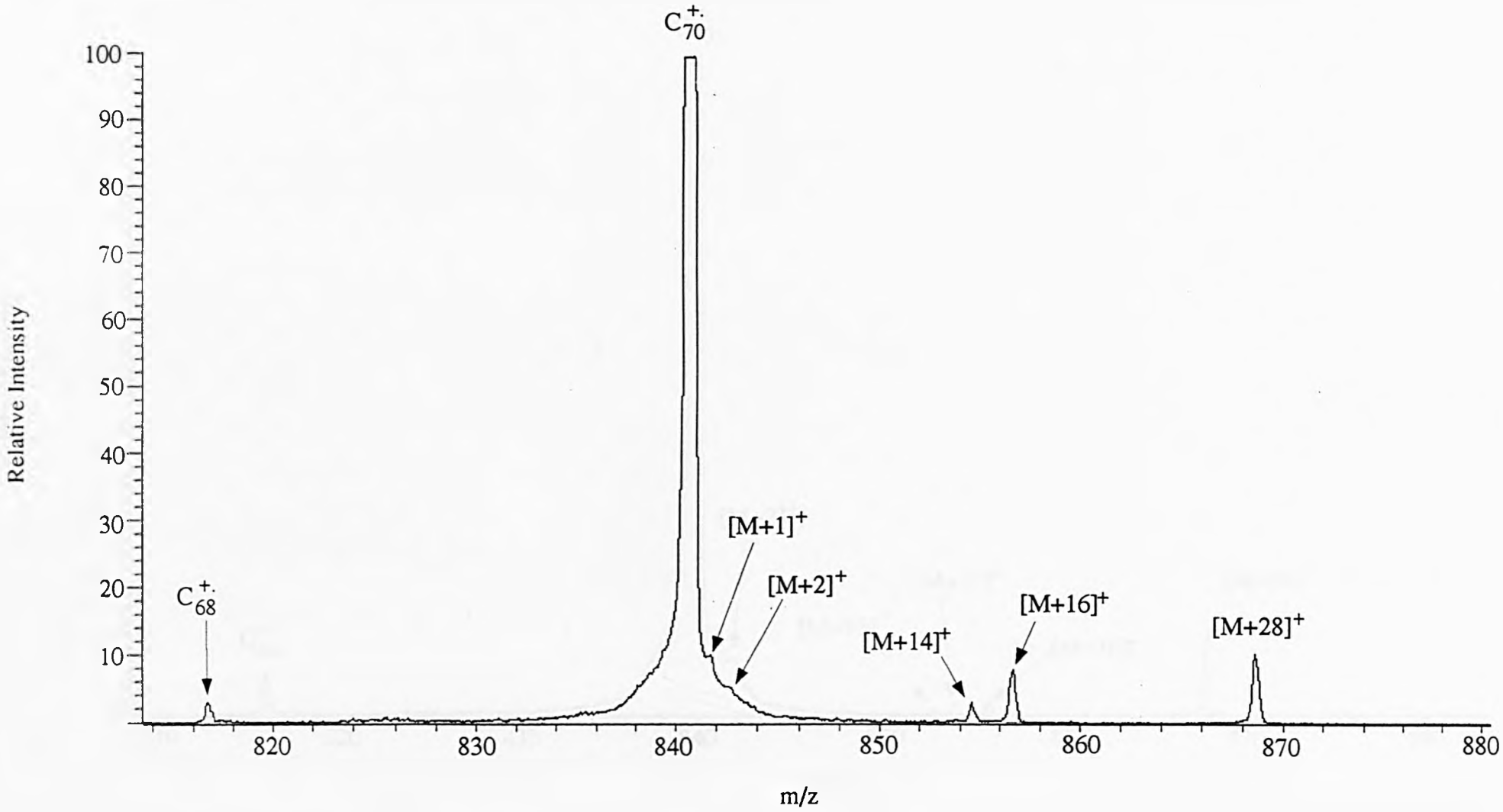

Figure 5.15: Magnet scan of $C_{70}^{+\cdot}$ and ethane at E_{lab} = 750 eV.

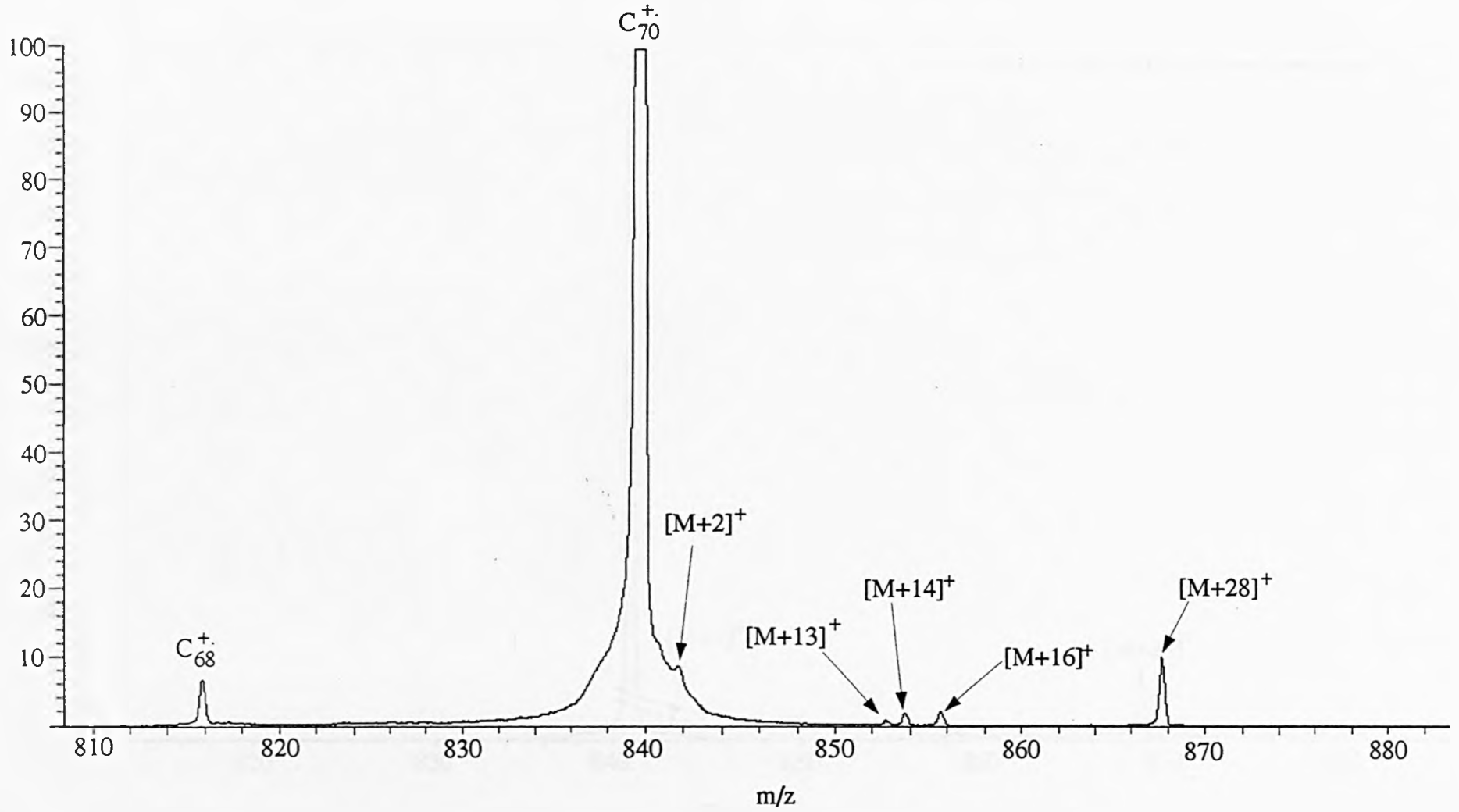

Figure 5.16: Magnet scan of $C_{70}^{+\cdot}$ and ethane at E_{lab} = 1000 eV.

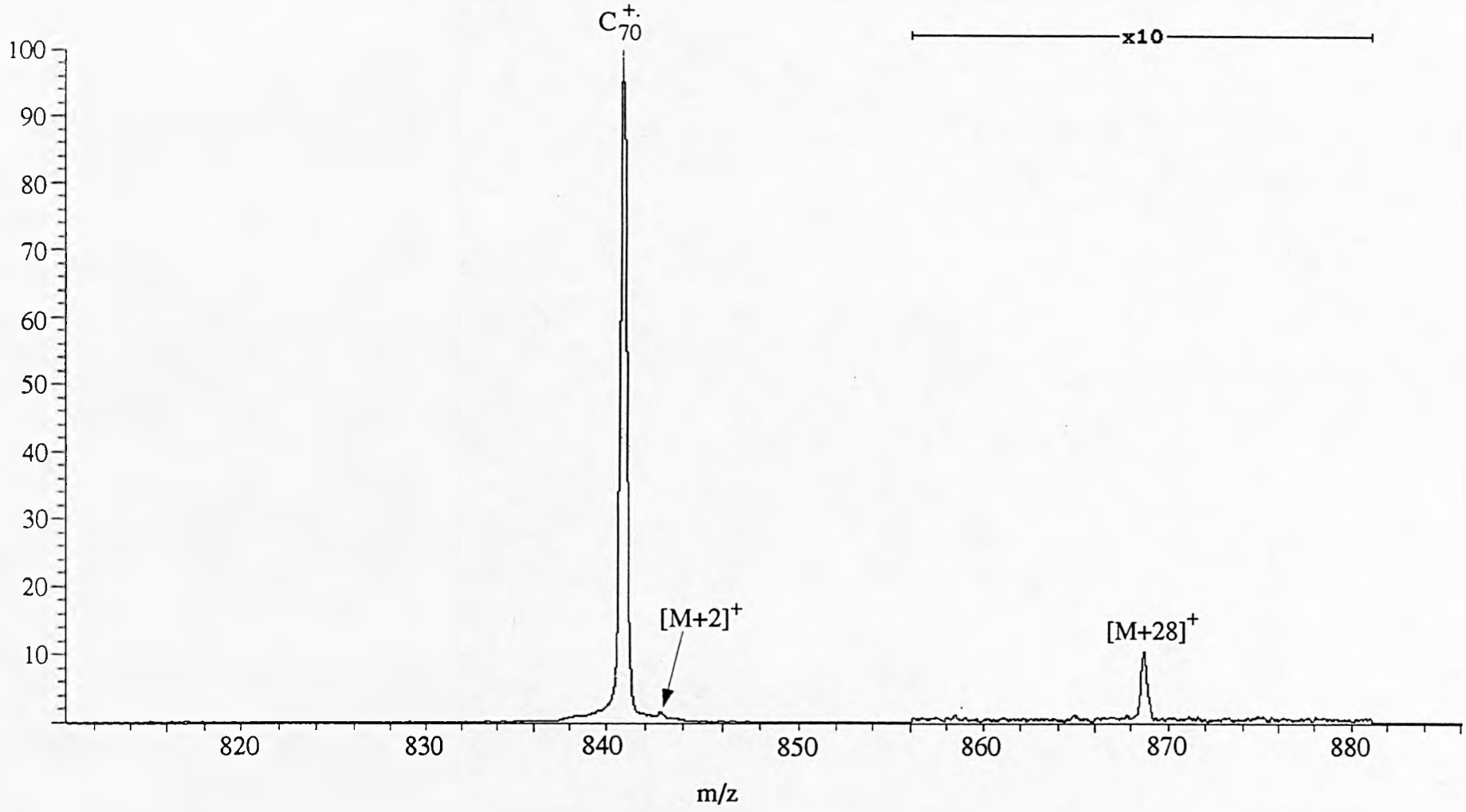

Figure 5.17: Magnet scan of $C_{70}^{+\cdot}$ and ethane at E_{lab} = 1250 eV.

Laboratory-frame collision energy /eV	Centre-of-mass collision energy /eV	Adduct ions observed
300	10.3	$[M + 16]^+$
500	17.2	$[M + 16]^+$ $[M + 14]^+$ $[M + 28]^+$ $[M + 29]^+$
750	25.9	$[M + 28]^+$ $[M + 16]^+$ $[M + 14]^+$ $[M + 2]^+$ $[M + 1]^+$
1000	34.5	$[M + 28]^+$ $[M + 16]^+$ $[M + 14]^+$ $[M + 13]^+$ $[M + 2]^+$
1250	43.1	$[M + 28]^+$ $[M + 2]^+$
1500	51.7	$[M + 28]^+$

Table 5.5: Laboratory-frame and centre-of-mass frame collision energies at which $C_{70}^{+\cdot}$/ethane adducts were observed.

5.4 Investigation of Collisions between Ethene and $C_{70}^{+\cdot}$ Radical Cations.

Reactive collisions between ethene and $C_{70}^{+\cdot}$ proved possible at gas pressures which reduced the parent ion signal to 30% of its original intensity. E2 settings were appropriate for energy deficits equal to the centre-of-mass collision energies. At a laboratory-frame collision energy of 300 eV, two adducts were observed, $[M + 24]^+$ and $[M + 28]^+$ (figure 5.18). $[M + 28]^+$ could correspond to the full ethene adduct $C_{70}C_2H_4^{+\cdot}$, but the possibility of a $C_{70}CH_2CH_2^{+\cdot}$ adduct cannot be excluded. The absence of full hydrocarbon adducts with methane or ethane target gases weakens any argument that $[M + 28]^+$ corresponds to $C_{70}C_2H_4^{+\cdot}$. Increasing the laboratory-frame collision energy caused the disappearance of $[M + 28]^+$ and the appearance of $[M + 14]^+$. This might suggest that the full adduct does form, but fragments at higher collision energies by the loss of CH_2 producing $C_{70}CH_2^{+\cdot}$. $[M + 24]^+$ assigned as $C_{70}C_2^{+\cdot}$ was present over the entire laboratory-frame collision energy range tested. At increased laboratory-frame collision energies of 500 eV, 750 eV (figure 5.19) and 1000 eV (figure 5.20) the largest array of adduct peaks were observed, which corresponded with findings from methane and ethane collisions. $[M + 12]^+$, $[M + 13]^+$ and $[M + 14]^+$ assigned as $C_{70}C^+$, $C_{70}CH^{+\cdot}$ and $C_{70}CH_2^{+\cdot}$ respectively were observed with ethene. The carbon-carbon double bond must have been cleaved in order to produce these species. The results over the energy range tested are summarised in table 5.6. E_{lab} = 750 eV appeared to provide the most effective collision conditions for producing adducts, in that at this collision energy $[M + 1]^+$ and $[M + 12]^+$ assigned as $C_{70}H^+$ and $C_{70}C^+$ were also observed. The $[M + 1]^+$ satellite peak was not observed under any other collision conditions with ethene as the target gas. It is possible that this satellite peak tended to be hidden in the wide base of the parent ion. $[M + 25]^+$, assigned as $C_{70}C_2H^+$ was observed from E_{lab} = 500 eV to E_{lab} = 1500 eV.

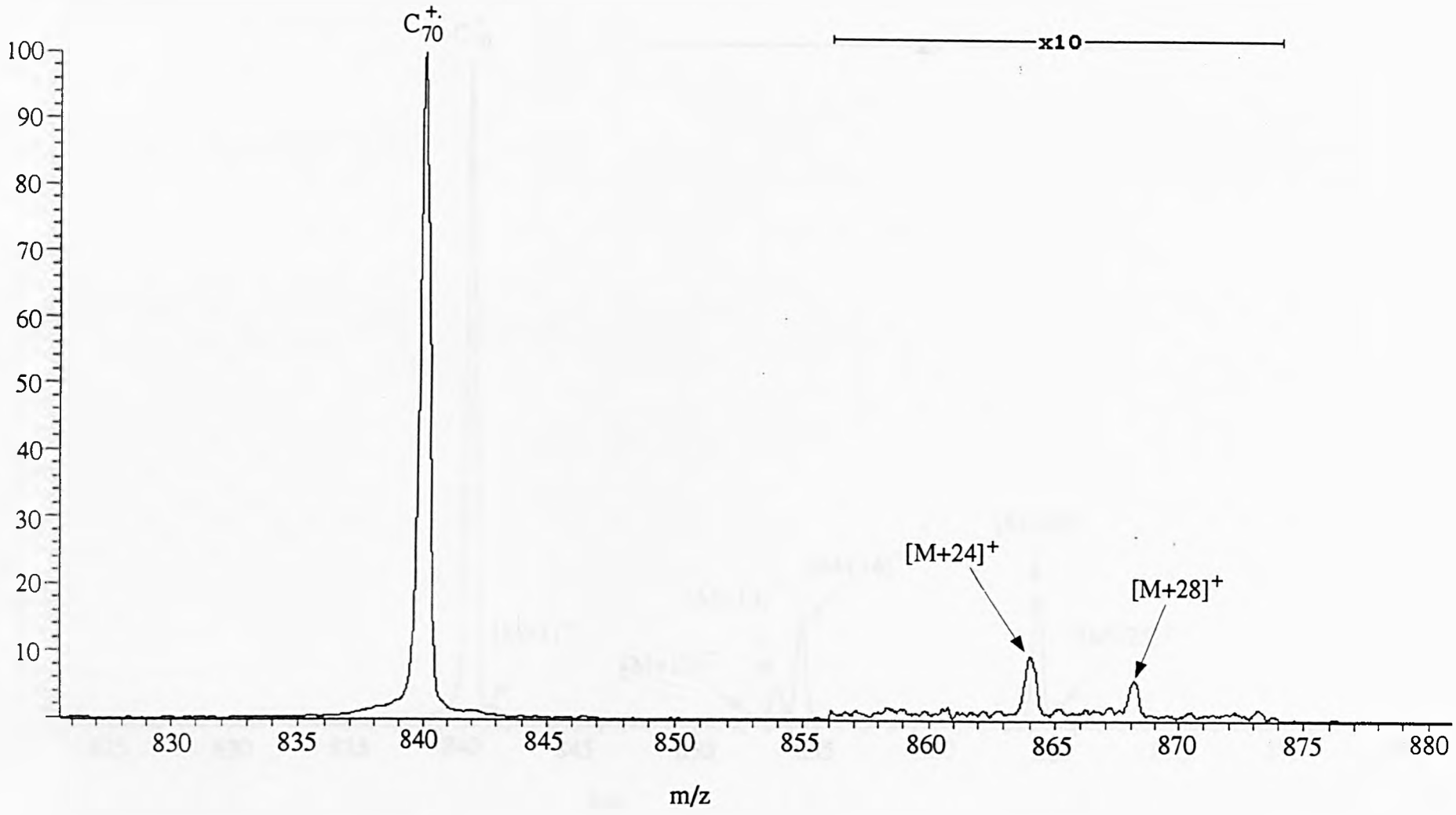

Figure 5.18: Magnet scan of $C_{70}^{+\cdot}$ and ethene at E_{lab} = 300 eV.

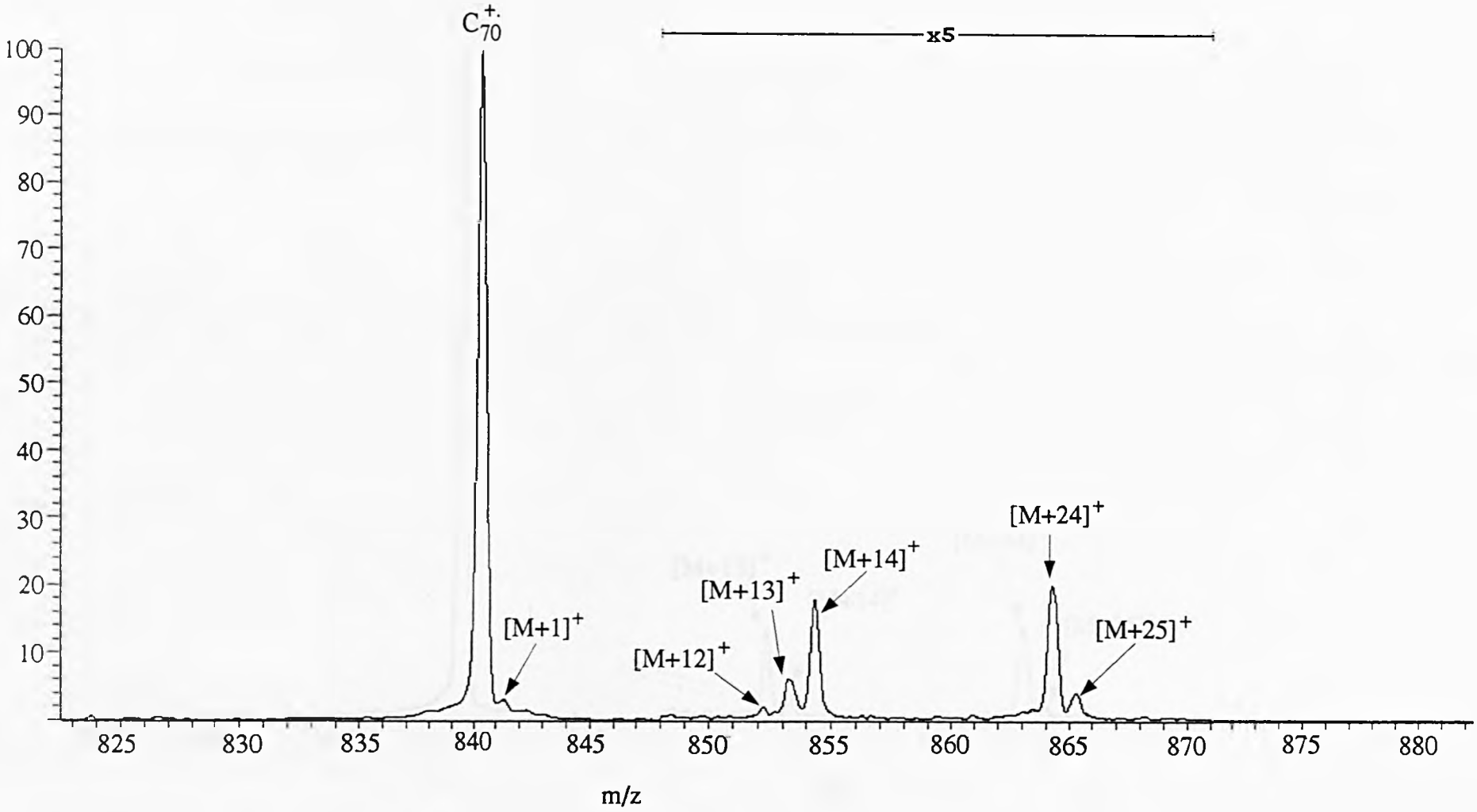

Figure 5.19: Magnet scan of $C_{70}^{+\cdot}$ and ethene at E_{lab} = 750 eV.

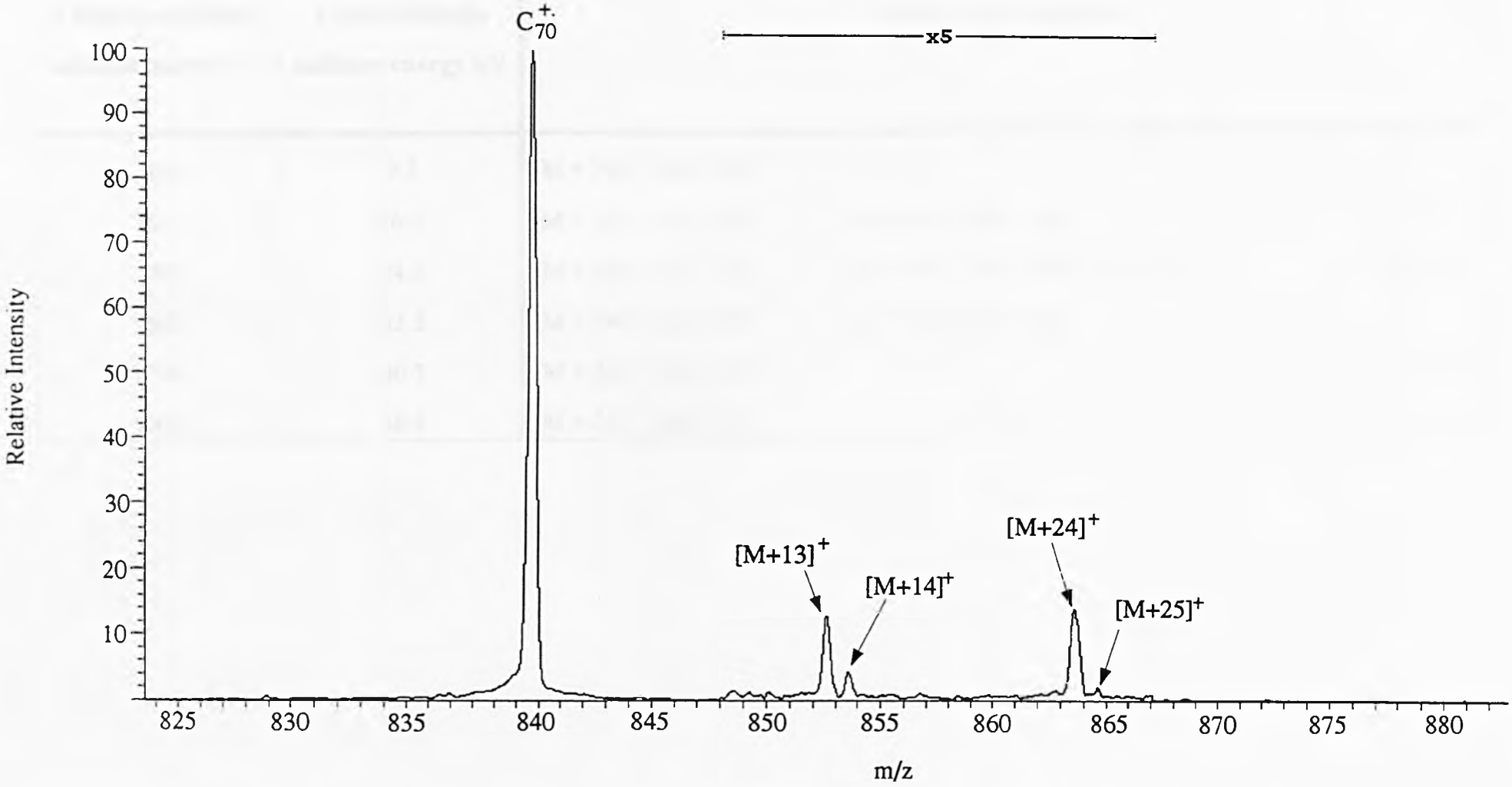

Figure 5.20: Magnet scan of $C_{70}^{+\cdot}$ and ethene at E_{lab} = 1000 eV.

Laboratory-frame collision energy /eV	Centre-of-mass collision energy /eV	Adduct ions observed
300	9.7	$[M + 24]^+$ $[M + 28]^+$
500	16.1	$[M + 24]^+$ $[M + 25]^+$ $[M + 14]^+$ $[M + 16]^+$
750	24.2	$[M + 24]^+$ $[M + 25]^+$ $[M + 14]^+$ $[M + 13]^+$ $[M + 12]^+$ $[M + 1]^+$
1000	32.3	$[M + 24]^+$ $[M + 25]^+$ $[M + 14]^+$ $[M + 13]^+$
1250	40.3	$[M + 24]^+$ $[M + 25]^+$
1500	48.4	$[M + 24]^+$ $[M + 25]^+$

Table 5.6: Laboratory-frame and centre-of-mass frame collision energies at which $C_{70}^{+\cdot}$/ethene adducts were observed.

5.5 Investigation of Collisions between Ethyne and $C_{70}^{+\cdot}$ Radical Cations.

Like ethane, high pressure of ethyne gave rise to electrical discharges within the collision cell. For this reason the maximum gas pressure used for these experiments was sufficient to reduce the parent ion intensity to 50% of its original strength. In all experiments E2 was set for the energy deficit equal to the centre-of-mass collision energy. Only one adduct , $[M + 24]^+$ assigned as $C_{70}C_2^{+\cdot}$, was observed over the whole laboratory-frame collision energy range investigated (figures 5.21 to 5.24 inclusive). There was evidence of a $[M + 13]^+$ peak, assigned as $C_{70}CH^{+\cdot}$, at laboratory-frame collision energies of 750 eV and 1000 eV (figures 5.22 and 5.23). Results are summarised in table 5.7. The carbon-carbon triple bond must have been cleaved in order for $C_{70}CH^{+\cdot}$ to be observed. Unlike the other multiatomic collision gases, there were no $[M + 1]^+$ or $[M + 2]^+$ satellite peaks around the parent ion.

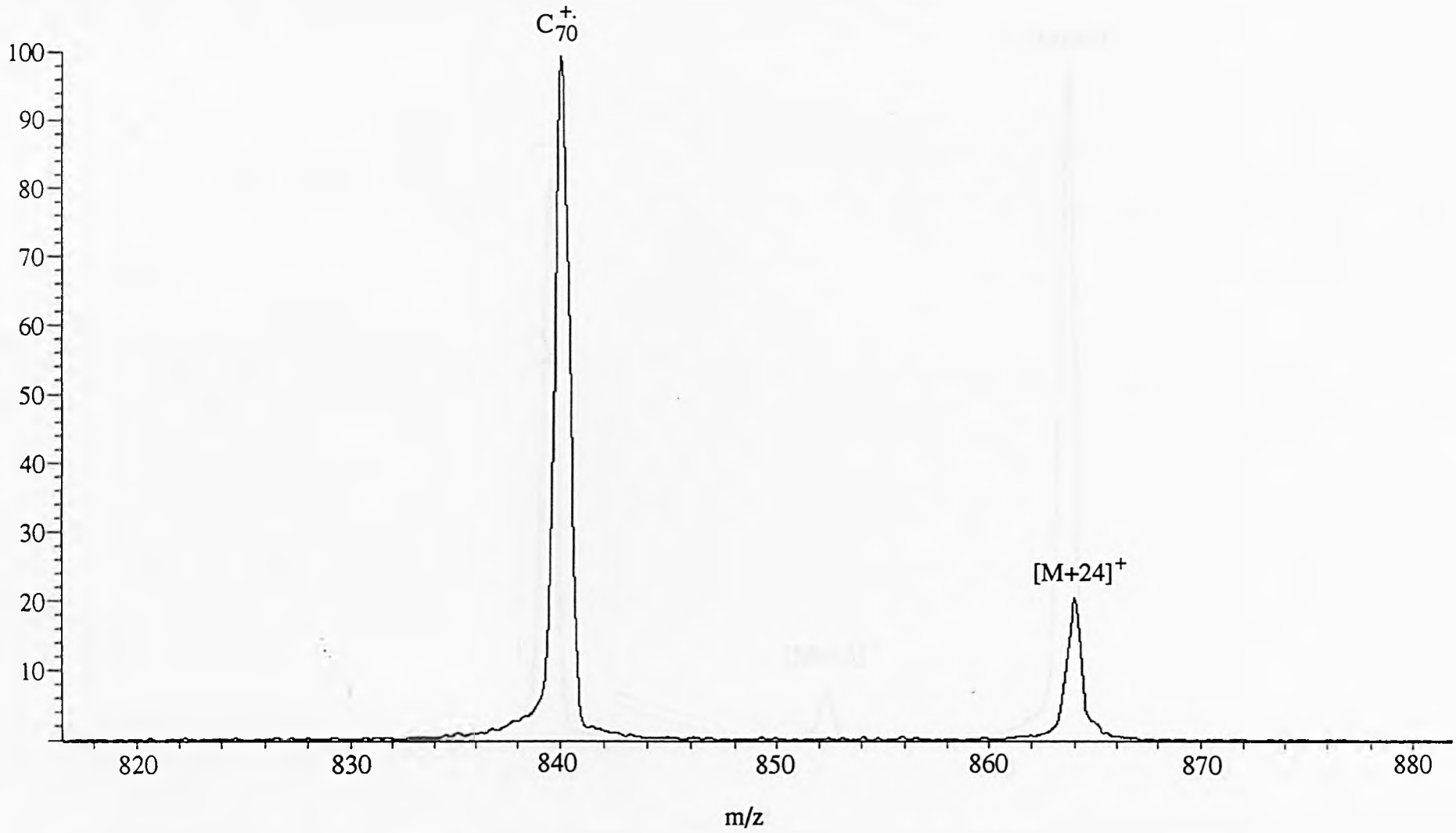

Figure 5.21: Magnet scan of $C_{70}^{+\cdot}$ and ethyne at E_{lab} = 500 eV.

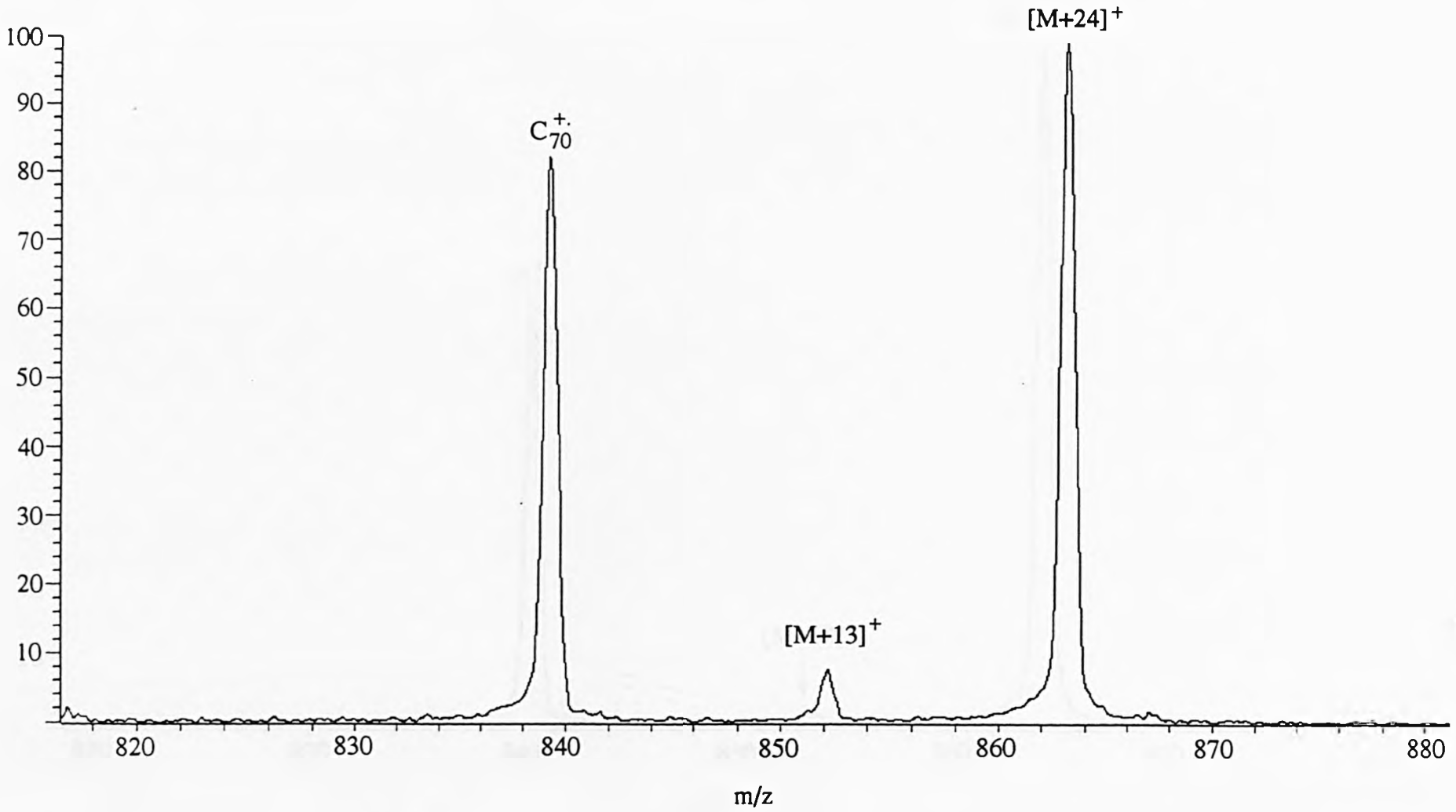

Figure 5.22: Magnet scan of $C_{70}^{+\cdot}$ and ethyne at E_{lab} = 750 eV.

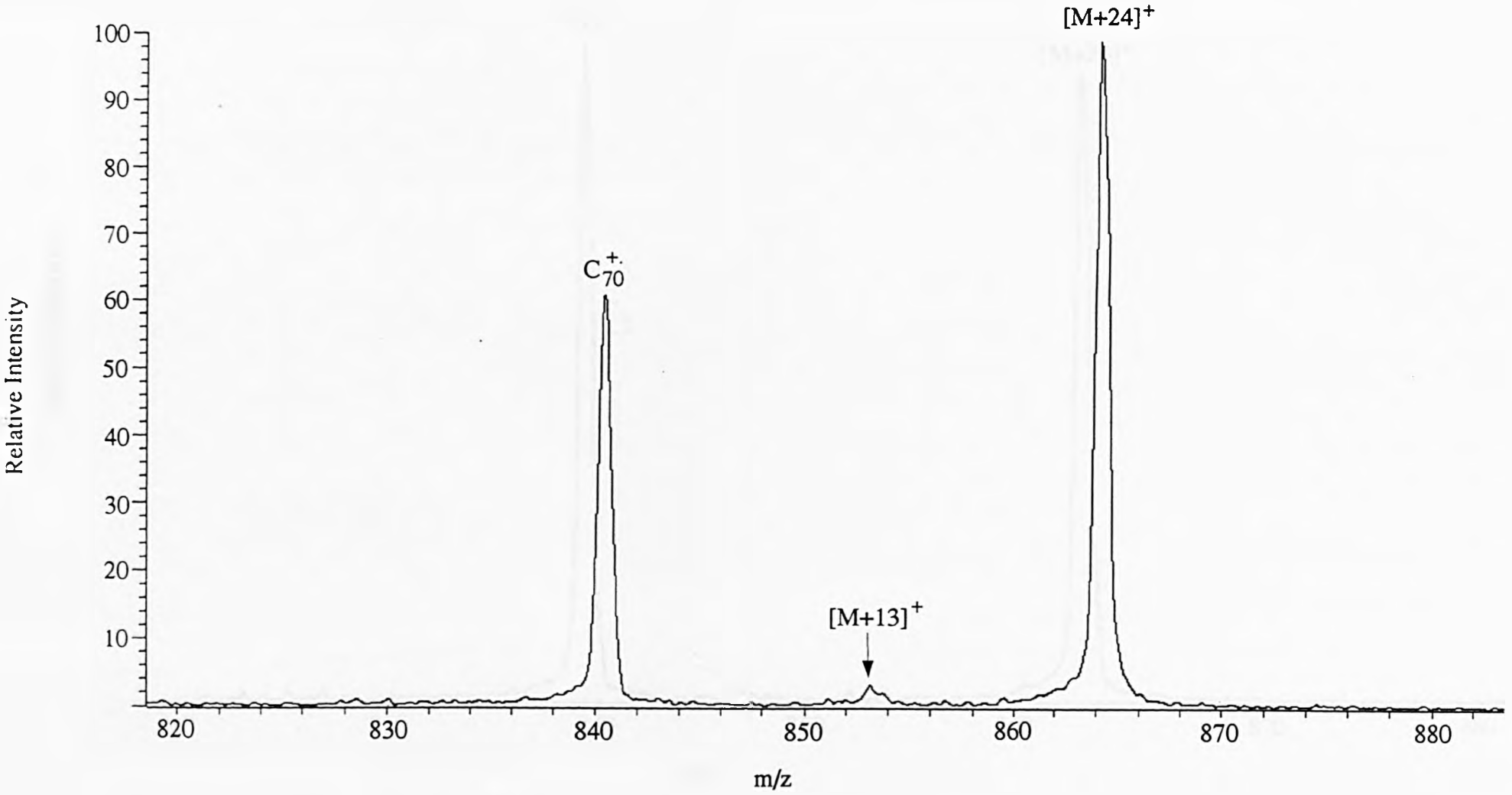

Figure 5.23: Magnet scan of $C_{70}^{+\cdot}$ and ethyne at E_{lab} = 1000 eV.

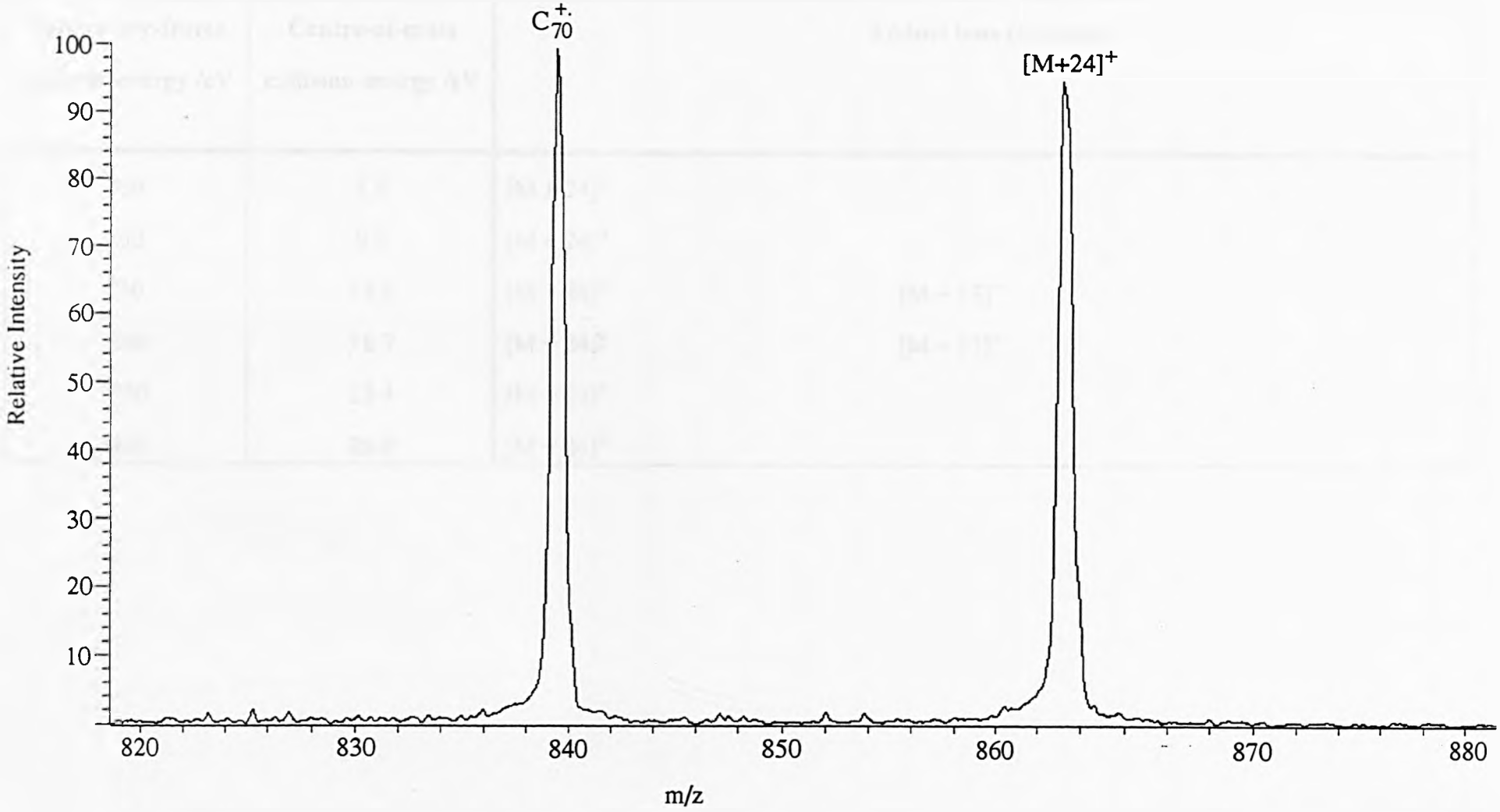

Figure 5.24: Magnet scan of $C_{70}^{+\cdot}$ and ethyne at E_{lab} = 1250 eV.

Laboratory-frame collision energy /eV	Centre-of-mass collision energy /eV	Adduct ions observed	
300	5.6	$[M + 24]^+$	
500	9.3	$[M + 24]^+$	
750	14.0	$[M + 24]^+$	$[M + 13]^+$
1000	18.7	$[M + 24]^+$	$[M + 13]^+$
1250	23.4	$[M + 24]^+$	
1500	28.0	$[M + 24]^+$	

Table 5.7: Laboratory-frame and centre-of-mass frame collision energies at which $C_{70}^{+\cdot}$/ethyne adducts were observed.

5.6 Investigation of Collisions between Propene and $C_{70}^{+\cdot}$ Radical Cations.

Research carried out using ethane, ethene and ethyne, when the two carbon atom are connected by both saturated or unsaturated bonds, produced interesting results. Propene combines the saturated and unsaturated carbon-carbon bond qualities of ethane, ethene and ethyne. For these experiments the gas pressure used was sufficient to reduce the parent ion intensity to 50% of its original strength. E2 was set for the energy deficits equal to the centre-of-mass collision energies. The most common adduct observed when propene was used as a target gas was $[M + 24]^+$ assigned as $C_{70}C_2^{+\cdot}$. Once more, the optimum collision energy with regards to the number of adducts observed was between E_{lab} = 500 eV and E_{lab} = 1000 eV. At E_{lab} = 500 eV and E_{lab} = 750 eV $[M + 13]^+$ and $[M + 14]^+$ as shown in (figures 5.25 and 5.26). Once more, it was evident that a carbon-carbon bond had been broken but no conclusions could be drawn as to whether it was the single, double or both bonds that were ruptured. $[M + 25]^+$ was observed at E_{lab} = 500 eV. From E_{lab} = 1000 eV to E_{lab} = 1250 eV, $[M + 13]^+$ was produced but $[M + 14]^+$ was no longer observed (figures 5.27 and 5.28). These results are summarised in table 5.8. There was no evidence for the full propene adduct, which was not unexpected following results obtained with other hydrocarbons.

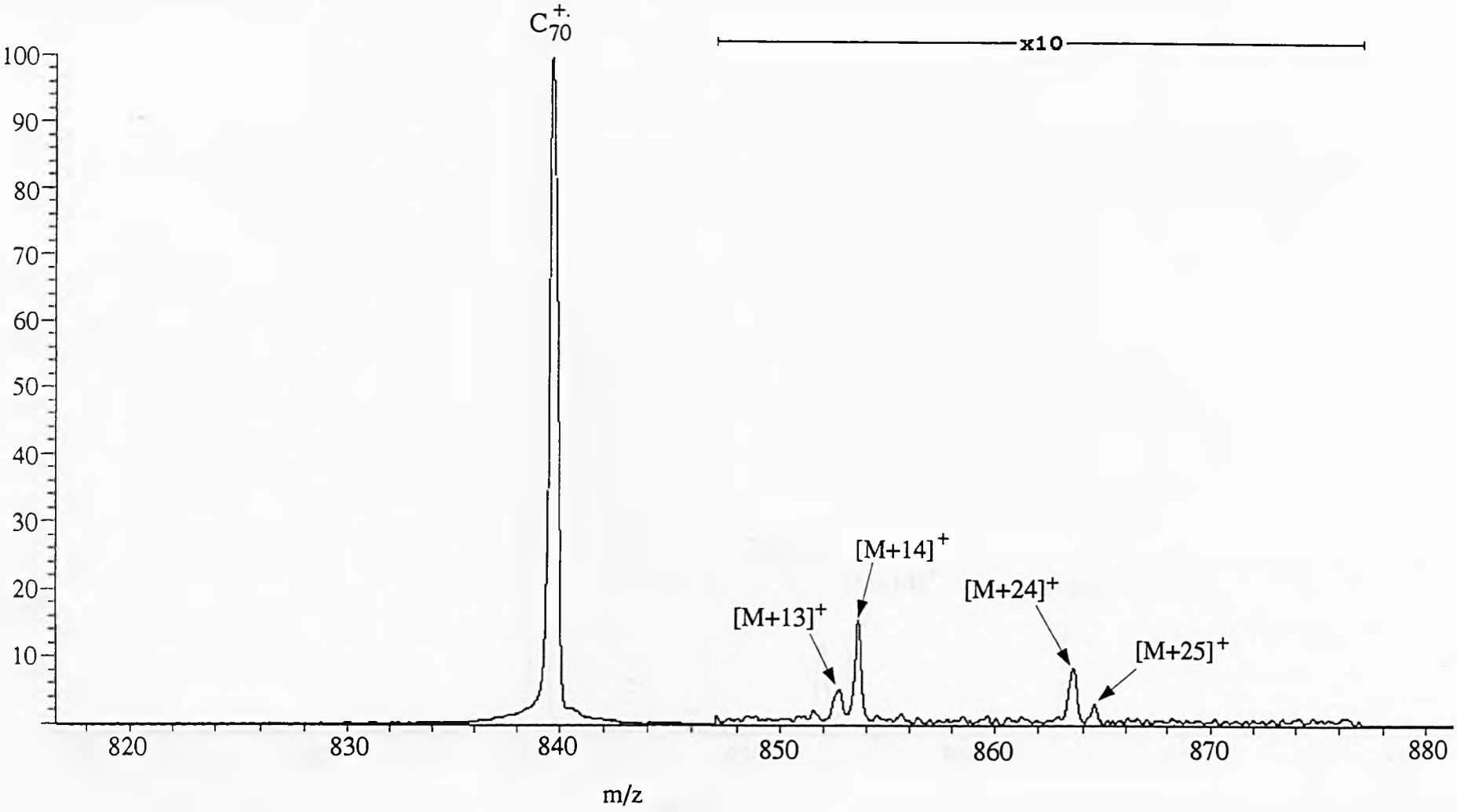

Figure 5.25: Magnet scan of $C_{70}^{+\cdot}$ and propene at E_{lab} = 500 eV.

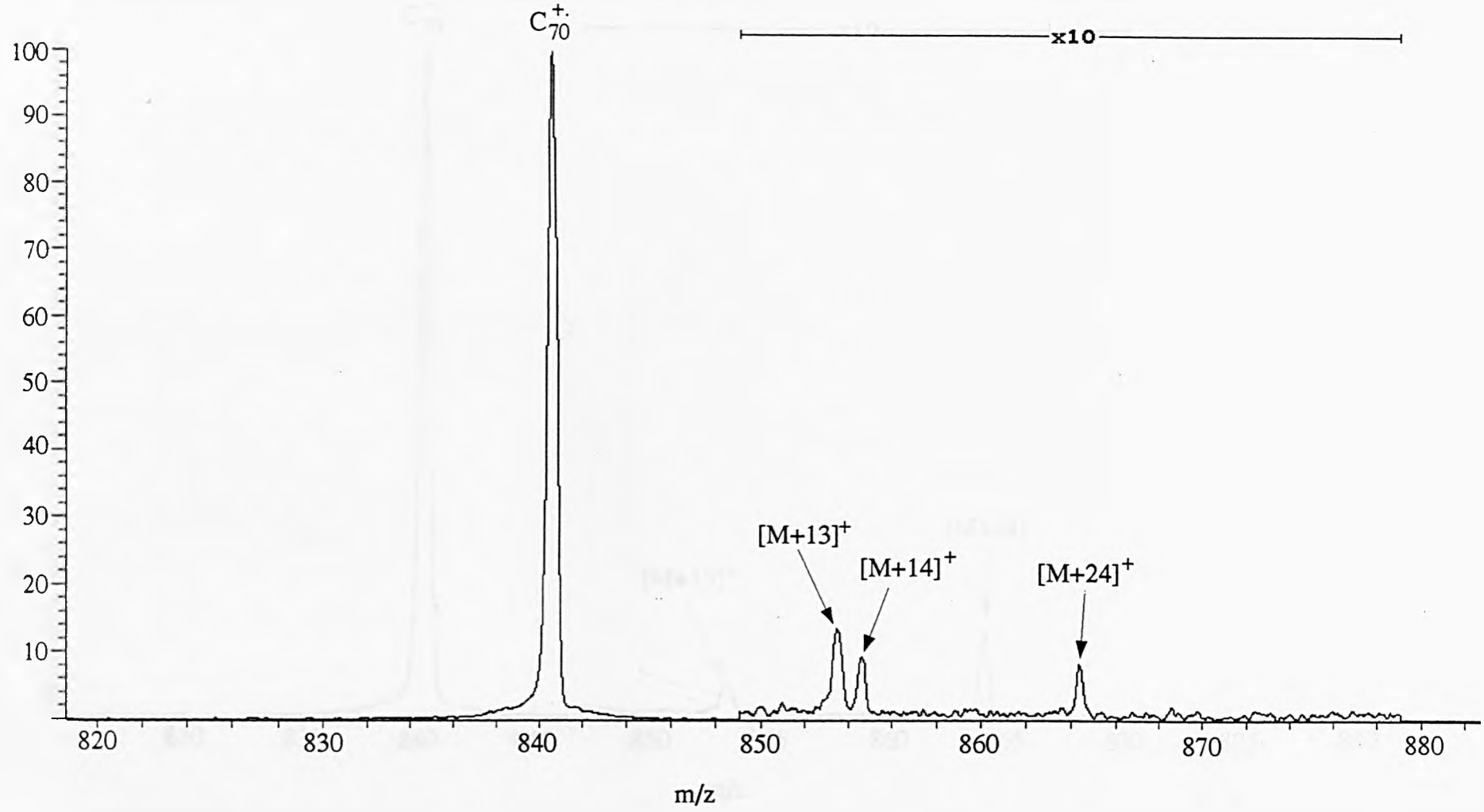

Figure 5.26: Magnet scan of $C_{70}^{+\cdot}$ and propene at E_{lab} = 750 eV.

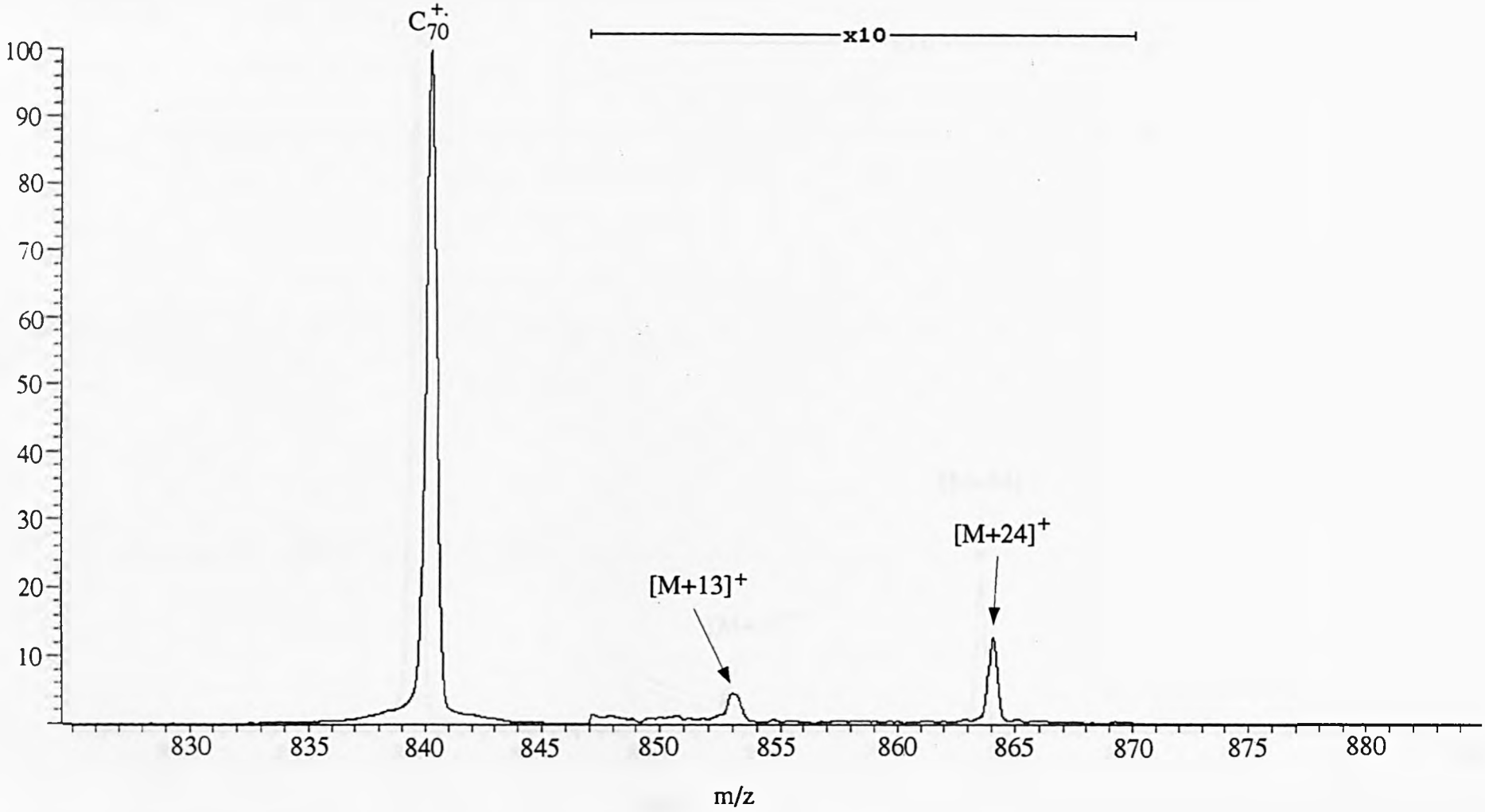

Figure 5.27: Magnet scan of $C_{70}^{+\cdot}$ and propene at E_{lab} = 1000 eV.

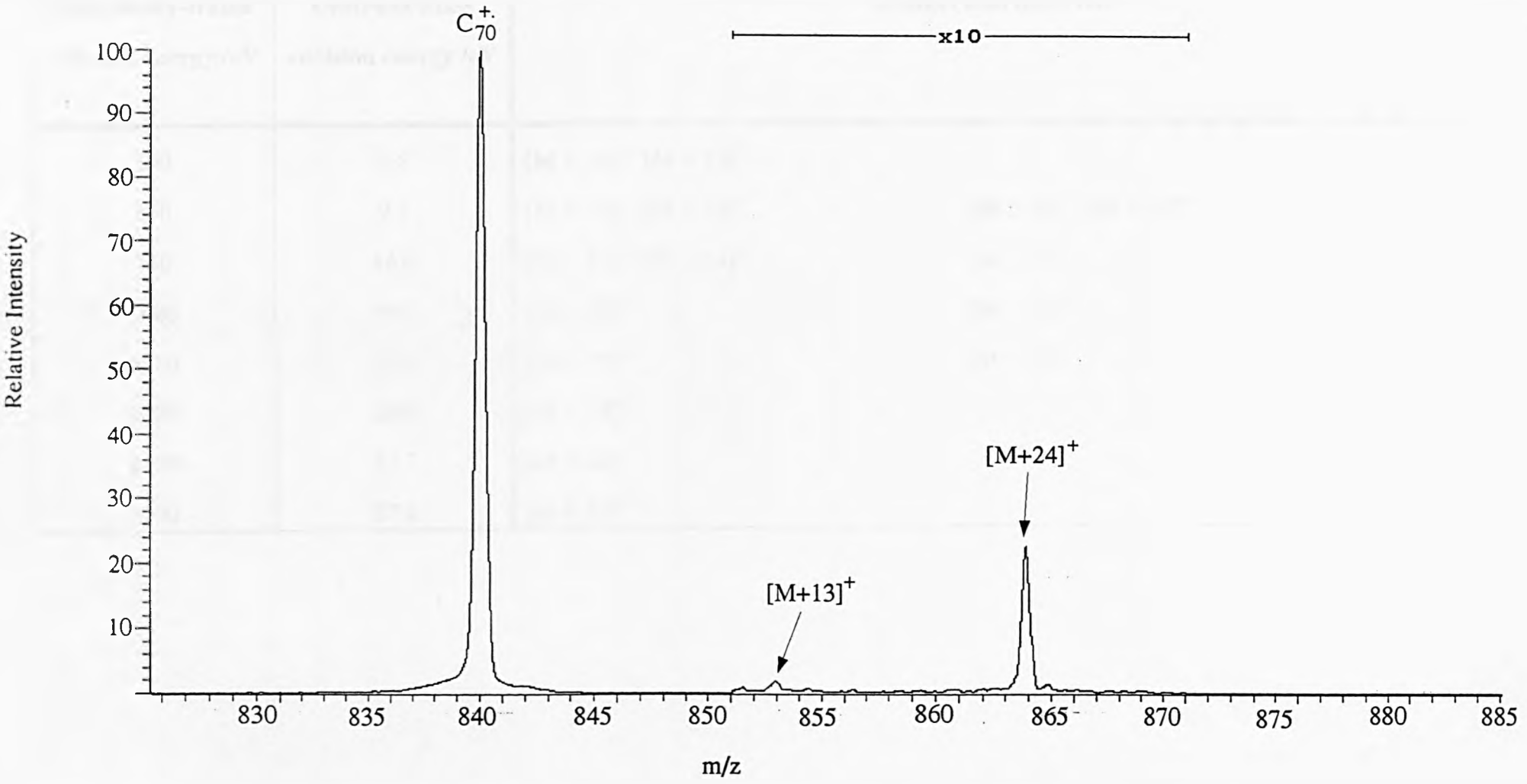

Figure 5.28: Magnet scan of $C_{70}^{+\cdot}$ and propene at E_{lab} = 1250 eV.

Laboratory-frame collision energy /eV	Centre-of-mass collision energy /eV	Adduct ions observed
300	5.6	$[M + 14]^+$ $[M + 13]^+$
500	9.3	$[M + 14]^+$ $[M + 13]^+$ $[M + 24]^+$ $[M + 25]^+$
750	14.0	$[M + 13]^+$ $[M + 14]^+$ $[M + 24]^+$
1000	18.7	$[M + 24]^+$ $[M + 13]^+$
1250	23.4	$[M + 24]^+$ $[M + 13]^+$
1500	28.0	$[M + 24]^+$
1750	32.7	$[M + 24]^+$
2000	37.4	$[M + 24]^+$

Table 5.8: Laboratory-frame and centre-of-mass frame collision energies at which $C_{70}^{+\cdot}$/propene adducts were observed.

CHAPTER SIX: *Target Capture of Methane by Protonated Peptides.*

6.1 Introduction.

As an extension of the work carried out on fullerene radical cations the possibility of target capture was explored for peptide chemistry. As discussed earlier, Fenselau *et al.* [183] reported the formation of adducts in collisions of protonated peptides with methane and ammonia. In this study several peptide/collision gas adducts were observed and the centre-of-mass frame and laboratory-frame collision energies at which they were formed were investigated. Two peptides were used extensively: bombesin and alytesin. Three target gases were investigated, namely methane, deuterated methane and ^{13}carbon methane. Renin-substrate was also used for target capture of methane, but only in preliminary experiments.

6.1.1 Bombesin, Alytesin and Renin-Substrate.

Bombesin is a tetradecapeptide with thermoregulatory and gastric effects in mammals [197-199]. It is extracted from the skin of European amphibians of the family Discoglossidae. There are thirty-nine other biologically active peptides related to bombesin [200], one of which is alytesin. Alytesin is one of the most closely related analogues of bombesin [201-202], to the extent that alytesin displays the same biological actions as bombesin and is also found in the skin of European amphibians of the family Discoglossidae. The second and sixth amino acid residue from the N-terminus are the only structural differences between these two peptides. Both peptides contain the uncommon amino-acid pyroglutamic acid at the N-terminus. This is the only uncommon amino-acid residue in either peptide sequence. The amino acid sequences of bombesin and alytesin are given in figures 6.1 and 6.2 respectively. Renin-substrate and substance P were also measured. Substance P, which is also an analogue of bombesin but is 10^4 times less biologically active, was used to carry out

sensitivity tests on the Kratos Concept IIHH four-sector tandem mass spectrometer. Renin-substrate is not analogous to bombesin. The amino acid sequences of renin-substrate and substance P are given in figures 6.3 and 6.4 respectively.

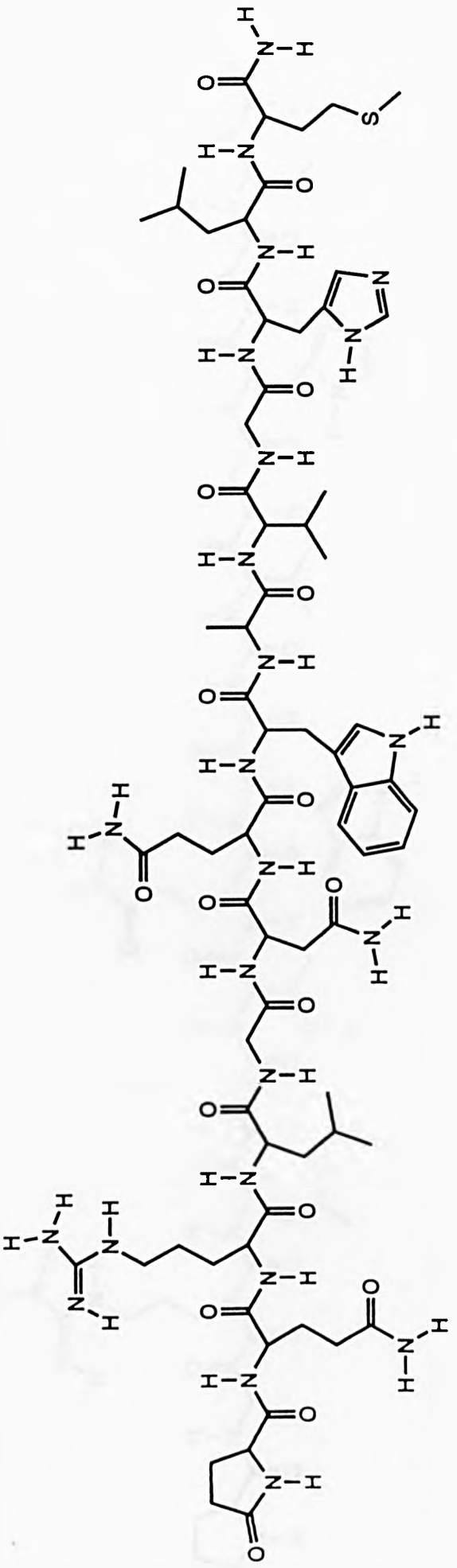

Pyr-Gln-Arg-Leu-Gly-Asn-Gln-Trp-Ala-Val-Gly-His-Leu-Met-NH_2

Figure 6.1: Amino acid sequence of bombesin.

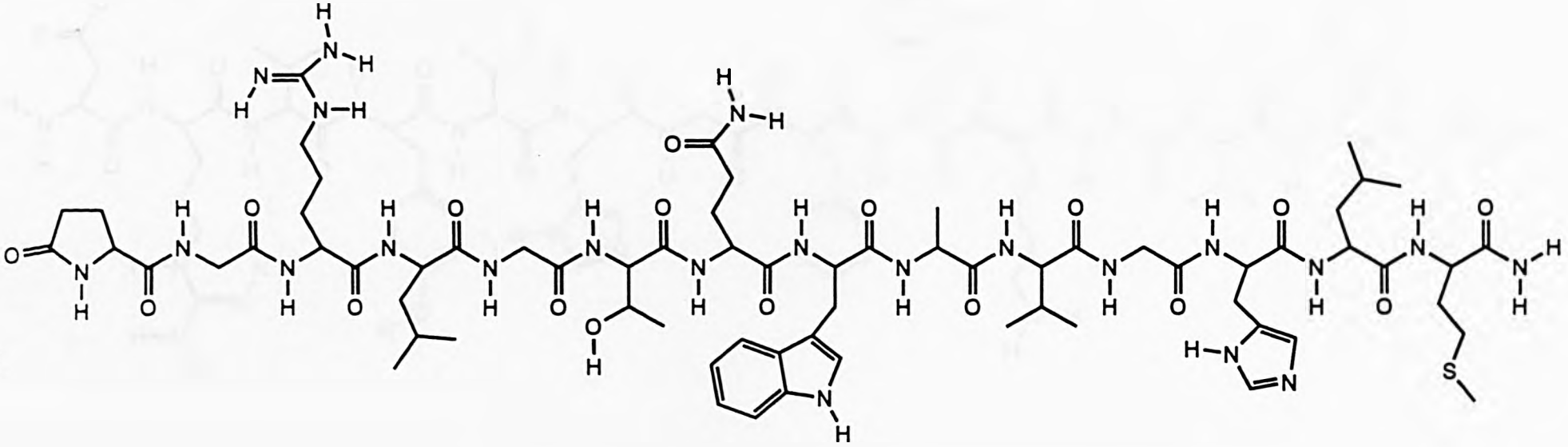

Pyr-Gly-Arg-Leu-Gly-Thr-Gln-Trp-Ala-Val-Gly-His-Leu-Met-NH_2

Figure 6.2: Amino acid sequence of alytesin.

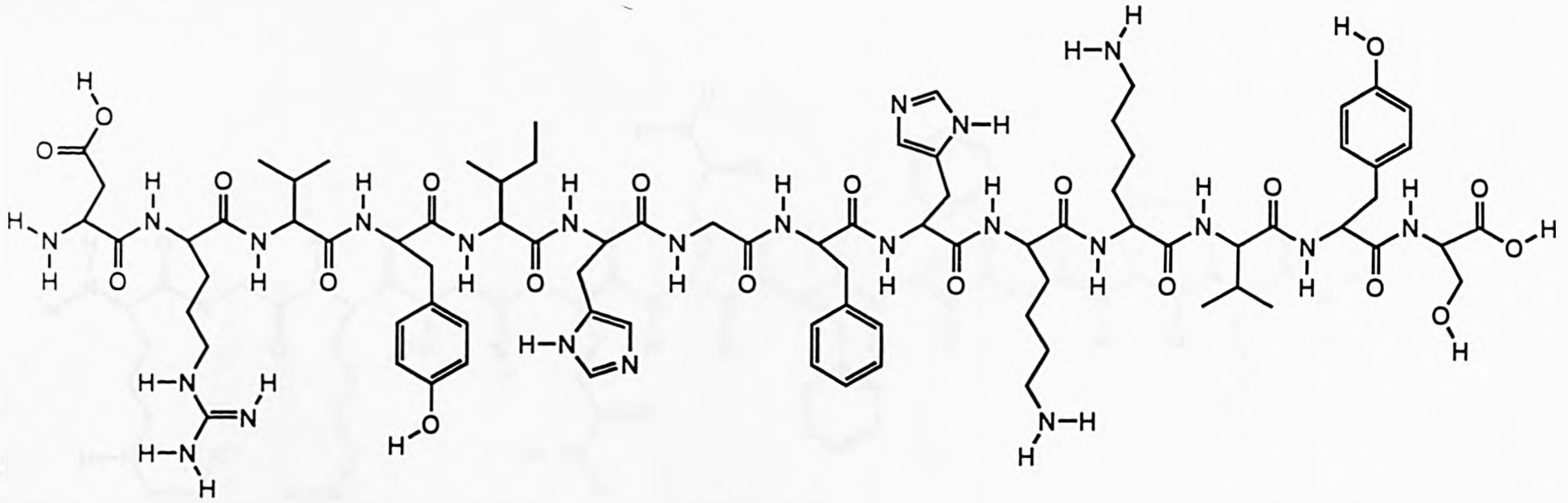

H-Asp-Arg-Val-Tyr-Ile-His-Pro-Phe-His-Leu-Leu-Val-Tyr-Ser-OH

Figure 6.3: Amino acid sequence of renin-substrate.

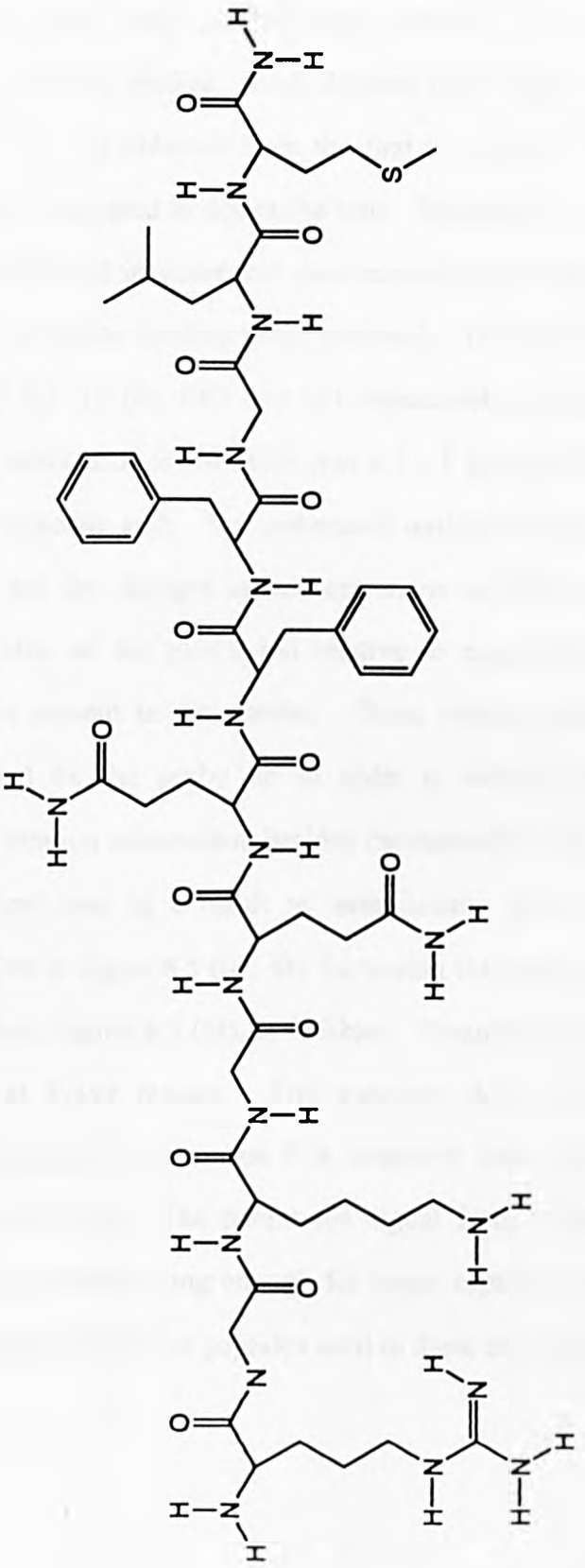

H-Arg-Pro-Lys-Pro-Gln-Gln-Phe-Phe-Gly-Leu-Met-NH_2

Figure 6.4: Amino acid sequence of substance P.

6.1.2 Sensitivity of the Kratos Concept IIHH Mass Spectrometer as tested using Substance P.

To ascertain the sensitivity of the Kratos Concept IIHH four-sector mass spectrometer when ionising large peptides, *i.e.* greater than 1000 Da, a series of dilutions were studied. Each dilution was ionised by LSIMS ionisation and a mass spectrum was obtained from the first two sectors, E1 and B1. A post-acceleration detector was used to detect the ions. Substance P, the peptide chosen for this study, was dissolved in water and concentrations such that 1, 10, 100 and 1000 picomoles per 1 μl probe loading were analysed. The resulting mass spectra can be seen in figure 6.5 (i), (ii), (iii) and (iv) respectively, representing increasing concentration. The matrix used in this case was a 1 : 1 mixture of thioglycerol : glycerol plus 1% trifluoroacetic acid. The protonated molecule can be seen at m/z 1348 Da in every case, but the changes in concentrations analysed are noticeable as changes in the intensities of the parent ion relative to matrix peaks and other background noise signals present in the spectra. These results show that at least 10 picomoles are required on the probe tip in order to obtain a good mass spectrum. At this concentration information besides the molecular mass is becoming available. Several fragment ions as a result of unimolecular decay in the source housing unit are apparent in figure 6.5 (ii). By increasing the concentration by a factor of 10 a clearer spectrum, figure 6.5 (iii), is obtained. Fragment ions are now clearly distinguishable, even at lower masses. The spectrum does not change significantly when the concentration of substance P is increased from 100 picomoles to 1 nanomole, (see figure 6.5 (iv)). The parent ion signal from 1 nanomole of substance P did not, however, survive long enough for target capture experiments to be performed hence the concentrations of peptides used in these experiments were higher .

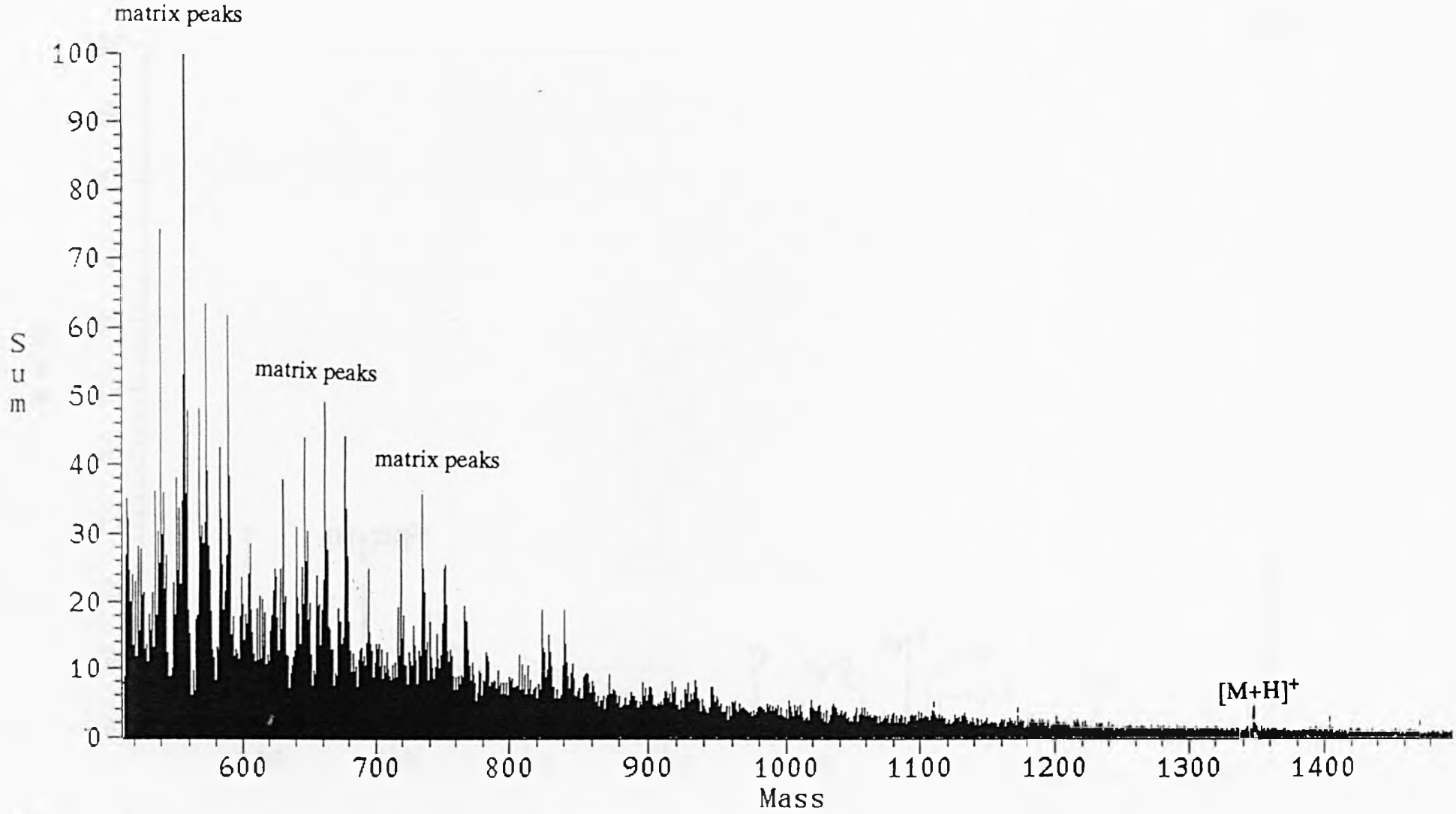

Figure 6.5(i): Mass spectrum of 1 picomole of substance P using thioglycerol:glycerol 1:1 + 1% trifluoroacetic acid as the matrix.

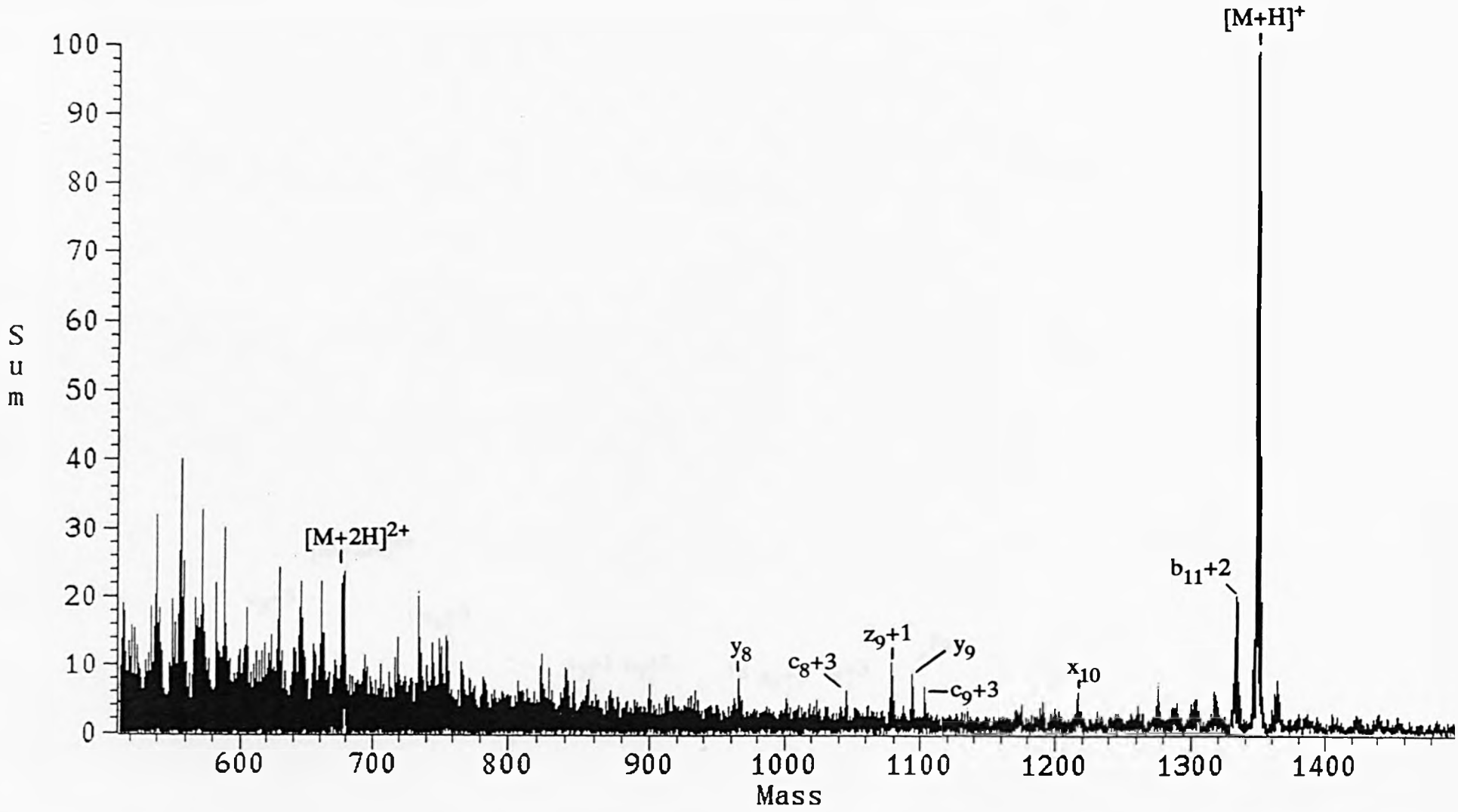

Figure 6.5(ii): Mass spectrum of 10 picomoles of substance P using thioglycerol:glycerol 1:1 + 1% trifluoroacetic acid as the matrix.

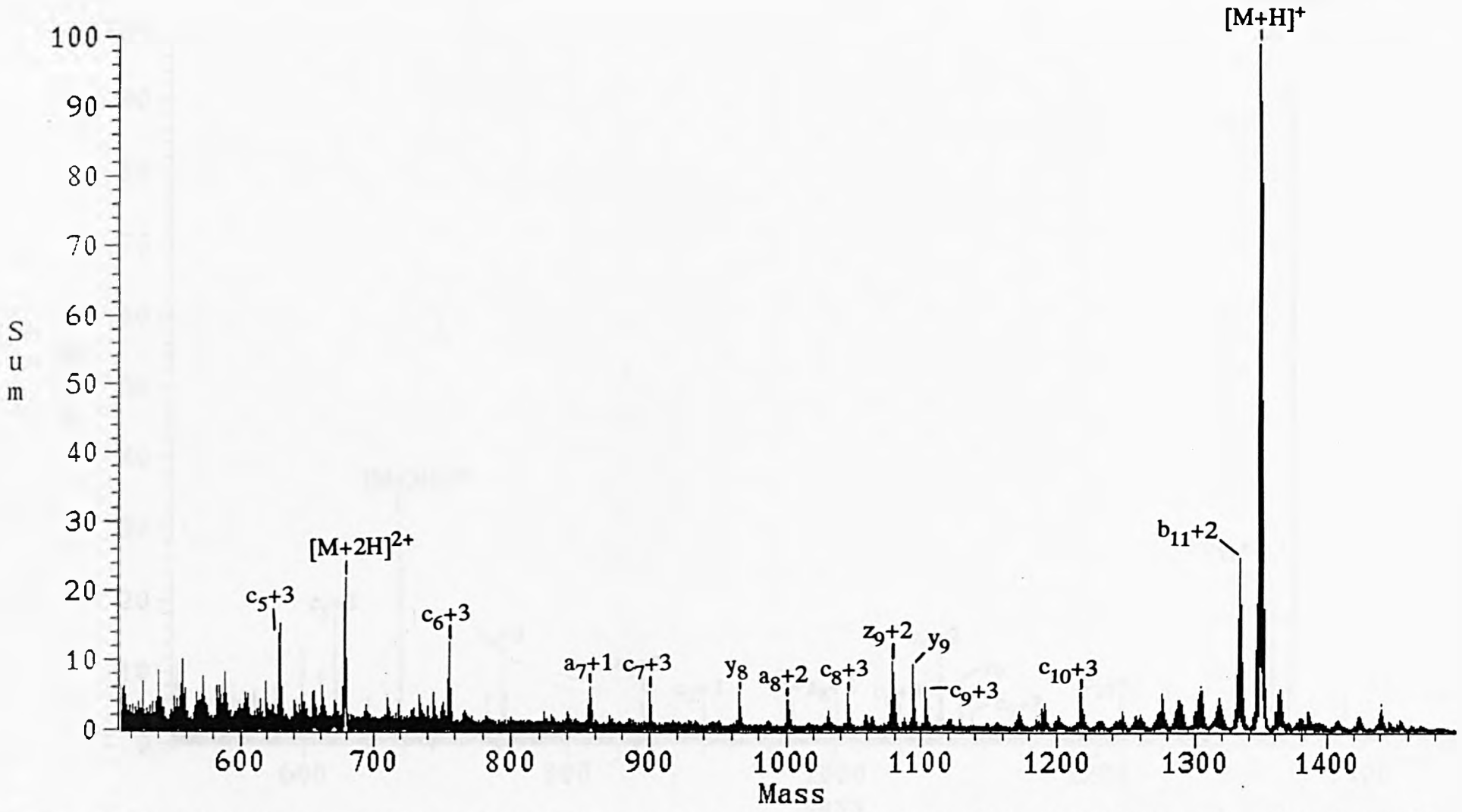

Figure 6.5(iii): Mass spectrum of 100 picomoles of substance P using thioglycerol:glycerol 1:1 + 1% trifluoroacetic acid as the matrix.

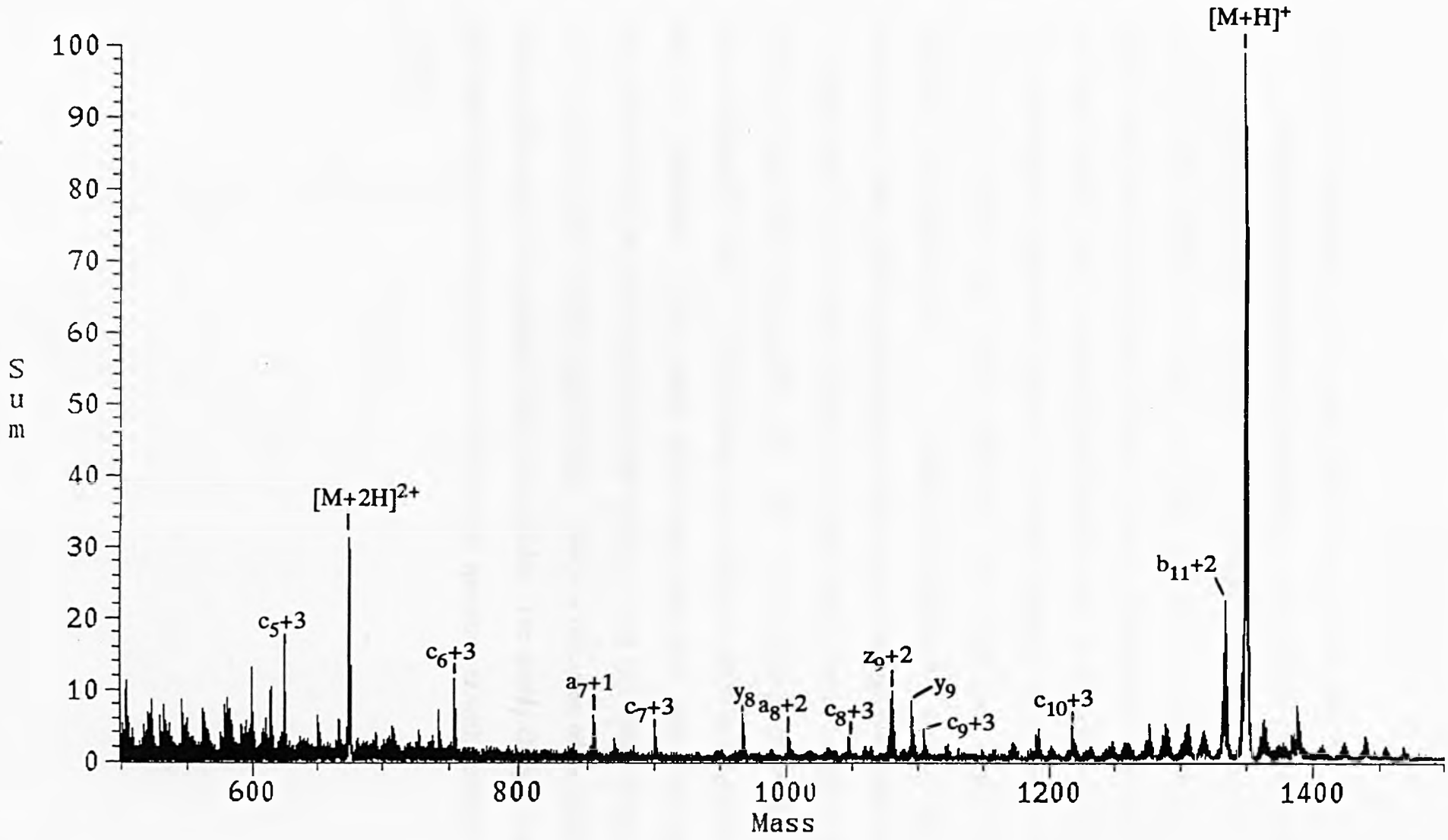

Figure 6.5(iv): Mass spectrum of 1000 picomoles of substance P using thioglycerol:glycerol 1:1 + 1% trifluoroacetic acid as the matrix.

6.1.3 Mass Spectrometry of Bombesin, Alytesin and Renin-Substrate.

The objective was to produce protonated molecules of bombesin, alytesin and renin-substrate using LSIMS ionisation. A 5 μl aliquot of a stock solution of the peptide would be placed on the probe tip giving 2 to 3 nanomoles per analysis. The solvent was removed by a stream of warm air prior to the addition of the matrix. A loading of between 2 and 3 nmoles of peptide on the probe tip for bombesin, alytesin and renin-substrate provided a signal of sufficient intensity which lasted for the duration of a typical target capture experiment. The matrix used in the case of bombesin and alytesin was a 1 : 1 mixture of thioglycerol : glycerol plus 1% trifluoroacetic acid. Renin-substrate was found to work better with the matrix known as '*magic bullet*'. Mass spectra showing the parent ions of bombesin ($[M + H]^+$ = 1619.8 average mass units), alytesin ($[M + H]^+$ = 1535.8 average mass units) and renin-substrate ($[M + H]^+$ = 1758.9 average mass units) are given in figures 6.6, 6.7 and 6.8 respectively. These spectra show strong and clear parent ion signals. Fragmentation can be seen to have occurred with 'a', 'd' and 'c_{+2}' series of fragment ions common to both bombesin and alytesin. This is a reflection of the similarity between the amino acid sequences of the two peptides. The doubly-charged doubly-protonated molecule is visible in the renin-substrate spectrum, as with bombesin and alytesin.

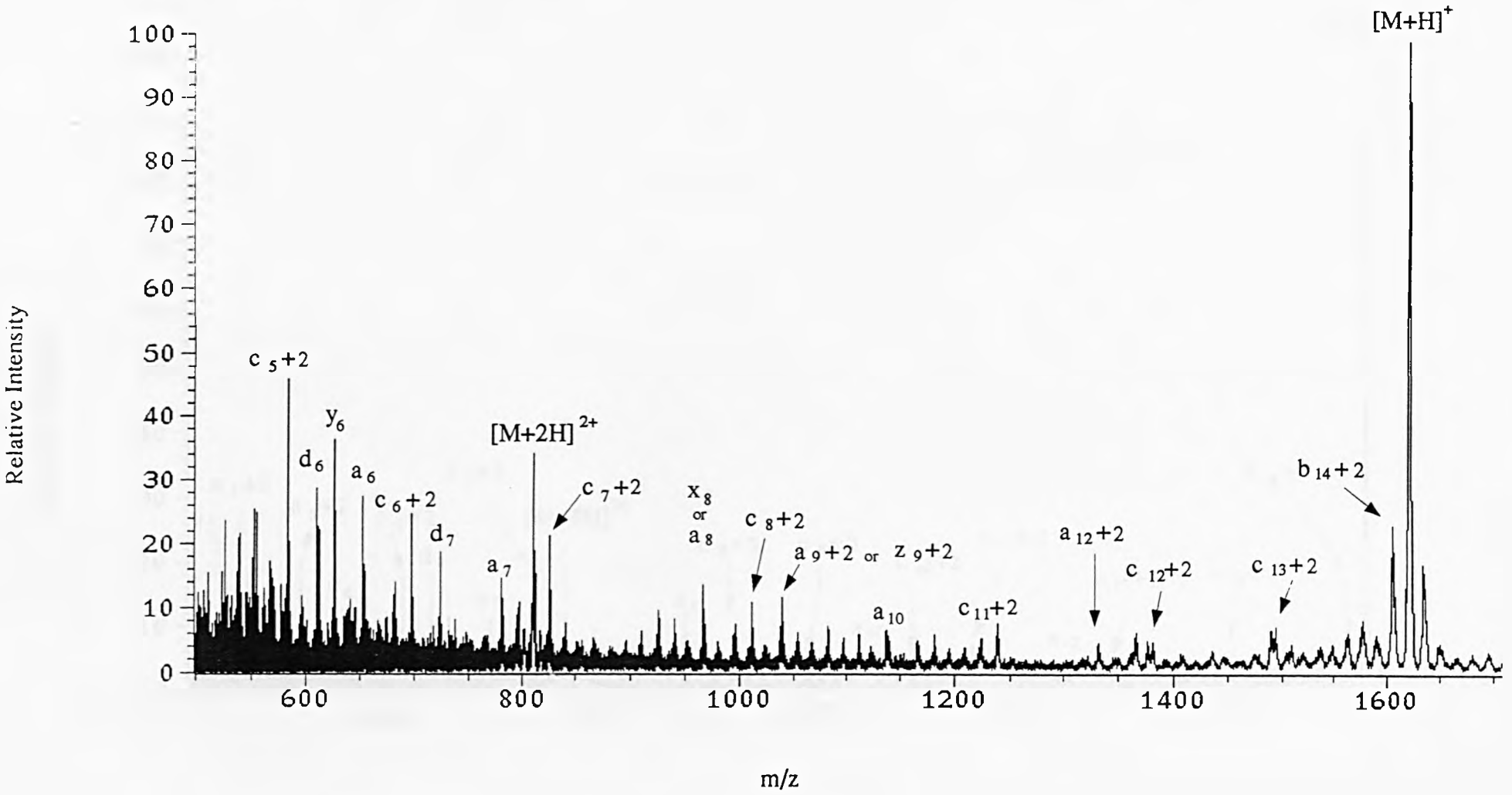

Figure 6.6: Mass spectrum of bombesin using thioglycerol:glycerol 1:1 + 1% trifluoroacetic acid as the matrix.

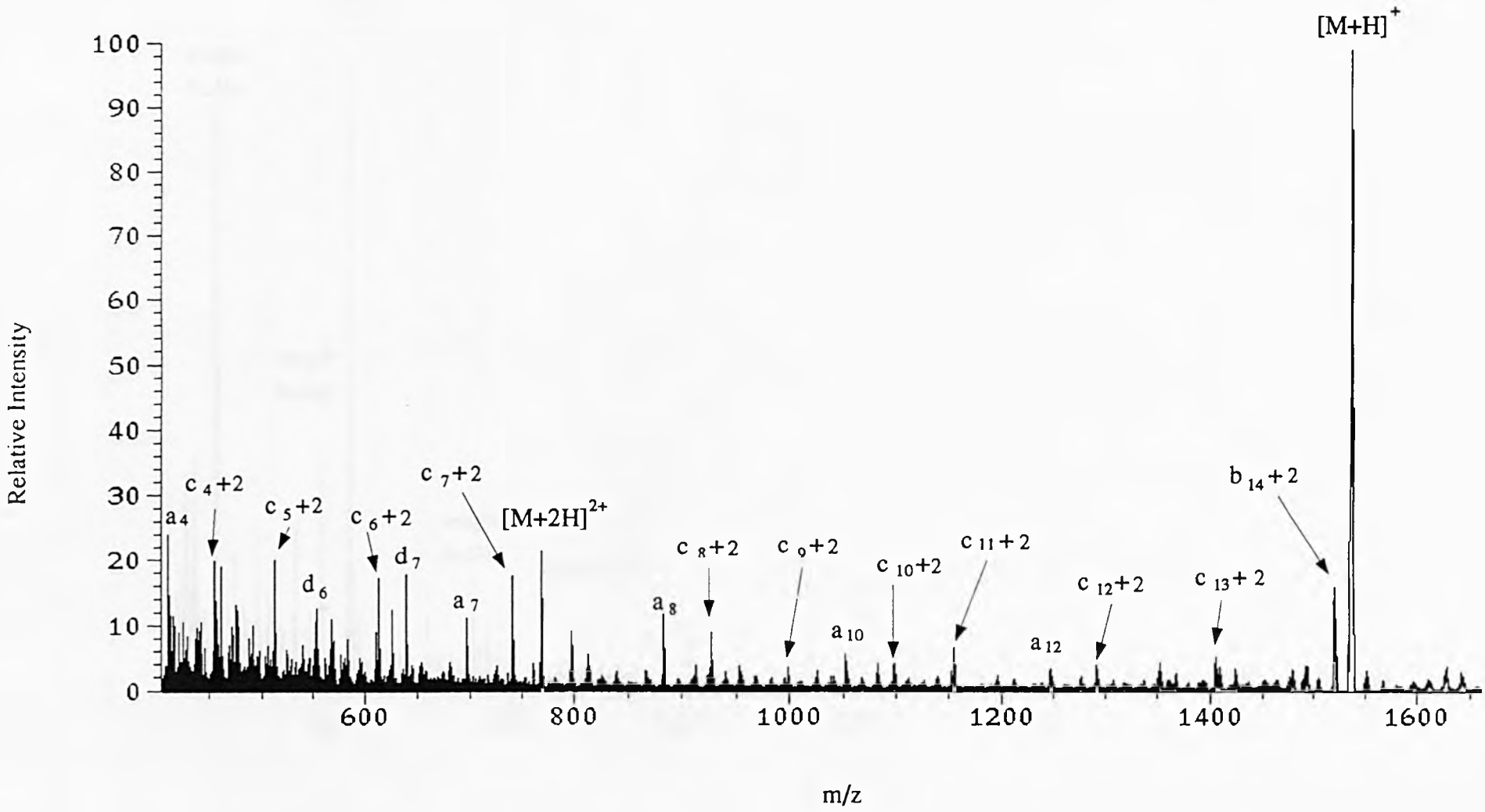

Figure 6.7: Mass spectrum of alytesin using thioglycerol:glycerol 1:1 + 1% trifluoroactic acid as the matrix.

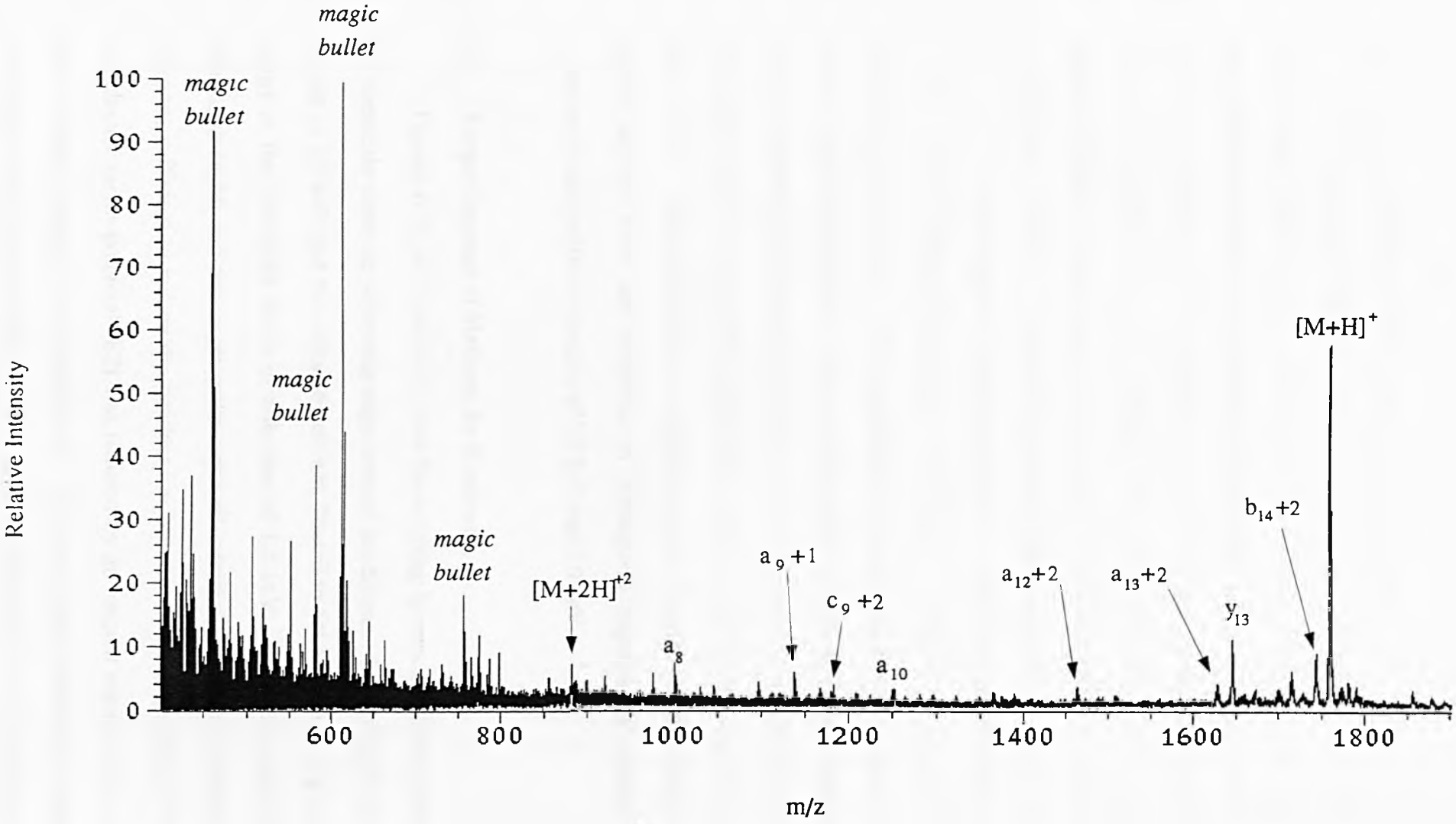

Figure 6.8: Mass spectrum of renin-substrate using *magic bullet* as a matrix.

6.2 Target Capture of Methane by Renin-Substrate.

To repeat and expand on the work done in Fenselau's laboratory [183] and to find working experimental conditions for the Kratos Concept IIHH instrument, experiments regarding renin-substrate collisions with methane were carried out. The protonated molecule of renin-substrate was focused into the collision cell of the four-sector mass spectrometer. The collision cell was floated above earth to provide a laboratory-frame collision energy of 2.4 keV. The β-slit width situated after the second electric sector was reduced to enhance energy resolution (N.B. Fenselau's group left the β-slits open in their experiments). Methane was introduced into the collision cell to attenuate the parent ion signal to 60% of its original intensity (Fenselau *et al* used 70%) . The second electric sector potential was reduced until the adduct ion could be observed. The second magnet was subsequently scanned. In the resulting spectra, an example of which is shown in figure 6.9, a peak at a mass of 14 Da greater than the mass of the protonated molecule was observed and assigned as $[MH + 14]^+$. This observation is consistent with Fenselau *et al*'s. findings [183]. Adduct species were not observed in subsequent experiments carried out at laboratory-frame collision energies of 2.0 keV and 3.0 keV.

6.3 Target Capture of Methane by Bombesin.

Figures 6.10, 6.11 and 6.12 show the resulting spectra obtained with methane and bombesin from the following experimental conditions. The incident ion energy was set to 7.9 keV and the collision cell was floated to 6.4 kV producing a collision energy in the laboratory frame of reference of 1.5 keV. The β-slit (after E2) was reduced in width and the target gases were all introduced into the collision cell at pressures sufficient to reduce the incident ion beam to 30% of its original intensity. The electric sector potential (E2) was reduced by an amount equal to the centre-of-mass collision energy, see equation (18). The two peaks observed in figure 6.10 correspond to the protonated molecule of bombesin $[M+H]^+$ and to an adduct species

$[MH+14]^+$. Figure 6.11 shows the spectrum observed when ^{13}carbon methane was used as the target gas. The adduct peak appears at $[MH+15]^+$. When the target gas was changed to perdeuterated methane, the adduct peak shifted to $[MH+17]^+$ as shown in figure 6.12.

Similar results were obtained when the collision cell potential was altered by small amounts. A floating potential of 5.9 kV created a laboratory-frame collision energy of 2.0 keV. Figures 6.13 and 6.14 show results from collisions of bombesin with methane and deuterated methane, respectively, at this laboratory-frame collision energy. Figure 6.13 was obtained from an E2 potential energy deficit of 175 eV and figure 6.14 was obtained from an E2 potential energy deficit equivalent to the centre-of-mass collision energy. Once more the β-slit was reduced to enhance energy resolution, gas pressure was sufficient to reduce the parent ion to 30% of its original intensity. Adduct peaks at $[MH+14]^+$ and $[MH+17]^+$ were observed. In total, five different laboratory-frame collision energies were tested for bombesin/methane collisions, as shown in table 6.1. Adducts were observed at 1.5 keV, 2.0 keV and 2.5 keV collision energies only. Deuterated methane collision experiments produced adducts at 1.0 keV, 1.5 keV and 2.0 keV collision energies only. Experiments with ^{13}carbon methane were only carried out at a laboratory-frame collision energy of 1.5 keV.

It would appear from the methane and ^{13}carbon methane collision experiments that the $[MH+14]^+$ and $[MH+15]^+$ peaks are either the result of CH_2 and $^{13}CH_2$ remaining associated with the protonated molecule $[M+H]^+$ or $CH_3^{\cdot}$ and $^{13}CH_3^{\cdot}$ associating with $[M]^{+\cdot}$ species. The results obtained with perdeuterated methane show the latter situation is the only feasible arrangement. If CD_2 from CD_4 associated with the $[M+H]^+$ ion, a mass shift of +16 Da from the parent ion would be expected. An adduct peak with a +17 Da mass increase from the parent ion, as shown in figures 6.12 and 6.14, was actually observed. The formation of a $[CD_3M]^+$ collision complex would result in the +17 Da mass increase. One hydrogen atom, therefore, has been removed from the protonated molecule and one

hydrogen/deuterium atom removed from the target gas. The peak at $[MH+14]^+$ with CH_4 therefore could the be assigned as $[MH+CH_4-2H]^+$. $[MH+15]^+$ with $^{13}CH_4$ would represent $[MH+^{13}CH_4-2H]^+$ and $[MH+17]^+$ with CD_4 would represent $[MH+CD_4-H-D]^+$. Fenselau *et al.* [183] concluded likewise.

6.4 Target Capture of Methane by Alytesin.

Figures 6.15, 6.16 and 6.17 show results for collisions between alytesin and methane, ^{13}carbon methane and perdeuterated methane, respectively, at a laboratory-frame collision energy of 1.5 keV and an E2 potential energy deficit that corresponded to the centre-of-mass collision energy. Methane and deuterated methane target gases gave the same results when the laboratory-frame collision energy was increased to 2.0 keV, (see figures 6.18 and 6.19). Figure 6.18 was obtained when the E2 potential was reduced by 175 eV. For an E2 potential energy deficit that corresponded to the centre-of-mass collision energy, figure 6.19 was obtained. As with bombesin, collisions of alytesin with methane resulted in an adduct peak $[MH+14]^+$. ^{13}Carbon methane gave rise to an adduct peak at $[MH+15]^+$ and perdeuterated methane produced an adduct peak at $[MH+17]^+$. Each collision gas was introduced into the collision cell such that the parent ion was reduced to 30% of its original intensity after the E2 β-slit had been reduced in width. Other laboratory-frame collision energies were tested and methane was found to form adduct species at 1.5 keV and 2.0 keV. Deuterated methane/alytesin collisions resulted in $[MH+17]^+$ peaks at 1.0 keV, 1.5 keV and 2.0 keV, see table 6.2. ^{13}Carbon methane was only studied at the one laboratory-frame collision energy: E_{lab} = 1.5 keV. As before $[MH+14]^+$ with CH_4 has been assigned as $[MH+CH_4-2H]^+$, $[MH+15]^+$ with $^{13}CH_4$ as $[MH+C^{13}H_4-2H]^+$ and $[MH+17]^+$ with CD_4 as $[MH+CD_4-H-D]^+$.

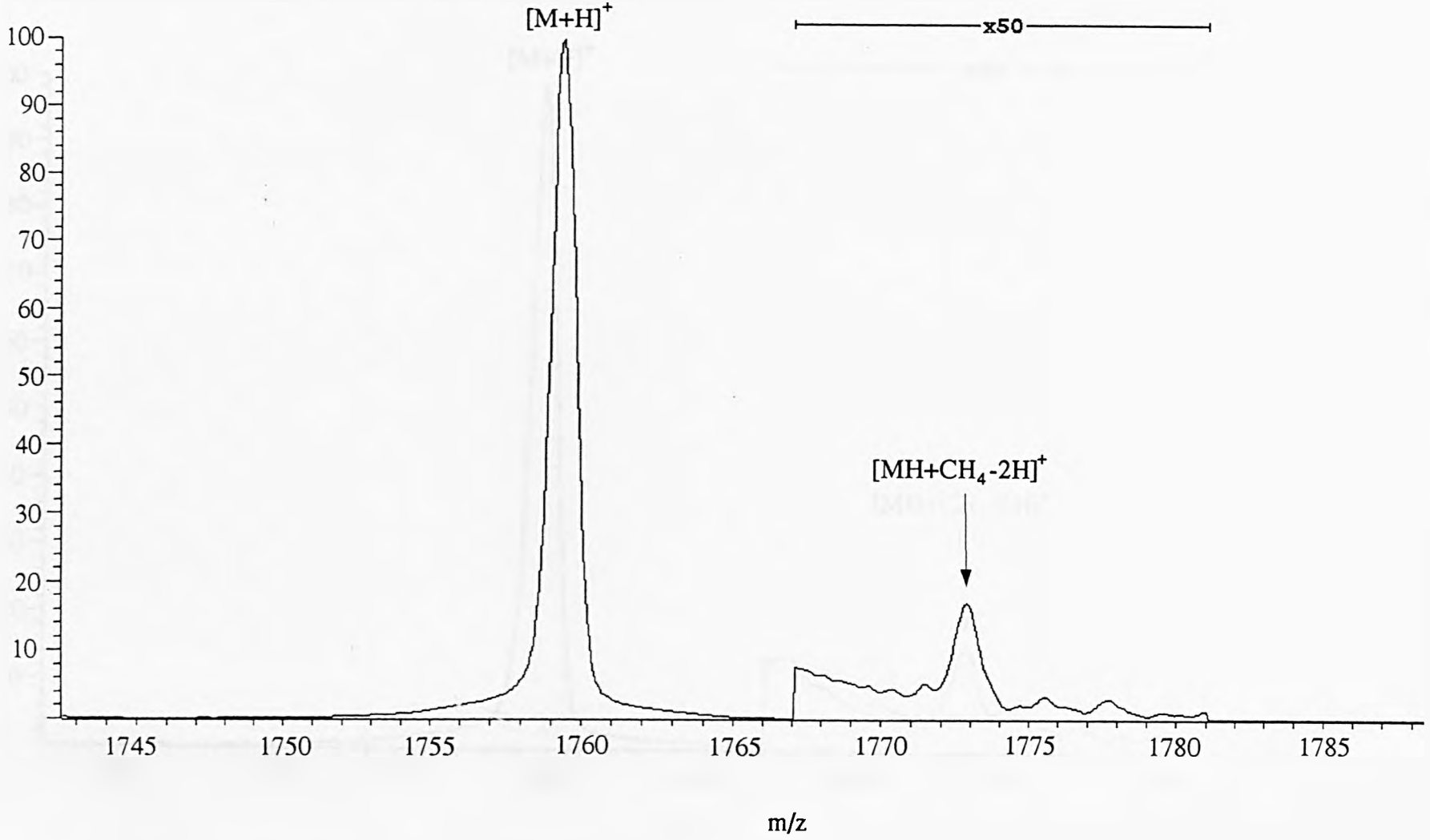

Figure 6.9: Magnet scan of renin-substrate and methane at E_{lab} = 2.4 keV.

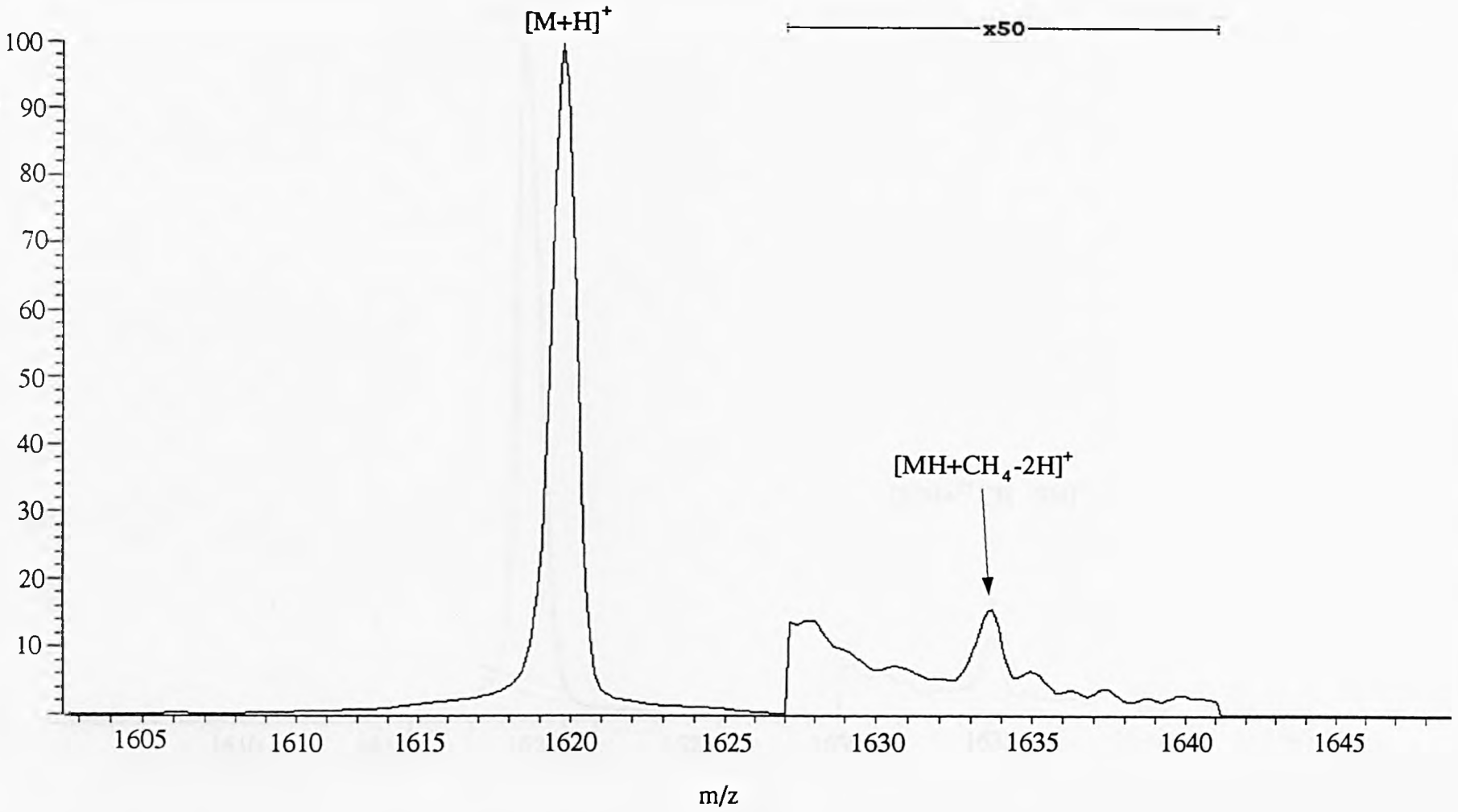

Figure 6.10: Magnet scan of bombesin and methane at E_{lab} = 1.5 keV.

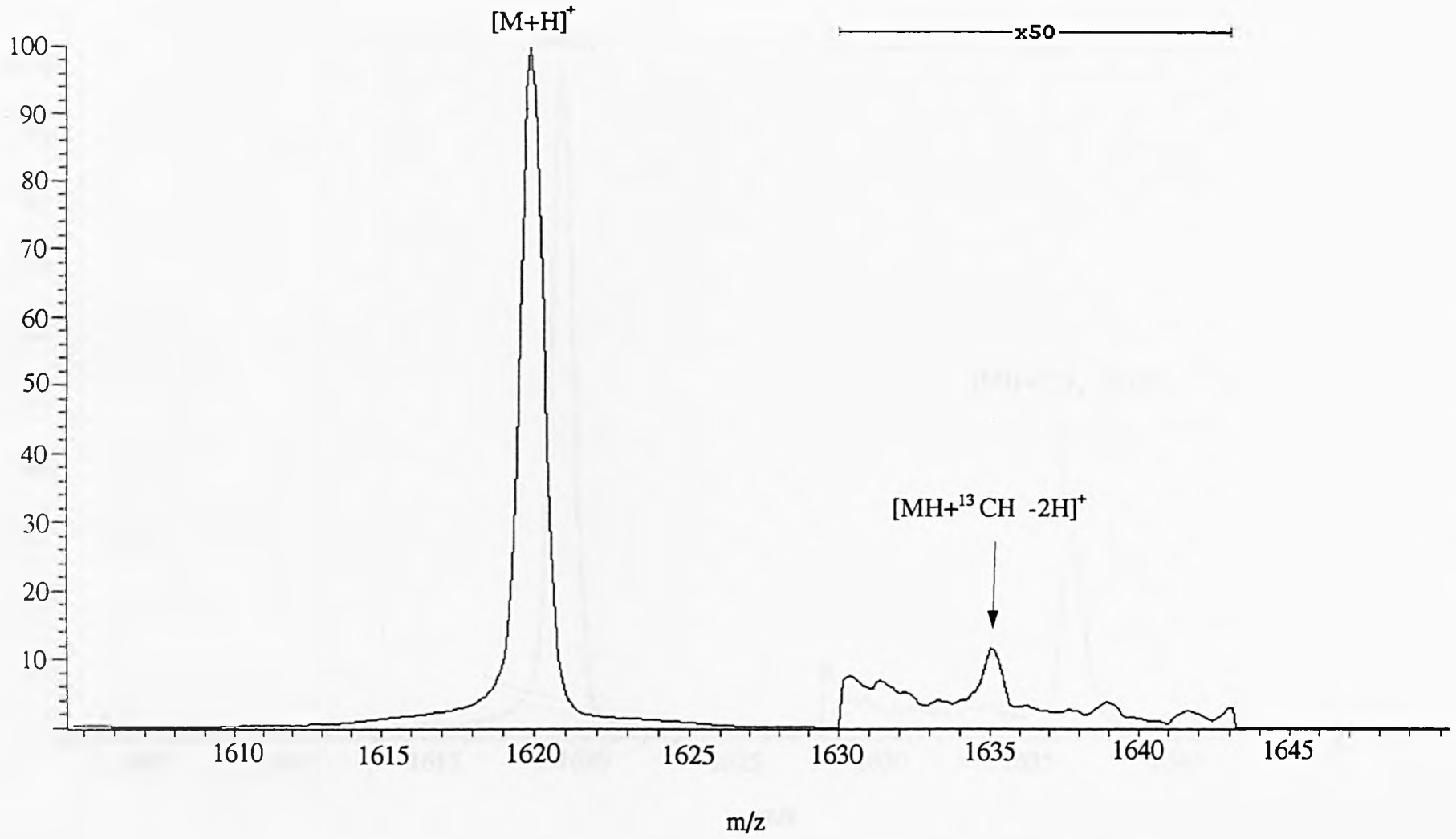

Figure 6.11: Magnet scan of bombesin and^{13} carbon methane at E_{lab} = 1.5 keV.

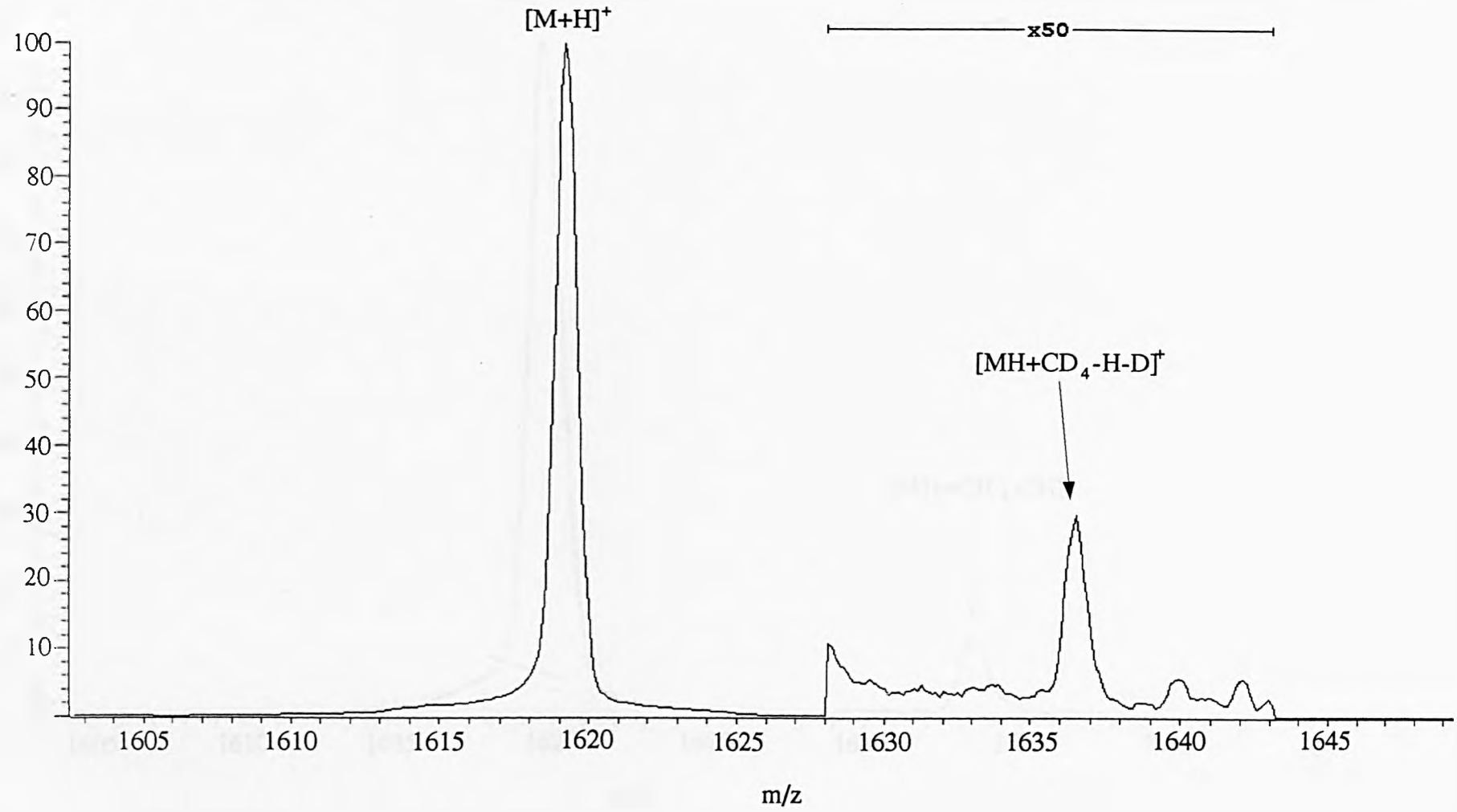

Figure 6.12: Magnet scan of bombesin and deuterated methane at E_{lab} = 1.5 keV.

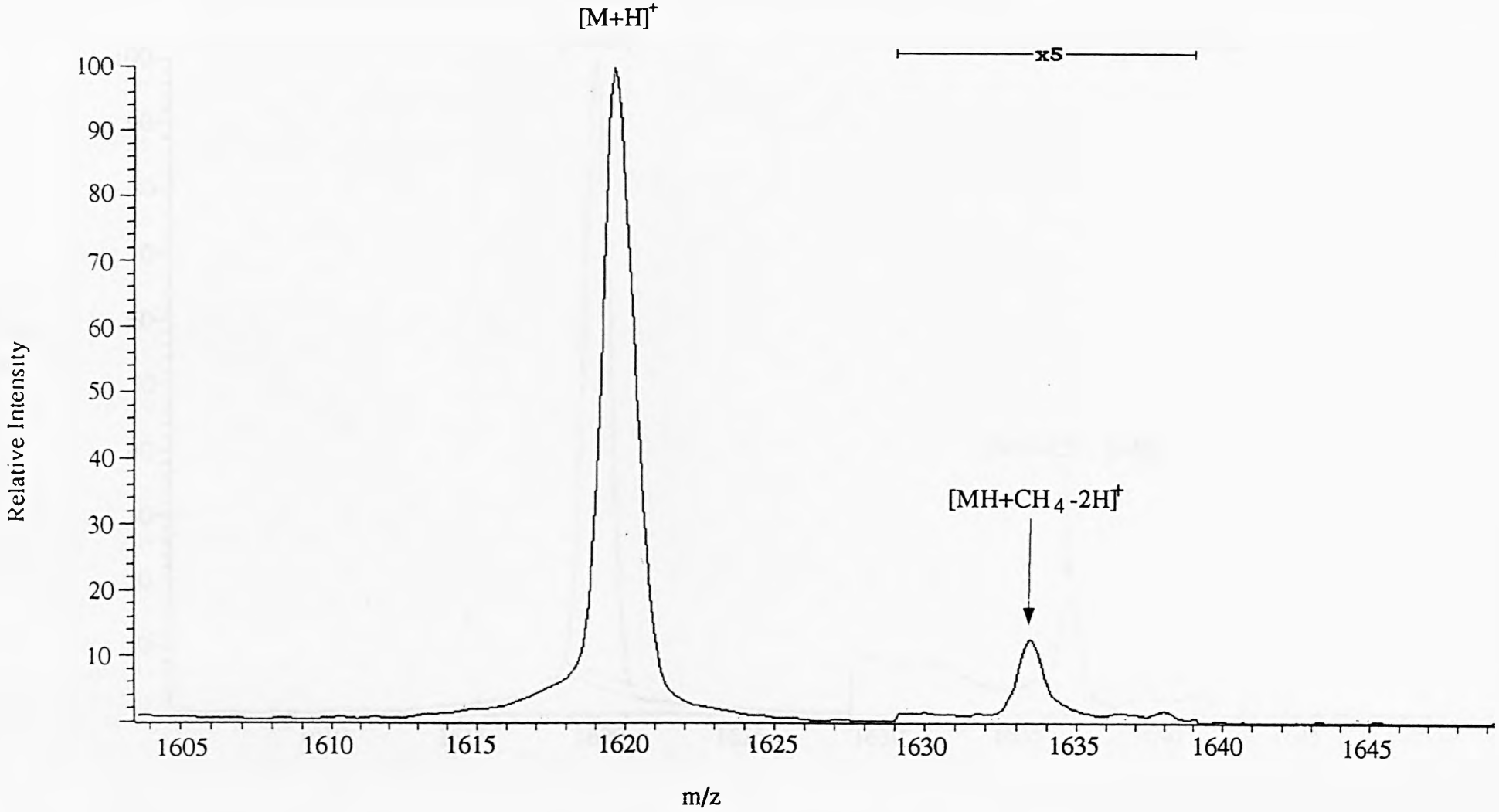

Figure 6.13: Magnet scan of bombesin and methane at E_{lab} = 2.0 keV.

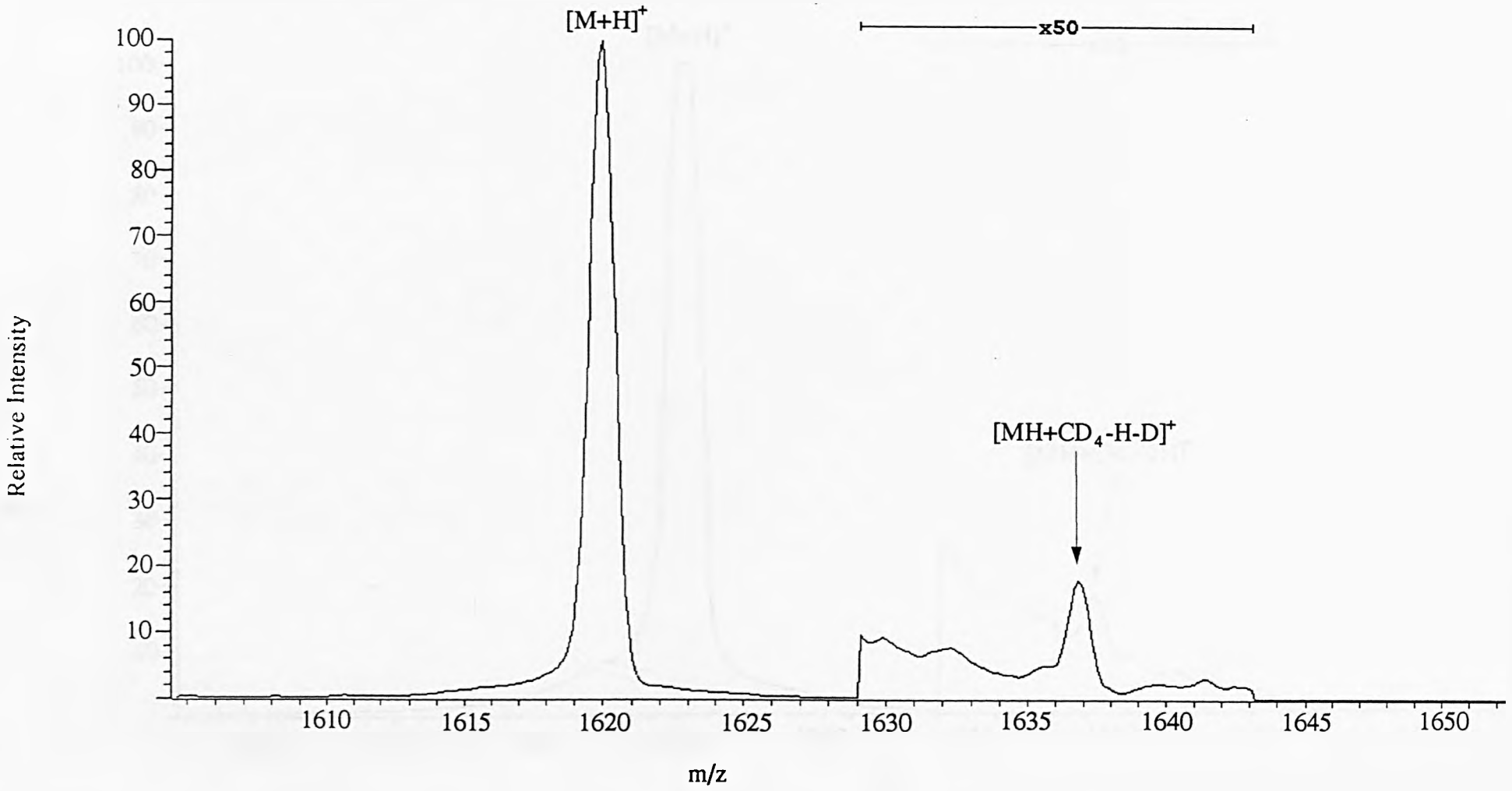

Figure 6.14: Magnet scan of bombesin and deuterated methane at E_{lab} = 2.0 keV.

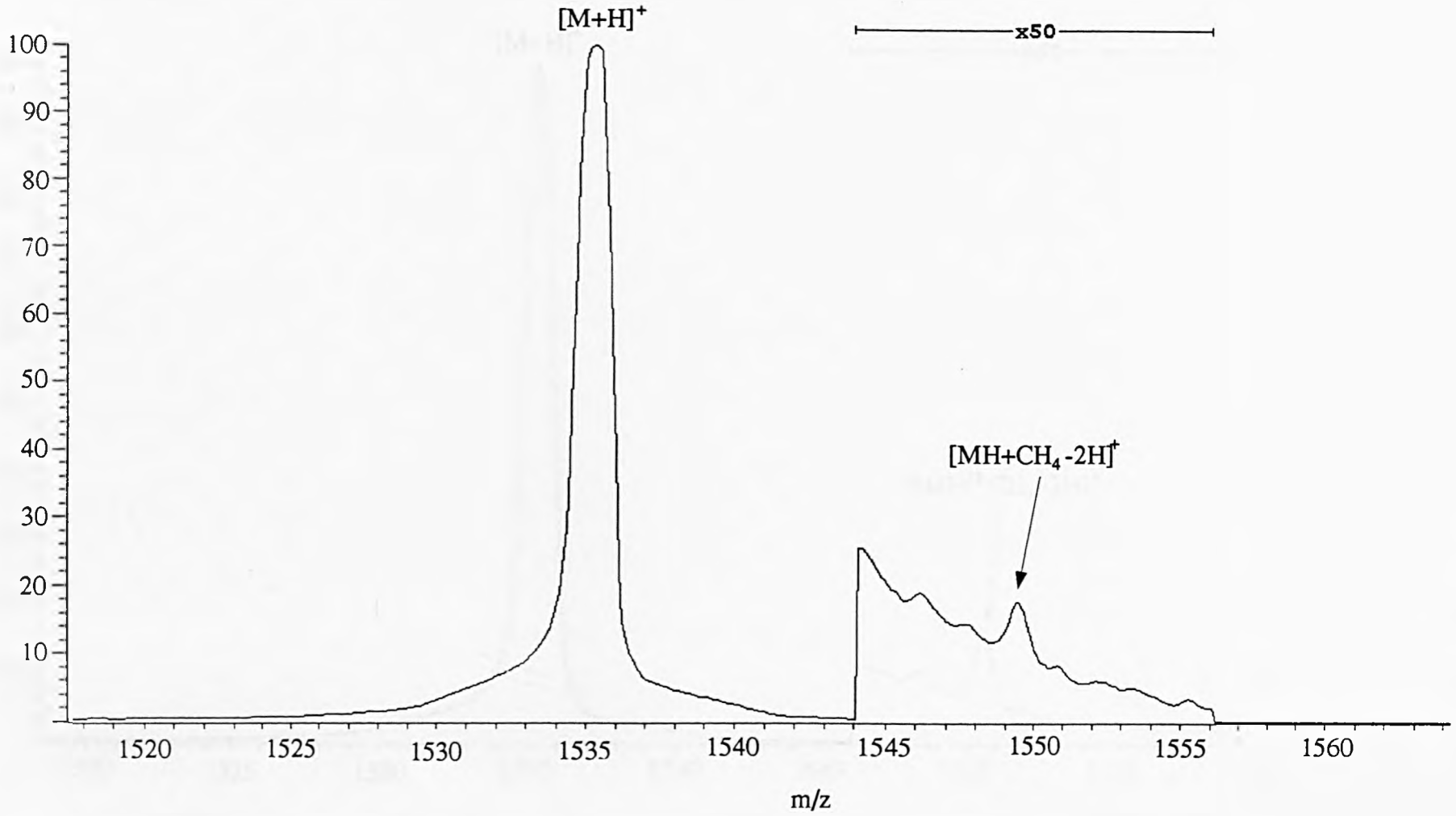

Figure 6.15: Magnet scan of alytesin and methane at E_{lab} = 1.5 keV.

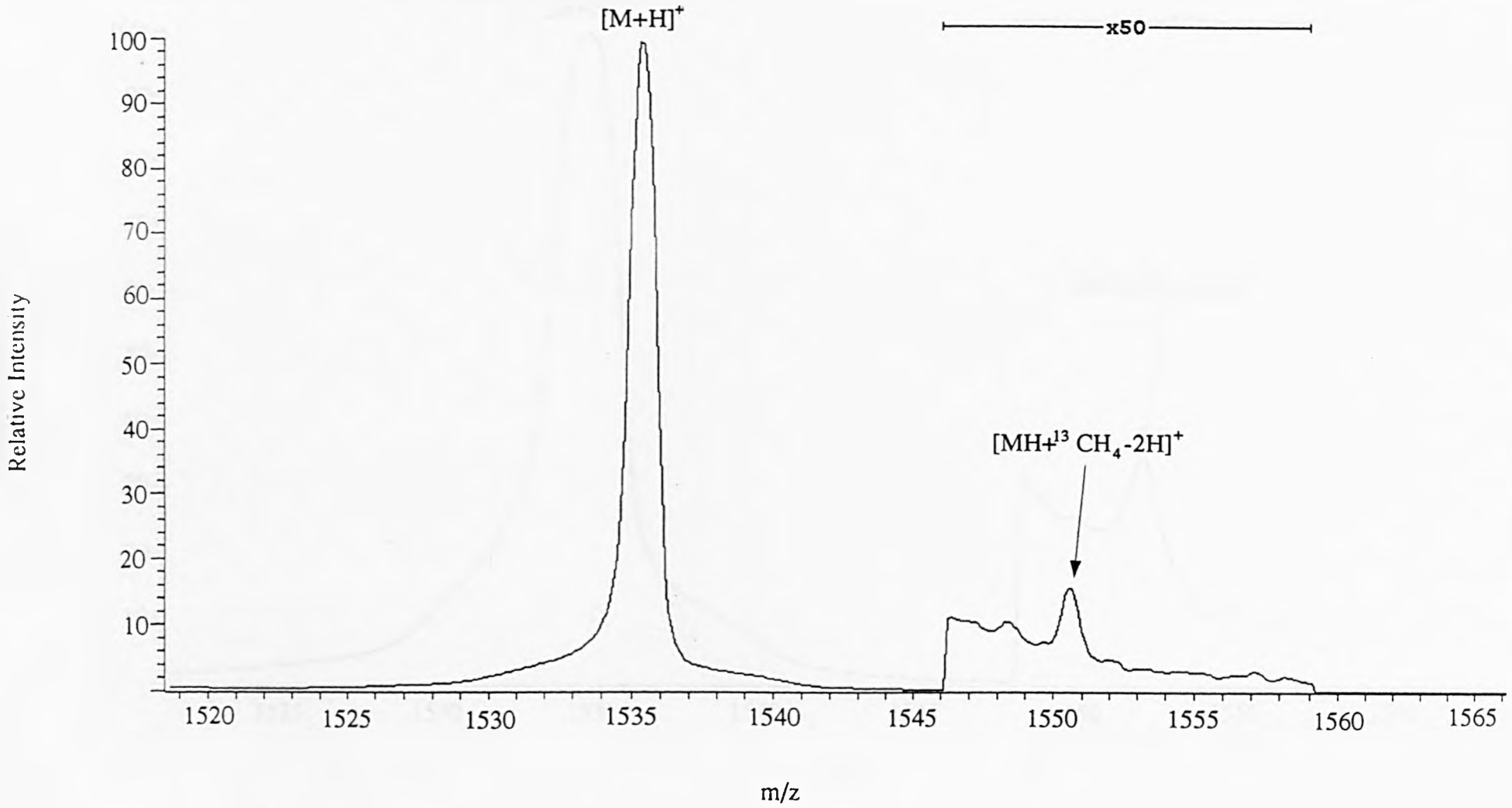

Figure 6.16: Magnet scan of alytesin and ^{13} carbon methane at E_{lab} = 1.5 keV.

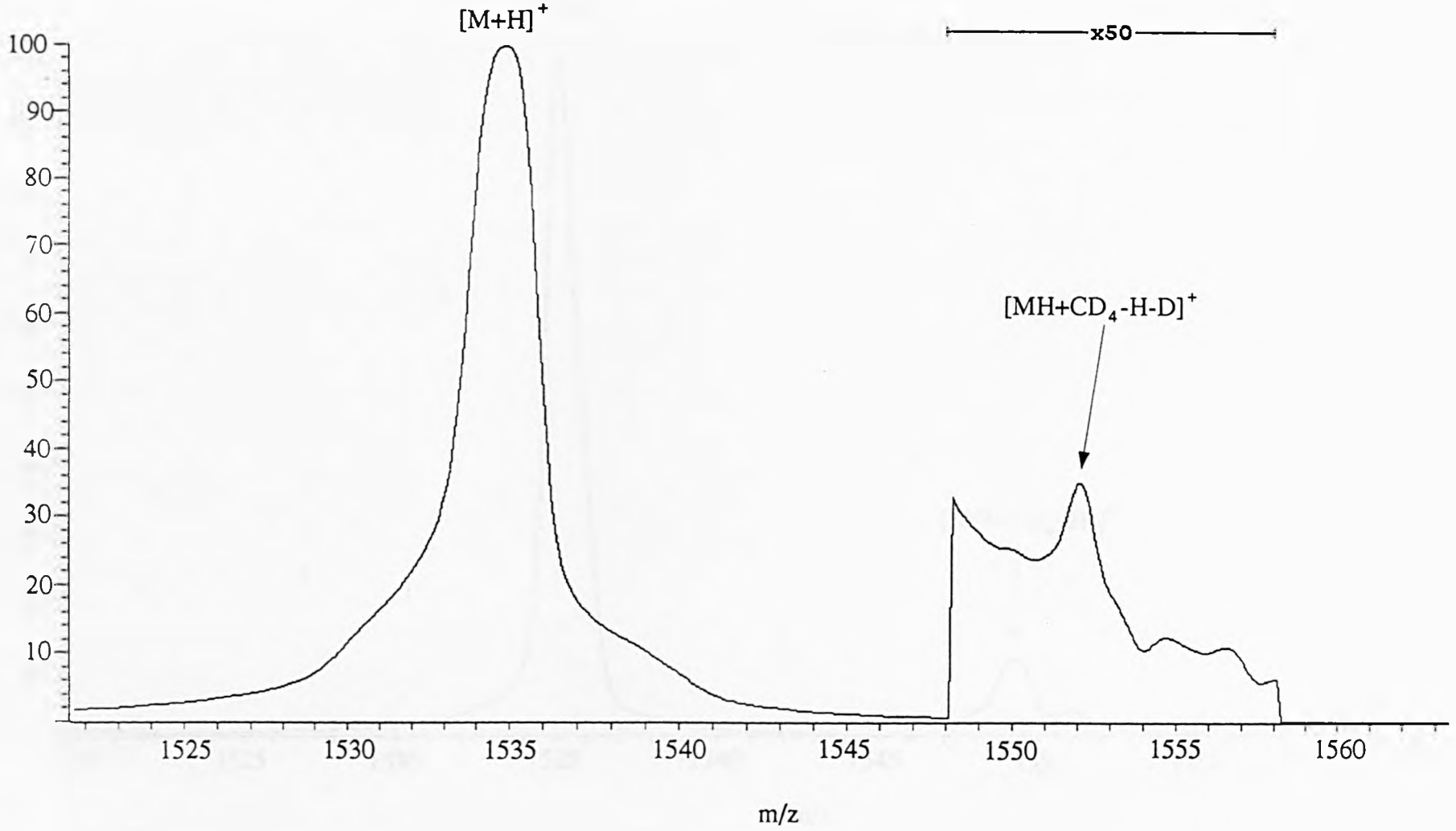

Figure 6.17: Magnet scan of alytesin and deuterated methane at E_{lab} = 1.5 keV.

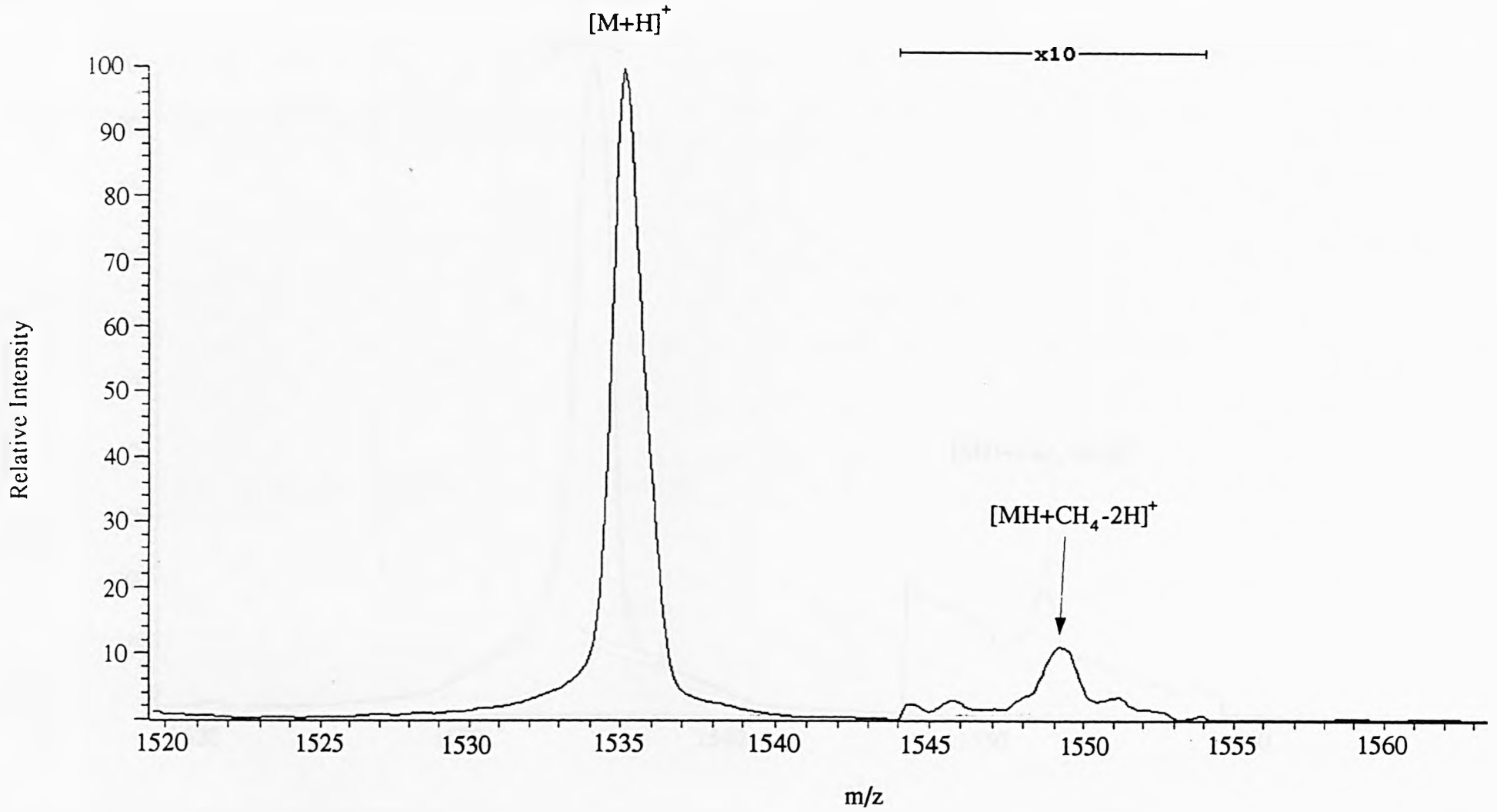

Figure 6.18: Magnet scan of alytesin and methane at E_{lab} = 2.0 keV.

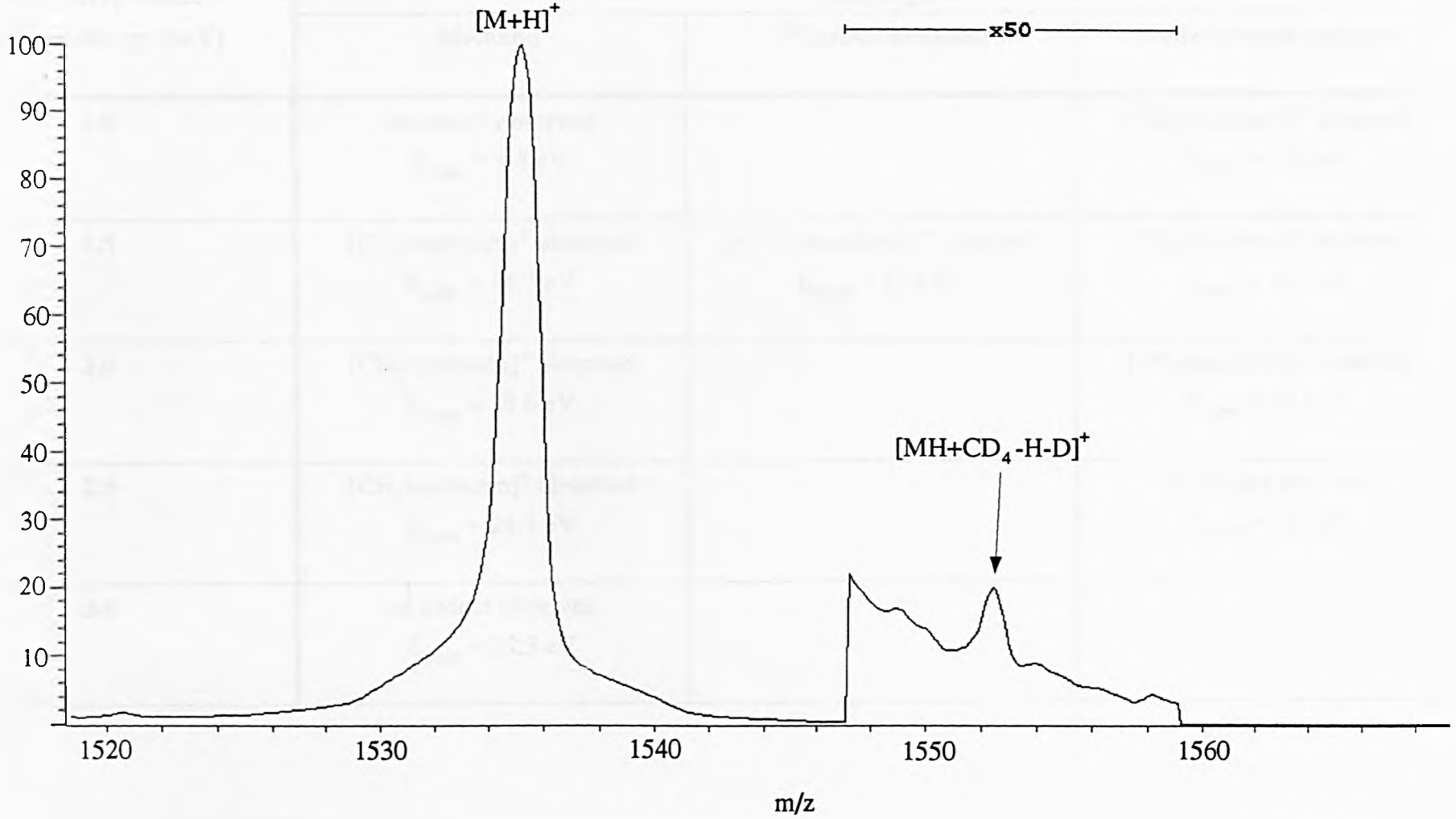

Figure 6.19: Magnet scan of alytesin and deuterated methane at E_{lab} = 2.0 keV.

Laboratory-frame collision energy (keV)	Target gas		
	Methane	**^{13}Carbon methane**	**Perdeuterated methane**
1.0	no adduct observed E_{com} = 9.8 eV		$[CD_3bombesin]^+$ observed E_{com} = 12.2 eV
1.5	$[CH_3bombesin]^+$ observed E_{com} = 14.7 eV	$[C^{13}H_3bombesin]^+$ observed E_{com} = 15.6 eV	$[CD_3bombesin]^+$ observed E_{com} = 18.3 eV
2.0	$[CH_3bombesin]^+$ observed E_{com} = 19.6 eV		$[CD_3bombesin]^+$ observed E_{com} = 24.4 eV
2.5	$[CH_3bombesin]^+$ observed E_{com} = 24.5 eV		no adduct observed E_{com} = 30.5 eV
3.0	no adduct observed E_{com} = 29.3 eV		

Table 6.1: Laboratory-frame and centre-of-mass collision energies (E_{com}) at which bombesin adduct species were observed.

Laboratory-frame collision energy (keV)	Target das		
	Methane	**^{13}Carbon methane**	**Perdeuterated methane**
1.0	no adduct observed E_{com} = 10.3 eV		$[CD_3alytesin]^+$ observed E_{com} = 12.9 eV
1.5	$[CH_3alytesin]^+$ observed E_{com} = 15.5 eV	$[C^{13}H_3alytesin]^+$ observed E_{com} = 16.4 eV	$[CD_3alytesin]^+$ observed E_{com} = 19.3 eV
2.0	$[CH_3alytesin]^+$ observed E_{com} = 20.6 eV		$[CD_3alytesin]^+$ observed E_{com} = 25.7 eV
2.5	no adduct observed E_{com} = 25.8 eV		no adduct observed E_{com} = 32.1 eV

Table 6.2: Laboratory-frame and centre-of-mass collision energies (E_{com}) at which alytesin adduct species were observed.

CHAPTER SEVEN: *Fragmentation and Translational Energy Losses Suffered by Protonated Peptides During Collision-Induced Decomposition.*

7.1 Introduction.

As a way of studying the effects of a collision gas on an incident ion, a series of experiments were undertaken on protonated peptides. The peptides chosen for this study were bombesin and alytesin [200]. This study concerned the collision-induced decompositions (CID) of the peptide $[M + H]^+$ ions and the translational energy losses they observed following high-energy collisions. These peptide ions were ionised by LSIMS ionisation. MS-I was used to mass select the $[M + H]^+$ ion for each peptide. The accelerating potential was 7.9 kV and the collision cell was interchanged between a grounded potential and floated potentials. Target gases were introduced into the collision cell at pressures sufficient to reduce the parent ion to 30% of its original intensity (*i.e.* transmission T = 30%). A B/E linked scan carried out on MS-II was used to obtain collision-induced decomposition spectra. These spectra were recorded by the scanning array detector. Translational energy losses were determined from mass-analysed ion kinetic energy (MIKE) spectra. These MIKE spectra, obtained by scanning the second electric sector (E2), were recorded with a post-acceleration detector (PAD). The β-slit situated between E2 and the PAD detector was used to control the width of the transmitted ion beam at that point, and thereby vary the energy resolution obtained in the spectra.

7.2 Collision-Induced Decomposition of Peptide ions.

7.2.1 Atomic Collision Gases.

Collision-induced decomposition mass spectra following collisions between protonated bombesin and helium, neon, argon, krypton and xenon at a laboratory-frame collision energy of 3.9 keV are shown in figures 7.1 to 7.5. The centre-of-mass

frame collision energies, were 10 eV, 48 eV, 94 eV, 192 eV, and 292 eV respectively, for helium, neon, argon, krypton and xenon. Increasing the laboratory-frame collision energy to 5.9 keV with helium, argon and xenon increased the centre-of-mass collision energies to 15 eV, 142 eV and 441 eV respectively. Analyses of the spectra obtained at E_{lab} = 3.9 keV and E_{lab} = 5.9 keV are given in tables 7.1(a) and (b) respectively. Almost complete series of a-type fragment ions and d-type fragment ions were observed. Noted exceptions were at the fifth and eleventh amino acids. In bombesin both the fifth and the eleventh amino acid is a glycine residue. Fragmentation resulting in d-type ions is generally observed when the amino acid involved has a sidechain with more than two carbon atoms on it or is cyclic [160]. Glycine has no sidechain and would not be expected to produce d-type ions. Backbone cleavage next to glycine appears to be unfavourable for many peptides [155]. At E_{lab} = 3.9 keV the a_9-ion and d_9-ion were absent. The amino acid in the ninth position corresponds to alanine which has the second smallest sidechain, a methyl group, after glycine.

Helium-collisions gave rise to a few a-type and d-type fragment peaks, mainly from cleavages towards the middle of the peptide. Increasing the centre-of-mass collision energy by increasing the mass of the target gas led to a clear increase in the number of fragment peaks observed. The intensities of the fragment peaks, relative to the parent ion peak, increased for neon and argon, compared to helium. Krypton and xenon gave rise to fragment peaks of low intensities, however the identities of the fragment ions observed remained the same. Increasing the centre-of-mass collision energy by increasing the laboratory-frame collision energy did little to affect the number of fragment peaks observed, except in the case of helium. A significant increase in the number of fragment peaks was observed in changing from E_{lab} = 3.9 keV to E_{lab} = 5.9 keV. The same experiment using either argon or xenon as the target gas sufficed only in producing 'cleaner' spectra with the baseline noise much reduced.

For collision-induced decomposition of protonated alytesin at laboratory-frame collision energies of 3.9 keV (figures 7.6 to 7.8) and 5.9 keV with helium, argon and xenon, observations were broadly similar to those with bombesin. Descriptions of

alytesin fragment ions observed are given in tables 7.2(a) and (b). Like bombesin, the majority of peaks observed were a-type and d-type fragment ions. Gaps in the sequence of d-type ions once more corresponded to presence of glycine at positions five and eleven in the peptide chain. As with bombesin the a_5-ion was also absent. Unlike bombesin, the a_{11}-ion was observed when using argon and xenon as collision gases.

As a result of increasing the mass of the target gas, the degrees of fragmentation noticeably increased from helium to neon to argon. There was little difference in this respect between the spectra obtained using argon and xenon. Increasing the amount of translational energy available for uptake as internal energy by the incident ion by increasing the laboratory-frame collision energy from 3.9 keV to 5.9 keV had little effect when using argon or xenon, other than to enhance the clarity of the spectra. With helium, fragmentation of alytesin was only observed from collisions at E_{lab} = 5.9 keV.

7.2.2 Molecular Collision Gases.

As an extension of the CID experiments carried out with atomic gases, methane was employed as a target gas. Figure 7.9 shows the bombesin spectrum at a laboratory-frame collision energy of 3.9 keV. The maximum amount of energy available, from a single collision, for uptake by protonated bombesin would have been 38 eV. The fragment ions observed were similar to those observed with the noble gases. Series of a-type fragment peaks and d-type fragment peaks from the fourth to the thirteenth amino acid dominated the spectrum with notable absences coinciding with the occurrence of glycine at two positions in the amino acid chain. A summary of fragment peaks observed is included in table 7.1(a).

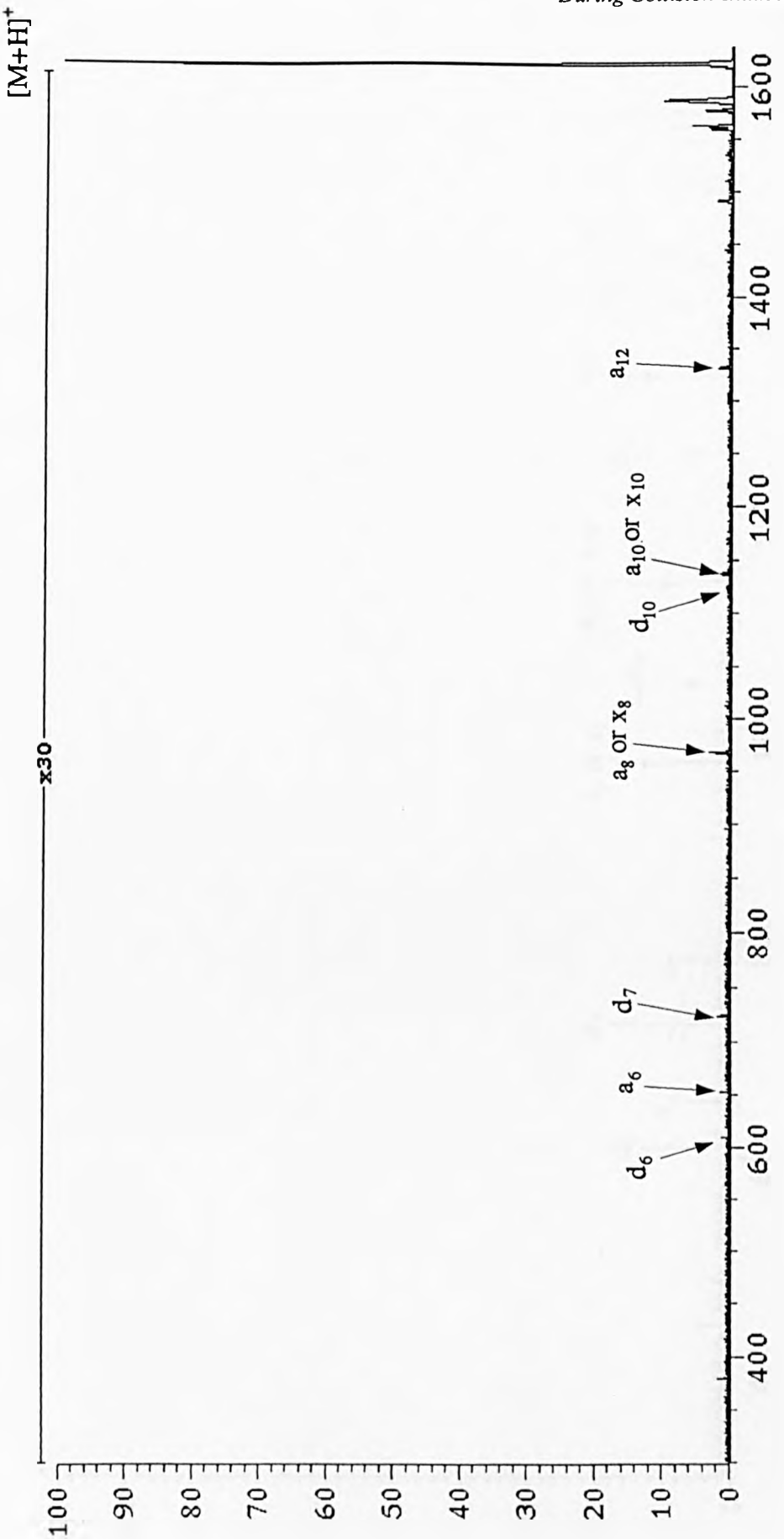

Figure 7.1: B/E scan of bombesin $[M+H]^+$ ion. Target gas was helium.

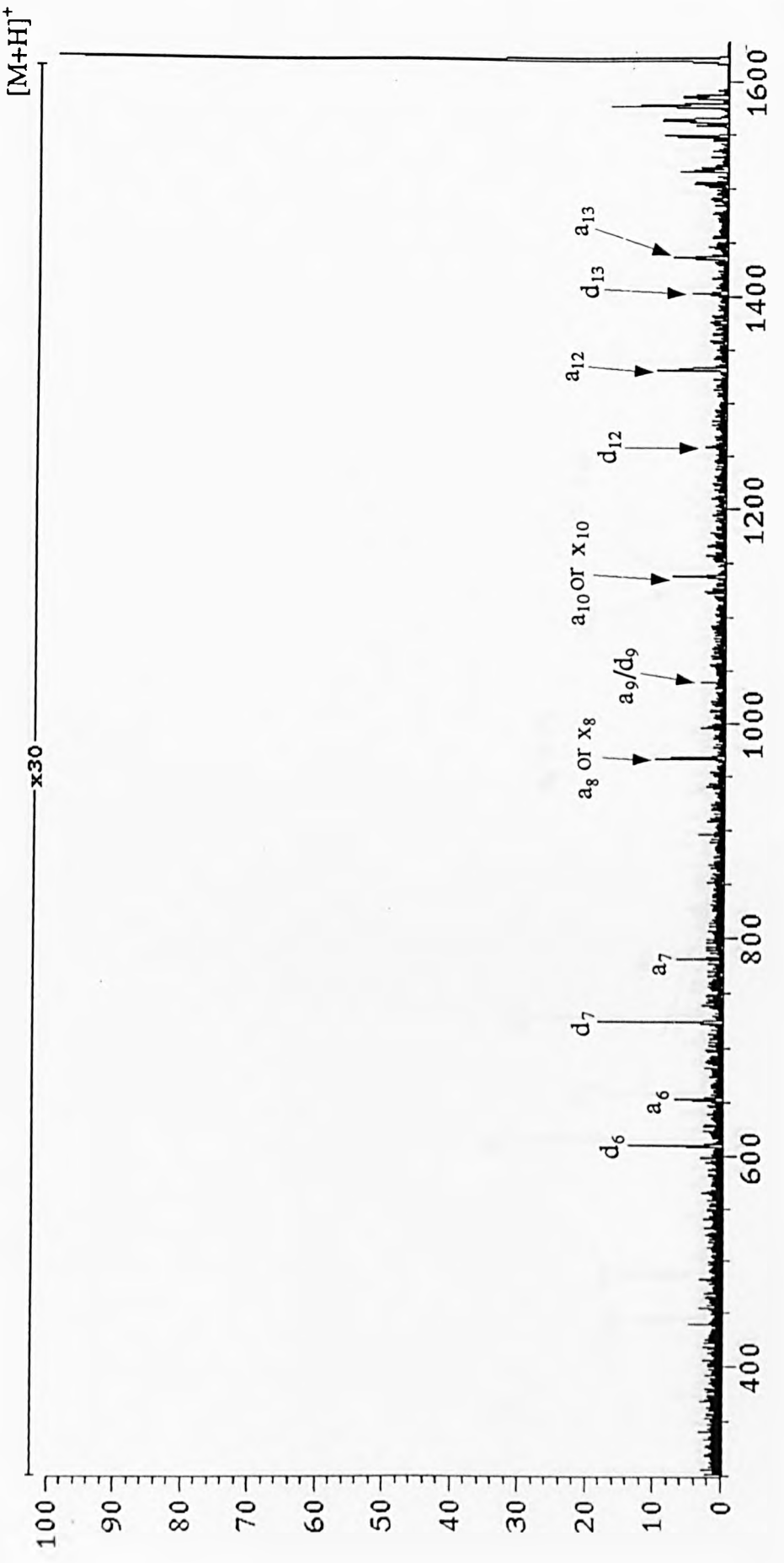

Figure 7.2: B/E scan of bombesin $[M+H]^+$ ion. Target gas was neon.

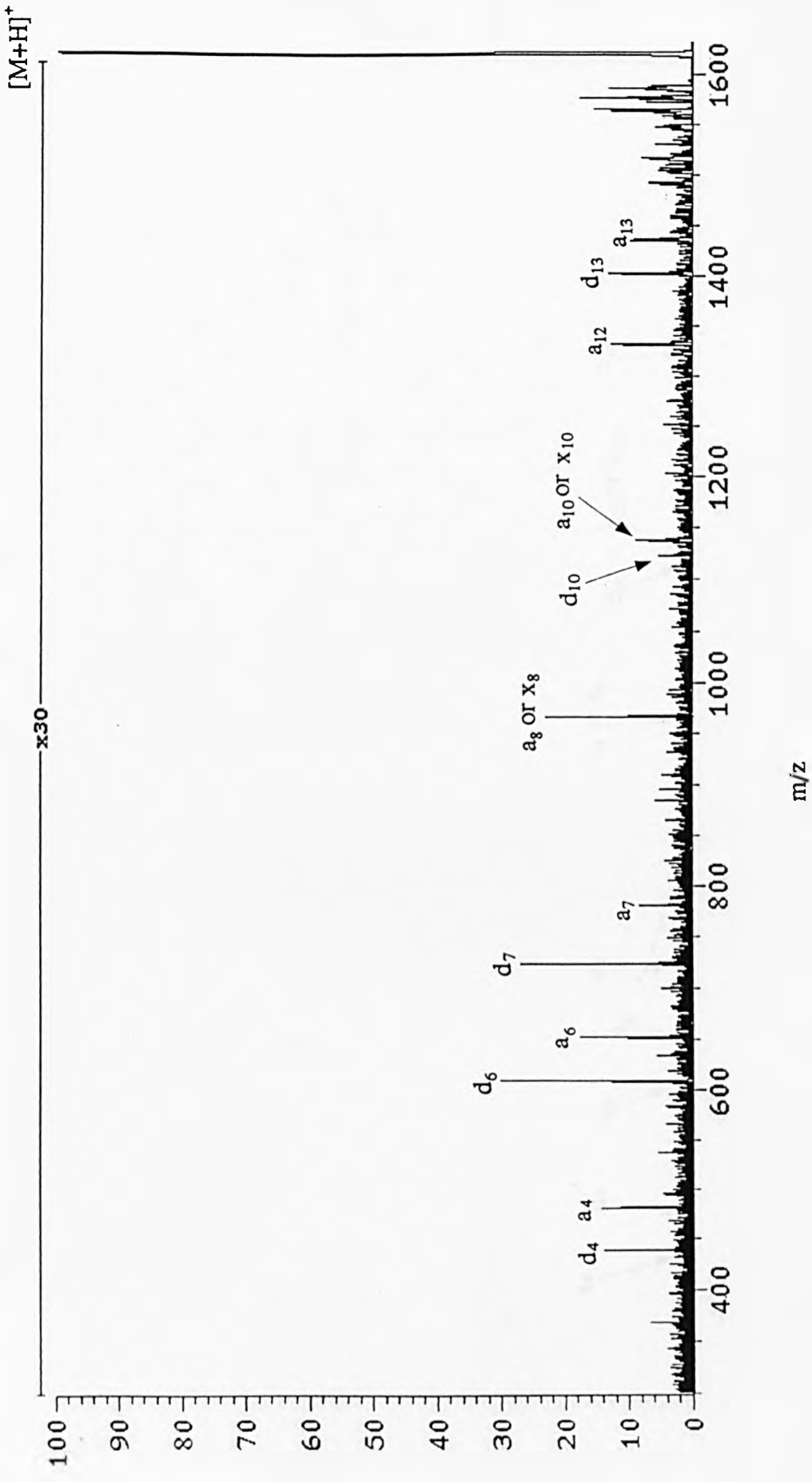

Figure 7.3: B/E scan of bombesin $[M+H]^+$ ion. Target gas was argon.

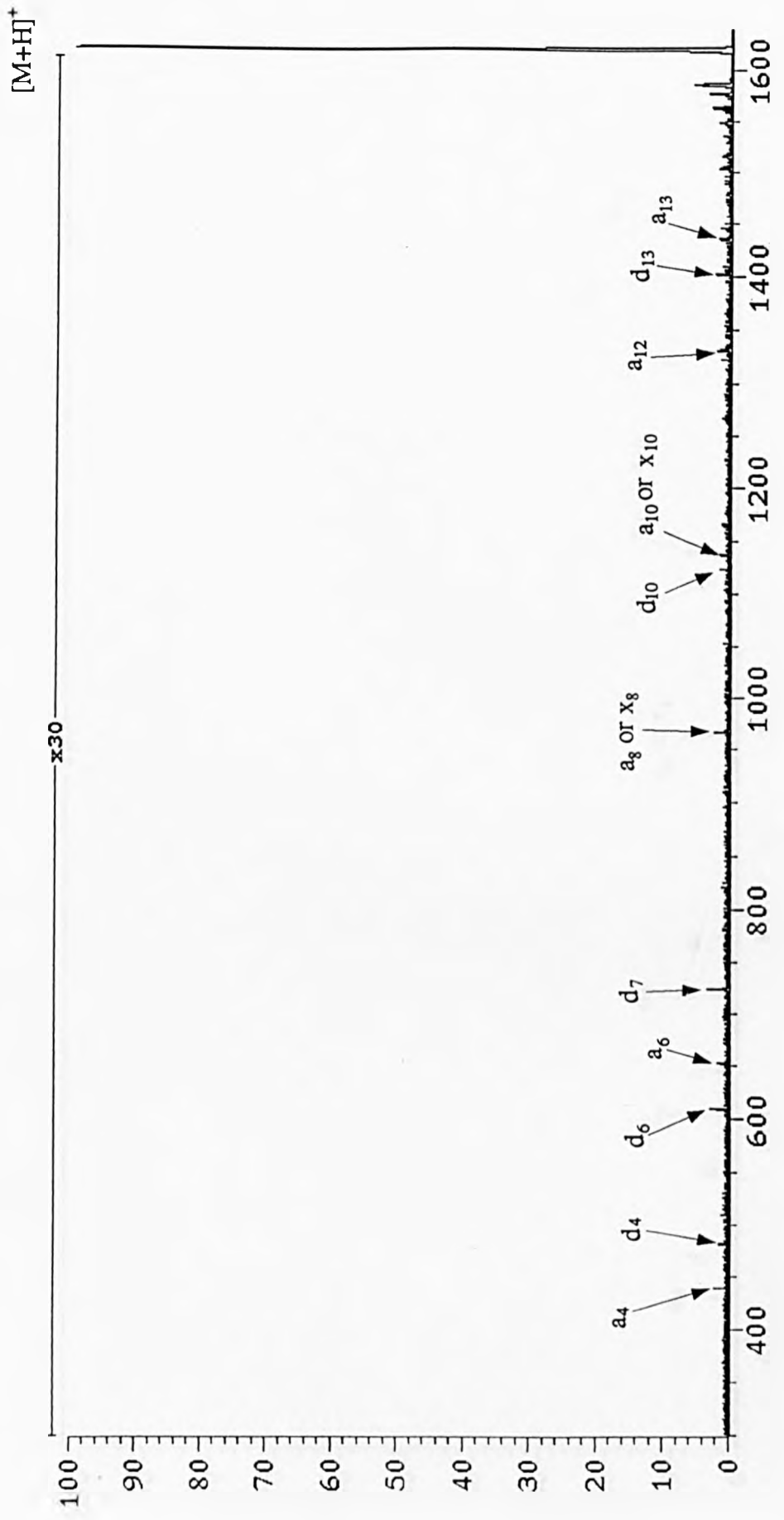

Figure 7.4: B/E scan of bombesin $[M+H]^+$ ion. Target gas was krypton.

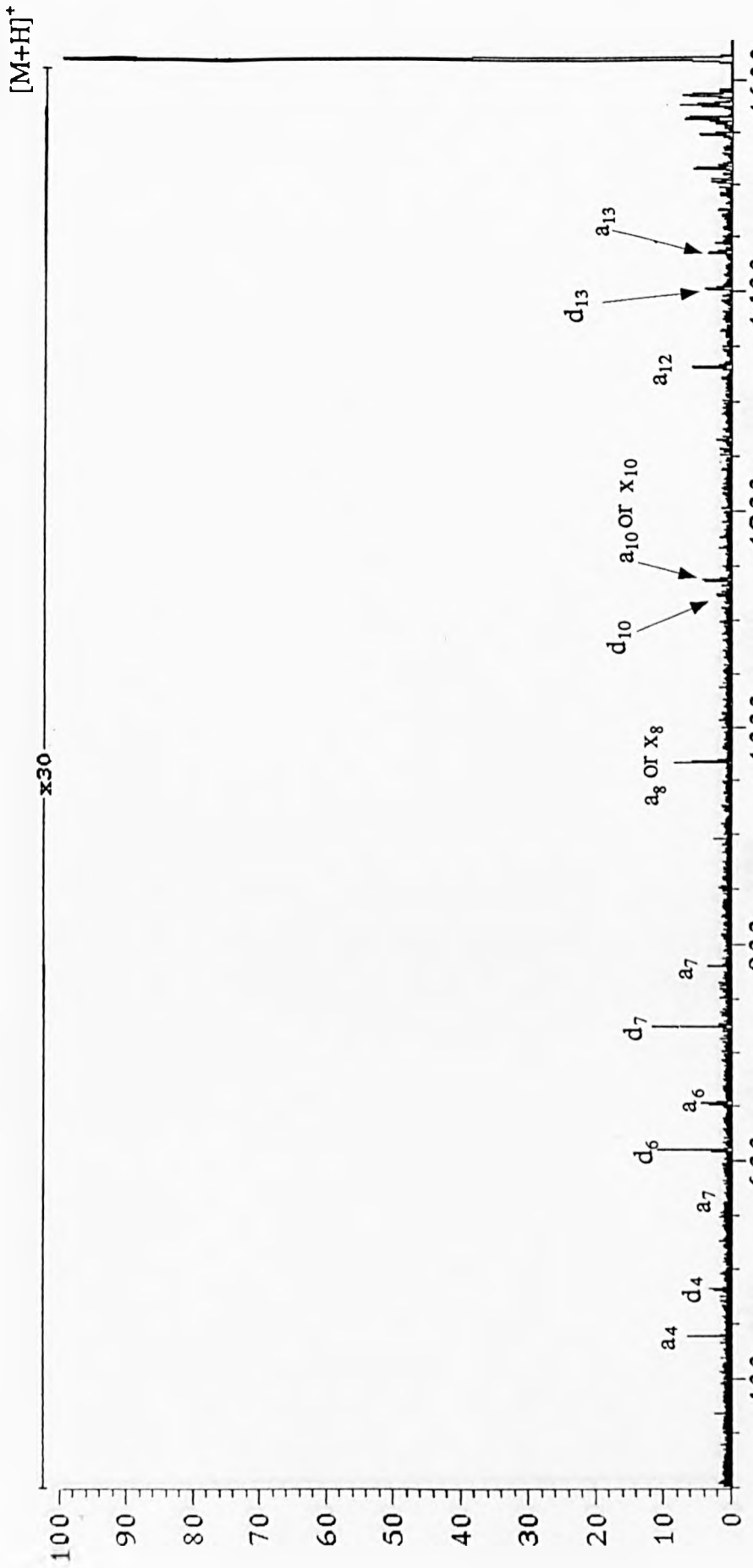

Figure 7.5: B/E scan of bombesin $[M+H]^+$ ion. Target gas was xenon.

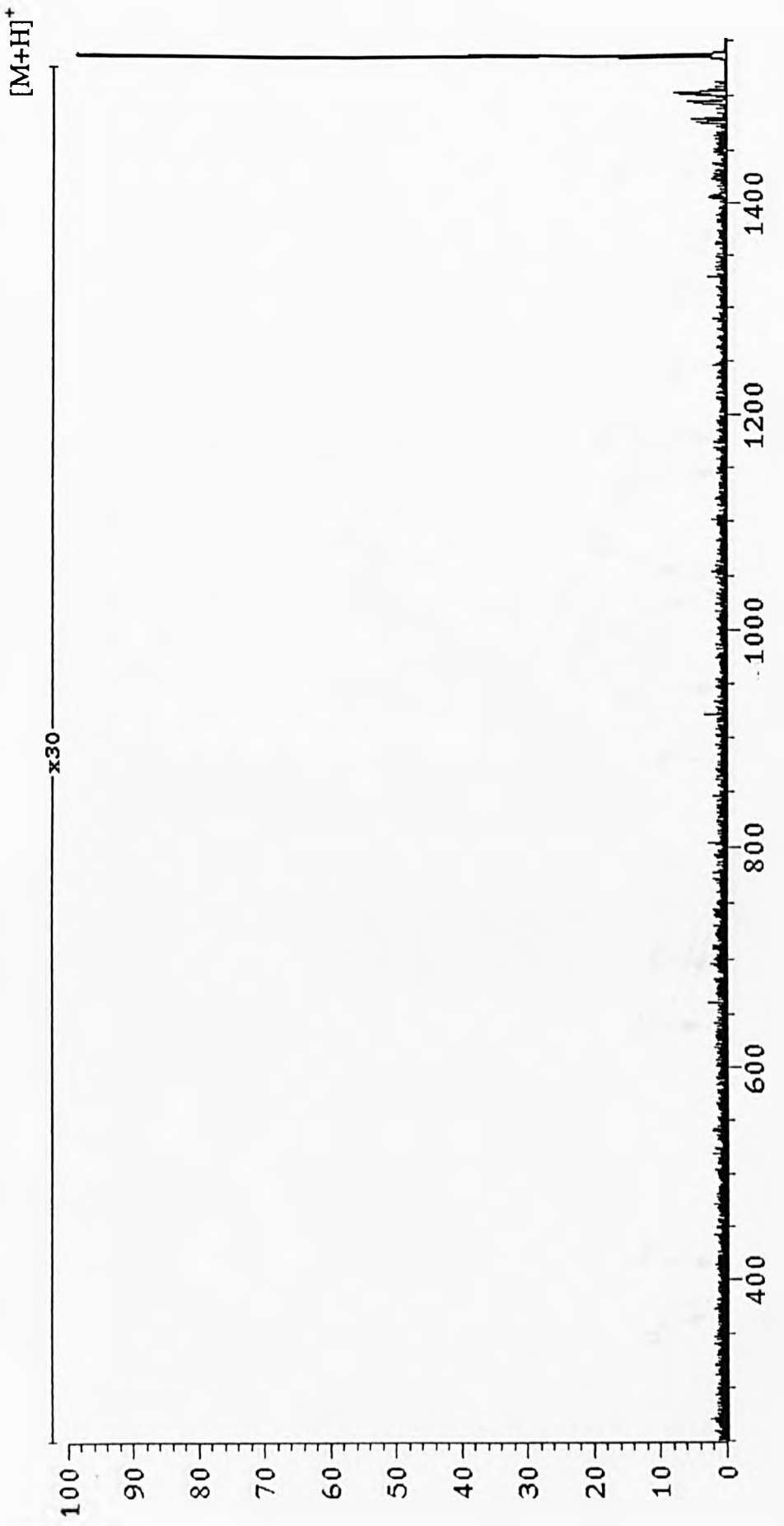

Figure 7.6: B/E scan of alytesin $[M+H]^+$ ion. Target gas was helium.

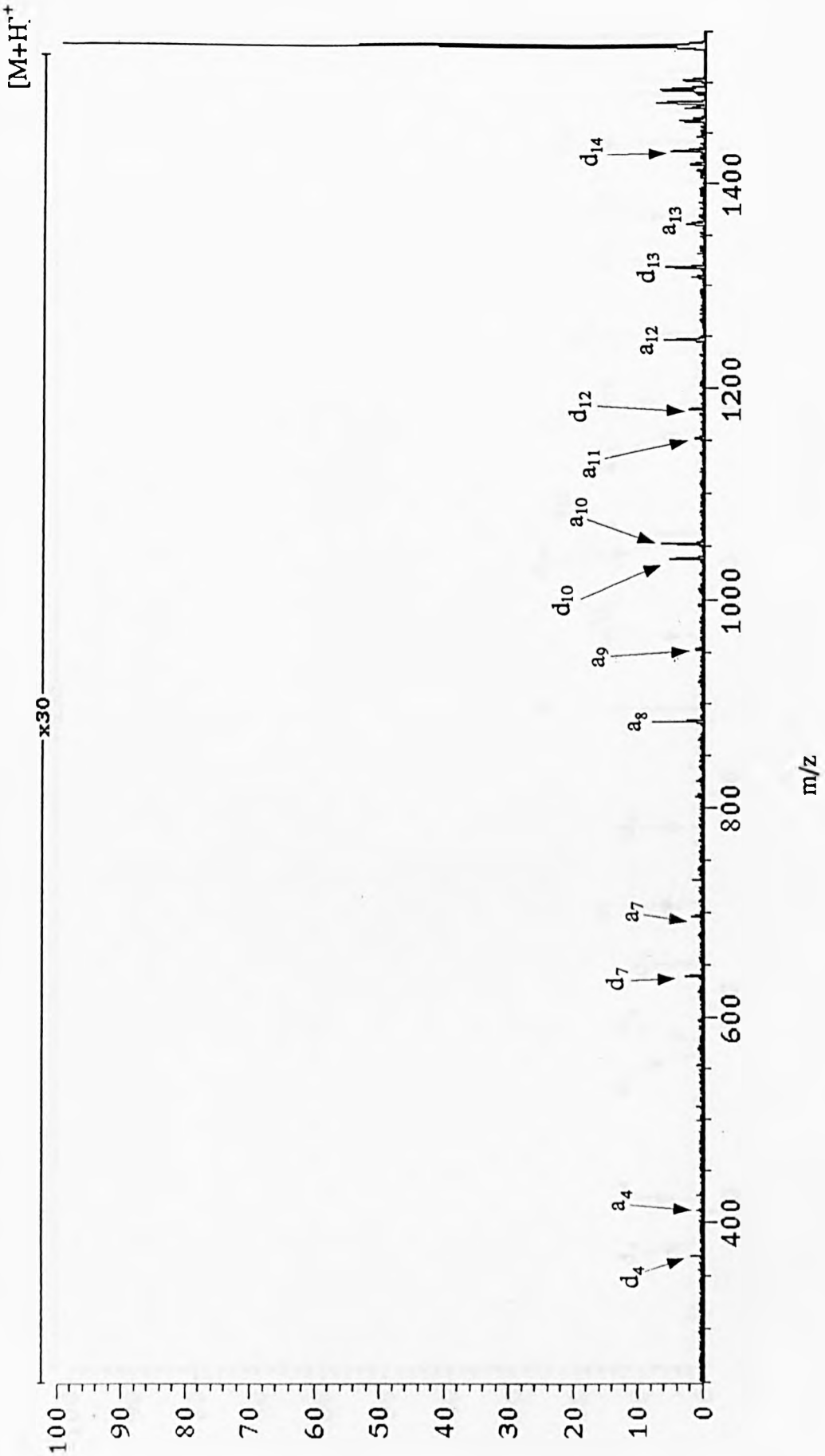

Figure 7.7: B/E scan of alytesin $[M+H]^+$ ion. Target gas was argon.

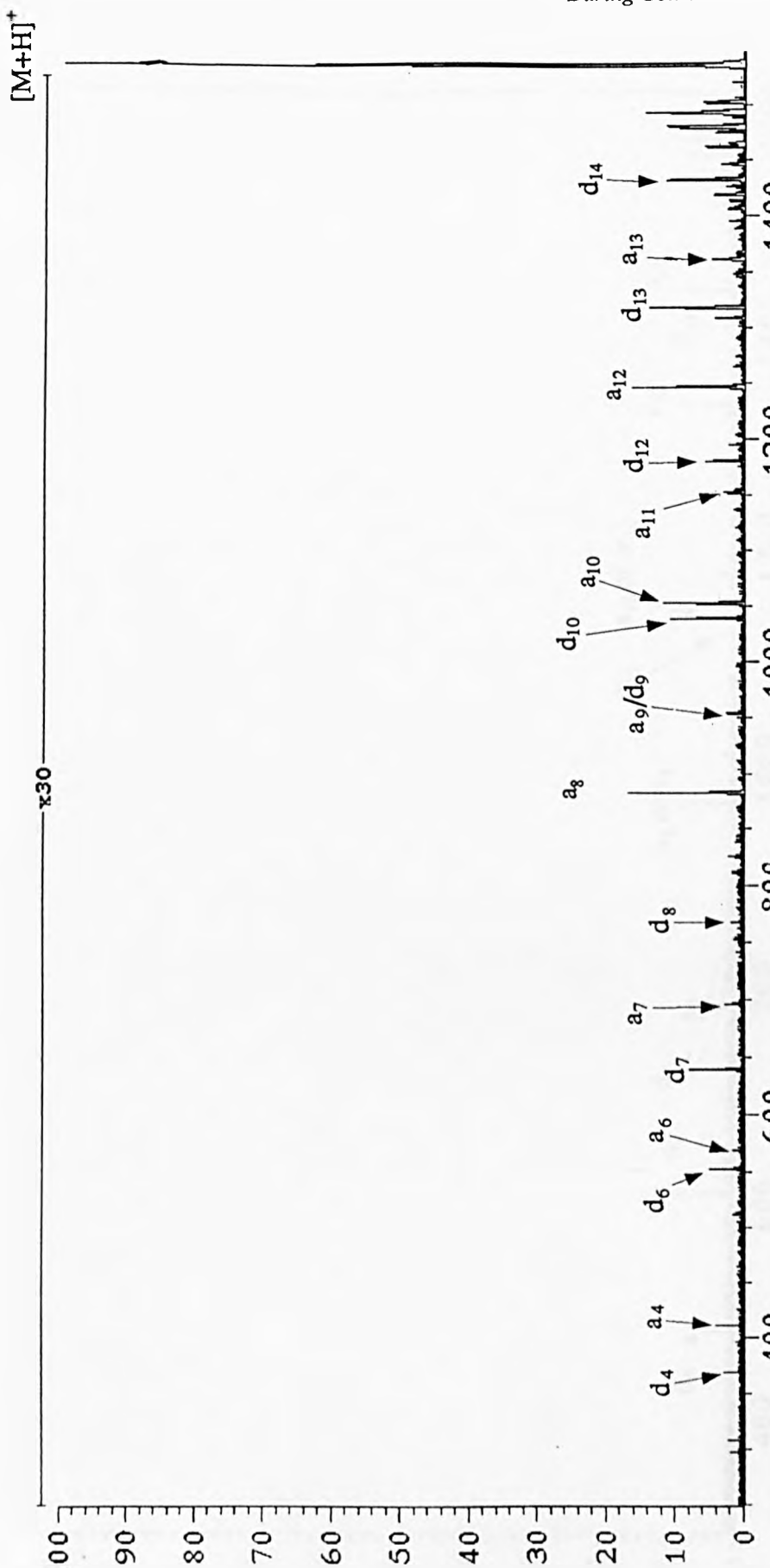

Figure 7.8: B/E scan of alytesin $[M+H]^+$ ion. Target gas was xenon.

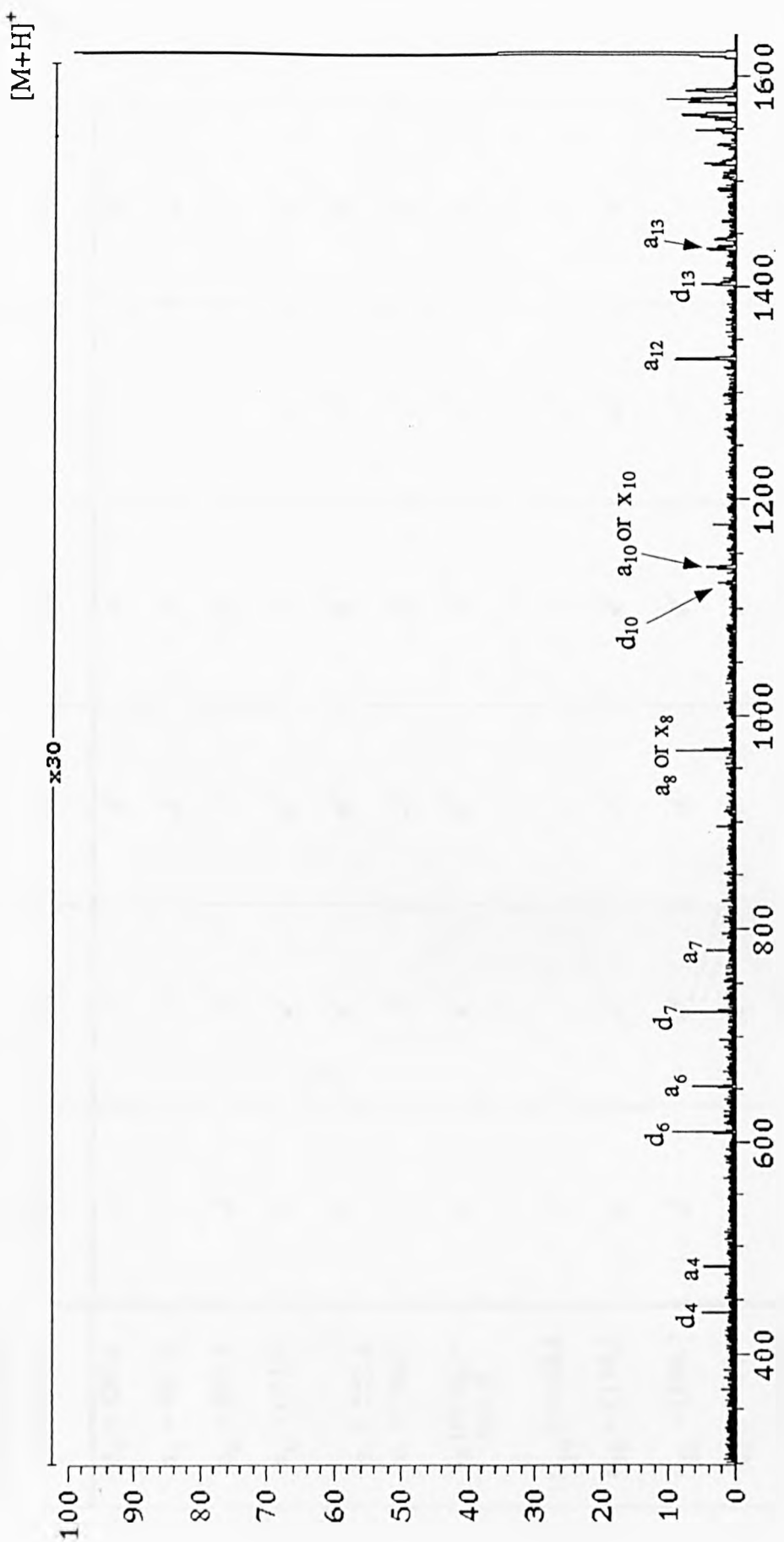

Figure 7.9: B/E scan of bombesin $[M+H]^+$ ion. Target gas was methane.

Fragment ion mass /Da	He	Ne	Ar	Kr	Xe	CH_4
d_4 = 439.2	-	-	✓	✓	-	✓
a_4 = 481.3	-	-	✓	✓	-	✓
d_6 = 609.4	✓	✓	✓	✓	-	✓
a_6 = 652.4	✓	✓	✓	✓	✓	✓
d_7 = 723.4	✓	✓	✓	✓	✓	✓
a_7 = 780.4	-	✓	✓	✓	✓	✓
a_8 (or x_8) = 966.5	✓	✓	✓	✓	✓	✓
d_{10} = 1122.6	-	-	-	-	✓	✓
a_{10} = 1136.6	✓	✓	✓	✓	✓	✓
a_{12} = 1330.7	✓	✓	✓	✓	✓	✓
d_{13} = 1401.7	-	✓	✓	✓	✓	✓
a_{13} = 1443.8	-	✓	✓	✓	✓	✓

Table 7.1(a): Fragment ions observed from collisions of the bombesin $[M+H]^+$ with various target gases. Laboratory-frame collision energy was 3.9 keV.

Fragment ion mass /Da	Helium	Argon	Xenon
$a_4 = 481.3$	-	-	✓
$d_6 = 609.4$	✓	✓	✓
$a_6 = 652.4$	-	-	✓
$d_7 = 723.4$	✓	✓	✓
$a_7 = 780.4$	✓	✓	✓
$d_8 = 851.5$	-	-	✓
$a_8 = 966.5$ (or $x_8 = 966.5$)	✓	✓	✓
$d_9 = 1037.6$ (and $a_9 = 1037.6$)	✓	✓	✓
$d_{10} = 1122.6$	✓	✓	✓
$a_{10} = 1136.6$	✓	✓	✓
$d_{12} = 1264.7$	-	✓	✓
$a_{12} = 1330.7$	✓	✓	✓
$d_{13} = 1401.7$	✓	✓	✓
$a_{13} = 1443.8$	✓	✓	-
$d_{14} = 1514.8$	✓	✓	-

Table 7.1(b): Fragment ions observed from collisions of the bombesin $[M+H]^+$ ion with various target gases. Laboratory-frame collision energy was 5.9 keV.

Fragment ion mass /Da	Helium	Argon	Xenon
$d_4 = 368.2$	-	✓	✓
$a_4 = 410.3$	-	✓	✓
$d_6 = 552.3$	-	-	✓
$a_6 = 568.3$	-	-	✓
$d_7 = 639.4$	-	✓	✓
$a_7 = 696.4$	-	✓	✓
$d_8 = 767.4$	-	-	✓
$a_8 = 882.5$	-	✓	✓
$d_9 = 953.5$ (and $a_9 = 953.5$)	-	✓	✓
$d_{10} = 1038.6$	-	✓	✓
$a_{10} = 1052.6$	-	✓	✓
$a_{11} = 1109.6$	-	✓	✓
$d_{12} = 1180.6$	-	✓	✓
$a_{12} = 1246.6$	-	✓	✓
$d_{13} = 1317.7$	-	✓	✓
$a_{13} = 1359.7$	-	✓	✓
$d_{14} = 1430.8$	-	✓	✓
$a_{14} = 1490.8$	-	✓	✓

Table 7.2(a): Fragment ions observed from collisions of the alytesin $[M+H]^+$ ion with various target gases. Laboratory-frame collision energy was 3.9 keV.

Fragment ion mass /Da	Helium	Argon	Xenon
$d_4 = 368.2$	-	-	-
$a_4 = 410.3$	-	-	✓
$d_6 = 552.3$	✓	-	-
$a_6 = 568.3$	✓	-	-
$d_7 = 639.4$	✓	✓	✓
$a_7 = 696.4$	✓	✓	✓
$a_8 = 882.5$	✓	✓	✓
$d_9 = 953.5$ (and $a_9 = 953.5$)	✓	✓	✓
$d_{10} = 1038.6$	✓	✓	✓
$a_{10} = 1052.6$	✓	✓	✓
$d_{12} = 1180.6$	-	✓	-
$a_{12} = 1246.6$	✓	✓	✓
$d_{13} = 1317.7$	✓	✓	✓
$a_{13} = 1359.7$	✓	✓	✓
$d_{14} = 1430.8$	✓	✓	✓
$a_{14} = 1490.8$	-	✓	✓

Table 7.2(b): Fragment ions observed from collisions of alytesin $[M+H]^+$ with various target gases. Laboratory-frame collision energy was 5.9 keV.

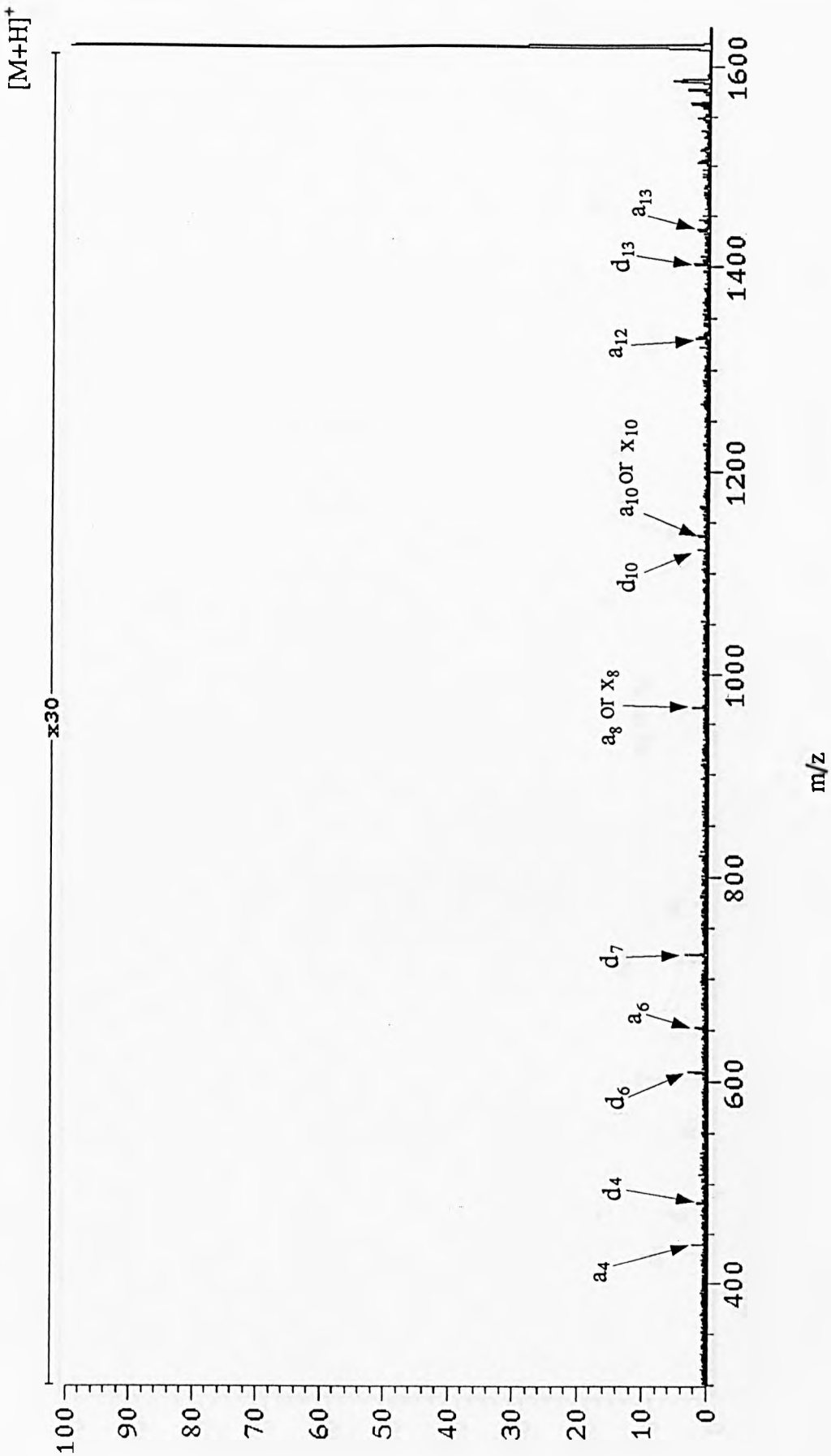

Figure 7.4: B/E scan of bombesin $[M+H]^+$ ion. Target gas was krypton.

n-terminus unlikely in the case of bombesin. Nevertheless x_8 and x_{10} remain in principle possible assignments.

The translational energy losses of the bombesin $[M + H]^+$ ion, determined from the presumed a_8, a_{10} and a_{12} fragment peak shifts, are summarised in table 7.3. Included in this table are the internal energy uptakes (Q /eV) for the bombesin $[M + H]^+$ ion as calculated on the basis of ICT theory [75-76]. That the translational energy losses determined from different fragment ions differ from each other is explained by distinct internal energy uptakes by the parent ion being associated with particular fragmentation pathways [81]. The translational energy losses and the internal energy uptakes were all of the same order of magnitude, namely tens of electron volts. There were no distinct trends on changing target gas from helium to xenon for any of the fragment ions studied. Methane induced larger translational energy losses than any of the noble gases. The calculated internal energy uptake by protonated bombesin from collisions with methane were most comparable to internal energy uptakes from collisions with helium.

7.3.2 Effects of Changing the Laboratory-Frame Collision Energy.

The bombesin fragment ions presumed to be a_8, a_{10} and a_{12} were again chosen for this study. The laboratory-frame collision energy was varied from 7.9 keV to 2.9 keV in 1 keV intervals. This gave rise to centre-of-mass frame collision energies of 19 eV, 17 eV, 15 eV, 10 eV and 7 eV for helium, 190 eV, 166 eV, 142 eV, 118 eV, 94 eV and 70 eV for argon and 77 eV, 67 eV, 56 eV, 48 eV, 38 eV and 28 eV for methane. Figure 7.16 shows the CID-MIKE spectra obtained using helium as the target gas at (a) E_{lab} = 7.9 keV and (b) E_{lab} = 5.9 keV. Figure 7.17 shows the CID-MIKE spectra when argon was the collision gas at (a) E_{lab} = 7.9 keV and (b) E_{lab} = 5.9 keV. Figure 7.18 was obtained when the target gas was methane at (a) E_{lab} = 7.9 keV and (b) E_{lab} = 5.9 keV. Figures 7.10, 7.12 and 7.15 show the CID-MIKE spectra with helium, argon and methane at E_{lab} = 3.9 keV. A shoulder on the low mass side of the bombesin $[M + H]^+$ ion was apparent with helium (figure 7.16). A similar

shoulder was present with methane and argon but was very weak in both cases (figures 7.17 and 7.18). This phenomenon was reported and discussed by Neumann *et al.* [63]. This shoulder was seen to become progressively more intense as the centre-of-mass frame collision energy was decreased, either by reducing the laboratory-frame collision energy and/or by reducing the mass of the target gas.

The translational energy losses of bombesin $[M + H]^+$ ion obtained from the peaks shifts of the fragment ions a_8, a_{10} and a_{12} peak shifts were of the order of tens of electron volts, reaching one hundred electron volts in some cases. The results are summarised in table 7.4(a). Table 7.4(b) gives the internal energy uptake by the bombesin $[M + H]^+$ ion, calculated using ICT theory. Dashes in the tables indicate that peaks were too weak to make accurate measurements upon them. The translational energy losses (and internal energy uptakes) of the parent ion at E_{lab} = 7.9 keV were significantly less than those obtained at lower laboratory-frame collision energies. This observation is due at least in point to instrumental effects. Floating the collision cell, and hence slowing the ions down as they enter the collision cell, allows the ions to be focused to a better degree as they are re-accelerated on exiting the cell. Thus, a wider spread of scattering angles would have been collected at the higher cell potentials. Translational energy losses increase with scattering angle.

The internal energy uptakes of the bombesin $[M + H]^+$ ion were found to be of the same order of magnitude in all cases. Methane and helium showed comparable internal energy uptakes for most of the laboratory-frame collision energies tested.

7.3.3 Effects of Changing the Peptide.

Alytesin also produced a_8, a_{10} and a_{12} fragment ions in the CID-B/E linked scan of the $[M + H]^+$ ion (figure 7.6 to 7.8). There was no ambiguity in assigning the a_8 and a_{10} alytesin fragment peaks, as the corresponding x-type ions, x_8 and x_{10}, have different masses. Figures 7.19 to 7.21 show the spectra obtained from the CID-MIKE experiments carried out with helium, argon and methane. CID-MIKE spectra of bombesin under the same collision conditions were shown in figures 7.16(a), 7.17(a)

and 7.18 (a). The collision cell was earthed for the alytesin measurements. Analysis of the alytesin spectra are summarised in table 7.5. Note that as before, fragmentations at the eighth and tenth amino acid residues from the N-terminus of bombesin, were assumed to give only the a_8 and a_{10} fragment ions.

The fragment ion a_8 was found to give translational energy losses for alytesin that were comparable to those for bombesin for the target gases helium, argon and methane. The translational energy loss for the alytesin $[M + H]^+$ ion, determined from the a_{10} fragment ion, was significantly lower than the translational energy loss for bombesin $[M + H]^+$ determined from the a_{10} fragment ion for the target gases helium, argon and methane. The fragment ion a_{12} resulted in comparable translational energy losses for the alytesin and bombesin $[M + H]^+$ ions in the case of helium. Comparisons between these molecules must be treated cautiously, but presumably the differences reflect the different structure of alytesin and bombesin and their fragment ions.

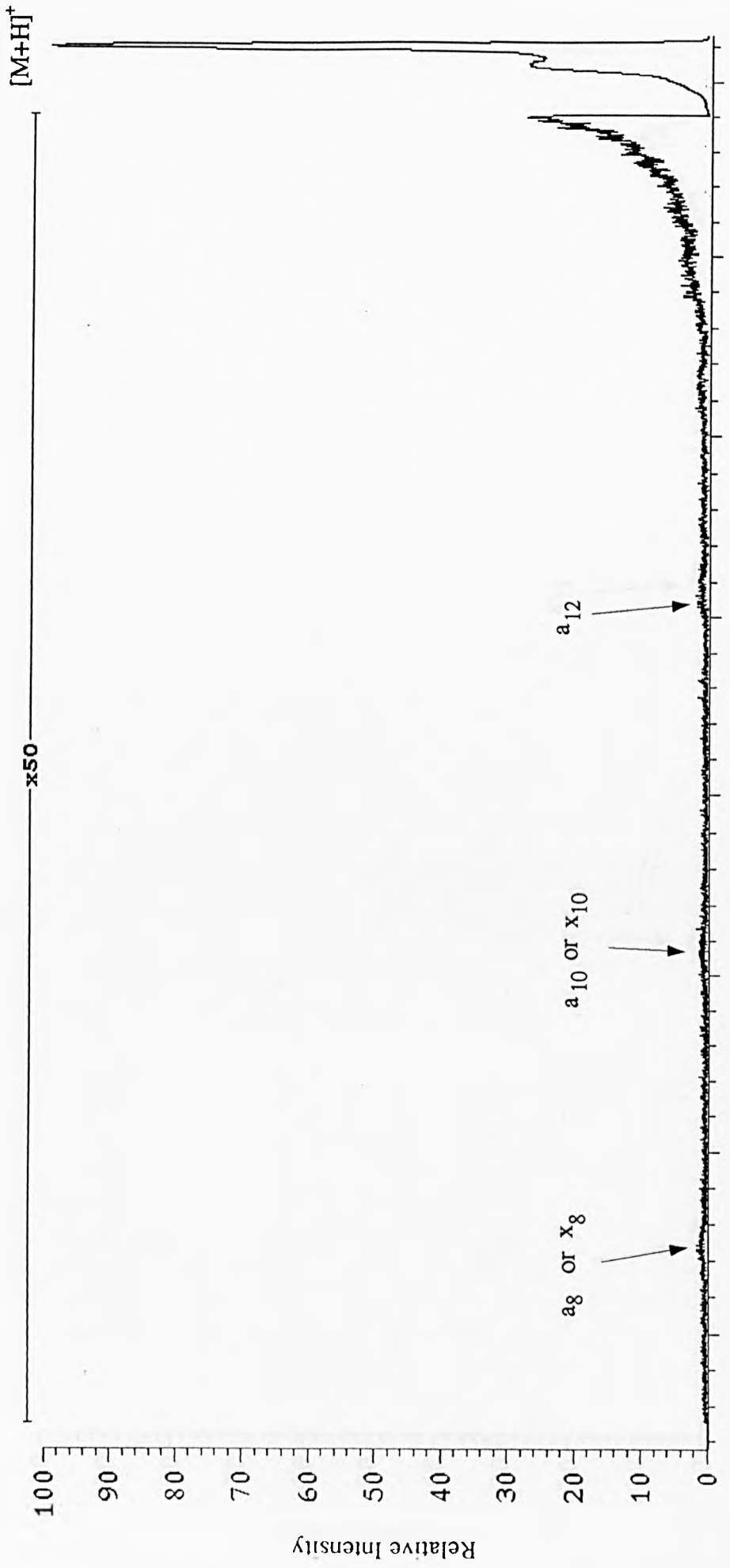

Figure 7.10: MIKE scan of bombesin $[M+H]^+$ ion. Target gas was helium.

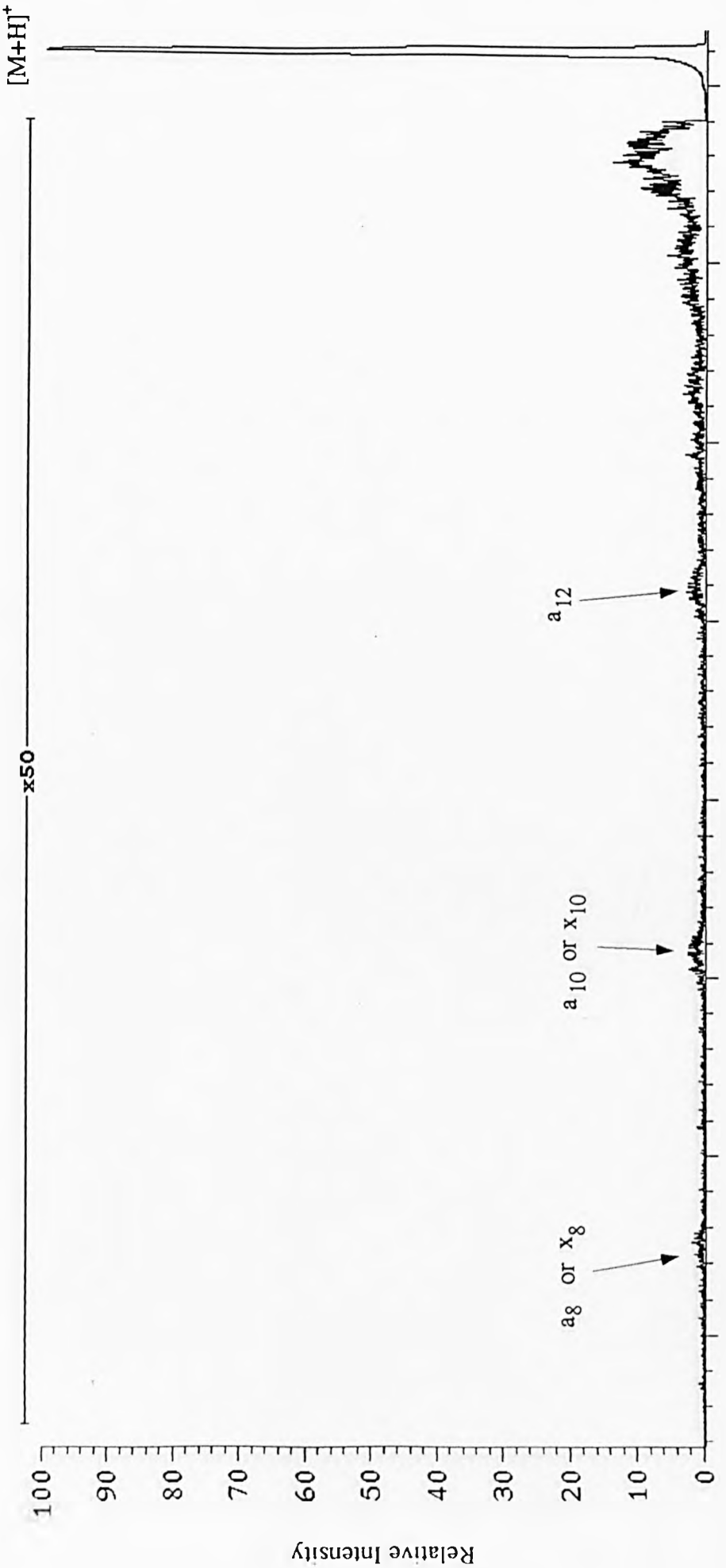

Figure 7.11: MIKE scan of bombesin $[M+H]^+$ ion. Target gas was neon.

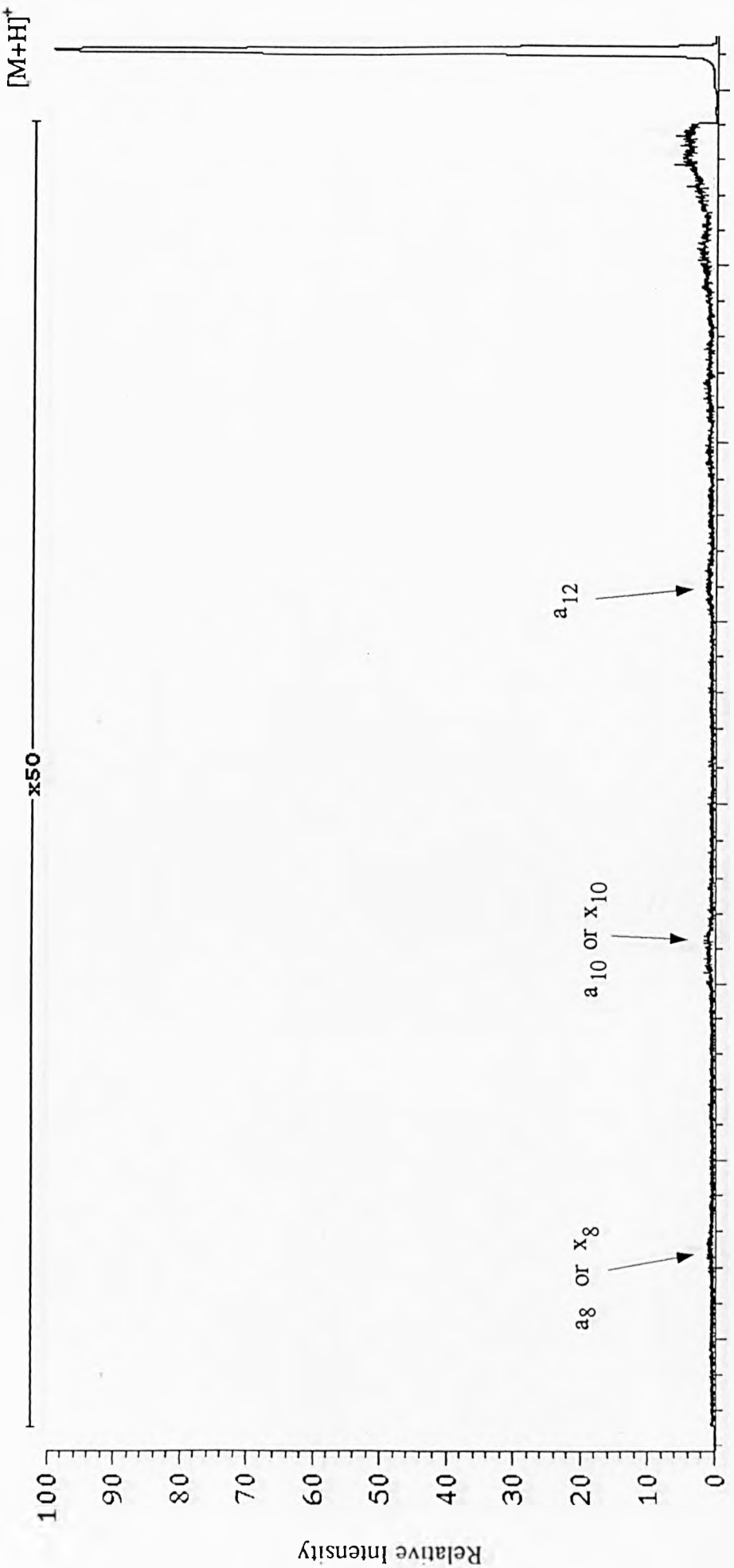

Figure 7.12: MIKE scan of bombesin $[M+H]^+$ ion. Target gas was argon.

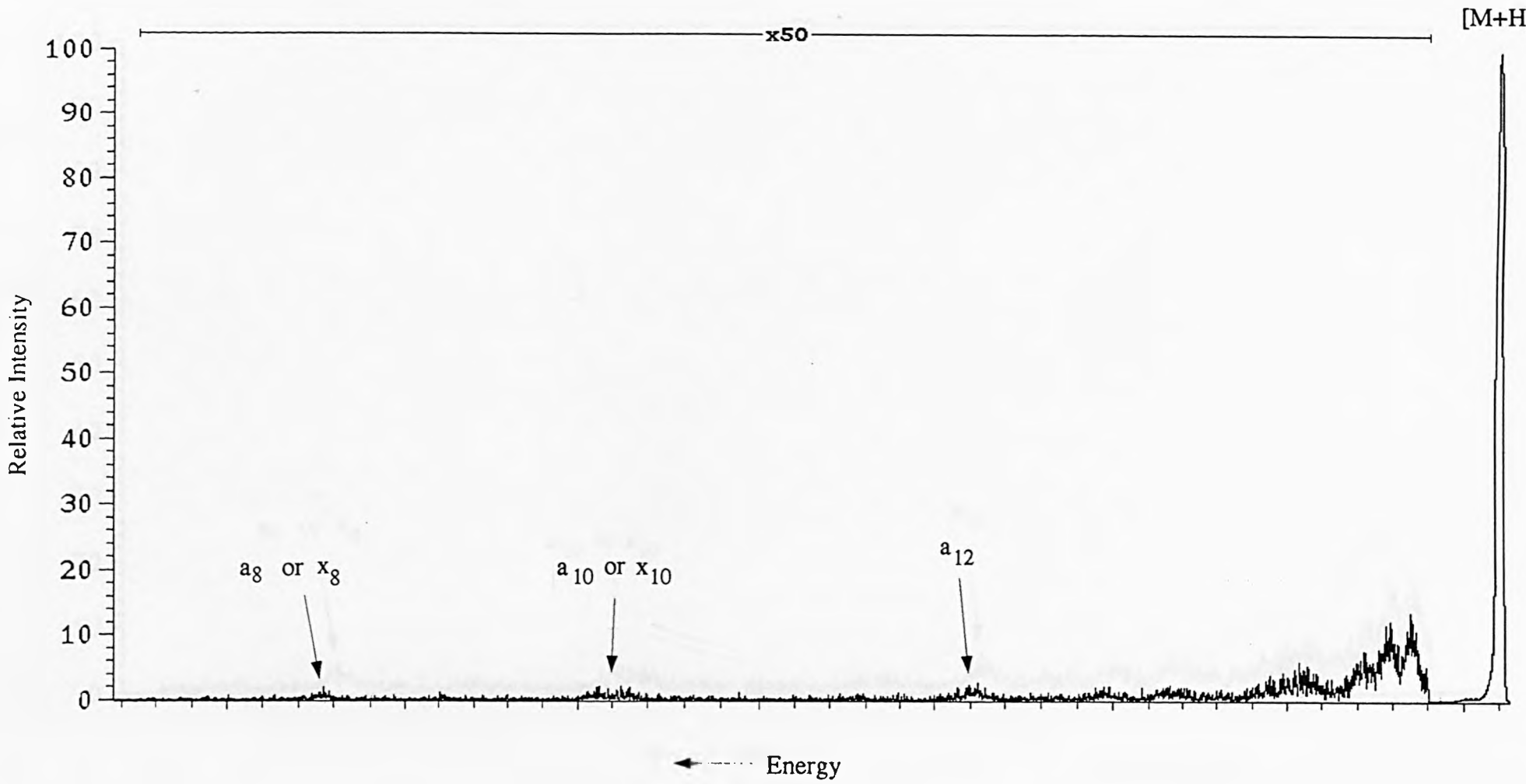

Figure 7.13: MIKE scan of bombesin $[M+H]^+$ ion. Target gas was krypton.

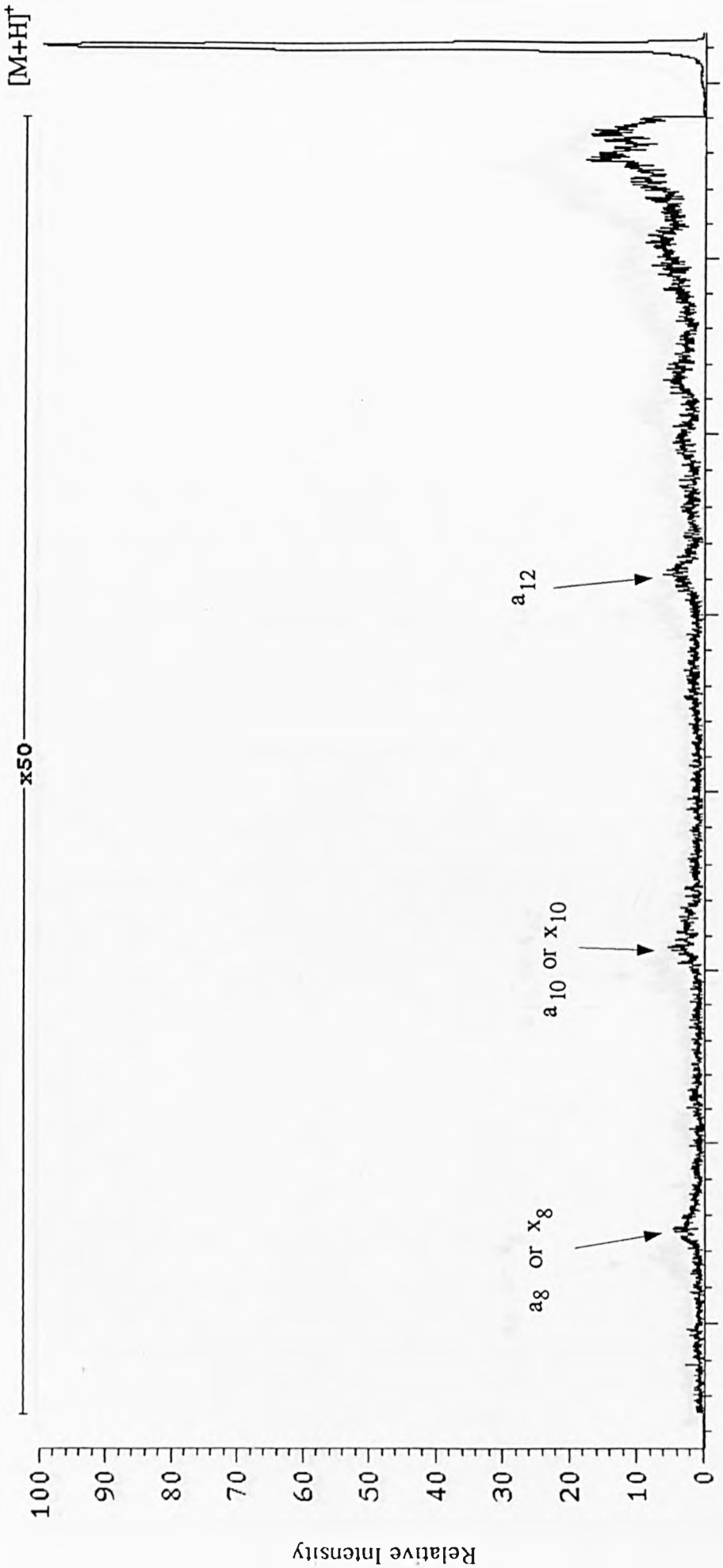

Figure 7.14: MIKE scan of bombesin $[M+H]^+$ ion. Target gas was xenon.

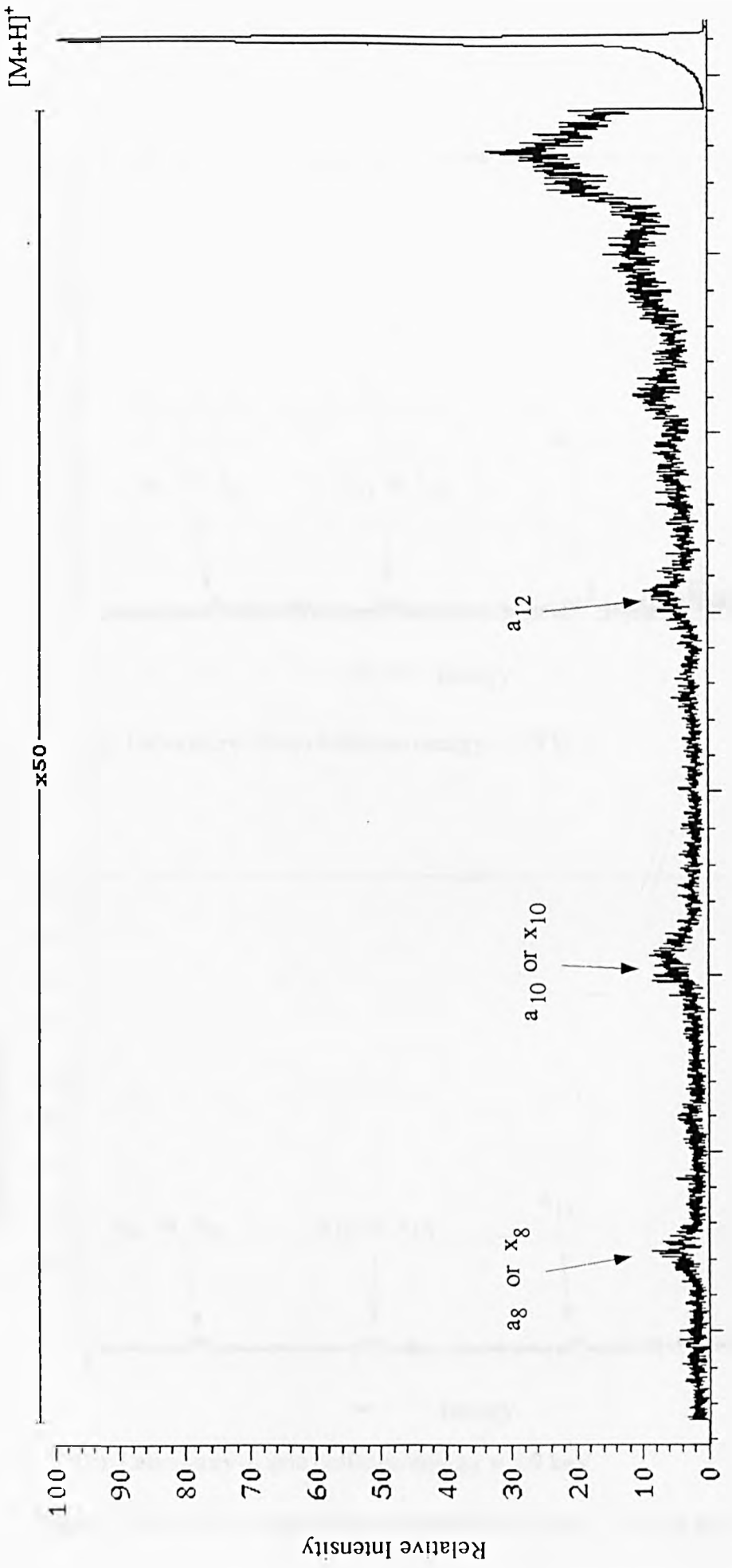

Figure 7.15: MIKE scan of bombesin $[M+H]^+$ ion. Target gas was methane.

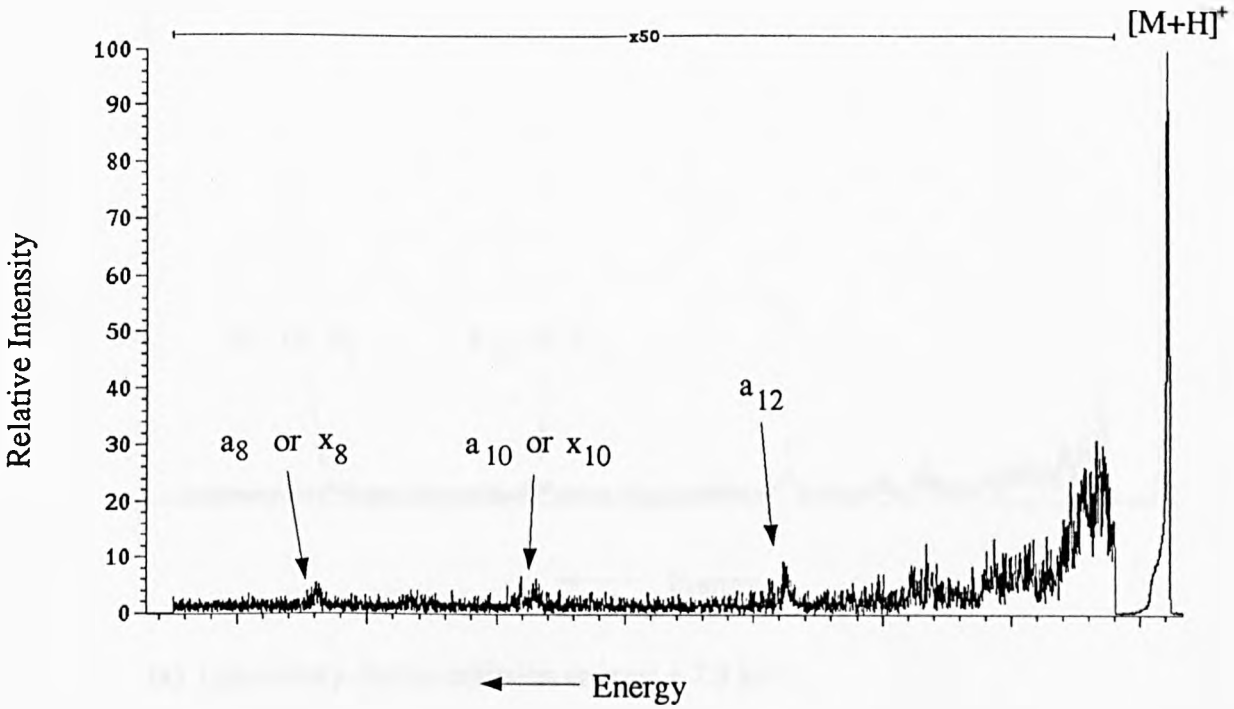

(a) Laboratory-frame collision energy = 7.9 keV.

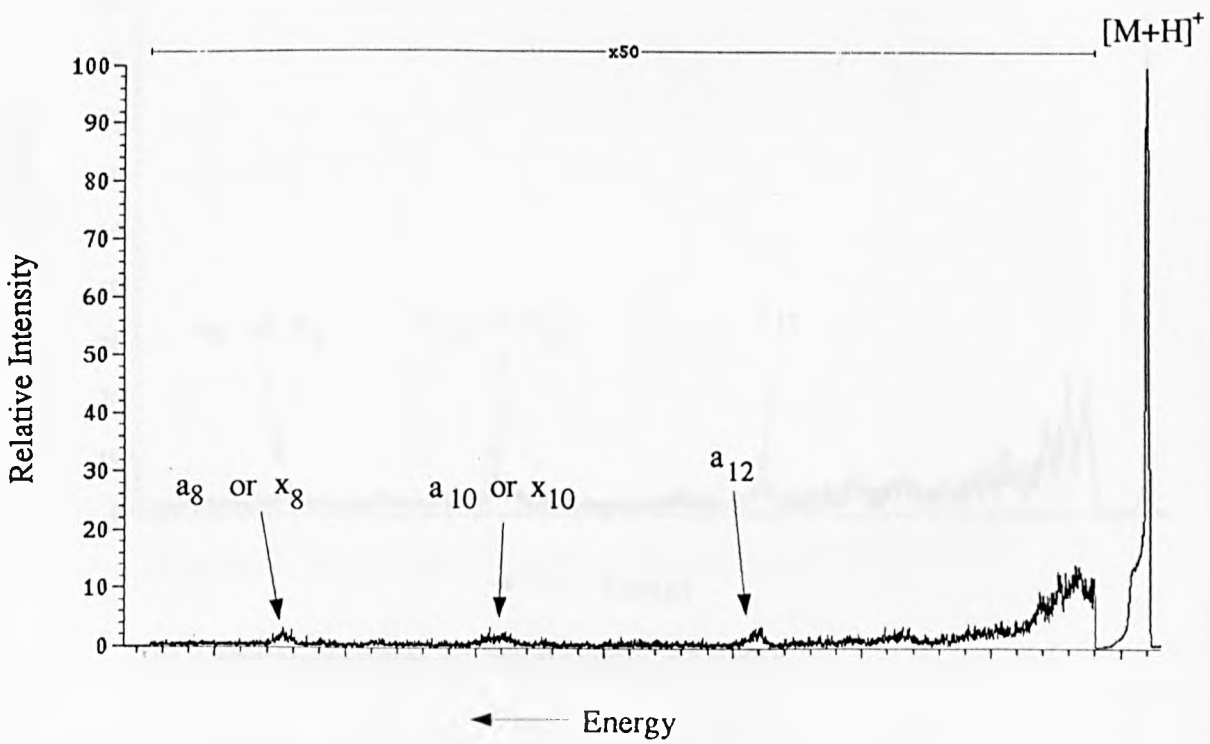

(b) Laboratory-frame collision energy = 5.9 keV.

Figure 7.16: MIKE scan of bombesin $[M+H]^+$ ion. Target gas was helium.

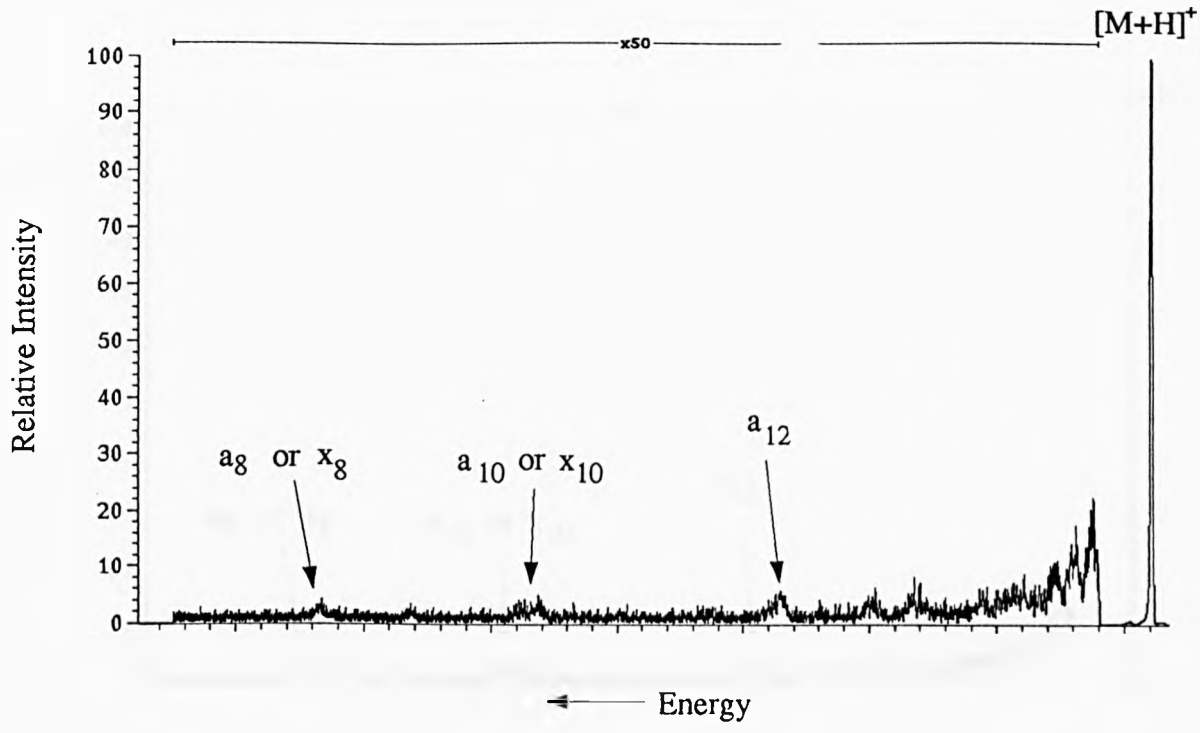

(a) Laboratory-frame collision energy = 7.9 keV.

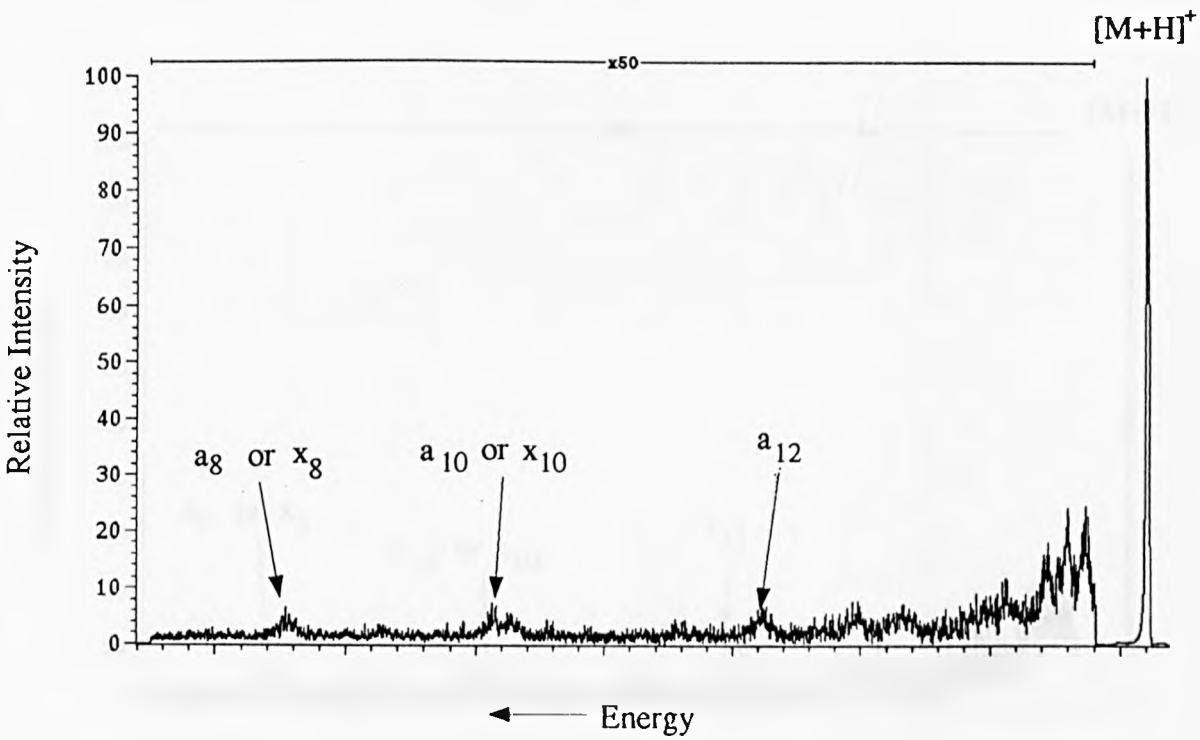

(b) Laboratory-frame collision energy = 5.9 keV.

Figure 7.17: MIKE scan of bombesin $[M+H]^+$ ion. Target gas was argon.

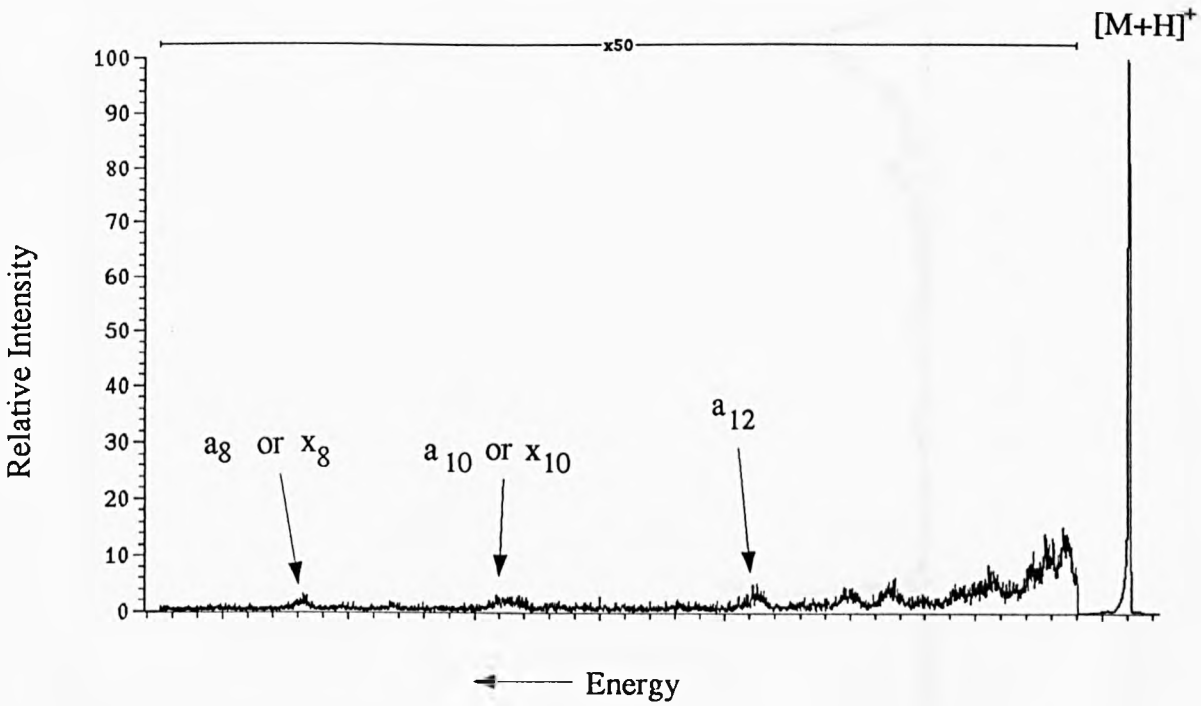

(a) Laboratory-frame collision energy = 7.9 keV.

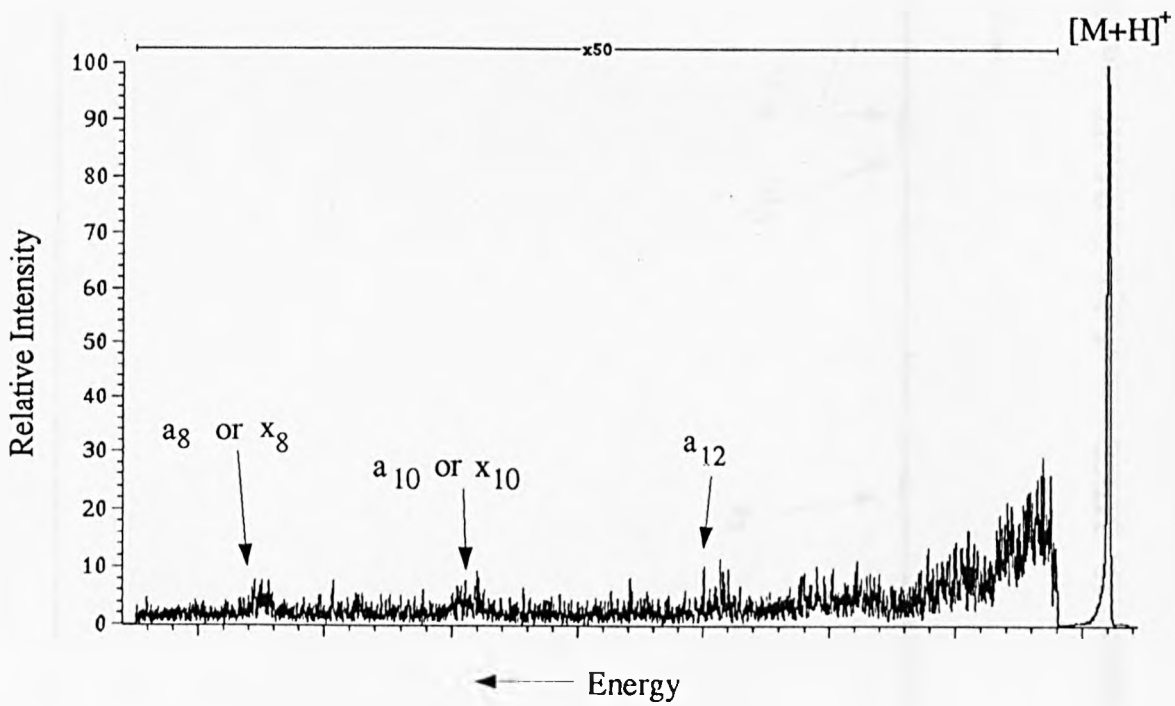

(b) Laboratory-frame collision energy = 5.9 keV.

Figure 7.18: MIKE scan of bombesin $[M+H]^+$ ion. Target gas was methane.

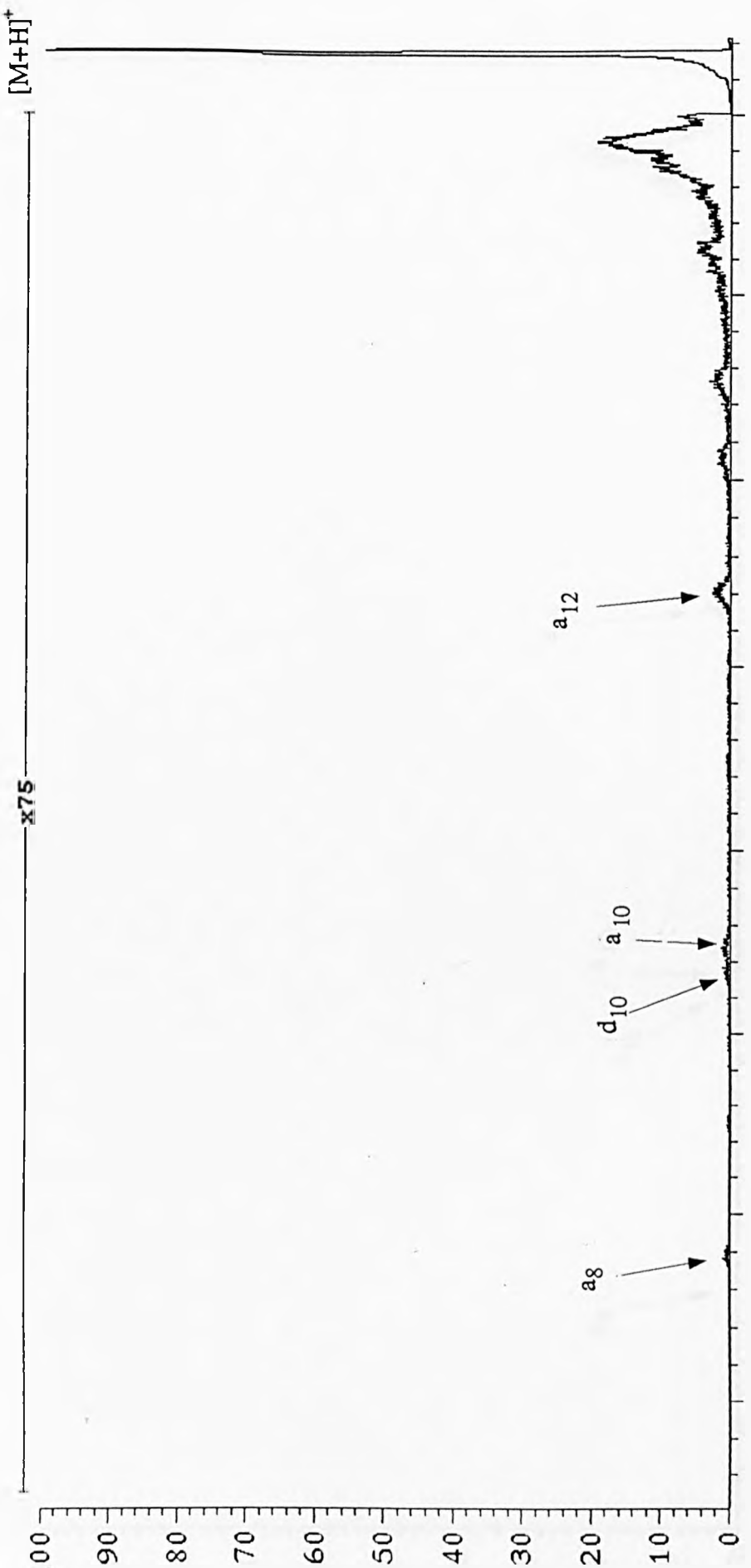

Figure 7.19: MIKE scan of alytesin $[M+H]^+$ ion. Target gas was helium.

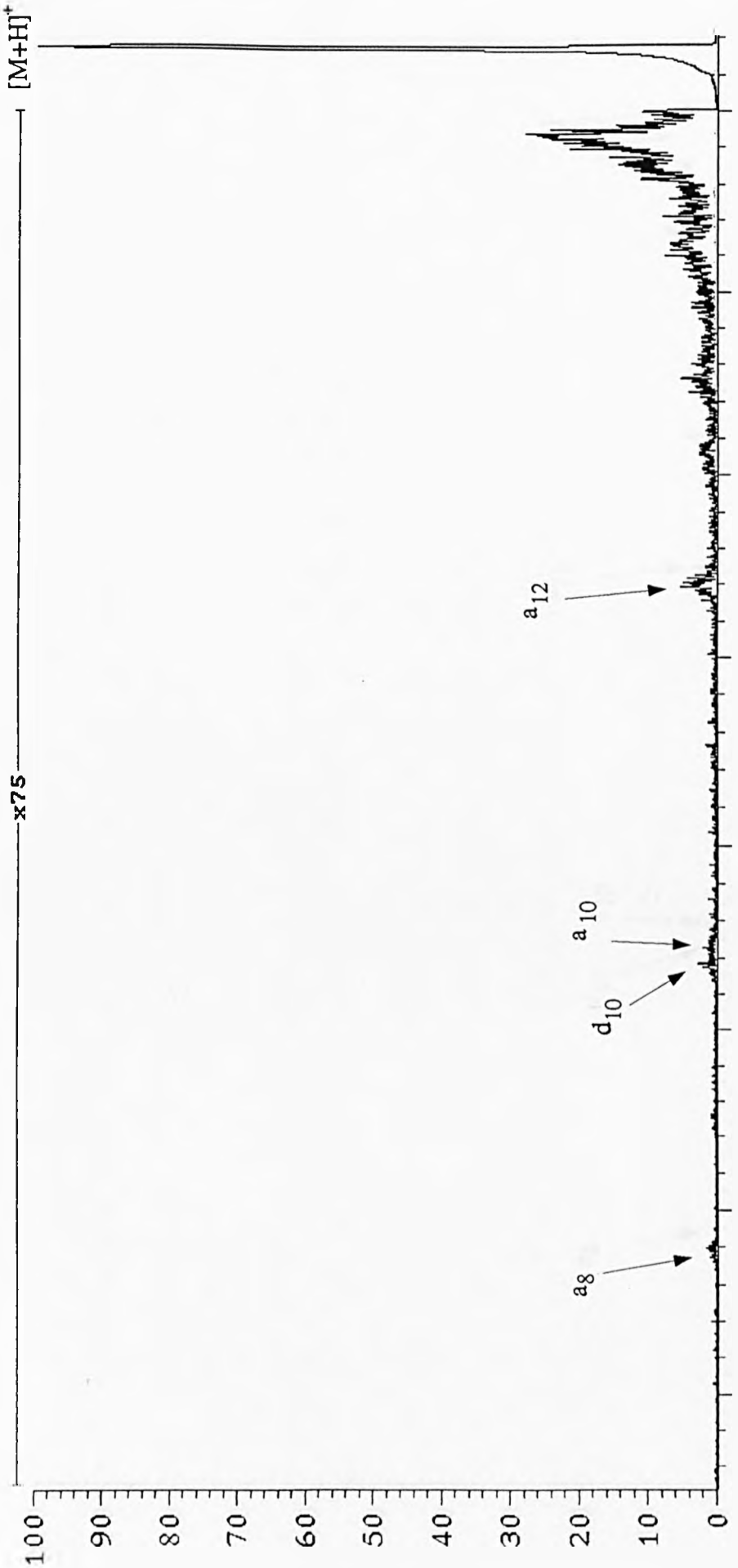

Figure 7.20: MIKE scan of alytesin $[M+H]^+$ ion. Target gas was argon.

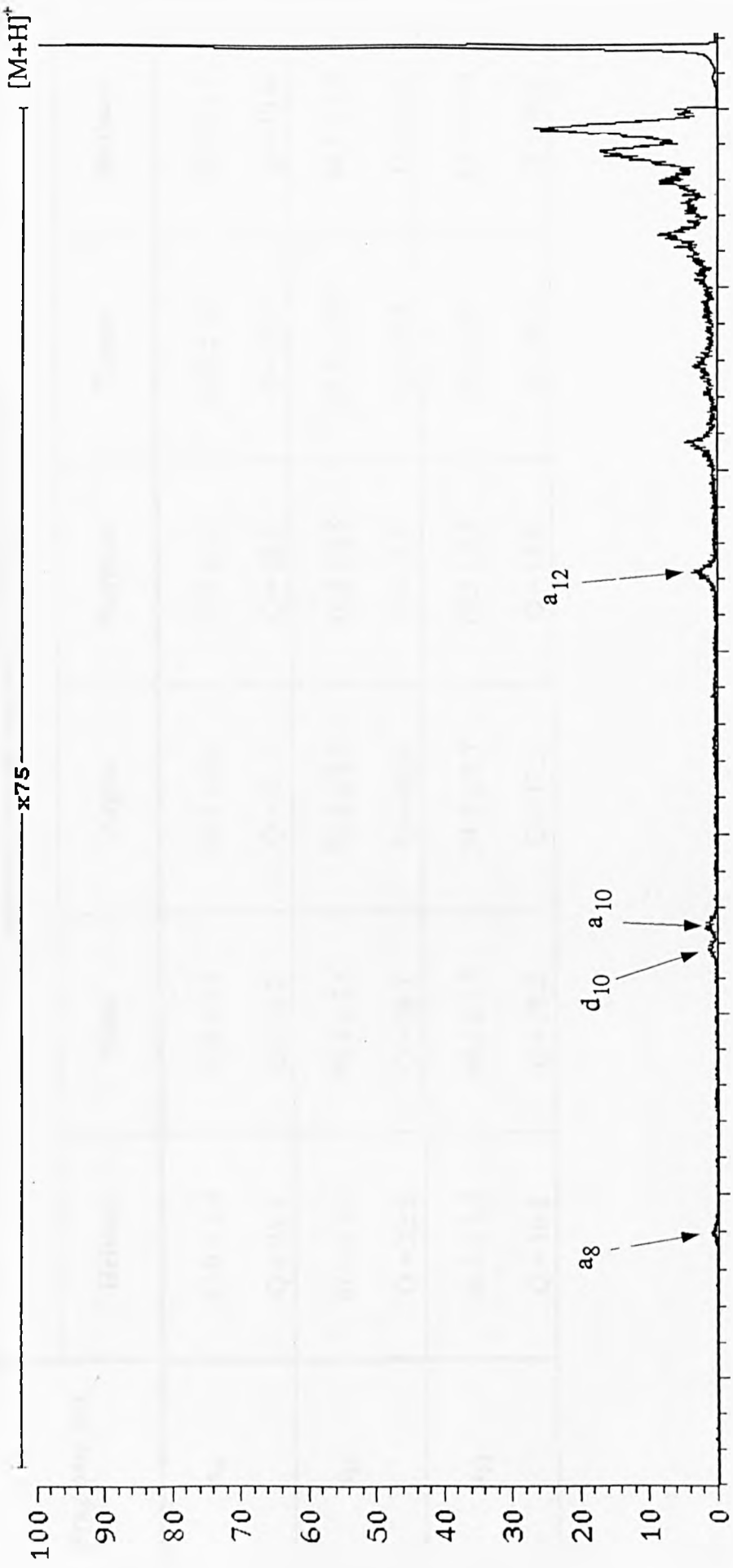

Figure 7.21: MIKE scan of alytesin $[M+H]^+$ ion. Target gas was methane.

Fragment ion	Translational energy loss by [BOMBESIN + H]$^+$ /eV					
	Helium	**Neon**	**Argon**	**Krypton**	**Xenon**	**Methane**
a_8	82.0 ± 2.4 Q = 25.1	73.8 ± 3.5 Q = 34.2	62.1 ± 2.1 Q = 31.9	52.0 ± 2.4 Q = 28.7	66.2 ± 2.3 Q = 37.5	88.7 ± 1.5 Q = 19.4
a_{10}	62.6 ± 2.1 Q = 22.5	70.3 ± 2.6 Q = 38.3	72.4 ± 2.5 Q = 43.8	48.8 ± 2.5 Q = 31.7	68.5 ± 2.9 Q = 45.6	89.3 ± 2.9 Q = 22.9
a_{12}	38.3 ± 1.1 Q = 16.1	44.2 ± 1.3 Q = 28.2	24.3 ± 0.7 Q = 17.2	19.2 ± 0.4 Q = 14.6	26.3 ± 0.8 Q = 20.5	55.0 ± 1.4 Q = 16.5

Table 7.3: Translational energy losses suffered by bombesin $[M+H]^+$ ion as determined from fragment ion peak shifts following collisions with various target gases. Q is the internal energy uptake by the parent ion, as calculated using ICT theory. Laboratory-frame collision energy was 3.9 keV.

		Translational energy loss by [BOMBESIN + H]$^+$ /eV					
Fragment ion	**Target gas**	**E_{lab} = 7.9 keV**	**E_{lab} = 6.9 keV**	**E_{lab} = 5.9 keV**	**E_{lab} = 4.9 keV**	**E_{lab} = 3.9 keV**	**E_{lab} = 2.9 keV**
a_8	**Helium**	37.6 ± 0.8	83.9 ± 2.7	92.6 ± 2.7	77.7 ± 1.9	82.0 ± 2.4	81.4 ± 3.2
	Argon	12.3 ± 0.2	76.1 ± 1.6	61.2 ± 1.4	62.2 ± 1.0	62.1 ± 2.1	51.3 ± 1.6
	Methane	22.7 ± 0.4	111.7 ± 2.5	99.7 ± 2.6	78.8 ± 2.1	88.7 ± 1.5	59.6 ± 1.3
a_{10}	**Helium**	66.3 ± 2.4	102.2 ± 4.2	93.4 ± 1.2	68.5 ± 1.2	62.6 ± 2.1	-
	Argon	83.9 ± 3.7	82.0 ± 2.6	112.2 ± 6.3	113.3 ± 4.8	72.4 ± 2.5	61.8 ± 3.4
	Methane	52.2 ± 2.5	157.7 ± 9.3	126.8 ± 3.7	88.2 ± 3.4	89.3 ± 2.9	74.6 ± 3.3
a_{12}	**Helium**	35.2 ± 0.7	50.4 ± 0.9	48.7 ± 0.8	58.3 ± 1.3	38.3 ± 1.1	-
	Argon	11.8 ± 0.2	31.1 ± 0.6	38.3 ± 0.4	22.9 ± 6.8	24.3 ± 0.7	39.3 ± 0.8
	Methane	35.7 ± 0.7	59.2 ± 0.9	62.5 ± 1.0	47.0 ± 1.3	55.0 ± 1.4	44.1 ± 1.7

Table 7.4(a): Translational energy losses suffered by bombesin parent ion as measured from fragment ion peak shifts following collisions with helium, argon and methane at various laboratory-frame collision energies.

		Internal energy uptake (Q) by [BOMBESIN + H]$^+$ /eV					
Fragment ion	**Target gas**	**E_{lab} = 7.9 keV**	**E_{lab} = 6.9 keV**	**E_{lab} = 5.9 keV**	**E_{lab} = 4.9 keV**	**E_{lab} = 3.9 keV**	**E_{lab} = 2.9 keV**
a_8	**Helium**	Q = 15.1	Q = 25.7	Q = 28.3	Q = 23.7	Q = 25.1	Q = 24.9
	Argon	Q = 6.3	Q = 39.1	Q = 31.5	Q = 32.0	Q = 31.9	Q = 26.4
	Methane	Q = 4.9	Q = 24.4	Q = 21.7	Q = 17.2	Q = 19.4	Q = 13.0
a_{10}	**Helium**	Q = 23.8	Q = 36.7	Q = 33.6	Q = 24.6	Q = 22.5	-
	Argon	Q = 50.7	Q = 49.6	Q = 67.8	Q = 68.5	Q = 43.8	Q = 37.4
	Methane	Q = 13.4	Q = 40.4	Q = 32.5	Q = 22.6	Q = 22.9	Q = 19.1
a_{12}	**Helium**	Q = 14.8	Q = 21.2	Q = 20.5	Q = 24.6	Q = 16.1	-
	Argon	Q = 13.4	Q = 22.0	Q = 27.1	Q = 16.2	Q = 17.2	Q = 27.8
	Methane	Q = 10.7	Q = 17.8	Q = 18.8	Q = 14.1	Q = 16.5	Q = 13.2

Table 7.4(b): Internal energy uptake by the bombesin [M + H]$^+$ ion as calculated by ICT theory.

		Translational energy loss and internal energy uptake (Q) by $[M + H]^+$ /eV		
Fragment ion	**Peptide**	**Helium**	**Argon**	**Methane**
a_8	**Bombesin**	37.6 ± 0.8 Q = 15.1	12.3 ± 0.2 Q = 6.3	22.7 ± 0.4 Q = 4.9
a_8	**Alytesin**	31.1 ± 0.6 Q = 9.2	19.5 ± 0.5 Q = 9.7	17.6 ± 0.3 Q = 3.7
a_{10}	**Bombesin**	66.3 ± 2.4 Q = 23.8	83.9 ± 3.7 Q = 50.7	52.2 ± 2.5 Q = 13.4
a_{10}	**Alytesin**	10.6 ± 0.5 Q = 3.7	47.8 ± 2.0 Q = 28.2	9.8 ± 0.2 Q = 2.4
a_{12}	**Bombesin**	35.2 ± 0.7 Q = 14.8	11.8 ± 0.2 Q = 13.4	35.7 ± 0.7 Q = 10.7
a_{12}	**Alytesin**	29.1 ± 0.5 Q = 12.2	26.8 ± 0.5 Q = 18.7	13.1 ± 0.2 Q = 3.9

Table 7.5: Translational energy losses suffered by protonated peptide ions as measured from fragment ion peak shifts following collisions with helium, argon and methane at a laboratory-frame collision energy of 7.9 keV. Q is the internal energy uptake by the parent ion, as calculated by ICT theory.

CHAPTER EIGHT: *Conclusion.*

Target capture is the point at which the maximum amount of translational energy is converted into internal energy. The formation of adduct species from the capture of a target gas, long enough lived for detection provides an ideal opportunity to study, at close quarters, the energy transfer during a collision between a molecule-ion and a stationary neutral. A further insight into the mechanism of energy transfer in a collision would be very useful to aid the understanding of collisional activation and unimolecular dissociation - the two processes of collision-induced decomposition. Collision conditions could then be optimised for particular systems and the means for obtaining structural information of massive ions, for which CID is most commonly employed, may be improved.

8.1 Target Capture by Fullerene Radical Cations.

The fullerenes C_{60} and C_{70} are both closed-cage structures. This provides a limited number of possibilities for derivatisation. Derivatives formed fall into one of only three categories: exohedral derivatives, endohedral derivatives and dopey-balls.

8.1.1 The Noble Gases.

The least complex type of collision gas, monoatomic, was chosen to initiate the study of target capture by fullerene radical cations. $He@C_{60}^{+\cdot}$, $Ne@C_{60}^{+\cdot}$, $He@C_{70}^{+\cdot}$ and $Ne@C_{70}^{+\cdot}$ had already been observed and were proposed to be endohedral in structure [111, 161] . This work shows that argon formed adducts with $C_{60}^{+\cdot}$ and $C_{70}^{+\cdot}$. Fragmentation of these adducts was shown to involve the loss of C_2 units from the fullerene cage. This observation, plus the fact that fragmented adduct ions were observed at energies corresponding to the loss of 2, 4, 6, 8 and 10 carbon atoms from the full adduct, suggests argon is retained during decomposition and therefore is most likely to be endohedrally bound by the fullerene cage [203]. If the argon were

exohedrally attached to the fullerene cage, fragmentation of the cage might be expected to include the loss of argon and this was not observed. The retention of argon as the fullerene cage fragments could be by the *'shrink-wrap'* mechanism [125]. Similar results were obtained for krypton and xenon although weak peaks lead to the assignments of the full adducts being somewhat tenuous.

At particular laboratory-frame collision energies all of the noble gases were found to form full adducts with $C_{60}^{+\cdot}$ and $C_{70}^{+\cdot}$ at energy deficits, relative to the uncollided parent ion, equivalent to the corresponding centre-of-mass collision energies. In terms of finding the laboratory-frame collision energies at which these adducts were observed, or optimised, a second experiment was instigated. Helium was seen to form adducts at notably lower centre-of-mass collision energies (changes of centre-of-mass collision energies that resulted from changing the laboratory-frame collision energies) than neon, argon, krypton or xenon. These latter four gases formed adducts at approximately similar centre-of-mass collision energies (achieved by changing the laboratory-frame collision energies). The suggestion here is that helium is incorporated into the fullerene cage from a slightly different mechanism than the rest of the noble gases. One proposed mechanism for the capture of helium by fullerenes envisages that the noble gas passes through the wall of the fullerene cage [111, 171]. Alternatively the bonds of the fullerene cage might be broken and a window formed through which the gas can pass. The fullerene cage is supposed to reform behind the captured gas [115-116]. If the agreed facts were that in ionic collisions *in vacuo*, helium and perhaps less readily neon, could be incorporated, but that at high pressure any one of the noble gases could be incorporated it would be reasonable to adopt the *'squeeze through'* mechanism for the former and the *'window mechanism'* for the latter. The argument would be that the small atoms were able to pass through the wall but the larger atoms could not by virtue of their size. These results show that argon and possibly krypton and xenon can be incorporated into the fullerene cage from ionic collisions. One conclusion to be drawn is that the *'window mechanism'* satisfactorily describes the encapsulation of the noble gases. The difference in centre-of-mass

collision energies, when the laboratory-frame collision energies were varied, at which helium and the rest of the noble gases were formed may be due to helium squeezing through a six membered ring as opposed to smashing its way into the cage. If this were so the helium may equally be expected to pass out of the fullerene cage by the same manner it got in. Alternatively, the difference in centre-of-mass collision energies at which helium and the rest of the noble gases were formed may be attributed to the size of window required to permit passage of an atom into the cage. Helium needs only a small window in comparison to the rest of the gases which would require the rupture of more carbon-carbon bonds. The *'window mechanism'* would be consistent with the highly localised interaction implicit with the impulsive collision transfer theory of collisions of massive ions with gaseous atoms [54, 75-76].

8.1.2 Diatomic Gases.

When diatomic gases were employed some very interesting results were obtained. For carbon monoxide and nitrogen the full diatomic adducts were seen to be more abundant at higher collision energies than the atomic adducts $C_{70}C^{+\cdot}$, $C_{70}N^{+\cdot}$ and $C_{70}O^{+\cdot}$. It would be counter-intuitive for a diatomic adduct to form yet decompose into atomic adducts on *reducing* the collision energy. It is reasonable to presume that the diatomic adducts and the atomic adducts differ in their mechanism of formation, a factor that would appear dependent upon collision energy. As proposed by Cooper [182] higher collision energies may provide enough energy for the diatomic species to penetrate the fullerene cage to form an endohedral structure. Following this proposal, the atomic adducts, $C_{70}C^{+\cdot}$, $C_{70}N^{+\cdot}$ and $C_{70}O^{+\cdot}$, produced preferentially at lower collision energies could possibly be exohedral structures. For oxygen and nitric oxide the full adducts were observed initially at low collision energies (300 eV in the laboratory-frame). At intermediate collision energies (500 eV in the laboratory-frame) the full nitric oxide adduct was no longer observed and the full oxygen adduct was greatly reduced in intensity, compared to the spectrum obtained at a laboratory-frame collision energy of 300 eV. When the laboratory-frame collision energy was increased

to 750 eV, in the case of NO the full adduct was observed once more and 1000 eV in the case of O_2 the full adduct became more intense. This reduction in intensity of the $C_{70}O_2^{+\cdot}$ species followed by increase in intensity, or in the case of $C_{70}NO^{+\cdot}$ presence of the peak which disappeared before reappearing, as the collision energy increases poses an interesting situation. It is concluded that at low collision energies $C_{70}O_2^{+\cdot}$ and $C_{70}NO^{+\cdot}$ are exohedral derivatives which decompose into the exohedral atomic adducts $C_{70}O^{+\cdot}$ and $C_{70}N^{+\cdot}$ on increasing the laboratory-frame collision energy. At even higher collision energies there is sufficient energy to insert the diatomic molecule inside the cage giving rise to an endohedral derivative. This evidence supports the conclusion that $C_{70}CO^{+\cdot}$ and $C_{70}N_2^{+\cdot}$ could be endohedral structures but the atomic adducts $C_{70}C^{+\cdot}$, $C_{70}O^{+\cdot}$ and $C_{70}N^{+\cdot}$ are probably exohedral structures. Prior to this study O_2 and mononitrogen fullerene derivatives had not been observed.

All of the diatomic adducts $C_{70}CO^{+\cdot}$, $C_{70}NO^{+\cdot}$, $C_{70}O_2^{+\cdot}$ and $C_{70}N_2^{+\cdot}$ were found to optimise at energy deficits, relative to the uncollided parent ion, equivalent to the appropriate centre-of-mass collision energies. The mechanism of formation of the atomic adducts was investigated in terms of finding the energies at which these species were formed. Formation of a diatomic adduct followed by decomposition to the atomic adduct or, alternatively, removal and capture of a single atom from the gas leaving the other gas atom behind as a stationary neutral were both considered possibilities for the formation of $C_{70}C^{+\cdot}$, $C_{70}N^{+\cdot}$ and $C_{70}O^{+\cdot}$. Evidence was produced in this study to suggest $C_{70}N^{+\cdot}$ results from the decomposition of the full $C_{70}N_2^{+\cdot}$ species at laboratory-frame collision energies of 500 eV and 750 eV. In the case of oxygen at the laboratory-frame collision energy of 300 eV the adduct $C_{70}O^{+\cdot}$ was found to form in the same manner as the $C_{70}N^{+\cdot}$ adduct (*i.e.* decomposition of $C_{70}O_2^{+\cdot}$ to $C_{70}O^{+\cdot}$). At a laboratory-frame collision energy of 1000 eV this mechanism of formation for $C_{70}O^{+\cdot}$ no longer applied. In this case $C_{70}O^{+\cdot}$ was found to form at an energy deficit, relative to the incident ion, equivalent to the calculated energy required for the removal and capture of O from O_2. The formation of $C_{60}O^{+\cdot}$ from what was proposed to be transient $C_{60}O_2^{+\cdot}$ at low collision energies and the

formation of $C_{60}O^{+\cdot}$ from removal and capture of O from O_2 by $C_{60}^{+\cdot}$ at higher collision energies, was observed by Cooper [182]. The conclusion concerning the formation of the $C_{70}O^{+\cdot}$ adduct from collisions with oxygen is that two mechanisms are involved, each dependent upon collision energy. Evidence for the formation of $C_{70}O_2^{+\cdot}$ provides complimentary support for the proposed existence of $C_{60}O_2^{+\cdot}$.

As well as fragmenting to form the atomic adducts $C_{70}C^{+\cdot}$, $C_{70}N^{+\cdot}$ and $C_{70}O^{+\cdot}$, evidence for formation of the species $C_{69}{}^{13}C^{+\cdot}$, $C_{69}N^{+\cdot}$ and $C_{69}O^{+\cdot}$ was obtained. For collisions with carbon monoxide, nitric oxide and oxygen, $C_{69}O^{+\cdot}$ was found to optimise at an energy deficit, relative to the uncollided parent ion, equivalent to the amount of energy required for the formation of the full adduct and its subsequent decomposition to $C_{69}O^{+\cdot}$. The same mechanism was found to apply to the formation of $C_{69}N^{+\cdot}$ and $C_{69}{}^{13}C^{+\cdot}$ from collisions with nitric oxide, nitrogen and carbon monoxide. The similarity between N and C or C and ^{13}C and to a lesser extent O and C atoms permits the suggestion that the species $C_{69}{}^{13}C^{+\cdot}$, $C_{69}N^{+\cdot}$ and $C_{69}O^{+\cdot}$ could be dopey-balls *i.e.* a fullerene cage carbon could be replaced by a nitrogen, oxygen or ^{13}carbon atom. $C_{69}^{+\cdot}$ was also observed from collisions with oxygen containing target gases. This species is known to be unfavourable and the suggestion is that it was formed by the loss of CO from the adduct $C_{70}O^{+}$. The loss of CN from $C_{69}N^{+\cdot}$, in the case of nitric oxide, is deemed unlikely as $C_{69}^{+\cdot}$ was absent from collisions with nitrogen. $C_{67}N^{+\cdot}$ was observed from collisions with nitrogen providing support to the theory that $C_{69}N^{+\cdot}$ is a dopey-ball: as $C_{70}^{+\cdot}$ is already known to fragment with the loss of C_2 it follows that nitrogen-doped $C_{70}^{+\cdot}$ may do the same. $C_{68}^{+\cdot}$ was observed in many of the spectra showing target capture by fullerene radical cations. In looking at the species $C_{69}N^{+\cdot}$ and $C_{69}O^{+\cdot}$ formed from collisions with nitric oxide, the species $C_{68}NO^{+\cdot}$ was observed. An investigation into the energy deficit at which this species was observed showed that it formed by the loss of C_2 from the full adduct. The structure of this species remains unknown.

There was a broad peak at m/z = 824, observed at a laboratory-frame collision energy of 500 eV for collisions with nitric oxide and at laboratory-frame collision

energies of 300 eV, 500 eV and 750 eV for collisions with oxygen. This peak was not observed with carbon monoxide, the only other oxygen containing diatomic gas used, which has the strongest bond for the diatomic gases employed in this study: CO > NO > N_2 > O_2. The width of the peak at m/z = 824 indicated that it may be formed from a metastable process. The mass of the peak was found to correspond to the metastable decay of $C_{70}O^{+\cdot}$ to $C_{70}^{+\cdot}$.

8.2.3 Small Gaseous Hydrocarbons.

Multiatomic collision gases, like the diatomic collision gases produced a range of adducts on colliding with $C_{70}^{+\cdot}$. Methane produced adducts with $C_{70}^{+\cdot}$ that support conclusions drawn previously following methane/$C_{60}^{+\cdot}$ collisions [178]. The species $C_{70}CH_3^+$, $C_{70}CH_2^{+\cdot}$, $C_{70}CH^+$, and $C_{70}C^{+\cdot}$ were observed and confirmation of their assignment was obtained from the observation of equivalent adducts formed from collisions with perdeuterated methane and ^{13}carbon methane. Capture of the full methane molecule was not achieved. It is known that similar adducts are formed from the decomposition of a transient $C_{60}CH_4^{+\cdot}$ species during high-energy collisions of $C_{60}^{+\cdot}$ and methane [178]. It is proposed that the species $C_{70}CH_3^+$, $C_{70}CH_2^{+\cdot}$, $C_{70}CH^+$, and $C_{70}C^{+\cdot}$ are formed from the decomposition of a transient $C_{70}CH_4^{+\cdot}$ species. As the laboratory-frame collision energy was increased the species $C_{70}CH_2^{+\cdot}$ (or isotopic equivalent) became less intense and the species $C_{70}CH^{+\cdot}$ (or isotopic equivalent) became more dominant. It would therefore appear that increasing the collision energy increased the amount of fragmentation of the proposed transient $C_{70}CH_4^{+\cdot}$ species.

In the case of the larger gaseous hydrocarbons two groups of adduct peaks were observed. The group of peaks at 12 Da to 16 Da above the parent ion showed $C_{70}CH_2^{+\cdot}$ and $C_{70}CH^{+\cdot}$ as the dominant species. This lower mass cluster of peaks show that the carbon-carbon bonds are ruptured in the case of all of the larger hydrocarbons. Increasing the collision energy gave rise to the same trends between these species as observed previously with methane, *i.e.* increase in collision energy led

to a promotion of the smaller of the two adduct ions. The absence of a peak to correspond to the species $C_{70}CH_4^{+\cdot}$ from collisions with methane supports the conclusion that the peak at M+16 Da, observed following collision between $C_{70}^{+\cdot}$ and ethane or ethene, is not due to the addition of a CH_4 molecule to the fullerene cage but to the addition of H_2 and CH_2 species or $CH_3\cdot$ and $H\cdot$ to the cage. The observation of M+1 and M+2 satellite peaks, only observed from collision with ethane or ethene, gives support to this theory. The absence of M+15, $C_{70}CH_3^{+\cdot}$, from collisions with any of the larger hydrocarbons suggests the former possibility may be the case. The absence of this peak from collisions with ethane was surprising as the cleavage of the ethane carbon-carbon bond may be expected lead to $CH_3\cdot$ species being produced. It would appear that one or two hydrogens are lost in addition to the rupture of the carbon-carbon bond. The rupture of the carbon-carbon double bond in ethene, and of the double or single carbon-carbon bonds in propene, resulted in the the observation of the same species as with ethane. Ethyne fragmented from cleavage of its triple bond to give only one adduct that corresponded in mass to exactly half of the mass of ethyne.

The second cluster of adduct ions was around 24 Da, 25 Da, 28 Da and 29 Da above the parent ion, evidence that the carbon-carbon bonds in the gases can remain intact. The peaks at M+24 Da and M+28 Da were the most abundant. Ethane and ethene were the only gaseous hydrocarbons to give rise to the peak at M+28 Da. This peak was very intense when produced by ethane, especially at higher collision energies. Ethene only gave very weak evidence for this peak at the lowest of the collision energies investigated (300 eV in the laboratory-frame). The conclusion drawn with ethene is that at low collision energies the full adduct $C_{70}C_2H_4^{+\cdot}$ was produced and that increasing the collision energy leads to the decomposition of this species primarily into $C_{70}CH_2^{+\cdot}$ and then $C_{70}CH^{+\cdot}$. For collision with ethane the peak at M+28 Da (and the less abundant peak at M+29 Da) were only observed at higher collision energies where they were more abundant than the lower mass cluster of peaks. The observation that the larger adducts were more abundant than the smaller adducts at higher collision energies was also noted for the +24 Da peak. This appears counter-intuitive following

the conclusion drawn with methane, that at higher collision energies there is more fragmentation of a transient adduct. The conclusion with the diatomic gases when this trend was observed was that the larger adducts may be endohedral and the smaller adducts may be exohedral, formed from the decomposition of full exohedral adducts, transient in the case of carbon monoxide and nitrogen. Once more different mechanisms seem to be involved in producing the lower mass group of peaks and the higher mass group of peaks. Following the conclusion that the full ethene adduct forms and decomposes on increasing the collision energy, it is tentatively proposed that the lower mass cluster of peaks may result from the formation of the full adduct, which like methane would be a transient species that then decomposes into the smaller observed adducts. The observation that M+24 was only produced from collisions with unsaturated hydrocarbon gases is an indication of the strength of unsaturated bonds compared to saturated bonds. This peak, predominant at higher collision energies, suggests that a C_2 species may be penetrating the fullerene cage, but that the hydrogen atoms from ethene and ethyne, and the hydrogen and the CH_3 from propene are lost during this process. There is some evidence that one hydrogen remains associated to the adduct when the target gas is ethene. The observation that M+28 was formed predominantly at higher collision energies with ethane does not fit in with this proposal. It is suggested that under these collision conditions C_2H_4 may add on to the fullerene cage across a double bond of the cage in the same way as oxygen does [107-110], although there is not evidence for this in the spectra.

No adducts were observed following collisions of $C_{70}^{+\cdot}$ with tetrafluoromethane. Nor were any fragment ions observed that may have originated if a transient species were produced prior to decomposition. The tenuous observation of a krypton/$C_{70}^{+\cdot}$ adduct but the clear evidence for fragments of a krypton/$C_{70}^{+\cdot}$ adduct leads to the conclusion that CF_4 is too big to be trapped by $C_{70}^{+\cdot}$ and yet too unreactive to be exohedrally attached to the fullerene. The proposal that krypton (which has approximately the same mass as CF_4 and is also inert) is endohedrally bound by the fullerene is thus supported.

8.2 Target Capture by Protonated Peptides.

The capture of molecular gases was also achieved with peptide ions. Bombesin and alytesin were shown to form adduct ions following high-energy collisions with methane. For both peptides, an adduct was observed at M+15 with methane. Investigations using deuterated methane and ^{13}carbon methane lead to the conclusion that the observed species were the addition of CH_3 from methane to the protonated peptide ion which had lost a hydrogen atom, *i.e.* $MH+CD_4$-H-D in the case of collisions with deuterated methane. The best results were obtained from laboratory-frame collision energies which had corresponding centre-of-mass collision energies between 12 eV and 24 eV. This supports the results obtained by Fenselau *et al.* [183]. When larger energy deficits, relative to the uncollided parent ion, were investigated the adduct ion still remained in evidence. It was apparent from the spectra that the adduct ion might be increasing in intensity, relative to the protonated peptide, as the energy deficit from the parent ion energy was increased. Thus the adduct did not appear to optimise in intensity, relative to the parent ion, at energy deficits equivalent to the centre-of-mass collision energy.

8.3 Collision-Induced Decomposition of Protonated Peptides.

The protonated peptides bombesin and alytesin, found to capture the molecular target gas methane under particular conditions, were made to under go collision-induced decomposition by increasing the energy involved in the collision. High-energy collisions produced almost complete series of a-type and d-type ions in the case of both peptides. Noted exceptions corresponded to the position of glycine in the amino acid sequence. This has been discussed elsewhere [155]. For CID by noble gases, increasing the centre-of-mass collision energy by increasing the mass of the gas, produced increased fragmentation of the peptide ions. Argon was observed to give the largest range of intense fragment ion peaks which supports observations by Neumann *et al.* [54]. When the translational energy losses by protonated bombesin from

collisions with the noble gases were measured, no distinct trends were observed by increasing the mass of the gas. The translational energy losses were of the order of tens of electron volts. Increasing the laboratory-frame collision energy showed the greatest difference with helium by producing a greater number of fragment ions; there was little effect when the laboratory-frame collision energy was increased for the other noble gases. Methane was found to be the best collision gas with regards to the fragmentation pattern obtained. The translational energy loss by protonated bombesin from collisions with methane were comparable to those obtained with helium and neon. The internal energy uptake by protonated bombesin as calculated by ICT theory [75-76], showed methane was more comparable to helium. It would appear that the mass of the gas or the centre-of-mass collision energy are not the only important factors to be considered for the choice of collision conditions for protonated peptides. The *'mass-match'* of the individual atoms that constitute the peptide and collision gas must also be taken into account. In conclusion methane would appear to be the best collision gas, out of those investigated, for the fragmentation of protonated bombesin and alytsein.

References.

[1] JJ Thomson; *Phil. Mag. VI*, 1910, 18, 824.

[2] JA Hipple and EU Condon; *Phys.Rev.*, 1945, 68, 54.

[3] KR Jennings; *Int. J. Mass Spectrom. Ion Phys.*, 1968, 1, 227.

[4] WF Haddon and FW McLafferty; *J. Am. Chem. Soc.*, 1968, 90, 4745.

[5] HM Rosenstock and CE Melton; *J. Chem. Phys.*, 1957, 26, 314.

[6] FW Aston; *Phil. Mag. VI*, 1920, 39, 449.

[7] AJ Dempster; *Phys. Rev.*, 1922, 20, 631.

[8] GA Valaskovic, NL Kelleher, DP Little and FW McLafferty; *Anal. Chem.*, 1995, 67, 3802.

[9] AJ Dempster; *Phys. Rev.*, 1918, 11, 316.

[10] MSB Munson and FH Field; *J. Am. Chem. Soc.*, 1966, 88, 2621.

[11] M Barber, RS Bordoli, RD Sedgwick and AN Tyler; *J. Chem. Soc. Chem. Commun.*, 1881, 7, 325.

[12] M Barber, RS Bordoli, RD Sedgwick and AN Tyler; *Nature*, 1981, 293, 270.

[13] W Aberth, KM Straub and AL Burlingame; *Anal. Chem.*, 1982, 54, 2029.

[14] AM Falick, GH Wang and FC Walls; *Anal. Chem.*, 1986, 58, 1308.

[15] M Karas and F Hillenkamp; *Anal. Chem.*, 1988, 60, 2299.

[16] RC Beavis; *Org. Mass Spectrom.*, 1992, 27, 653.

[17] DF Torgerson, RP Skowronski and RD McFarlane; *Biochem. and Biophys. Res. Commun.*, 1974, 60, 616.

[18] JB Fenn, M Mann, CK Meng, SF Wong and CM Whitehouse; *Science*, 1989, 246, 64.

[19] M Mann; *Org. Mass Spectrom.*, 1990, 25, 575.

[20] P Kebarle and L Tang; *Anal. Chem.*, 1993, 65, 973.

[21] JJ Carmody, CR Blakely and ML Vestal; *29th Annual Conference on Mass Spectrometry*, Minneapolis, 1981, 156.

[22] HD Beckey; *Int. J. Mass Spectrom. Ion Phys.*, 1969, 2, 500.

[23] AO Nier; *Rev. Sci. Instrum.*, 1940, 11, 212.

[24] AO Nier and TR Roberts; *Phys. Rev.*, 1951, 81, 507.

[25] W Paul and H Steinwedel; *Z. Natursforsch.*, 1953, 8a, 448.

[26] W Paul and M Raether; *Z. Phys.*, 1955, 140, 262.

[27] VI Karateav, BA Mamyrin and DV Schmikk; *Sov. Phys. Tech. Phys.*, 1972, 16, 1177.

[28] W Gohl, R Kutscher, HJ Lane and H Wollnik; *Int. J. Mass Spectrom. Ion Phys.*, 1982, 48, 411.

[29] PH Dawson, JB French, JA Buckley, DJ Douglas and D Simmons; *Org. Mass Spectrom.*, 1982, 17, 205.

[30] H Sommer, HA Thomas and JA Hipple; *Phys. Rev.*, 1949, 76, 1877.

[31] H Sommer, HA Thomas and JA Hipple; *Phys. Rev.*, 1951, 82, 697.

[32] JJ Thomson; *"Rays of Positive Electricity and Their Applications to Chemical Analysis"*, Longmans, London, 1913.

[33] FW Aston; *Proc. Chem. Phil. Soc.*, 1919, 19, 317.

[34] MB Comisarow and AG Marshall; *Chem. Phys. Letts.*, 1974, 25, 282.

[35] MB Comisarow and AG Marshall; *Chem. Phys. Letts.*, 1974, 26, 489.

[36] *"Practical Mass Spectrometry."*, BS Middleditch (ed.), Plenum Press, New York, 1979.

[37] *"Mass Spectrometry: Applications in Science and Engineering."*, FA White and GM Wood, John Wiley and Sons, Inc., 1986.

[38] *"Detectors."*, by S Evans in *"Methods in Enzymology."*, JA Mcloskey (ed.) vol. 193 (Mass Spectrometry), Academic Press, Inc.,San Diego, 1990.

[39] *"Tandem Mass Spectrometry."*, FW McLafferty (ed.), Wiley Interscience Publication, 1983.

[40] *"Mass Spectrometry/Mass Spectrometry: Techniques and Applications of Tandem Mass Spectrometry."*, KL Busch, GL Glish and SA McLuckey, VCH Publishers, Inc., 1988.

[41] *"Mass Analysers."*, by KR Jennings and GG Dolnikowski in *"Methods in Enzymology."*, JA Mcloskey (ed.) vol. 193 (Mass Spectrometry), Academic Press, Inc.,San Diego, 1990.

[42] *"Metastable Ions."*, RG Cooks, JH Beynon, RM Capriloi and GR Lister, Elsiever, Amsterdam, 1973.

[43] DJ Bell, MD Brightwell, M Haran, WA Neville and A West; *Org. Mass Spectrom.*, 1991, 26, 454.

[44] RK Boyd; *Int. J. Mass Spectrom. and Ion Proc.*, 1987, 75, 243.

[45] RK Boyd, CJ Porter and JH Beynon; *Org. Mass Spectrom.*, 1981, 16, 490.

[46] K Sato, T Asada, M Ishihara, F Kunitiro, Y Kammei, E Kubota, CE Costello, SA Martin HA Scoble and K Biemann; *Anal. Chem.*,1987, 59, 1652.

[47] RK Boyd, DJ Harvan and JR Mass; *Int. J. Mass Spectrom. Ion Proc.*, 1985, 65, 273.

[48] AP Bruins, KR Jennings and S Evans; *Int. J. Mass Spectrom. Ion Proc.*, 1978, 26, 395.

[49] *"Collision Spectroscopy."*, RG Cooks, Plenum Press, New York, 1978.

[50] RK Boyd, EE Kingston, AG Brenton and JH Beynon; *Proc. R. Soc. London Ser. A*, 1984, 59, 392.

[51] JH Beynon, RG Cooks, JW Amy, WE Baiting and TY Ridley; *Anal. Chem.*, 1973, 45, 1023a.

[52] K Levsen and H Schwarz; *Mass Spectrom. Rev.*, 1983, 2, 77.

[53] FA Lindemann; *Trans. Faraday Soc.*, 1922, 17, 598.

[54] GM Neumann, MM Sheil and PJ Derrick; *Z. Natursforsch.*, 1984, 39a, 584.

[55] JH Beynon; *Proc. R. Soc. Lond. Ser. A*, 1981, 378, 1.

[56] DL Bunker and FM Wang; *J. Am. Cem. Soc.*,1977, 99 7457.

[57] HM Rosenstock, MB Wallenstein, AL Wahrhaftig and H Eyring; *Proc. Nat. Acad. Sci. USA*, 1952, 38, 667.

[58] *"Unimolecular Dissociations of Gaseous Ions."* by AL Wahrhaftig in *"Gaseous Ion Chemistry and Mass Spectrometry."*, JH Futrell (ed.), Wiley Interscience Publication, 1986.

[59] J Durup in *"Recent Developments in Mass Spectrometry."*, K Ogata and T Hagakawa (eds.), University Park Press, Baltimore, 1970.

[60] H Yamaoka, D Pham and J Durup; *J. Phys. Chem.*, 1969, 51, 3465.

[61] HWS Massey; *Rep. Prog, Phys.*, 1949, 12, 248.

[62] MS Kim; *Org. Mass Spectrom.*, 1991, 26, 565.

[63] GM Neumann and PJ Derrick; *Org. Mass Spectrom.*, 1984, 19, 165.

[64] MM Sheil and PJ Derrick; *Org. Mass Spectrom.*, 1988, 23, 429.

[65] RG Gilbert, MM Sheil and PJ Derrick; *Org. Mass Spectrom.*, 1985, 20, 431.

[66] RG Gilbert, MM Sheil and PJ Derrick in *"Advances in Mass Spectrometry."*, JFJ Todd (ed.), Wiley, Chichester, 1986.

[67] CD Bradley and PJ Derrick; *Org. Mass Spectrom.*, 1991, 26, 395.

[68] CD Bradley, JM Curtis, PJ Derrick and B Wright; *Anal. Chem.*, 1992, 64, 2628.

[69] R Guevremont and RK Boyd; *Rapid Commun. in Mass Spectrom.*, 1988, 2, 1.

[70] DL Bricker and DH Russel; *J. Am. Chem. Soc.*, 1986, 108, 6174.

[71] AL Alexander, P Thibault and RK Boyd; *J. Am. Chem. Soc.*, 1990, 112, 2484.

[72] RK Boyd, CE Kingston, AG Brenton and JH Beynon; *Proc. R.. Soc. Lond. Ser. A*, 1984, 392, 59.

[73] A Russek; *Physica*, 1970, 48, 165.

[74] MM Sheil, E Uggerud and PJ Derrick; *Adv. in Mass Spectrom.*, 1989, 11, 1012.

[75] E Uggerud and PJ Derrick; *J. Phys. Chem.*, 1991, 95, 1430.

[76] HJ Cooper, PJ, Derrick, HDB Jenkins and E Uggerud; *J. Phys. Chem.*, 1993, 93, 5443.

[77] MF Jarrold and JE Bower; *J. Chem. Phys.*, 1992, 96, 9180.

[78] MF Jarrold and EC Honea; *J. Phys. Chem.*, 1991, 95, 9181.

[79] MF Jarrold and JE Bower; *J. Am. Chem. Soc.*, 1992, 114, 459.

[80] CD Bradley and PJ Derrick; *Org. Mass Spectrom.*, 1993, 28, 390.

[81] CD Bradley, JM Curtis, PJ Derrick and MM Sheil, *J. Chem. Soc. Faraday Trans.*, 1994, 90, 239.

[82] GL Shield; *Personal Commun.*,1994.

[83] CD Bradley, PhD Thesis, University of Warwick, Coventry, UK, 1992.

[84] JA Laramee, P Cameron and RG Cooks; *J. Am. Chem. Soc.*, 1981, 103, 12.

[85] RS Bordoli and RH Bateman; *Int. J. Mas Spectrom. Ion Proc.*, 1992, 122, 243.

[86] J Bordas-Nagy, D Despeyroux, KR Jennings and SJ Gaskell; *Org. Mass Spectrom.*, 1992, 27, 406.

[87] J Bordas-Nagy, D Despeyroux and KR Jennings; *J. Am. Soc. Mass Spectrom.*, 1992, 3, 502.

[88] K Vekey and G Czira; *Org. Mass Spectrom.*, 1993, 28, 546.

[89] K Vekey and K Ludanyi; *Org. Mass Spectrom.*, 1994, 29, 615.

[90] RK Boyd, DJ Harvan and JR Hass; *Int. J. Mass Spectrom. Ion Proc.*, 1985, 65, 273.

[91] *"Physical Chemistry."*, by RS Berry, SA Rice and J Ross (eds.) with the assistance of GP Flynn and JN Kushick, John Wiley and Sons, Inc., 1980.

[92] HW Kroto, JR Heath, SC O'Brien, RF Curl and RE Smalley; *Nature*, 1985, 318, 162.

[93] HW Kroto; *Nature*, 1987, 329, 529.

[94] JM Hawkins, A Meyer, TA Lewis, S Loren and FJ Hollander; *Science*, 1991, 252, 312.

[95] H Schwarz; *Angew. Chem. Int. Ed. Engl.*, 1993, 32, 1412.

[96] SW McElvany amd MM Ross; *J. Am. Soc. Mass Spectrom.*, 1992, 3, 268.

[97] GA Olah, I Bucsi, C Lambert, R Aniszfeld, NJ Trivedi, DK Sensharma and GK Surya Prakash; *J. Am. Chem. Soc.*, 1991, 113, 9385.

[98] PJ Fagan, JC Calabrese and B Malone; *Acc. Chem. Res.*, 1992, 25, 134.

[99] SZ Kan, SA Lee, YG Byun and BS Freiser; *J. Mass Spectrom.*, 1995, 30, 194.

[100] SZ Kan, YG Byun and BS Freiser; *J. Am. Chem. Soc.*, 1995, 117, 1177.

[101] JM Wood, B Kahr, SH Hoke, L Dejarme, RG Cooks and D Ben-Amotz; *J. Am. Chem. Soc.*, 1991, 113, 5907.

[102] JH Callahan, SW McElvany and MM Ross; *Int. J. Mass Spectrom. Ion Proc.*, 1994, 138, 221.

[103] JW Bausch, GK Surya Prakash, GA Olah, DS Tse, DC Lorents, YK Bae and R Malhotra; *J. Am. Chem. Soc.*, 1991, 113, 3205.

[104] AG Avent, PR Birkett, C Christides, JD Crane, AD Darwish, PB Hitchcock, HW Kroto. MF Prassides, R Taylor and DRM Walton; *J. Molec. Struct.*, 1994, 325, 1.

[105] F Wudl; *Acc. Chem. Res.*, 1992, 25, 157.

[106] G Chen, RG Cooks, E Corpuz and LT Scott; *J. Am. Soc. Mass Spectrom.*, 1996, 7, 618.

[107] K Raghavachari; *Chem. Phys. Letts.*, 1992, 195, 221.

[108] M Menon and KR Subbaswamy; *Chem. Phys. Letts.*, 1993, 201, 321.

[109] K Raghavachari; *Chem. Phys. Letts.*, 1993, 209, 223.

[110] KM Creegan, JL Robbins, WK Robbins, JM Millar, RD Sherwood, PJ Tindall, DM Cox, AB Smith, JP McCauley, DR Jones and RT Gallagher; *J. Am. Chem. Soc.*, 1992, 114, 1103.

[111] T Weiske, DK Bohme, J Hrusak, W Kratschmer and H Schwarz; *Angew.Chem. Int. Ed. Engl.*, 1991, 30, 884.

[112] JR Heath, SC O'Brien, Q Zhang, Y Liu, RF Curl, HW Kroto, FK Tittel and RE Smalley; *J. Am. Chem. Soc.*, 1985, 107, 7779.

[113] DM Cox, DJ Trevor, KC Reichman and A Kaldor; *J. Am. Chem. Soc.*, 1986, 108, 2457.

[114] Y Chai, T Guo, C Jin, R.E Haufler, L.P.F Chibante, J Fure, L Wang J.M Alford and R.E Smalley; *J. Phys. Chem.*, 1991, 95, 7564.

[115] JF Christian, Z Wan, SL Anderson; *J. Chem. Phys.*, 1993, 99, 3468.

[116] M Saunders, HA Jimenez-Vazquez, RJ Cross and RJ Poreda; *Science*, 1993, 259, 1428.

[117] M Saunders, HA Jimenez-Vazquez, RJ Cross, S Mroczkowski, ML Gross, DE Giblin and RJ Poreda; *J. Am. Chem. Soc.*, 1994, 116, 2193.

[118] BA DiCamillo, RL Hettich, G Giochon, RN Compton, M Saunders, HA Jimenez-Vazquez, A Khong and RJ Cross; *J. Phys. Chem.*, 1996, 100, 9197.

[119] L Pang and F Brisse; *J. Phys. Chem.*, 1993, 97, 8562.

[120] MS Son and YK Sung; *Chem. Phys. Letts.*, 1995, 245, 113.

[121] J Ciowlowski; *J. Am. Chem. Soc.*, 1991, 113, 4139.

[122] *"Science of Fullerenes and Carbon Nanotubes."* by MS Dresselhaus, G Dresselhaus and PC Eklund, Academic Press, Inc., 1996.

[123] RD Johnson, DS Bethune and CS Yannoni; *Acc. Chem. Res.*, 1992, 25, 169.

[124] AV Nikolaev, TJS Dennis, K Prassides and AK Soper; *Chem. Phys. Letts.*, 1994, 223, 143.

[125] T Guo, C Jin and R.E Smalley; *J. Phys. Chem.*, 1991, 95, 4948.

[126] W Andreoni, F Gygi and M Parrinello; *Chem. Phys. Letts.*, 1992, 190, 159.

[127] I Lamparth, B Nuber, G Schick, A Skiebe, T Grosser and A Hirsch; *Angew. Chem. Int. Ed. Engl.*, 1995, 34, 2257.

[128] *"Perfect Symmetry, The Accidental Discovery of Buckminsterfullerene."*, J Baggot, Oxford University Press, Inc., 1996.

[129] PM Ajayan and S Iijima; *Nature*, 1993, 361, 333.

[130] S Iijima; *Nature*, 1991, 354, 56.

[131] D Ugarte; *Nature*, 1992, 359, 707.

[132] FG Hopwood, IG Dance, KJ Fisher, GD Willet, MA Wilson, LSK Pang and JV Hanna; *Org. Mass Spectrom.*, 1992, 27, 1006.

[133] SH Friedman, DL DiCamp, R Sijbesma, F Wudl and GL Kenyon; *J. Am. Chem. Soc.*, 1993, 115, 6506.

[134] R Sijbesma, G Srdanov, F Wudl, JA Castoro, C Wilkins, SH Friedman, DL DiCamp and GL Kenyon; *J. Am. Chem. Soc.*, 1993, 115, 6510.

[135] The Times, 10th October 1996, pgs 1, 7.

[136] W Kratschmer, LD Lamb, K Fostiropoulos and DR Huffman; *Nature*, 1990, 347, 354.

[137] B Schnider and H Budzikiewicz; *Rapid Commun. in Mass Spectrom.*, 1990, 4, 552.

[138] L Michalak, KJ Fisher, DS Aldernice DR Jardine and GD Willet; *Org. Mass Spectrom.*, 1994, 29, 512.

[139] SR Wilson and Y Wu; *Org. Mass Spectrom.*, 1994, 29, 186.

[140] H Ajie, MM Alvarez, SJ Anz, RD Beck, F Diederion, K Fostiropoulos, DR Huffman, W Kratschmer, Y Rubin, KE Schriver D Sensharma amd RL Whetten; *J. Phys. Chem.*, 1990, 94, 8630.

[141] JM Miller and LZ Chen; *Rapid Commun. in Mass Spectrom.*,1992, 6, 184.

[142] A Mandelbaum and A Etinger; *Org. Mass Spectrom.*, 1993, 28, 487.

[143] AB Young, LM Cousinsand AG Harrison; *Rapid Commun. in Mass Spectrom.*,1991, 5, 226.

[144] T Drewello, KD Asmus, J Starch, R Herzschuh, M Kao and CS Foote; *J. Phys. Chem.*, 1991, 95, 10554.

[145] RJ Doyle and MM Ross; *J. Phys. Chem.*, 1991, 95, 4954.

[146] H Morand, S Hoke, M Eberlin, G Payne and RG Cooks; *Org. Mass Spectrom.*, 1992, 27, 284.

[147] SW McElvany, MM Ross and JH Callahan; *Acc. Chem. Res.*, 1992, 25, 162.

[148] PF Greenwood; *Org. Mass Spectrom.*, 1994, 29, 61.

[149] KH McHale, MJ Polce and C Wesdemiotis; *J. Mass Spectrom.*, 1995, 30, 33.

[150] C Lifshitz, M Iraqi, T Peres and JE Fischer; *Rapid Commun. in Mass Spectrom.*,1991, 5, 238.

[151] SC O'Brien, JR Heath, RF Curl, RE Smalley; *J. Chem. Phys.*, 1988, 88, 220.

[152] QL Zhang, SC O'Brien, JR Heath, RF Curl, HW Kroto and RE Smalley; *J. Phys. Chem.*, 1986, 90, 525.

[153] J Wang, V Baranov and DK Bohme; *J. Am. Soc. Mass Spectrom.*, 1996, 7, 260.

[154] K Biemann; *Biomed. and Environ. Mass Spectrom.*, 1988, 16, 99.

[155] SA Martin and K Biemann; *Int. J. Mass Spectrom. Ion Proc.*, 1987, 78, 213.

[156] P Roepstorff and J Fohlman; *Biomed Mass Spectrom.*, 1984, 11, 601.

[157] RS Johnson, SA Martin and K Biemann; *Int. J. Mass Spectrom. Ion Proc.*, 1988, 86, 137.

[158] AG Craig and JE Rivier; *Org. Mass Spectrom.*, 1992, 27, 549.

[159] TD Lee and S Vemuri; *Biomed. and Environ. Mass Spectrom.*, 1990, 19, 639.

[160] *"Four-Sector Tandem Mass Spectrometry of Peptides."* by AE Ashcroft and PJ Derrick in *"Mass Spectrometry of Peptides"*, DM Desiderio (ed.), CRC Press Inc., 1991.

[161] MM Ross and JH Callahan; *J. Phys.Chem.*, 1991, 95, 5720.

[162] T Weiske, T Wang, W Kratschmer, JK Terlouw and H Schwarz; *Angew. Chem. Int. Ed. Engl.*, 1992, 31, 183.

[163] JH Callahan, MM Ross, T Weiske and H Schwarz; *J. Phys. Chem.*, 1993, 97, 20.

[164] T Weiske, J Hrusak, DK Bohme and H Schwarz; *Chem. Phys. Letts.*,1991, 186, 459.

[165] T Weiske, DK Bohme and H Schwarz; *J. Phys. Chem.*, 1991, 95, 8451.

[166] T Weiske and H Schwarz; *Angew. Chem. Int. Ed. Engl.*, 1992, 31, 605.

[167] KA Caldwell, DE Giblin CS Hsu, DM Cox and ML Gross; *J. Am. Chem. Soc.*, 1991, 113, 8519.

[168] Z Wan, JF Christian and SL Anderson; *J. Chem. Phys.*, 1992, 96, 3344.

[169] JF Christian, Z Wan and SL Anderson; *J. Phys. Chem.*, 1993, 99, 3486.

[170] KA Caldwell, DE Giblin and ML Gross; *J. Am. Chem. Soc.*, 1992, 114, 3743.

[171] T Weiske, J Hrusak, D.K Bohme and H Schwarz; *Helv. Chim. Acta*, 1992, 75, 79.

[172] JJ Stry and JF Garvey; *Int. J. Mass Spectrom. Ion Proc.*, 1994, 138, 241.

[173] H Spang, A Mahlkow and EEB Campbell; *Chem. Phys. Letts.*,1994, 227, 91.

[174] T Weiske, H Schwarz, D.E Giblin and M.L Gross; *Chem. Phys. Letts.*,1994, 227, 87.

[175] T Weiske, H Schwarz, A Hirsch and T Grosser; *Chem. Phys. Letts.*,1992, 199, 640.

[176] CN McEwen, RG McKay and BS Larsen; *J. Am. Chem. Soc.*, 1992, 114, 4413.

[177] S Petrie, G Javahery, J Wang and DK Bohme; *J. Phys. Chem.*, 1992, 96, 6121.

[178] HJ Cooper, RT Gallagher, PF Greenwood, T Vulpius and PJ Derrick; *J. Chem. Soc., Chem. Commun.*, 1995, 1459.

[179] JF Christian, Z Wan and SL Anderson; *Chem. Phys. Letts.*, 1992, 199, 373.

[180] JF Christian, Z Wan and SL Anderson; *J. Phys. Chem.*, 1992, 96, 10597.

[181] JF Christian, Z Wan and SL Anderson; *Int. J. Mass Spectrom. Ion Proc.*, 1994, 138, 173.

[182] HJ Cooper; PhD Thesis, University of Warwick, Coventry, UK, 1995.

[183] X Cheng and C Fenselau; *J. Am. Chem. Soc.*, 1993, 115, 10327.

[184] Kratos Analytical, Barton Dock Road, Urmston, Manchester, UK.

[185] CG Johnson ans AO Nier; *Phys. Rev.*, 1953, 91, 10.

[186] Sun Microsystems LTD., City Gate Cross Street, Sale, Cheshire, UK

[187] S Chen, PJ Derrick, FA Mellon and KR Price; *Anal. Biochem.*, 1994, 218, 157.

[188] Sigma-Aldrich Chemical Company LTD., Fancy Road, Poole Dorset, UK.

[189] BDH, Merek LTD., Magna Park, Lutterworth, Leicestershire, UK

[190] RS Components, PO Box, Corby, Northants, UK

[191] C Fenselau and RJ Cotter; *Chem. Rev.*, 1987, 87, 501.

[192] Fisons, Bishop Meadow Road, Loughborough, Leicestershire, UK

[193] JL Witten, MH Schaffer, M O'Shea, JC Cook, ME Hemling and KL Rinehart; *Biochem. and Biophys. Res. Commun.*, 1984, 124, 350.

[194] CSIRO, Dept of Petroleum Resources, PO Box 126, Nth Ryde 2113, New South Wales, Australia

[195] BOC Special Gases, The Priestly Centre, 10 Priestly Road, Surrey Research Park, Guilford, Surrey, UK

[196] Fluorochem LTD., Wesley Street, Old Glossop, Derbyshire, UK

[197] G Bertaccini, V Erspamer, P Melchiorri and N Sopranzi; *Br. J. Pharmac.*, 1974, 52, 219.

[198] V Erspamer, G Improta, P Melchiorri and N Sopranzi; *Br. J. Pharmac.*, 1974, 52, 227.

[199] SR Nagalla, BW Gibson, D Tang, JR Reeve and ER Spindel; *J. Biol. Chem.*, 1992, 267, 6916.

[200] JE Rivier and MR Brown; *Biochem.*, 1978, 17, 1767.

[201] V Erspamer, GF Erspamer and M Inselvini; *J. Pharm. Pharmacol.*, 1970, 22, 875.

[202] A Anastasi, V Erspamer and M Bucci; *Experientia*, 1971, 27, 166.

[203] JA Mosely, HJ Cooper, RT Gallagher and PJ Derrick; *Eur. Mass Spectrom.*, 1995, 1, 501.